Inaugural dissertation

for

obtaining the doctoral degree

of the

Combined Faculty of Mathematics, Engineering and Natural Sciences

Of the

Ruprecht-Karls-University

Heidelberg

Presented by

Camila Micaela Metz Zumarán, M. Sc.

Born in Darmstadt, Germany

Oral examination: December 15th, 2023

# The impact of the population context on virus infection, IFN response, and homeostatic immune signaling in mucosal epithelial cells

Referees:

Prof. Dr. Oliver Fackler

Prof. Dr. Steeve Boulant

# Table of contents

## Acknowledgments

This work was conducted under the supervision of Prof. Dr. Steeve Boulant in the Virology Department of University Hospital Heidelberg and in the Department of Molecular Genetics and Microbiology at the University of Florida, and was supported by the DFG.

I want to express my great gratitude to Steeve for giving me the opportunity to perform my PhD in his group and to work on such interesting and versatile projects. I feel inspired by your passion for science, which motivated me to keep working hard and not lose my curiosity. I learned to think outside the box, to develop and plan projects, and tackle problems from a different angle than usual. I also thank you for your advice outside my professional life, and your understanding of personal matters. My gratitude also goes to my co-supervisor Megan. You thought me to work independent, pay attention to detail, think ahead and always be at the best of my performance. I admire your strength in managing all aspects in life, and you showed me how we need to fight as women to get to the top. Thanks to the both of you for your support, and to help me become more confident and a good professional.

I want to thank Prof. Dr. Oliver Fackler for being my first examiner, always helpful and approachable. Thank you for the scientific discussions and guidance through the formal PhD process. I am also thankful to Dr. Ada Cavalcanti-Adam and Dr. Frederik Graw for the great support and the valuable input during my TAC meetings. Your comments were important to steer the project in the right direction. My gratitude extends to Dr. Marco Binder and Prof. Dr. Nina Papavasiliou for agreeing and taking the time to examine my thesis. Additionally, I would like to acknowledge the CIID in Heidelberg (Germany) and the Department of Molecular Genetics and Microbiology in Gainesville (Florida, USA), and all current and former colleagues part of these institutes for providing a stimulating research environment with excellent facilities.

This PhD would of course not have been possible without all the members of the Boulant/Stanifer lab: thank you for all the scientific discussion and, much more importantly, for the friendly atmosphere, emotional supports and super fun times. I am so grateful that everyone received me in such a warm way, you made all those days and nights we spent together very enjoyable. I am so grateful to have met Carmon and Patricio, in which I found dearest friends that I will have for life. You were my little family in Heidelberg. You still support me in the worst times without judgment, always cheer me up and make me realize that everything is not that bad. I had amazing days and nights with you guys! From the Heidelberg lab I also want thank Jose, Markus and Nick, and their omnipresent friendship. Of course the Florida lab has been as amazing, and a big thank to all my colleagues for making me feel at home here and finding new friends. A special thanks goes to Zina for supporting me as a friend, her ever-present love for science, and all the help with the thesis and projects, although she herself had so much work on her own plate. To Sorin for the interesting scientific input, her knowledge about literally everything, making me see different aspects in life and welcoming me so warmly in Florida. To Gigi, you are such a good friend and you made me realize how much a person can reach by working hard; I learned how to see a different perspective of daily life from you. To James for all the help inside and outside the lab in these 2 years, and making me feel immensely welcome here. And to Yagmur, for starting this challenging journey in US with me and for the large scientific help, without which my project wouldn't be where it is. It was a pleasure to be part of the Boulant/Stanifer team all this years, I am grateful that I could meet such amazing people.

This journey would definitely not have been possible without my family and friends, which never left my side. An enormous thank you goes to Manuel; throughout the years you were my rock. You were the person that understood this journey the most, that believed in me, and made me feel that I had the strength to be successful as a woman in a world of men. Over the years you helped me grow personally and professionally, and supported all of my steps. I have such an immense gratitude towards you. I want to thank my entire family for your unconditional support from everywhere in the world. A special thanks goes to my parents Teresa and Uli. Ustedes me equiparon con tantas buenas cualidades en esta vida y me hicieron como soy. Les estoy inmensamente agradecida por su soporte incondicional en todos los aspectos y siempre; no puedo imaginarme padres mejores. Obviamente agradezco demasiado a mi hermana Verena, tú sabes que eres lo mejor que me ha pasado, no sería yo sin ti. Y sin tu inteligencia emocional y entendimiento de mi persona no me entendería ni yo. ¡Gracias por tu apoyo incondicional! I want to also thank all my incredible friends that had a significant impact in my PhD and are my chosen family: ¡Gracias Jaz y Manu, son las mejores amigas que una puede tener, y gracias por estar allí para mí a lo cerca y a la distancia, las adoro! Vielen Dank Clarita, ich spüre Deine Liebe immer und schätze unheimlich Deine Ratschläge und Deine Art zu Denken. Danke an Adrian, Joscha, Greta und Jaro, ihr seid meine Familie und habt mich unheimlich viel unterstützt, und ich freue mich auf die nächsten Jahre mit euch! Y gracias Franco, por tu ayuda incondicional y entendimiento de mi persona, me hiciste conocerme mejor y salir adelante.

This has been an incredible journey with lots of ups and downs, and I am grateful for the unwavering support of so many brilliant individuals! I am excited to start a new chapter in my life and keep contributing to the field, and much more important to me, to fight for professional equality and demonstrate that women can also make it.

## Publications

### Accepted first author publication:

**C. Metz-Zumaran***, C. Kee*, P. Doldan*, C. Guo, M. L. Stanifer and S. Boulant. Increased Sensitivity of SARS-CoV-2 to Type III Interferon in Human Intestinal Epithelial Cells. *Journal of Virology* (2022). 96(7):e0170521, doi: 10.1128/jvi.01705-21. (Research Article) **Indicates shared first authors*

### Submitted or in preparation first author publications:

**C. Metz-Zumaran**, Z. M. Uckeley, P. Doldan, F. Muraca, Y. Keser, P. Lukas, B. Kuropka, L. Küchenhoff, S. Rastgou Talemi, T. Höfer, C. Freund, E. A. Cavalcanti-Adam, F. Graw, M. Stanifer and S. Boulant. Population context drives cell-to-cell variability in interferon response in epithelial cells. Research article in revision in *Molecular System Biology* (2023). Pre-print doi: 10.1101/2023.05.22.541682. (Research Article)

**C. Metz-Zumaran**, Z. M. Uckeley, Y. Keser, D. Doncevic, C. Herrmann, M. Stanifer and S. Boulant. Homeostatic IFNλ3 expression is controlled by the population context in epithelial cells and serves as an additional layer of protection against virus infection. *Manuscript in preparation* (2023). (Research Article)

### Co-author publications:

M. L. Stanifer, C. Kee, M. Cortese, **C. Metz-Zumaran**, S. Triana, M. Mukenhirn, H. G. Kraeusslich, T. Alexandrov, R. Bartenschlager and S. Boulant. Critical Role of Type III Interferon in Controlling SARS-CoV-2 Infection in Human Intestinal Epithelial Cells. *Cell Reports* (2020). 32(1):107863, doi: 10.1016/j.celrep.2020.107863. (Research Article)

S. Triana, **C. Metz-Zumaran**, C. Ramirez, C. Kee, P. Doldan, M. Shahraz, D. Schraivogel, A. R. Gschwind, A. K. Sharma, L. M. Steinmetz, C. Herrmann, T. Alexandrov, S. Boulant and M. L. Stanifer. Single-cell analyses reveal SARS-CoV-2 interference with intrinsic immune response in the human gut. *Molecular System Biology* (2021). 17(4):e10232, doi: 10.15252/msb.202110232. (Research Article)

S. Triana*, M. L. Stanifer*, **C. Metz-Zumaran**, M. Shahraz, M. Mukenhirn, C. Kee, C. Serger, R. Koschny, D. Ordoñez-Rueda, M. Paulsen, V. Benes, S. Boulant and T. Alexandrov. Single-cell transcriptomics reveals immune response of intestinal cell types to viral infection. *Molecular System Biology* (2021). 17(7):e9833. doi: 10.15252/msb.20209833. (Research Article) **Indicates shared first authors*

P. Doldan, J. Dai, **C. Metz-Zumaran**, J. T. Patton, M. L. Stanifer and S. Boulant. Type III and Not Type I Interferons Efficiently Prevent the Spread of Rotavirus in Human Intestinal Epithelial

Cells. *Journal of Virology* (2022). 96(17):e0070622, doi: 10.1128/jvi.00706-22. (Research Article)

**Conference presentations:**

30th Annual Meeting of the Society for Virology (GfV) – digital 2021. “Treatment of human intestinal epithelial cells with type III IFNs rapidly and efficiently depletes SARS-CoV-2 infection” (oral presentation).

41st Annual Meeting of the American Society for Virology (ASV) – Madison, Wisconsin, USA 2022. “Micropatterning method unraveled distinct cell behavior at intestinal wounds during virus infection” (poster presentation).

42nd Annual Meeting of the American Society for Virology (ASV) – Athens, Georgia, USA 2023. “Basal type III IFN signaling primes the intestinal epithelium against virus infection” (oral presentation).

## List of Abbreviations

| | |
|---|---|
| ACE2 | Angiotensin-converting enzyme 2 |
| AP1 | Activating protein 1 |
| Arbovirus | Arthropode-borne virus |
| cGAS | Cyclic GMP/AMP synthase |
| CCP | Clathrin-coated pits |
| CME | Clathrin-mediated endocytosis |
| DNA | Deoxyribonucleic acid |
| ER | Endoplasmic Reticulum |
| ERGIC | ER-Golgi intermediate compartment |
| GERV | Germiston Virus |
| GFP | Green Fluorescent Protein |
| h | Hours |
| hpi | Hours post infection |
| HAstV | Human Astrovirus |
| IEC | Intestinal epithelial cell |
| IFIT1 | Interferon-induced protein with tetratricopeptide repeats 1 |
| IFN | Interferon |
| IFNAR | IFN alpha receptor |
| IFNLR | IFN lambda receptor |
| IKK | IkB kinase |
| IL | Interleukin |
| IRF | Interferon regulatory factor |
| ISG | IFN stimulated gene |
| ISGF3 | IFN-stimulated gene factor 3 |
| JAK | Janus kinase |
| JAM | Junctional adhesion molecule |
| KD | Knock-down |
| KO | Knock-out |
| MAPK | Mitogen-activated protein kinase |
| MAVS | Mitochondrial antiviral signaling protein |
| MDA5 | Melanoma differentiation-associated protein 5 |
| min | minutes |
| MRV | Mammalian Orthoreovirus |
| mtDNA | Mitochondrial DNA |
| MyD88 | Myeloid differentiation primary-response protein 88 |
| NFκB | Nuclear factor-kappa B |
| PAMP | Pathogen associated molecular patterns |
| PAR3 | Partitioning defective 3 |
| PBS | Phosphate buffered saline |
| PFA | Paraformaldehyde |
| PRR | Pattern recognition receptor |
| RT-q-PCR | Reverse transcription quantitative polymerase chain reaction |
| RIG-I | Retinoic acid-inducible gene I |
| RLR | RIG-I-like receptors |
| RNA | Ribonucleic acid |
| RVFV | Rift Valley fever virus |

| | |
|---|---|
| s | Seconds |
| shRNA | Short hairpin RNA |
| SEV | Semliki Forest Virus |
| SLE | Systemic lupus erythematosus |
| STAT | Signal Transducer and Activator of Transcription |
| STING | Stimulator of IFN genes |
| T3D | Type 3 Dearing |
| TCID50 | 50% tissue culture infectious dose |
| TBK1 | TANK-binding kinase 1 |
| TBS | Tris buffered saline |
| TEER | Transepithelial electrical resistance |
| TLR | Toll-like receptor |
| TOSV | Toscana Virus |
| TRIF | TIR domain-containing adaptor protein inducing IFN-β |
| UUKV | Uukuniemi virus |
| VSV | Vesicular Stomatitis Virus |
| VV | Vaccinia Virus |
| WT | Wild type |
| ZO | Zona occludens |

# Abstract

Mucosal tissues act as a protective barrier in constant contact with microbiota. Epithelial cells on these surfaces must mount an effective immune response for protection from pathogens while minimizing adverse reactions to commensal microbiota. Each cell within these tissues has a specific population context, which is determined by the local cell density, cell-to-cell contacts, and relative location within the population. The aim of this thesis was to comprehensively elucidate how the cellular population context shapes viral infection and immune signaling pathways in epithelial tissues.

To this end, I employed human intestinal epithelial cells (IECs) as a model system for mucosal tissues. I developed a density-based approach and a micropatterning system to place cells in controlled microenvironments, which I combined with bio-molecular methods and microscopy/ sequencing-based high-content data bioinformatics analyses. My findings show that IECs embedded in a dense monolayer polarize, leading to a basolateral localization of the interferon (IFN) receptors. Hence, cells located in the center of a dense population did not induce antiviral protection upon apical IFN treatment due the receptor inaccessibility. Additionally, I discovered that the cellular microenvironment, especially the local cell density, controls homeostatic immune pathways. Confluent IEC expressed significant basal levels of IFNλ3 and downstream interferon stimulated genes, while sparse cells elicited no basal IFN-signaling. The basal type III IFN expression was induced by the cGAS-STING pathway after recognition of mitochondrial DNA. Importantly, the Hippo pathway emerged as the master regulator controlling homeostatic immune signaling, which senses the population context (e.g. cellular density and cell-to-cell contacts) to adjust cell behavior to its microenvironment. Finally, I established that the population context governs virus particle binding and active pathogen replication within a cell colony, leading to increased edge cell infection while center cells remained protected.

This thesis shows that the population context *in vitro* directly shapes homeostatic and antiviral processes in epithelial cells. Cells embedded in the intact monolayer elicit higher basal IFNλ3 expression and less virus infection, demonstrating that a physiological micro-environment supports the barrier function of mucosal surfaces. My work strongly suggests that the population context should be considered when planning experiments *in vitro*, and it also underlines the importance of studying the population context and its implications *in vivo*.

In light of the COVID-19 pandemic, I additionally characterized the role of type I and III IFNs signaling in controlling SARS-CoV-2 infection in the gut. My results indicate that type III IFNs are more efficient than type I IFNs in clearing SARS-CoV-2 infection in human intestinal epithelial cells. These findings further our understanding of host-pathogen interactions and could contribute to a development of improved treatment options.

## Zusammenfassung

Schleimhautgewebe bilden eine Schutzbarriere, die in ständigem Kontakt mit Mikrobiota steht. Es ist von entscheidender Bedeutung, dass die Epithelzellen an diesen Schleimhautoberflächen eine angemessene Immunreaktion hervorrufen, die den Schutz vor Krankheitserregern gewährleistet und gleichzeitig die Reaktion auf die kommensale Mikrobiota begrenzt. Jede Zelle in diesen Geweben hat einen spezifischen Populationskontext, der durch die lokale Zelldichte, Zell-zu-Zell-Kontakte und die relative Zellposition innerhalb der Population bestimmt wird. Ziel dieser Arbeit war es, umfassend aufzuklären, wie der zelluläre Populationskontext die Virusinfektion und die Immunsignalwege in epithelialen Geweben beeinflusst.

Zu diesem Zweck verwendete ich menschliche Darmepithelzellen als Modellsystem für Schleimhautgewebe. Ich entwickelte Ansätze auf Grundlage von Zelldichte und einem "Micropatterning" System, um Zellen in präzise gesteuerte Mikroumgebungen/Milieu zu platzieren. Diese Ansätze kombinierte ich mit bio-molekularen Methoden und Mikroskopie/Sequenzierung-basierten bioinformatischen Analysen. Meine Ergebnisse zeigen, dass Darmepithelzellen, die in einer konfluenten Monolayerschicht eingebettet sind, polarisieren, was zu einer basolateralen Lokalisierung der Interferon (IFN)-Rezeptoren führt. Zellen, die sich in der Mitte einer dichten Population befinden, induzieren daher keinen antiviralen Schutz bei apikaler IFN-Behandlung, da der Rezeptor nicht zugänglich ist. Außerdem entdeckte ich, dass das zelluläre Milieu, insbesondere die lokale Zelldichte, homöostatische Immun-Signalwege steuert. Konfluente Darmepithelzellen zeigten signifikante basale Expression von IFNλ3 und IFN-stimulierten Genen, während Zellen mit geringer Dichte keine basale IFN-Expression aufwiesen. Die basale Typ-III-IFN-Expression wurde durch den cGAS-STING-Signalweg induziert, nach Erkennung endogener mitochondrialer DNA. Von besonderer Bedeutung ist, dass sich der Hippo-Signalweg als Hauptregulator herausstellte, der die homöostatische Immunsignalgebung steuert indem es den Populationskontext (z. B. Zelldichte und Zell-Zell-Kontakte) wahrnimmt und das Zellverhalten an seine Mikroumgebung/Milieu anpasst. Schließlich konnte ich nachweisen, dass der Populationskontext die Bindung von Viruspartikeln und die aktive Virusreplikation in einer Zellkolonie steuert. Dies führt zu einer verstärkten Infektion der Zellen die am Rand lokalisiert sind, während die Zellen in der Mitte der Kolonie geschützt bleiben.

Diese Arbeit verdeutlicht, dass der Populationskontext *in vitro* direkte Auswirkungen auf homöostatische und antivirale Prozesse in Epithelzellen hat. Zellen, die in eine intakte Monolayer eingebettet sind, wie es auch im Darmepithel vorkommt, zeigen eine höhere basale Expression von IFNλ3 und eine geringere Virusinfektion. Diese Ergebnisse weisen darauf hin, dass eine physiologische Mikroumgebung/Milieu die Barrierefunktion von

Schleimhautoberflächen unterstützt. Meine Arbeit unterstreicht die Notwendigkeit, den Populationskontext bei der Planung von *in vitro* Experimenten zu berücksichtigen, und betont die Bedeutung der Untersuchung des Populationskontexts und seiner Auswirkungen in lebenden Organismen.

Im Zusammenhang mit der COVID-19-Pandemie habe ich zusätzlich die Rolle der Typ-I- und Typ-III-IFN-Signalübertragung bei der Kontrolle der SARS-CoV-2-Infektion im Darm untersucht. Meine Ergebnisse deuten darauf hin, dass Typ-III-IFNs bei der Beiseitigung einer SARS-CoV-2-Infektion in menschlichen Darmepithelzellen effizienter sind als Typ-I-IFNs. Diese Erkenntnisse tragen zu einem besseren Verständnis der Wechselwirkungen zwischen Wirt und Krankheitserreger bei, und könnten zur Entwicklung fortschrittlicherer Behandlungsmöglichkeiten beitragen.

# 1. Introduction

## 1.1. Viral infections and interferons

### 1.1.1. Viral infection cycle

Viruses infecting eukaryotes are intracellular infectious parasites ranging from ~18 to ~2000 nm, exclusively replicating within host cells. They consist of genetic material, either in the form of DNA or RNA (Fig. 1), which is encapsulated by a proteinaceous capsid, and they can possess an outer lipid envelope or be non-enveloped (naked) (Fig. 1) (*1*).

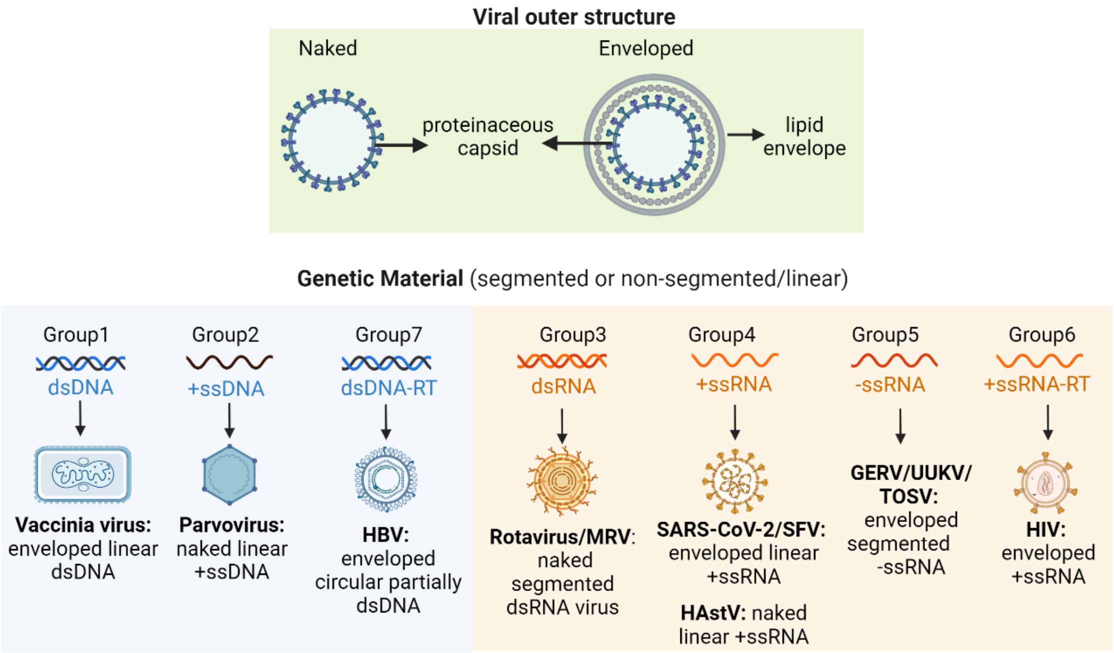

**Fig. 1. Virus structure and classification.** Viruses are formed by a proteinaceous capsid which can be non-enveloped or enveloped by a lipid layer. The capsid encloses the genetic material, composed by either DNA or RNA which is double-stranded (ds), positive-sense single-stranded (+ss) or negative-sense single-stranded (-ss), and segmented or linear. Moreover, for some virus the reverse transcriptase (RT) can be present in the capsid. The Baltimore classification separates viruses into seven groups depending on their mRNA synthesis. Some examples for viruses classified within each group are listed.

To establish infection and an efficient replication cycle, virus particles must first enter the target cell. Virus binding and entry into host cells are complex multistep processes that engage many cellular factors, which are highly dynamic, interconnected, and coordinated in time and space. Virus binding to the surface involve specific virus receptors but can also exploit other attachment factors (i.e. heparin sulfate, sialic acid, ganglioside), and the induction of lipid raft formation or receptor clustering (*2*). This often generates a receptor-rich membrane microdomain that differs from the rest of the plasma membrane in protein and lipid composition (*3*, *4*). These microdomains serve as platforms for transmembrane signaling, which can be connected to a complex virus mobility profile involving cellular actin rearrangement, recruitment of cytoplasmic proteins, and to the assembly of the endocytic machinery (*2*).

After binding, some viruses directly penetrate the cell or fuse with the plasma membrane (endocytosis-independent receptor-mediated entry) (Fig. 2, right panel). However, most viruses depend on cellular endocytic mechanisms, so-called receptor-mediated endocytosis (Fig. 2, left panel) (*2*). Clathrin-mediated endocytosis (CME) is the most common mechanism for endocytosis of small and medium-size virus particles (500-200 nm diameter) (*5*). However, some viruses also take advantage of caveolar endocytosis, clathrin- and caveolin-independent endocytosis, macropinocytosis and other cellular internalization pathways (Fig. 3) (*5*). For most viruses many basic questions on how they enter a cell remain elusive, as for example the cellular receptor and the endocytic pathway they use. Furthermore, while viruses often prefer a specific endocytic pathway, many have the capability to employ alternative pathways when necessary (*2*). The ability of using various endocytic routes adds to the challenge of comprehensively understanding virus entry.

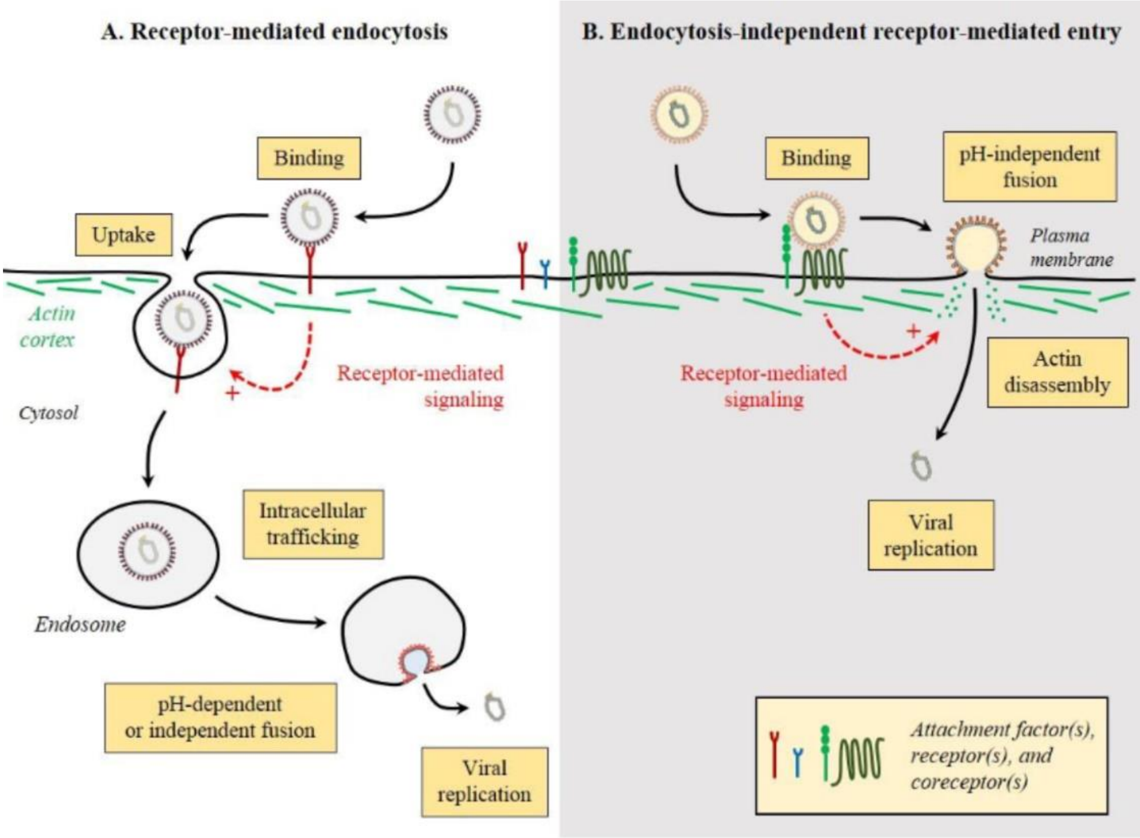

Adapted from *Boulant et al., Viruses (2015)*

**Fig. 2. Strategies of virus entry.** Viruses can use two strategies to gain access to the cytoplasm. (A) Viruses enter by endocytic internalization and then penetration from endosomal compartments in a process known as receptor-mediated endocytosis. (B) Viruses enter by direct penetration from the plasma membrane. Each step of the viral entry process is depicted. Although enveloped viruses are shown, non-enveloped viruses have developed similar strategies. Figure adapted from (*2*).

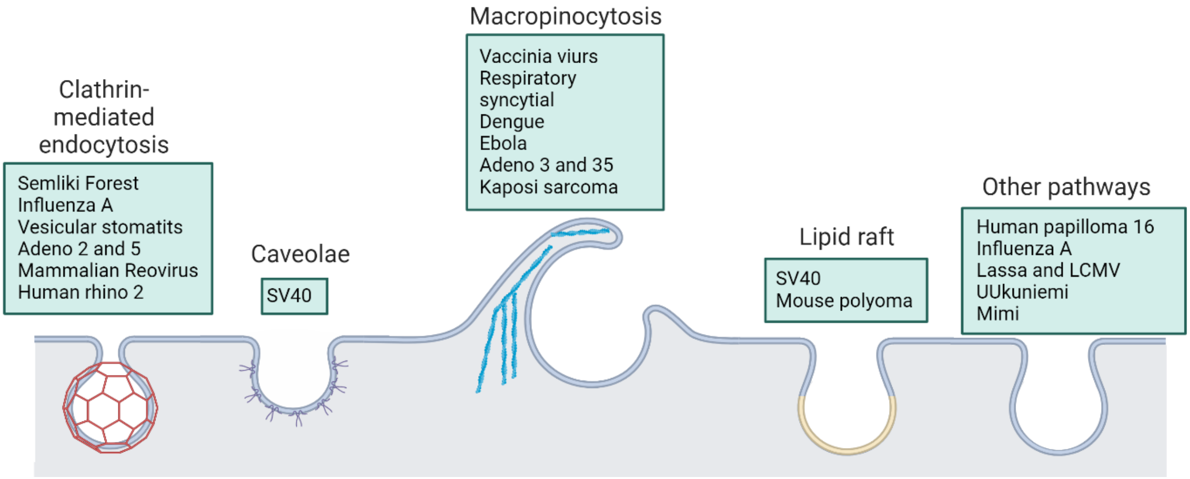

**Fig. 3. Virus internalization through host endocytic processes.** Following attachment to the cell surface, viruses are internalized through a variety of endocytic processes including clathrin-mediated endocytosis (CME), caveolae, macropinocytosis, lipid rafts and other mechanisms (clathrin- and caveolin-independent). Some viruses using these endocytic processes are listed. Figure adapted from (*6*)

After entry into the host cell, the next crucial step is re-localization of the virus genome to the adequate sub-cellular compartment for replication. Viruses taken up by endocytic mechanisms enter a complex network of endocytic organelles, which they use to transit deeper into the cell until they penetrate into the cytosol (Fig. 2). Virus uncoating to expose the viral genome for transcription and genome replication can occur within the endosomal network or in the cytosol (*1*). The replication strategy depends on the virus genome composition and is nicely depicted in the Baltimore scheme (Fig. 4) (*7*). Most DNA viruses replicate exclusively in the nucleus and are dependent on cellular factors. An exception are poxviruses, which carry all necessary factors for transcription and replication in their genomes, and replicate in the cytoplasm (*1*). RNA viruses possess their own transcriptase and most RNA viruses replicate in the cytoplasm, except for bornaviruses, orthomyxoviruses, and retroviruses (*1*). Interestingly, retroviruses reverse transcribe their RNA genome into DNA, which can then be stably integrated into the host cell chromatin (*1*).

After viral genome transcription, translation of viral proteins, and replication of the viral genome, all the components are assembled to a new virus particle and released from the cell. Classically, non-enveloped virus particles were thought to be released solely via cell lysis. However, recent works show that non-enveloped viruses can exit the cell as semi-enveloped or quasi-enveloped variants, which in turn leads to a distinct infection pattern compared to their non-enveloped counterparts (*8*, *9*). Enveloped viruses typically exit via budding through cellular compartments such as ER, ERGIC, Golgi, or plasma membrane thereby acquiring their lipid envelope (*1*). Virus release and maturation leads to infectious particles, which can infect new cells, tissues, and hosts. Importantly, recent studies made clear that virus exit and inter-cellular transmission can be very complex. For example, a noteworthy phenomenon involves the infection of neighboring cells without the need for virus release into the extracellular environment, achieved through direct cell-to-cell transmission, for example via virus synapses (*10*).

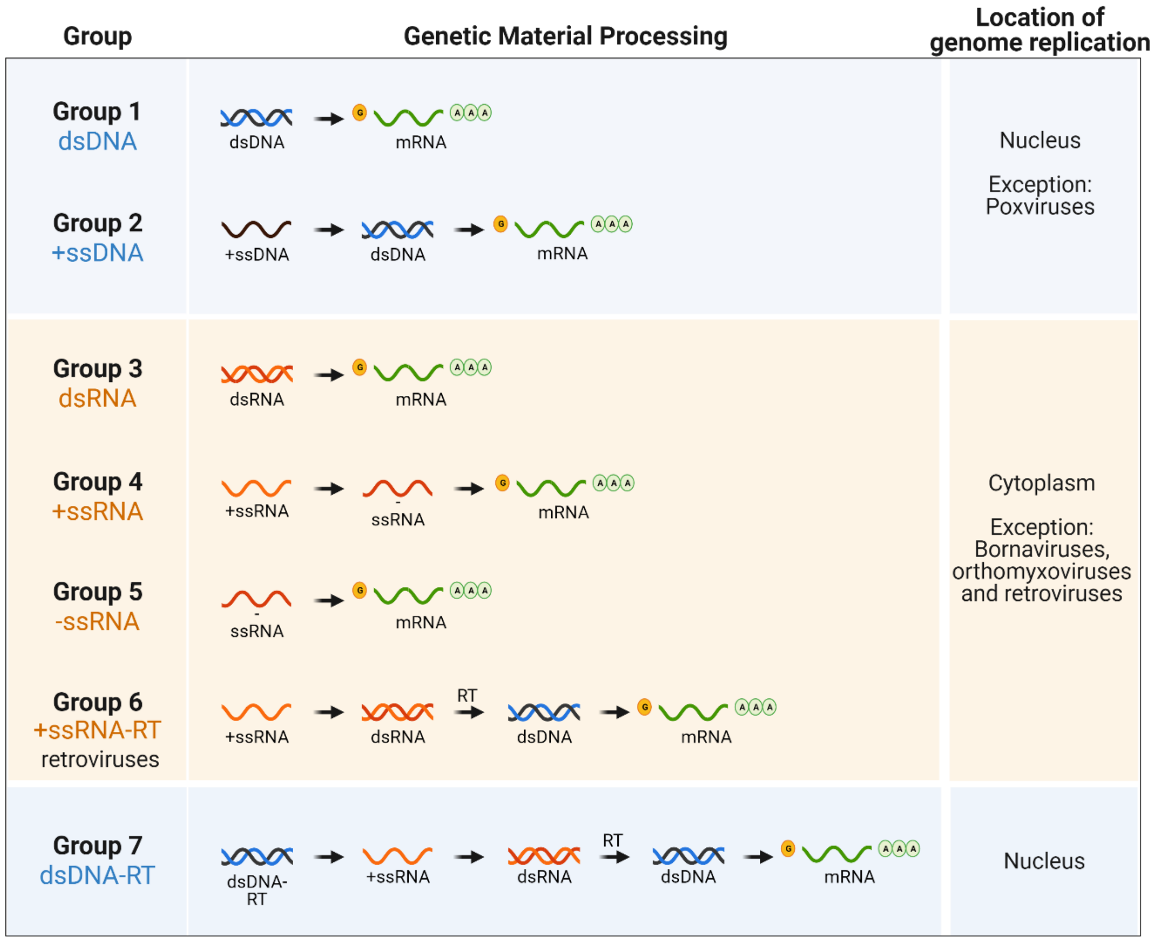

**Fig. 4. Baltimore scheme.** The Baltimore classification separates viruses into seven groups depending on their mRNA synthesis. Viruses genome replication occurs either in the nucleus or the cytoplasm. Abbreviations: double-stranded (ds), positive-sense single-stranded (+ss), negative-sense single-stranded (-ss), reverse transcriptase (RT).

### 1.1.2. Viruses used in this work

During my PhD, I used various viruses that possess different genetic material and envelope, that have different replication strategies, and that target different sites for infection. In this section I will provide an overview of the viruses that are relevant to my research.

#### *1.1.2.1. Enteric viruses*

Enteric viruses utilize the gastrointestinal tract as their primary route of entry to the host. These viruses infect and replicate in cells at the epithelial tissue or the underlying *lamina propia*, potentially leading to the development of acute enteritis.

Rotavirus is the main cause of viral gastroenteritis worldwide, with an estimated 1.76 million hospitalizations in children below the age of 5 attributed to rotavirus in 2019 (*11*). Rotaviruses are non-enveloped icosahedral viruses of 70 nm diameter, that belong to the genus *Rotavirus* within the *Reoviridae* family. The rotavirus genome consists of 11 dsRNA segments. Six of these segments code for structural proteins (VP1, VP2, VP3, VP4, VP6 and VP7), and five for non-structural proteins (NSP1, NSP2, NSP3, NSP4 and NSP5/6) (*12*). The genome is surrounded by triple-layer of viral proteins (VPs) comprising a core (VP1, VP2, VP3), an inner capsid (VP6), and an outer capsid (VP4, VP7) (Fig. 5 A) (*1*). *In vivo*, these viruses primarily infect mature enterocytes in the intestinal epithelium (*13*). Prior to infection, host trypsin-like proteases cleave VP4 into two subunits, VP8 and VP9, which is required for the virus to enter the cell (*13*). The process of virus entry is not fully characterized and differs from strain to strain. Several glycans have been identified as receptors for rotavirus, and it is known that the VP8 domain of VP4 mediates the initial interaction with the cell surface (*13*). After binding, rotavirus has been proposed to interact with integrins, hsc70, tight junction proteins (JAM-A, occludin and ZO1) and gangliosides (*14–16*). The virus enters the cell through receptor mediated endocytosis (*13*, *17*). While different strains use different endocytic pathways, most tested rotavirus enter the cell by clathrin-mediated endocytosis (CME) (*17*, *18*). After entry, rotavirus is transported across the endosomal machinery, until outer layer proteins lyse the endosomal membrane releasing the particles into the cytoplasm (*19*), where transcription complexes formed by VP1 (a RNA-dependent RNA polymerase) and VP3 (a capping enzyme) are in charge of genome replication and viral protein expression (*20*). *De novo* particles are then assembled and released from the cell by lysis or budding (*21*, *22*).

The mammalian orthoreovirus (MRV) belongs to the genus *Orthoreovirus* in the *Reoviridae* family, and has been the major model system for molecular understanding of the *Reoviridae* family (*23*). MRV can cause enteric, respiratory and central nervous system pathologies in humans (*24*, *25*), however it is only rarely associated with disease and mostly in young children. Three MRV serotypes have been isolated from human hosts, namely type 1 Lang (T1L), type 2 Jones (T2J) and type 3 Dearing (T3D) (*23*). MRV is a dsRNA non-enveloped virus of 60-100 nm in diameter, characterized by a double-layer icosahedral capsid (*26*). The total genome size is approximately 24,500 basepairs (bp) and consists of three large (L1–L3), three medium (M1–M3), and four small (S1–S4) segments (10 segments in total). The L1, L2, L3, M1, M2, S1, S2, and S4 segments encode eight structural proteins (λ1, λ2, λ3, μ1, μ2, σ1, σ2, and σ3, respectively), whereas the M3 segment encodes two non-structural proteins (μNS and μNSC), and the S1 and S3 segments each encode a non-structural protein (σ1s and σNS, respectively) (Fig. 5 B) (*26*). σ1 mediates virus attachment to the cell surface by interacting with sialic acid and the tight junction protein JAM-A (*27*). β1 integrin then facilitates MRV internalization (*28*). The virus takes advantage of various internalization processes, including

CME, calveolar endocytosis and macropinocytosis (*29*). After trafficking in the endosomal machinery, viral particles penetrate the late endosomes and replicate in the cytoplasm within viral factories (Fig. 5 D). The non-structural protein µNS serves as a scaffold protein for viral factories and is essential for virus replication (*30*). Progeny particles are known to egress the cell in both, lytic and non-lytic manner (*29*).

Human astrovirus (HAstV) causes diarrhea, mostly in infants under the age of 12 months. HAstV belongs to the genus *Mammastrovirus* in the family *Astroviridae*, and is a 28-30 nm diameter non-enveloped virus (*1*). The genome consists of polyadenylated single-stranded positive-sense RNA, containing three open reading frames (ORF1a, -1b, and -2) which encode three polyproteins: ORF1a and -1b code for nonstructural proteins and ORF2 codes for the capsid protein (Fig. 5 C) (*31*). The HAstV replication cycle is poorly understood, and many steps have yet to be elucidated. The cellular receptors are not well characterized; however, CME appears to be one endocytic route which the virus uses to enter the cell (*32*, *33*). After endocytosis, the genome is released into the cytoplasm at the late endosome (*32*, *33*). Similar to the other here described enteric viruses, HAstV replicates and assembles in the cytoplasm, and exits the cells in a lytic or non-lytic manner (*31*).

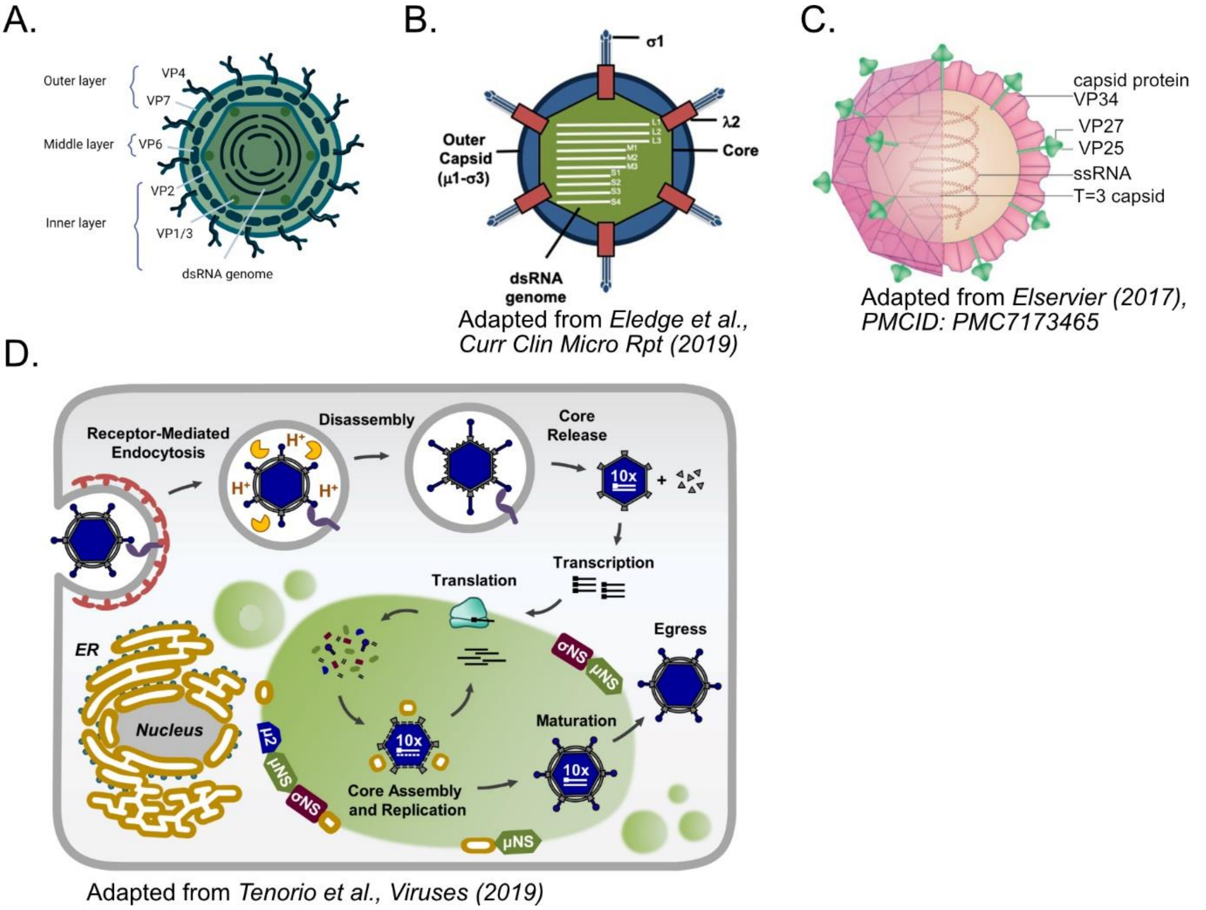

Adapted from *Eledge et al., Curr Clin Micro Rpt (2019)*

Adapted from *Elservier (2017), PMCID: PMC7173465*

Adapted from *Tenorio et al., Viruses (2019)*

**Fig. 5. Enteric viruses**. Schematic of the (A) rotavirus, (B) reovirus (figure adapted from (*34*)) and (C) Astrovirus (figure adapted from (*35*) structure. (D) Reovirus replication cycle. Figure adapted from (*36*).

### *1.1.2.2. Arboviruses*

Arthropod-borne viruses (arboviruses) constitute a supergroup of viruses, which rely on arthropod vectors (e.g. mosquitoes, sandflies and ticks) for transmission to vertebrate hosts, including humans. Many arboviruses are regarded as emerging or reemerging pathogens as for example Zika virus (*37*), and as potential pandemic threats such as Chikungunya (CHIKV), Crimean-Congo hemorrhagic fever orthonairovirus (CCHFV), Rift Valley Fever virus and yellow fever virus (*38*).

Within the bunyaviruses, the *Phenuiviridae* family is of particular importance, with over 100 members in 19 genera. Many members of this family are emerging pathogens affecting both, humans and livestock. I worked with two different viruses within this family: Toscana virus (TOSV) belongs to the *Phlebovirus* genus and is transmitted by sandflies. TOSV infection can induce flu-like symptoms and is the leading cause of meningitis or encephalitis in Southern Europe during summer (*39*, *40*). Uukuniemi virus (UUKV) in the *Uukuvirus* genus is transmitted by ticks, and is a frequently used as a non-pathogenic surrogate for many highly pathogenic thick-borne burnyaviruses such as CCHFV and Dabie virus (DABV). Additionally, I worked with Germinston virus (GERV) which belongs to the genus *Orthobunyavirus* in the *Peribunyaviridae* family, and is employed as a surrogate to the more pathogenic La Crosse virus, a major causative of pediatric encephalitis (*41*).

Both, Orthobunyaviruses and Phenuiviruses, are roughly spherical and 80-160 nm in diameter (*42–44*). The viral genome consists of a tri-segmented negative single stranded RNA genome, which is surrounded by a host-derived lipid bilayer embedding viral glycoproteins $G_N$ and $G_C$ (Fig. 6A). Large (L) segment encodes the RNA-dependent RNA polymerase (RdRp), the medium (M) segment codes for the viral glycoproteins Gn and Gc, and the small (S) segment encodes the N protein and the non-structural protein NSs in an ambisense strategy (*45*). The cellular attachment factors and entry pathways used by Orthobunyaviruses and Phenuiviruses is largely uncharacterized. For Orthobunyaviruses, sulfation, heparin sulfates and C-lectins have been found to be involved in binding of the virus to the cell surface (*46–48*), and the human C-type lectin dendritic cell-specific intercellular adhesion molecule-3-grabbing nonintegrin (DC-SIGN) has been reported to promote infection (*49*). Orthobunyaviruses make use of the endocytic machinery to enter cells and various studies suggest that CME is involved in virus internalization (*49–52*). In the case of Phenuiviruses, various attachment factors have been described for entry. DC-SIGN is a primary entry receptor for UUKV and TOSV, which was also shown to be involved in endocytic internalization (*53*). Virus binding to the cell is followed by receptor-mediated endocytosis. While CME was suggested as the internalization pathway for DABV, uptake of UUKV is less characterized and was shown to be independent of clathrin (*54*). The assembled ribonucleoproteins are then transported to membranes of the

Golgi complex, where they acquire their lipid bilayer by budding through ERGIC/Golgi compartments (Fig. 6 C). Vesicles containing virions are trafficked to the cell surface, and fusion the plasma membrane leads to the release of infectious virions via exocytosis (*45*, *55*, *56*).

Semliki forest virus (SFV) belongs from genus *Alphavirus* (family *Togaviridae*) is closely related to the rapidly spreading CHIKV, and is used as a surrogate to study more pathogenic mosquito-borne alphaviruses (*57*). SFV is a ~70 nm in diameter enveloped virus. The positive-sense single stranded RNA genome is organized in two ORFs, encoding nine functional proteins: nonstructural proteins responsible for viral RNA synthesis, and the structural proteins to form the capsid (C protein) and the envelope (E1, E2 and E3 proteins) (Fig. 6 B) (*57*). Several receptors (such as NRAMP, prohibitin-1 and MXRA8) and attachment factors (heparan sulfate, C-type lectins, and phosphatidylserine) have been identified for alphaviruses (*58*). Alphaviruses were shown to be internalized principally by CME, and membrane fusion in endosomes releases the viral genome into the cytoplasm (*59*–*61*). After virus replication, nascent virus buds from the host cell membrane (*62*, *63*).

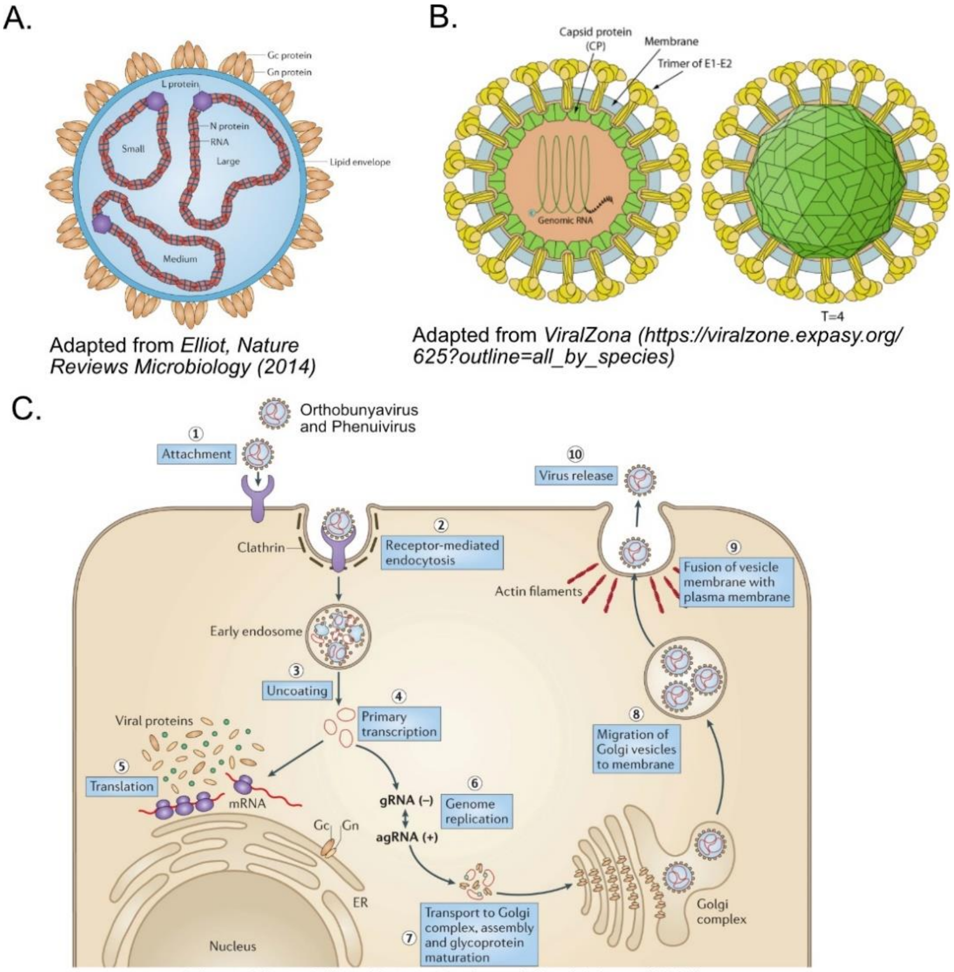

Adapted from *Elliot, Nature Reviews Microbiology (2014)*

Adapted from *ViralZona (https://viralzone.expasy.org/625?outline=all_by_species)*

Adapted from *Elliot, Nature Reviews Microbiology (2014)*

**Fig. 6. Bunyaviruses**. Schematic of the (A) orthobunyavirus and phenuivirus (figure adapted from (*45*) and (B) alphavirus (figure adapted from (*64*)) virion. (C) Orthobunyavirus and phenuivirus replication cycle. Figure adapted from (*45*).

### *1.1.2.3. Vaccinia Virus*

Vaccinia virus belongs to the genus *Orthopoxyvirus* in the *Poxviridae* family and is the prototype of this family. Vaccinia virus has been used to induce cross-protection against variola virus (causative agent of smallpox) as part of the modern smallpox vaccine, thanks to highly conserved structural proteins with variola virus, reduced virulence, and high immunogenicity (*65*, *66*). In 1980, the World Health Assembly declared smallpox as eradicated due to the global vaccination campaign (*67*).

Poxviruses are large enveloped viruses (~300 by 230 nm in size), with a linear double stranded DNA genome (130 to 230 kilo bp). Poxviruses produce two types of infectious particles: mature virions (MVs) which are thought to mediate host-to-host transmission, and extracellular virions (EVs) mediating virus spread within an infected host (Fig. 7A) (*68*). Importantly, MV and EV particles do not share common viral surface epitopes, which is why the use different attachment factors (*69*). While several attachment factors have been described for MVs (such as glycosaminglycans, heparin sulfate and chondroitin sulfate), no cellular attachment factors have been identified for EVs (*68*). For EVs, electron microscopy data suggested that entry can occur directly at the plasma membrane by fusion with the viral membrane (*70*). However, recent studies demonstrated that fusion of the virus with cellular membranes occurs mostly after endocytic uptake of viral particles and not at the cell membrane (*71–75*). The main internalization route exploited by both EVs and MVs is macropinocytosis (*71*, *76*), which is signaling-induced and involves dramatic actin rearrangements and many cellular factors (*77*). Importantly, macropinocytosis is not the only endocytic route used by the virus, as MV entry into CHO cells is likely independent of macropinocytosis (*73*).

After fusion of the viral membrane with the cellular membrane, the viral core is deposited in the host cell cytosol. Unlike other DNA viruses, poxviruses genome replication occurs in the cytoplasm within virus factories, and relies heavily on virus encoded proteins (*78*). These viral factories are also the sites of viral mRNA transcription and translation, as well as virion assembly (*79*). The initial infectious form, the so called mature virus (MV), has a single external membrane (*80*, *81*). Some MVs are wrapped with Golgi-derived membrane resulting in the wrapped virions, while other MVs remain in the cytoplasm until liberation by cell lysis (*80*). The wrapped virions are further transported on microtubules to the periphery of the cell, where they fuses to the cell membrane resulting in the release of the extracellular enveloped virion (EV) (*80*, *81*). Basically, EVs are MVs with an additional layer. (Fig. 7 B)

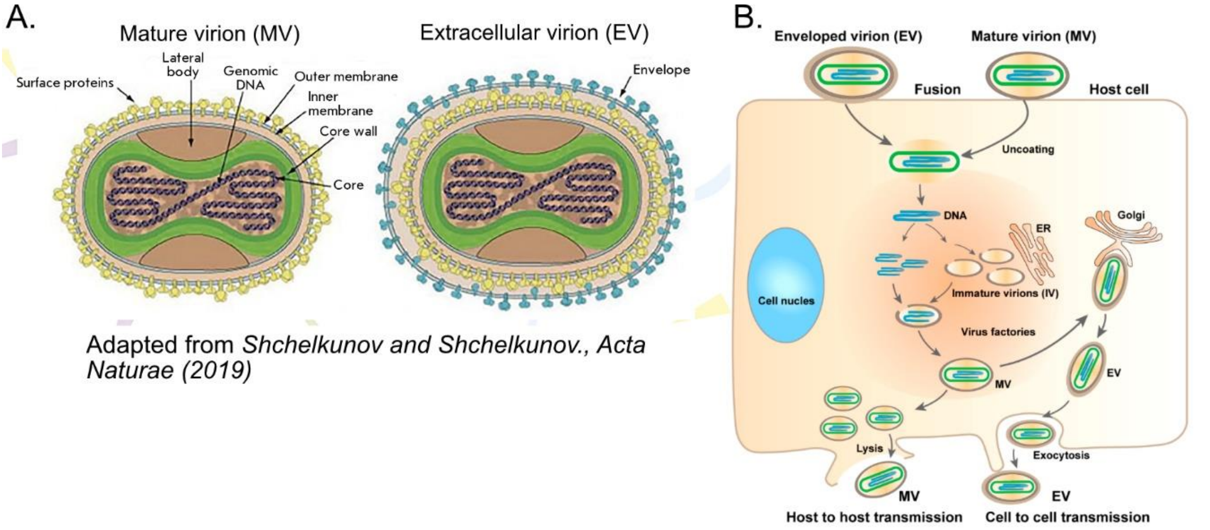

Adapted from *Shchelkunov and Shchelkunov., Acta Naturae (2019)*

Adapted from *Shi et al., Molecules (2022)*

**Fig. 7. Vaccinia virus**. (A) Schematic of the vaccinia virus mature virion (MV) and extracellular virion (EV). Figure adapted from (*82*). (B) Vaccinia virus replication cycle. Figure adapted from (*83*).

#### *1.1.2.4. SARS-CoV-2*

In light of the COVID-19 pandemic, significant endeavors were necessary to understand SARS-CoV-2 infection and pathogenesis. During my thesis, my lab has been extensively involved in SARS-CoV-2 related research and I oriented my research effort on understanding protection induced by type I and III IFNs in the human intestinal epithelium against this virus. A more detailed introduction on this virus and its interaction with IFN-dependent signaling can be found in section '1.1.9. SARS-CoV-2 and IFNs'.

### 1.1.3. Cellular responses to viral infection

Host protection from virus infection relies on intrinsic innate immune recognition of the pathogen and in mounting an adequate immune response. Upon infection, cellular pattern-recognition receptors (PRRs) recognize pathogen-associated molecular patterns (PAMPs). The most common viral PAMPs are nucleic acids, precisely their subcellular localization and biochemical features (*84*). The major PRRs, their respective PAMPs and downstream signaling is summarized in Fig. 8. In Fig. 8 only pathways leading to IFN expression are outlined, and not pathways inducing other cytokines or effector proteins.

Upon virus entry through the endosomal machinery, the viral genome is recognized by PRRs located inside endosomes, the so-called Toll-like receptors (TLRs). TLR3, 7, and 8 detect dsRNA and ssRNA, and TLR9 detects dsDNA (*84*). When the viral PAMPs are localized in the cytosol, three related RNA helicases called retinoic acid inducible gene I (RIG-I), melanoma differentiation-associated gene 5 (MDA5), and LGP2 function as sensors of RNA virus infection. RIG-I and MDA5 signal the presence of primarily 5'-phosphorylated RNA and long dsRNA, respectively, while LGP2 appears to play a regulatory role in RNA recognition (*85*). Cytosolic viral DNA is sensed by cyclic GMP-AMP synthase (cGAS) (*86*). Importantly, RNA viruses also induce a cGAS-dependent response (*87*, *88*), for example by inducing cellular damage and mitochondrial DNA release into cytoplasm, which is then sensed by cGAS (*89*, *90*).

Following the recognition of PAMPs, PRRs initiate an immune signaling cascade through activation of specific adaptor proteins and serine/threonine kinases. For example, TLR3 recruits TIR-domain-containing adapter-inducing interferon-β (TRIF) and TLR7-9 recruit the adaptor myeloid differentiation primary response gene 88 (MyD88). After detecting immunostimulatory RNAs, RIG-I or MDA5 oligomerize, thereby recruiting mitochondrial antiviral-signaling protein (MAVS), which serves as the essential effector protein for RLRs signal transduction (*85*). Binding of cGAS to dsDNA in the cytoplasm leads to production of its second messenger product 2’3’-cyclic GMP-AMP (2’3’-cGAMP). 2’3’-cGAMP binds to the endoplasmic reticulum (ER) localized adaptor STING (Stimulator of interferon genes) inducing its oligomerization, conformational changes and trafficking through the ER-Golgi intermediate compartment (ERGIC) to the Golgi apparatus, where STING executes its effector function (*91*).

These signal transductions induced by the various PRRs and adaptor proteins eventually activate transcription factors, such as nuclear factor-κB (NF-κB) and interferon-regulatory factor (IRF) 3 and 7. Following activation, these transcription factors translocate in the nucleus and upregulate the expression of antiviral effector proteins, chemokines, and cytokines (*84*).

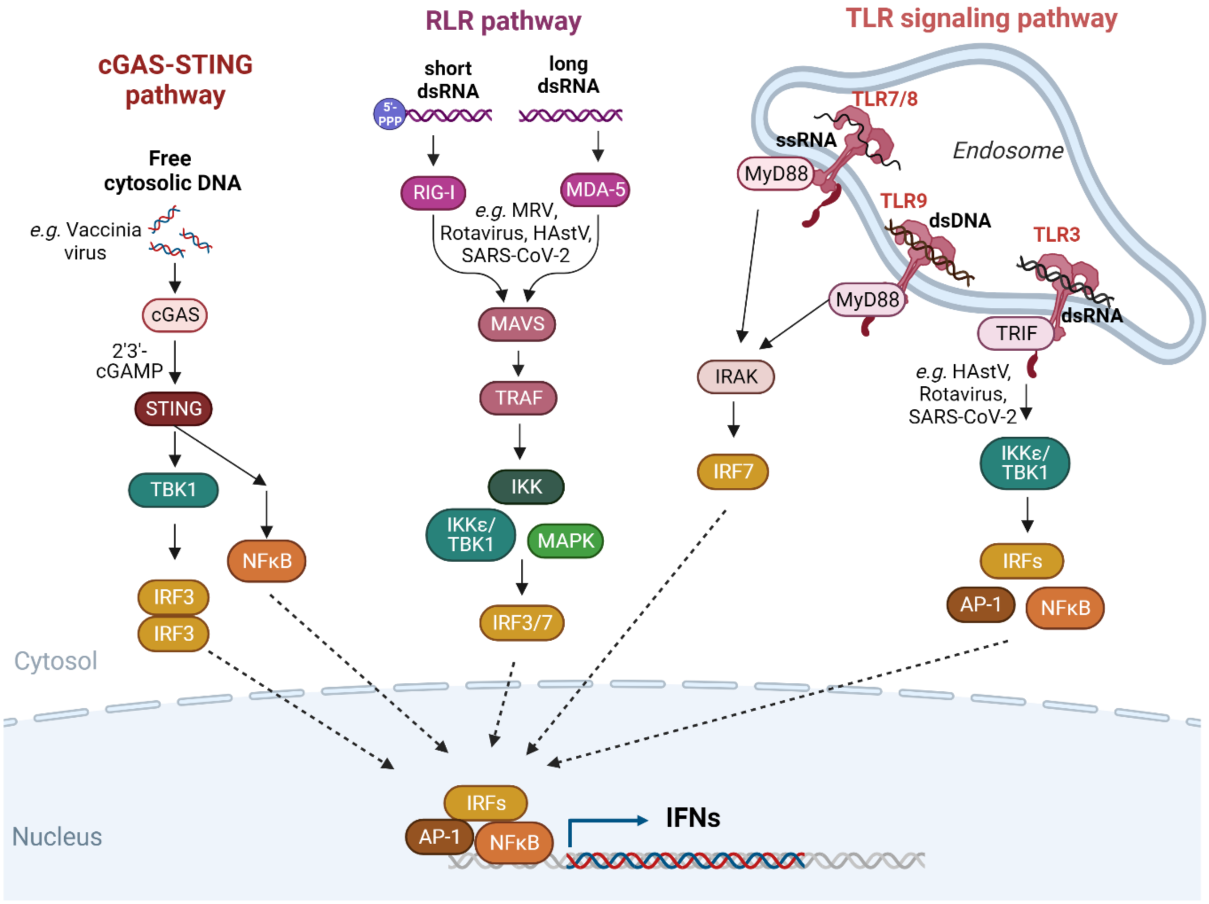

**Fig. 8. Sensing of viral PAMPs by PRRs and induction of IFN expression.** PRRs receptors sense viral RNA and DNA, and induce a signaling cascade which culminates in the transcription of IFNs. cGAS recognizes cytosolic dsDNA, leading to the synthesis of the second messenger 2'3'-cGAMP, which binds and activates STING. The RLRs RIG-I and MDA-5 sense cytosolic dsRNA recruiting MAVS and leading to the activation of the adaptor TRAF. TLRs recognize viral nucleic acids in endosomes activating MyD88, IRAK and TRIF. The different signaling pathways then induce kinases, including TBK1, IKK and MAPK, which phosphorylate and activate the transcription factors IRF3/7, NFκB and AP1. The transcription factors translocate to the nucleus, bind to their specific promoter and lead to the transcription of IFNs. Some examples for viruses triggering the different signaling cascades are listed.

### 1.1.4. Types of interferons

Interferons (IFNs) are the predominant cytokines made to combat virus infection. IFNs are classified into three types, depending on the set of receptors they use: Type I, II and III IFNs. Type I IFNs are the first and best described family, consisting of 13 subtypes of IFNα, a single subtype of IFNβ and several other poorly characterized type I IFN genes (ε, κ, and ω) that are encoded in chromosome 9 and sharing great similarity in their sequence.

All cells are able to produce type I IFNs, but different cell types preferentially produce specific subtypes. For example, IFNα is preferentially produced by monocytes and macrophages, while IFNβ is preferentially produced by fibroblasts (*92*). Type I IFNs signal through the heterodimeric receptor IFN-α receptor 1 (IFNAR1) and IFN-α receptor 2 (IFNAR2), which is expressed by all cells in the body (*93*). The type II IFN family only counts one member, IFNγ, produced mainly by immune cells including activated T cells, natural killer cells and macrophages. Type II IFNs act through the tetrameric receptor complex composed by two subunits of IFN-γ receptor 1 (IFNGR1) and two subunits of IFN-γ receptor 2 (IFNGR2) (*93*). The most recently discovered family of IFNs are the type III IFNs, consisting of IFNλ1 (also known as interleukin (IL)-29), IFNλ2 (also known as IL-28a), IFNλ3 (also known as IL-28b), and IFNλ4. Genes encoding type III IFNs are clustered on chromosome 9 (*94*), and show similarity in their sequence with the IL-10 superfamily of cytokines (*95*). Consequently, this family of IFNs signals through the heterodimeric receptor composed of IL-10R subunit and the IFN-λ receptor 1 (IFNLR1) subunit. Importantly, while all cell types express type III IFNs, expression of the IFNLR1 is restricted to epithelial and some immune cells (*96*).

The three IFN families exhibit divergent roles, determined by their expression pattern, respective receptor expression, receptor interaction, and downstream gene induction. While the type II IFN IFNγ was initially associated to antiviral responses, recently it is considered crucial in response to parasite, fungi, and bacterial infections, acting as an immunomodulatory cytokine (*97*, *98*). Similar to type II IFNs, both type I and type III IFNs have been recognized for their ability to stimulate an immune response against diverse pathogens (*93*). However, their primary association remains with the inhibition of virus infection and propagation. Interestingly, type I and type III IFNs exhibit great similarities in terms of antiviral immune response, and were long supposed to have redundant functions. However, recently crucial differences have been unraveled in the mode of action and function between type I and type III IFNs, supporting unique role for each of the IFN families (*99*, *100*). The focus of this thesis lies on type I and III IFNs.

### 1.1.5. Induction of IFNs

#### *1.1.5.1. Signaling downstream of host PRRs after recognition of viral PAMPs*

Upon infection, viral PAMPs are detected by PRRs, which induces a signaling cascade ultimately leading to IFN expression. A central event during signal transduction involves the recruitment of kinases, that induce a phosphorylation cascade, culminating in the phosphorylation and subsequent activation of the transcription factors (*101*).

After RLR-induced MAVS aggregation, adaptors of the TRAF (tumor necrosis factor receptor associated factor) family are recruited, which in turn recruit the kinases mitogen activated protein (MAP) kinases, the IκB kinase (IKK) complex and the IKK-related kinases IκB kinase-ε (IKKε)/TANK-binding kinase-1 (TBK1) (*84*, *101*). These kinases phosphorylate and activate the transcription factors activator protein 1 (AP-1), NF-κB and IRF3 and 7 (Fig. 8). Similarly, after cGAS-dependent recognition of cytosolic DNA, the downstream activation of the adaptor protein STING leads to recruitment of TBK1. The STING-TBK1 complex recruits the transcription factor IRF3, which is phosphorylated, enabling its dimerization and nuclear translocation (Fig. 8) (*86*). Stimulation of cGAS-STING also promotes NF-κB-mediated transcriptional activation, however the molecular interaction between STING and NF-κB is not fully understood. Similar to the other PRRs, TLR3 downstream signaling recruits TBK1/IKKε through its adaptor protein TRIF, inducing to phosphorylation of IRFs (Fig. 8). TLR3 signaling can also culminate in NF-κB and AP-1 activation. Interestingly, TLR7 and 9 signaling through their adaptor MyD88 leads to Interleukin-1 receptor associated kinase (IRAK) recruitment, and IRAK can directly phosphorylate the transcription factor IRF7 (Fig. 8) (*84*, *101*).

Indeed, a common pattern in signal transduction following pathogen recognition becomes apparent: PRRs recognizing viral factors activate adaptor proteins such as STING, MAVS, the TRAF family, TRIF, and MyD88. Adaptor proteins subsequently recruit pivotal kinases, one of them being IKKε/TBK1. These kinases play a central role by phosphorylating and activating transcription factors, including IRF3, IRF7, NF-κB, and AP1, which ultimately induces IFN transcription (*84*, *101*).

### *1.1.5.2. DAMPs as ligands for PRRs*

PRRs also recognize non-infectious material comprised of endogenous “Self” molecules that are released or mislocalized during cellular stress (*102*, *103*). These are named damage-associated molecular patterns (DAMPs) and induce a potent innate immune response (*102*, *103*).

Prototypical DAMPs are endogenous factors sequestered intracellularly under physiological conditions, which are released into the extracellular environment by dying cells during cellular stress (e.g. ischemia) or tissue injury (*102*). As such, prototypical DAMPs derive from necrotic cells (cell death occurring under conditions of extreme damage) and include the chromatin-associated protein high-mobility group box 1(HMGB1) (*104*), heat shock proteins (HSPs) (*105*), and purine metabolites, such as ATP (*106*) and uric acid (*107*). These prototypical DAMPs trigger an immune response especially in immune cells such as macrophages, dendritic cells and neutrophils (*102*). Recently, it has become evident that DAMPs are not only secreted, but also found within the cytoplasm as a results of loss of homeostasis. One example of such a DAMP is mitochondrial DNA (mtDNA) released into the cytoplasm (*108*). Importantly, mtDNA can also leak into the cytosol during cellular stress induced by virus infection (*89*, *90*, *109*, *110*).

DAMPs can trigger various PRRs and induce IFN-dependent signaling. For example, TLR4 located at the plasma membrane senses extracellular HMGB1 and HSPs, inducing MyD88 and TRIF dependent pathways, which turns on IKKs, MAPKs and TBK1 (*111*, *112*). These kinases activate NFκB and IRF3, culminating in IFN expression (*111*, *112*). Cytoplasmic mtDNA is recognized by the dsDNA sensor cGAS, inducing STING signaling and an IFN response (*113*, *114*). Interestingly, leaked mtDNA resulting from RNA virus infection also induces the cGAS and STING (*89*, *90*, *109*, *110*), leading to the activation of a pathway that is mostly associated to DNA virus sensing.

#### *1.1.5.3. Transcription factors for IFN expression*

IFN gene expression can be induced by a variety of transcription factors, which bind to the IFN promoter. For example, in the context of virus-induced activation of the IFNβ promoter, NF-κB, IRF3, and IRF7 are regarded as the most important transcription factors cooperating for induction of IFN transcription. However, other IRFs as well as AP-1 can occupy the IFNβ promoter (*101*). For IFNα transcription, members of the IRF family are essential, with IRF3 and IRF7 playing a global role, while the other family members regulate IFN production in a highly cell type-specific manner (*101*). Finally, genes for the type III IFN family display AP-1, IRF and NF-κB binding sites at their promoters. However, only IRF3, 7 and NF-κB are essential for induction of type III IFN transcription (*100*). Importantly, early studies suggested that IFN-λ1 was regulated similarly to IFN-β, dependent on IRF3 and NF-κB, while IFNλ2/3 regulation resembled IFN-α, dependent on IRF7 (*115*, *116*).

### 1.1.6. JAK-STAT signaling and ISGs

IFNs are transcribed, translated and secreted by the cells. Secreted IFNs act in an autocrine and paracrine manner through the respective heterodimeric receptor. IFN signal transduction is depicted in Fig. 9 (*117*). Type I IFNs bind IFNAR2 with high affinity and then recruit the low-affinity IFNAR1. Type III IFNs first bind to IFNLR1 with high affinity and then recruit the low-affinity IL10Rβ. IFN binding induces conformational changes in the receptor intracellular region, bringing them closer to each other. Constitutively bound members of the Janus Kinases (JAK) family (JAK1, JAK2 and TYK2) can now trans-phosphorylate tyrosine residues on the opposite heterodimeric receptor. This leads to recruitment of signal transducer and activator of transcription (STAT) proteins to these sites, and the subsequent phosphorylation of STATs by JAKs. Upon phosphorylation, STAT1 and STAT2 molecules undergo homodimer or heterodimer formation, subsequently binding with interferon regulatory factor 9 (IRF9). This interaction leads to the assembly of the ISGF3 complex. The ISGF3 complex translocates into the nucleus and induces the transcription of hundreds of Interferon Stimulated Genes (ISGs) by binding to IFN-stimulated response elements (ISREs) in the upstream promoter regions. (*117*)

Over the past years, many studies compared which ISGs were specifically induced by type I or type III IFN treatment, and only few IFN-specific ISGs have been uncovered (*118–120*). The general notion is that type I and type III IFNs prompt similar set of ISGs. Notably, both types of IFNs activate antiviral ISGs like Mx1, Viperin, and members of the IFITM, IFIT, and OAS families. However, type I IFNs exhibit a higher magnitude of ISG induction, particularly at lower doses and in the early timepoints (*115*, *121*). Additionally, the temporal patterns of ISG induction differ between the two types of IFNs. Type I IFNs trigger a rapid but short-lived peak in ISG expression, whereas type III IFNs lead to a more gradual and sustained increase in ISG expression over time (*122–125*).

Subtle differences in the signaling pathways induced by type I and III IFNs can contribute to their distinct ISG expression pattern. Although both type of IFNs use JAK1 to trigger the ISGF3 complex, type III IFNs also requires JAK2 signaling in certain cell types (*126*, *127*), and MAPK signaling to induce its antiviral activity (*128*). Moreover, studies suggest that only type I and not type III IFN signaling depends on TYK2 (*129–134*). In addition to STAT1 and STAT2, type I IFNs can also signal through STAT3. In this scenario, STAT3 was shown to either act as a negative regulator of type I IFN signaling by inhibiting STAT1-dependent gene activation (*135*, *136*), or by contributing to type I IFN antiviral response against influenza A virus and vaccinia virus (*137*) . Importantly, type I IFN signaling is negatively regulated by the IFNLR, while type III IFN signaling is positively regulated by IFNAR (*138*). Additional research is necessary to address differences at the chromatin and transcriptional level that arise following IFN signaling between type I and type III IFNs. This could provide insights into the distinct pattern of ISG induction observed between these two types of IFNs.

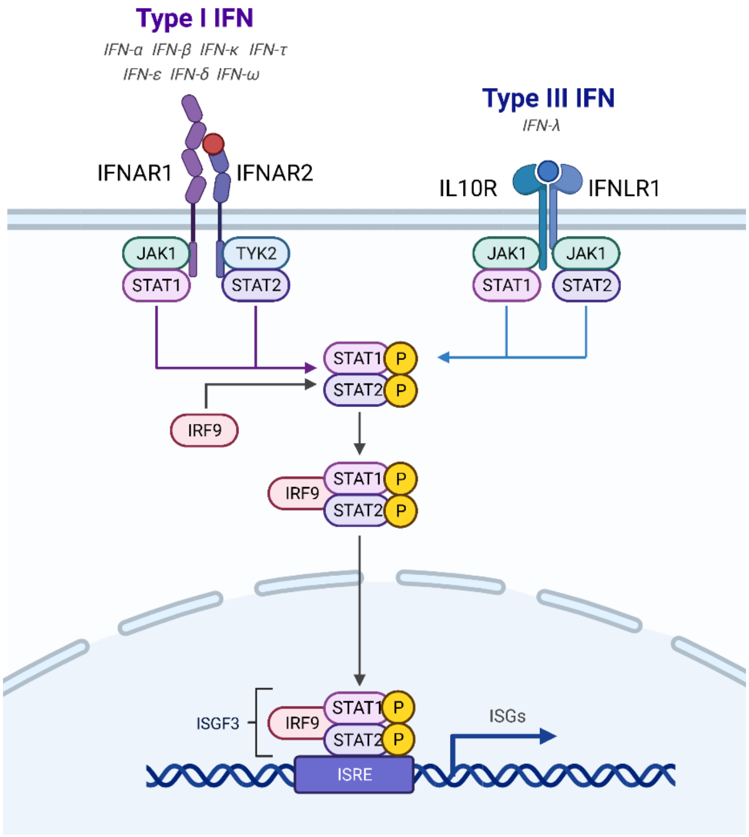

**Fig. 9. Type I and III IFN signaling pathway**. Type I IFNs bind to the heterodimeric IFNAR1/IFNAR2 receptor and type III IFNs bind to the heterodimeric IL10R/IFNLR1 receptor. This leads to the activation of Janus kinases (JAK1, JAK2, TYK1), and the subsequent recruitment and phosphorylation of STAT1 and STAT2. STAT1 and STAT2 form hetero- or homodimers, and associate with IRF9 forming the transcription complex ISGF3. ISGF3 translocates to the nucleus and binds to IFN-stimulated response elements (ISRE) inducing the transcription of interferon stimulated genes (ISGs).

### 1.1.7. Function and antiviral properties of ISGs

ISGs enclose all genes that are stimulated by IFN treatment of a cell. Depending on the cell type, IFN dose, and time of treatment, microarray studies identified 50-1000 ISGs (*139*). Considering the large amount of ISGs, it is not surprising that they exhibit a broad range of functions. A number of ISGs reinforce pathogen detection and IFN signaling. Included in this group are PRRs, IRFs and several signal transducing proteins such as JAK2, STAT1/2 and IRF9. These are major IFN signaling components present at baseline levels in the cell, but their transcription is further enhanced by IFNs (*140*), making sensing of PAMPs and signal transduction more efficient. ISGs also act as negative regulators of IFN signaling, to avoid an exacerbated immune response and facilitate the return to cellular homeostasis. For example, SOCS proteins play a role in early IFN desensitization by targeting JAK/STAT signaling, while USP18 is important in establishing and maintaining long-term desensitization to type I IFN signaling but not to type III IFNs (*140*). Current, there is no known negative regulator, like USP18, that targets the type III IFN receptor. This might explain why type III IFN signaling shows a more sustained ISG expression compared to type I IFNs. Importantly, ISGs encompass a broader range of functions, including roles in cell-to-cell communication through upregulation of chemokines and chemokine receptors (*140*) and apoptosis as reported for PKR, OAS and ISG15 (*141–143*). Interestingly, ISG15 was shown to stimulate cell death via a mitochondrial pathway (*143*). However, their pivotal role lies in controlling pathogen infections, especially viruses.

To be antiviral, ISGs can potentially intervene at every stage of the virus infection cycle. The ISG Mx1 is a broad inhibitor affecting virus entry. Mx1 belongs to small family of dynamin-like large GTPase, and evidence suggest that Mx1 traps incoming viral components preventing them from reaching their cellular destination (*144*, *145*). A number of ISGs inhibit virus replication, including members of the IFIT family, the OAS-RNaseL pathway, Viperin and ISG15. Viperin can down-regulate various metabolic pathways important for viral transcription and translation, or directly target viral proteins for degradation (*146*). ISG15 inhibits viral replication and infectivity by post-translational modification of viral or host proteins (*147*). Precisely, ISG15 can be covalently conjugated to target proteins, a process called ISGylation, changing the fate of the modified proteins (*147*). Moreover, Viperin was shown be an inhibitor of viral egress. Viperin interacts with the cellular enzyme farnesyl diphosphate synthase to perturb lipid rafts, resulting in inhibition of influenza virus release (*148*). These are only few examples for the diverse properties demonstrated for ISGs, and significant efforts are being dedicated to screen for potential ISGs and to characterize their antiviral effectors (*139*).

### 1.1.7. IFNs at epithelial surfaces

As outlined earlier, substantial distinctions exist between type I and III IFNs concerning their transcriptional regulation and their kinetics of ISG induction. However, the most notable contrast emerges from their receptor expression and the cell types capable of responding to each IFN. The type I IFN receptor is ubiquitously expressed, while the expression of IFNLR1 is restricted to epithelial cells (such as intestinal, lung, vaginal and hepatocytes) as well as a specific subset of immune cells (such as NK cells, pDCs, DCs as well as neutrophils in mice and B cells in humans) (*96*, *149–151*). This limited tropism of the receptor supports a model in which type III IFNs possess a unique role at mucosal surfaces.

The pivotal role of type III IFN signaling at mucosal surfaces becomes apparent through studies examining how it controls virus infections in epithelial cells. Antiviral responses in the gut are dominated by type III rather than type I IFN signaling. This is a direct consequence of high IFNLR1 and low IFNAR expression on intestinal epithelial cells (IECs), as compared to IFN receptor expression levels in cells located at the *lamina propia* (*152*). Furthermore, in response to enteric virus infection, IECs preferentially express type III over type I IFNs (*128*, *152–156*). Consequently, type III and not type I IFNs are key factors to protect IECs from pathogens. This was demonstrated in studies in which mice (*153*, *157*) and human IECs (*158–161*) were depleted of the type III IFN receptor and infected with different enteric viruses (norovirus, reovirus, SARS-CoV-2 and rotavirus). Conversely, type I IFNs mainly restricts systemic spread of enteric viruses if they invade beyond the epithelial cells (*152*, *162*). Collectively, the expression, signaling, and function of type I and type III IFNs are compartmentalized in the gut. The compartmentalization results in type I IFNs protecting the *lamina propria* and preventing viral dissemination throughout the body, while type III IFNs serve to protect the epithelial surface itself (Fig. 10).

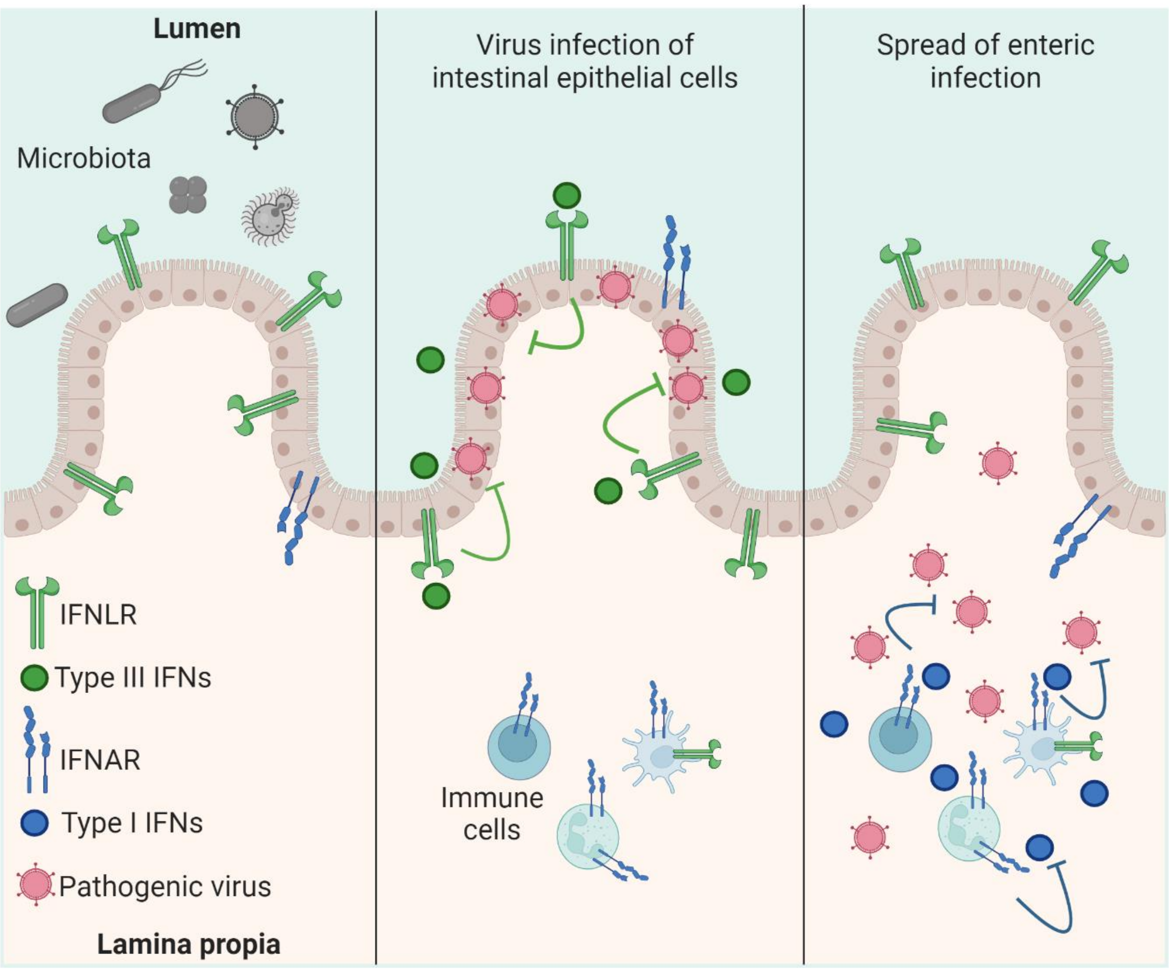

**Fig. 10. Compartmentalization of type I and III IFN signaling in the gut.** The intestinal epithelium is a mucosal surface in constant contact with commensal and pathogenic microbiota from the apical luminal side, and simultaneously facing the sterile *lamina propia* from the basal side. Consequently, IECs need to maintain a protective state without inducing an exacerbated immune response that can cause tissue damage. This fine-tuned immune equilibrium is achieved in part by compartmentalization of type I and III IFN signaling between the epithelium and the underlying *lamina propia*, given that these two types of IFNs possess different kinetics. Specifically, the type III IFN receptor (IFNLR) is expressed at higher levels in IECs compared to cells in the *lamina propia*, whereas the type I IFN receptor (IFNAR) is more highly expressed in the *lamina propia* than in IECs. Moreover, type III IFNs are key to protect IECs against enteric infection. Conversely, upon systemic spread of infection, type I IFNs act against viruses at the *lamina propia*.

The differential role between type I and III IFNs on respiratory tract epithelial cells is more complex. Mice lacking either the type I or the type III IFN receptor were more susceptible to infections with respiratory viruses such as influenza A virus, influenza B virus, respiratory syncytial virus, human metapneumovirus and SARS (*115*, *150*), suggesting that both type of IFNs play a redundant role in controlling infection in the lung. However, recent studies have revealed differences in how type I and type III IFNs control respiratory infections regarding location, cell type, and kinetic. When infected with respiratory pathogens, airway epithelial cells first produced type III IFNs, while type I IFNs were expressed delayed and/or in smaller amounts (*115*, *163–167*). Interestingly, at the upper respiratory tract, type III IFNs are critical to control Influenza A virus infection (*165*, *168*). Meanwhile, both type I and III IFNs are important to combat infection in the lower respiratory tract (*115*, *150*, *165*).

The unique role of type III IFNs became clear in a study showing that, during influenza infection of respiratory epithelial cells, type III IFNs were initially produced and cleared the infection if the viral load remained low; however, with a higher viral load, type I IFNs became necessary to control the infection (*150*, *165*). The original discrepancies in the function of type I and type III IFNs in the airway epithelium were the result of different inoculation strategies to infect mice with IAV promoting either an upper airway infection (type III IFN dependent) or a global airway infection (type I and III IFN dependent). Importantly, many studies demonstrated that type I IFNs restrict virus infection in the lung but can promote inflammation-induced disease (*165*, *169*, *170*). These findings suggest a model where type III IFNs act as the initial defense mechanism to control viral infections within airway epithelial cells, aiming to limit immune-related damage. This model, however, was recently opposed by Broggi et al. (*171*), which showed that that chronic type III IFN secretion by dendritic cells after viral burden causes damage to the lung epithelium, increasing the susceptibility to bacterial superinfections. Altogether, it becomes apparent, that location, timing and duration of IFN exposure in the lung determine the immune outcome.

In addition to their antiviral effects, IFNs act on epithelial surfaces by supporting physical barrier formation, thereby indirectly hindering infections by preventing pathogen intrusion. In a mechanism independent of STAT1 signaling, both type I and III IFNs induce cell junction tightening in brain microvasculature endothelial cells (*172*, *173*). This in turn reduces the blood brain barrier permeability, protecting mice from virus neuroinvasion (*172–174*). The effect of IFNs on epithelial barrier function is not unique to the central nervous system, but has also been reporter for the respiratory and gastrointestinal tract. Type I IFNs in the airway epithelium induced the production of tight junctions thereby preventing bacteria transmigration (*175*), and counteracted tight junction dissociation during rhinovirus infection (*176*). Similarly, type III IFNs enhanced intestinal barrier formation, protecting human IECs from bacteria (*177*) and *Cryptosporidium parvum* (*178*) infection. Contrary to this, recent studies demonstrated that sustained IFNλ treatment disrupts the airway epithelial barrier, thereby predisposing the host to bacterial superinfections (*171*, *179*). Similarly, it was reported that both type I and III IFNs disrupt airway epithelial repair during recovery from viral infections (*180*). Discrepancies in the impact of IFNs on epithelial barrier function can be attributed to differences in the cytokine amount and the duration of cytokine exposure. Further work is necessary to characterize the function of IFNs in promoting barrier functions. It is possible that IFNs (type I or III) can promote or damage tight junctions in a cell type specific manner, or that the balance between promoting and damaging is controlled by other cytokines acting in concert with IFNs on the same cell.

The constant exposure of epithelial surfaces to commensal and pathogenic microbes requires a balanced immune response that ensures protection while preventing damage. The spatial segregation of the IFNLR expression to epithelial cells designates type III IFNs with a crucial role at mucosal surfaces. The distinctive ISG expression pattern, characterized by lower intensity and prolonged duration compared to type I IFNs, positions type III IFNs as a perfect candidate to control infection while limiting excessive inflammation. Currently a model has emerged wherein type III IFN signaling serves as an initial, lower-intensity, and less pro-inflammatory primary defense in epithelial cells (*99*, *181*). If infection is not controlled and when immune cells are actively recruited to infected mucosal surfaces, the more inflammatory type I IFNs are activated. This can provide additional protection to the epithelial cells of the mucosa, and, more importantly, will provide systemic protection against viral pathogen as they may spread beyond the epithelial barriers.

### 1.1.8. SARS-CoV-2 and IFNs

Coronaviruses (CoV) can cause acute and persistent infections in mammals and birds. Seven coronaviruses are known to cause human infections. While four of these viruses are associated with mild respiratory illness, SARS (severe acute respiratory syndrome)-CoV, MERS (Middle East respiratory syndrome)-CoV, and SARS-CoV-2 can cause severe disease, including death. SARS-CoV-2 is responsible for the human coronavirus disease 19 (COVID-19), and emerged as a zoonotic pathogen in 2019, quickly causing a pandemic that has spread around the world with more than 770 million confirmed cases and approximately 6.9 million deaths to date (World Health Organization).

Transmission of SARS-CoV-2 among humans is mainly by respiratory droplets (*182*). Therefore, the initial site of infection is the airway epithelium, leading to respiratory symptoms that span from cough and shortness of breath to severe lung injury (*183*). Interestingly, patients with COVID-19 frequently reported gastrointestinal symptoms (*183–186*) and viral RNA was detected in stools samples of infected and convalescent patients (*187–191*). Direct evidence for SARS-CoV-2 infection of the gut was provided by endoscopic samples (*186*, *192*, *193*), and *in vitro* studies showing infection of immortalized human intestinal epithelial cells and primary human minigut organoids (*161*, *194–196*). This highlights the intestinal epithelium as a potential location for virus production and spread, contributing to the development of diseases.

SARS-CoV-2 is an enveloped positive-sense single-stranded RNA Betacoronavirus in the *Coronaviridae* family. The ~30,000 base RNA genome is capped and methylated, and encodes 4 major structural proteins and 16 nonstructural proteins (NSPs) that mediate virus replication, infection, and pathogenesis. The virion consists of nucleocapsid (N), membrane (M) envelope (E) and spike (S) protein (Fig. 11 A) (*197*). Virus attachment to the target cell is mediated by the viral S protein and engagement of the host receptor ACE2 (Fig. 11 B). In addition, several host factors have been proposed to be involved in viral attachment (*198*). SARS-CoV-2 enters the cell either by CME into endolysosomes, or through direct fusion with the cell plasma membrane (*198*). After entry and uncoating of viral RNA, replication of the viral genome occurs in endoplasmic reticulum (ER)-associated replication complexes by a virus-encoded RNA-dependent RNA polymerase (Fig. 11 B). Virion assembly and budding occurs along the ER-to-Golgi network, and new virions are released by exocytosis (*197*). Throughout the SARS-CoV-2 replication cycle, many PAMPs are generated and recognized by cell-intrinsic host defense mechanism. The RLRs MDA5 and RIG-I, as well as TLR2, TLR3 and TLR7/8 have been shown to directly recognize SARS-CoV-2 factors (*199*). Moreover, various studies demonstrated indirect activation of the STING pathway through DAMPs (*199*).

SARS-CoV-2 recognition by the cell induces a robust IFN-dependent immune response, which can be counteracted by the virus (*199*, *200*). Interestingly, while induction of IFN and downstream ISGs was reported after SARS-CoV-2 infection of lung epithelium (*201*, *202*), other studies described limited or absent IFN response in lung epithelial cells (*203–206*). The latter observation could result from viral strategy to evade the host immune response (*195*, *207*). Less is known about the IFN-dependent response in intestinal epithelial cells. However, there is clear evidence showing a typical induction of type I and III dependent signaling after SARS-CoV-2 infection (*161*, *194*, *204*). The importance of IFN signaling to control SARS-CoV-2 infection has been supported by reports showing that mutations in the type I IFN pathway were enriched in patients with severe symptoms as compared to control patients, resulting in low type I IFN levels in the blood (*200*). Similarly, patients with life-threatening symptoms had autoantibodies against type I IFNs, which were able to neutralize secreted IFNs (*200*). In contrast, these autoantibodies were not present in any of the patients with asymptomatic or mild SARS-CoV-2 infection (*200*). Importantly, treatment of epithelial cells with type I (*202*, *205*, *206*, *208–210*) and type III (*161*, *206*, *208*, *211*) IFNs induced a protective state in the cells and inhibited SARS-CoV-2 infection. Given their potent antiviral role, IFNs are promising candidates for treatment against SARS-CoV-2.

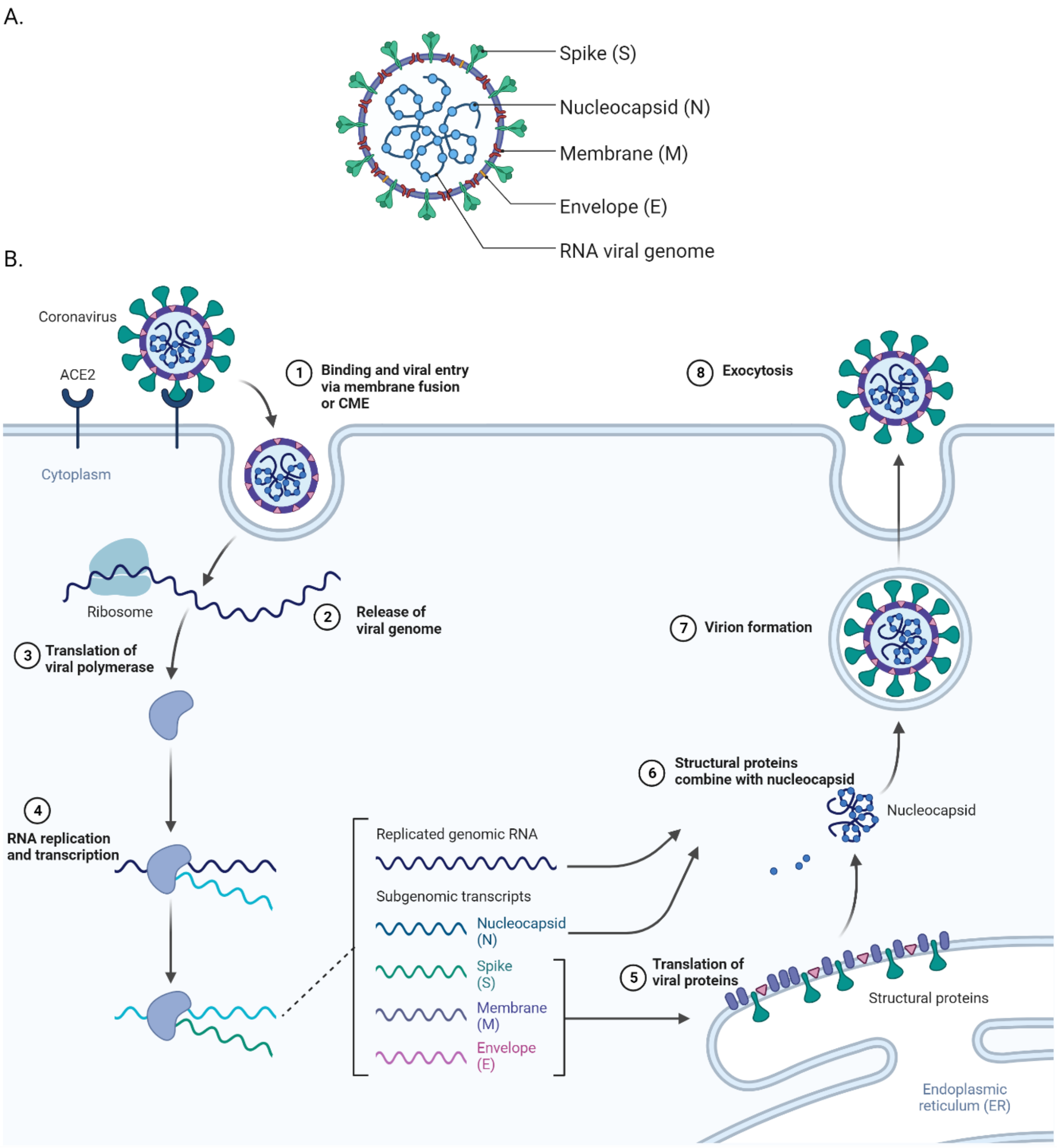

**Fig. 11. SARS-CoV-2**. (A) Schematic of SARS-CoV-2 structure. (B) SARS-CoV-2 replication cycle.

Intriguingly, exacerbated and/or dysregulated IFN-dependent responses to SARS-CoV-2 were associated with severe COVID-19. Type I responses were upregulated in peripheral blood mononuclear cells and lungs of patients with severe disease, accompanied by a proinflammatory (TNF and IL-1β) immune signature (*212–218*). The proinflammatory roles of type I IFNs were described in other studies, which suggest that IFNs support an exacerbated immune response and pathogenesis (*218*, *219*). Conversely, when production of type I and III IFN was delayed or diminished, proinflammatory cytokines were produced leading to pathogenesis (*220*). It is now clear that the IFN-dependent response to SARS-CoV-2 must be precisely fine-tuned to elicit a protective state against the virus, and not an exacerbated immune response which can lead to hyperinflammation. Therefore, a more detailed understanding on the IFN kinetics are required to fully grasp the IFN-dependent immune response to SARS-CoV-2.

## 1.2. Basal IFN expression and basal IFN-dependent signaling

### 1.2.1. Definition and function of basal IFN-dependent signaling

Although IFN genes and their transcription is tightly regulated in response to a pathogenic trigger, it has become clear that IFNs are also constitutively produced under sterile conditions, albeit at significantly low but physiologically relevant levels (*221*, *222*). This leads to basal IFN-dependent signaling, required to maintain homeostasis and immune responsiveness.

A widely accepted model suggests that basally expressed type I IFNs maintain homeostatic levels of important signaling components such as JAKs and STATs, priming cells for a rapid and robust response to subsequent pathogenic challenge (Fig. 12 A) (*222*). In line with this, cells lacking proper IFNβ signaling exhibited reduced concentrations of STAT1, STAT2, IRF1, and IRF7 in contrast to wild-type cells within a sterile environment (*223*, *224*). Basal IFN expression and signaling also has a direct anti-pathogenic function. IFNε is a unique type I IFN constitutively expressed along the female reproductive tract and regulated by female sex hormone fluctuations. Various studies demonstrated that the basal IFNε-dependent signaling is pivotal to protect the female reproductive tract from bacterial (chlamydia) (*225*) and viral (HSV2 and Zika) (*225*, *226*) infections. Basal IFN-signaling was also shown to protect from Hepatitis virus (*227*) and Rotavirus (*228*) infection. However, it is not clear to which extent this is dependent on basal IFN expression levels, as the studies suggest that an unphosphorylated variant of the ISGF3 complex was responsible to maintain basal transcription of ISGs in the absence of IFN stimulation (*227*, *228*).

Beyond the cellular level, basal type I IFN expression is necessary at the organismal level. Mice lacking the type I IFN receptor displayed a reduction in hematopoietic stem cells (HSC) compared to WT mice, suggesting that basal IFN signaling maintains the HSC niche and supports HSC mobilization (*229*). Moreover, constitutive type I IFN expression is essential to maintain homeostatic cell type abundance and activity of the myeloid lineage as well as immune cells (*222*). The question raises on how can basal type I IFN signaling have such an impact at the multicellular level? A possible explanation is that the absence of basal IFN concentrations leads to diminished expression of STAT and other regulatory proteins (Fig. 12 A) (*222*). Lack or low levels of these regulatory proteins could results in an impaired communication between different cytokine signaling networks and impaired signaling of other

STAT dependent pathways, which are essential for the regulation of the myeloid and immune cell lineage abundance, differentiation and mobilization (*222*).

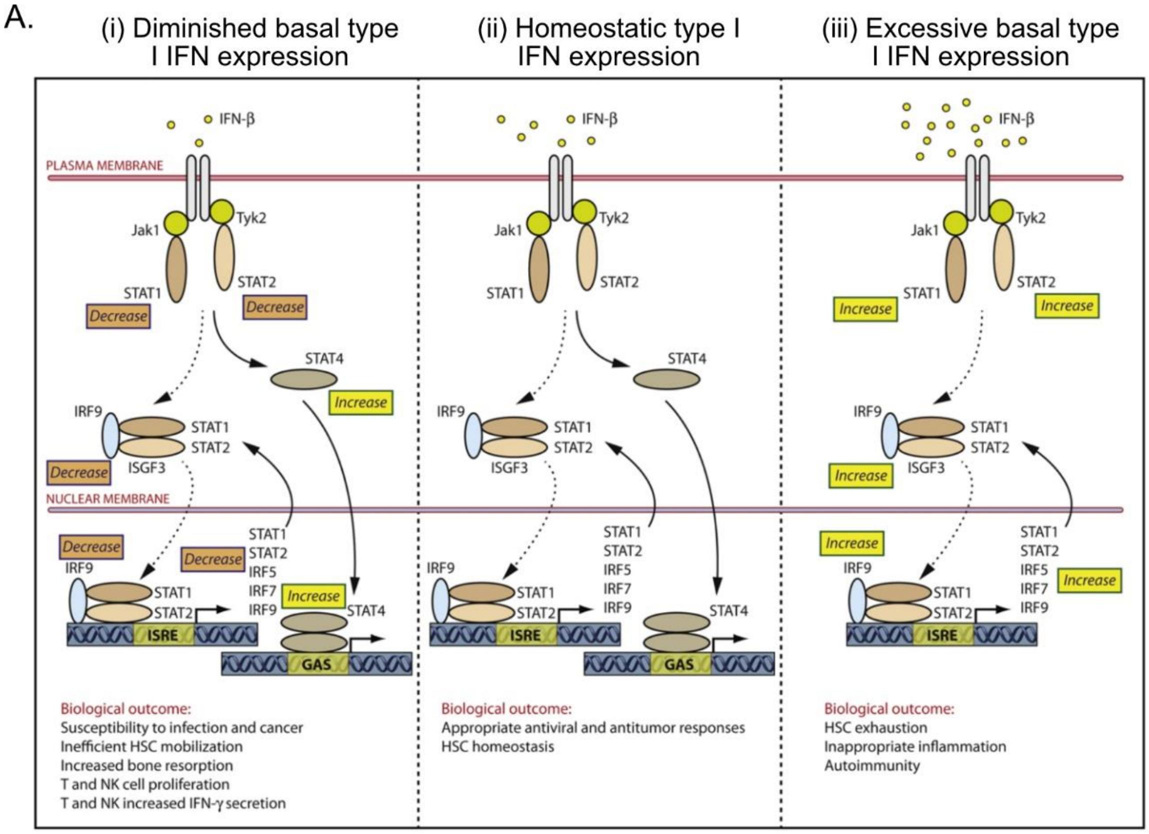

Adapted from *Gough et al., Immunity (2012)*

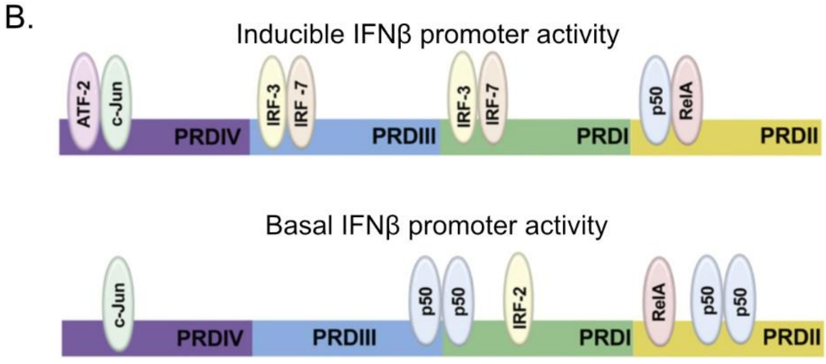

Adapted from *Gough et al., Immunity (2012)*

**Fig. 12. Basal type I IFN signaling.** (A) (ii) Under homeostasis, low amounts of type I IFNs are expressed and secreted at a basal level, which maintains appropriate levels of signaling intermediates including the transcription factors STAT1, STAT2, IRF7 and IRF9. This homeostatic type I IFN expression enables an appropriate antiviral and antitumor response, and hematopoietic stem cell (HSC) balance. (i) Diminished or (iii) excessive basal type I IFN secretion results in an imbalance of signaling molecules. (i) Diminished basal IFN culminates in susceptibility to infection and cancer, inefficient HSC mobilization and increased bone resorption. (iii) Excessive type I IFN expression initiates an inflammatory environment that can result in autoimmunity and exhaustion of the HSC niche. (B) Transcription factors for inducible and constitutive/homeostatic IFNβ promoter activity. The *Ifnb* promoter contains four positive regulatory domains, namely PRDI–PRDIV. During stimulation-dependent induction of *Ifnb* expression, the transcription factors IRF-3 and/or IRF-7, ATF-2 and c-Jun, p50 and RelA, and the architectural protein HMGA1 (not pictured) are recruited to the promoter, leading to rapid and robust IFNβ expression. In the absence of stimulation, the *Ifnb* promoter is occupied by c-Jun and RelA to promote basal IFNβ expression, and IRF-2 and p50 homodimers, which negatively regulate IFNβ production. (A, B) Figures adapted from (*222*).

### 1.2.2. Induction and regulation of basal IFN expression

While some research has been conducted on the functions of constitutive IFN expression and signaling, the upstream factor and/or pathway responsible to induce basal IFN transcription remains poorly characterized.

It is well established that the cGAS-STING pathway is activated by pathogen-derived DNA or cyclic di-nucleotides (*86*). Additionally, pathogen infection and cellular perturbations can result in organelle damage and the subsequent release of nuclear or mitochondrial DNA, so-called DAMPs (defined in section '1.1.5.2. DAMPs as ligands for PRRs'), also leading to the activation of cGAS (*86*). Therefore, until recently, the cGAS-STING pathway was thought to be inactive at homeostasis, and only activated in response to pathogen infections or disruptions in cellular processes. However, the activation of the cGAS-STING pathway only in response to cellular stress and pathogen infections does not explain a number of observations. For instance, cells and mice lacking cGAS or STING exhibit increased susceptibility to infection by various RNA viruses, even though the majority of RNA viruses do not directly or indirectly (e.g., through mitochondrial DNA release) activate cGAS/STING (*89*, *230*, *231*). Additionally, gain-of-function SAVI mutants (STING-associated vasculopathy with onset in infancy) chronically activate STING signaling without pathogen-associated DNA exposure (*232*). These observations suggest that cGAS-STING is operational at homeostasis, leading to basal IFN expression which is protective against RNA viruses, and leading to disease in case of imbalance. Indeed, recently Wang et al. (*233*) and Tu et al. (*234*) finally demonstrated that the cGAS-STING pathway is constitutively signaling, inducing basal type I IFN production. Importantly, Tu et al. (*234*) found satellite DNA, mitochondria DNA, and retroelement DNA but not genomic DNA bound to cGAS at resting state, serving as potential immunogenic triggers. Additional research is needed to gain a more comprehensive understanding of cGAS-STING induction and activity under homeostatic conditions, and whether this activity influences not only type I IFN expression but also type III IFN expression.

Even less is known about the induction of basal IFNs at a transcriptional level, and whether it is differently regulated to IFN transcription during antiviral defense. Regulation of basal IFN signaling depends on the same PRRs that are used during pathogen challenges, but these PRRs are activated at basal level in sterile conditions. Signal transduction downstream these PRRs might be different in sterile vs. pathogen challenge conditions. Unlike the IFNβ induction during viral infections, the constitutive expression of IFNβ seems to be independent of IRF3 and IRF7, but relies on the AP1 subunit c-Jun and the NF-κB subunit RelA (Fig. 12 B) (*224*, *235–237*). Further studies should explore the distinctions in transcriptional regulation between virus-induced and constitutive IFN expression, encompassing both type I and type III IFNs.

Basal IFN expression needs to be tightly regulated, as an imbalance can contribute to pathology such as autoimmune disease and cancer. Wang et al. (*238*) shed light into a mechanism inhibiting aberrant IFN upregulation in homeostasis. They discovered that caspase-8 suppresses basal production of type I IFNs by cleaving RIPK1. In cells and mice lacking caspase-8, RIPK1 interacts with TBK1, enhancing homeostatic type I IFN production (Fig. 13) (*238*). This leads to increased antiviral resistance and an early onset of lymphadenopathy (*238*). Previous studies also examined the regulation of basal immune activation at a transcriptional level, and found that IRF2 and p50 homodimers engage with the IFNβ promoter to function as repressors, consequently regulating the levels of constitutively secreted IFNβ (*239*–*243*). Which transcriptional repressors and activators play a role in regulating other type I and III IFNs needs to be further studied.

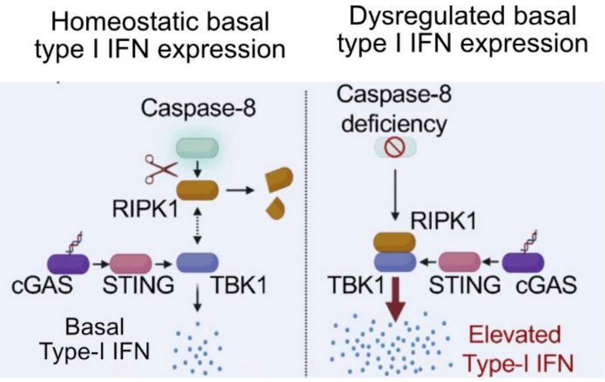

Adapted from *Wang et al., Cell Reports (2022)*

**Fig. 13. Regulation of basal type I IFN production by caspase-8 and RIPK1.** Caspase-8 regulates basal type I IFN expression trough the RIPK1-TBK1 axis. Loss of caspase-8 allows for RIPK1 interaction with TBK1, enhancing basal type I IFN production. Figure adapted from (*233*).

### 1.2.3. Dysregulation of basal IFN signaling and disease

A range of mutations have been documented in malignancies associated with cancer development, which either impede IFN production or reduce responsiveness to IFNs. A few examples of such mutations include the deletion of IFN genes in acute leukemia cells (*244*) and malignant T cells (*245*); downregulation of IFNAR in hairy cell leukemia (*246*), gastric cancer (*247*) and lymphoblastoid cells (*248*); loss of JAK1 in lung carcinoma (*249*); and downregulation of IFN signaling components in melanoma (*250*) and chronic myeloid leukemia (*251*). Whether the absence of basal IFN expression or the incapacity to react to exogenous IFNs contributes to tumor development remains to be fully elucidated. Nonetheless, these reports suggest that basal IFN expression and signaling, or rather the lack of it, could support tumorigenesis.

The development and progression of autoimmunity is multifactorial, however increased secretion of type I IFNs is typical in patients with autoimmune diseases, including systemic lupus erythematosus (SLE), Sjögren's syndrome, or type I diabetes mellitus (DM) (*222*, *252*–*254*). Moreover, type I IFN expression levels correlate with increased disease severity. In the case of interferonopathies including Aicardi–Goutières syndrome and STING-associated vasculopathy with onset in infancy (SAVI), IFNs directly drives the disease (*255*). Aberrant induction of type I IFN expression and signaling in these diverse inflammatory diseases has been linked to the activation of the cGAS-STING pathway, the RLR-pathway or other pathways recognizing immunogenic molecules (*85*, *86*, *222*, *255*). Activation of these pathways occur through alterations of the RNA and DNA metabolism, loss- and gain-of-function mutations, and molecular trafficking problems. Moreover, significant amount of mutations in molecules along the IFN dependent signaling pathway, as well as dysregulation of regulatory mechanisms, have been identified to contribute to increase IFN signaling (*222*, *255*).

Importantly, studies in which homeostatic IFN expression was directly disrupted, shed light on the immediate consequences of basal IFN dysregulation. Increasing the homeostatic type I IFN production by depleting Caspase-8 in mice resulted in early onset of lymphadenopathy (*238*). Furthermore, disruption of STING post-Golgi trafficking in mice, which enhances basal IFN signaling, significantly elevated levels of IgM autoantibodies targeting a broad spectrum of antigens associated with lupus and other autoimmune disorders (*234*).

These findings support a concept of IFN-driven homeostasis. Appropriate basal IFN levels are required to maintain a diverse range of essential signaling molecules for both immunity and tissue stability. Deviations from these levels, whether lower or higher, lead to detrimental outcomes. While these insights stem from studies centered on type I IFNs, it is crucial to extend research in this area to basal type III IFN expression and signaling. Especially considering the significance of type III IFNs at mucosal surfaces, where a finely tuned equilibrium between tolerance to (commensal) microbes and immune responsiveness is essential to maintain homeostasis.

## 1.3. Polarized epithelial cells

### 1.3.1. Apical-basolateral polarity of epithelial cells

Epithelial tissues are found on the surfaces of all organs thereby acting as a barrier between compartments or to the outside environment. A hallmark of epithelial cells is their polarized phenotype along the apical-basal axis. This results in three distinct membrane domains, which have a differential composition of proteins and lipids (Fig. 14 A): The apical domain, often containing specialized structures such as microvilli or cilia, are in contact with the lumen or the outside environment. The lateral domain adheres to adjacent cells, sealing paracellular spaces. And the basal domain is anchored to the basement membrane. The basal and lateral membranes share similar components, and are often referred to as basolateral membrane. The key characteristics of polarized epithelial cells include the formation of intercellular junctions, the asymmetric cytoskeleton distribution, organelle rearrangement and the specific allocation of polarity complex proteins and membrane lipids. Each of these components is tightly regulated by signaling pathway, with Rho GTPases (pivotal components of actin cytoskeletal regulation) serving as key regulatory factors. Polarization enables cells to sense and to generate proper spatiotemporal responses to cues that arise from neighboring cells and from the surrounding microenvironment, with responses adapted to whether the stimuli was coming from the apical or basolateral membranes (*256*).

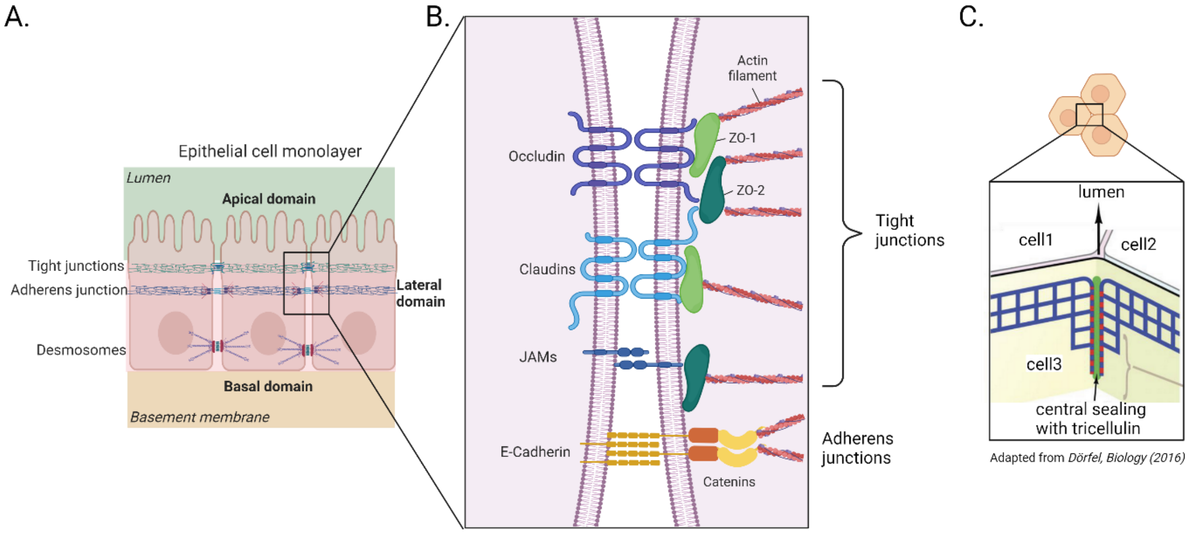

**Fig. 14. Apical-basolateral polarity of epithelial cells and junctional complexes.** (A) Epithelial cells polarize along the apical-basal axis, resulting in three distinct membrane domains. The apical domain is in contact with the lumen or the outside environment, the basal domain is anchored to the basement membrane, and the lateral domain adheres to adjacent cells through tight junctions, adherens junctions and desmosomes. (B) Tight junctions are essential to establish a semipermeable monolayer by regulating the passage of ions, water and molecules across the paracellular spaces, and are essential to maintain cell polarity. Tight junctions are composed by transmembrane proteins (such as occludin, claudin and junctional adhesion molecule (JAM)) and cytoplasmic proteins, including ZO1-3, which serve as link with the intracellular cytoskeleton. Adherens junctions adhere neighboring cells to each other, and comprise two families of transmembrane spanning receptors (cadherins and nectins) which interact with intracellular proteins (such as catenins) and the cytoskeleton. (C) Tricellulin is a transmembrane tight junction protein localized vertically at the meeting membranes of three cells. Figure adapted from (*257*).

### 1.3.2. Physical barrier formation at epithelial surfaces

Epithelial cells act as a barrier between compartments or the outside environment. Especially at mucosal surfaces, such as the gastrointestinal and airway tract, fine tuning of the barrier function is critical to tolerate the commensal flora while maintaining responsiveness to invading pathogens. Foremost, epithelial cells form a physical barrier preventing unwanted material from entering the body while maintaining selective permeability. To bridge epithelial cells together into an organized monolayer, structural and signaling components assemble into junctional complexes at the lateral membrane of polarized cells forming tight junctions, adherens junction, desmosomes, and hemidesmosomes (Fig. 14 B). Desmosomes and hemidesmosomes are localized towards the basal portion of polarized epithelial cells, and facilitate adhesion between epithelial cells or anchoring to the basement membrane (*258*). Adherens and tight junctions are arranged at the apical portion of the cell.

The main function of adherens junctions is to adhere cells to their neighboring cells. They comprise two families of transmembrane spanning receptors: cadherins and nectins. The extracellular region of these proteins interact with the extracellular region of the same protein from neighboring cells, hence mediating adhesion. The intracellular domains interact with an array of proteins, connecting the cluster to the actin cytoskeleton and stimulating signaling pathways (Fig. 14 B) (*259*).

Tight junctions regulate the passage of ions, water, and macromolecules across the paracellular spaces (regions between cells), and are essential to maintain cell polarity by restricting the distribution of lipids within the membrane (*259*). Tight junctions are composed of more than 40 proteins, which can be classified into two groups: The transmembrane proteins whose extracellular domains interact with their partners on adjacent cells, consisting of occludin, claudin, junctional adhesion molecule (JAM), and tricellulin (Fig. 14 B-C) (*260*). The cytoplasmic scaffolding proteins located at the intracellular side of the plasma membrane, which provide a direct link between transmembrane tight junction proteins and the intracellular cytoskeleton (*259*) (Fig. 14 B). Zona Occludens (ZO) proteins are central cytoplasmic scaffolding proteins and comprise three closely related isomers ZO1-3. While both ZO1 and ZO2 play a crucial role in maintaining epithelial barrier function, ZO3 seems to be unessential at least for intestinal integrity (*261*, *262*). Given that ZO proteins interact with most of the transmembrane tight junction proteins, they provide the structural basis for the formation of tight junctions (*260*). In addition to tight junction proteins, ZO-1 binds the adherens junction proteins afadin and α-catenin, linking the two junctional complexes (*259*).

Historically, the major function of junctional complexes was thought to maintain the structural integrity of the semipermeable monolayer of polarized epithelial cells. However, recent studies revealed that the epithelial junctions can also control processes including regulation of innate immunity, stress response, autophagy, lysosome, and proteasome-mediated degradation (*258*). For example, adherens junctions were found to suppress the inflammatory response of skin and bronchial epithelial cells by interaction between the junctional catenin family proteins and key regulator of the NF-κB pathway (*263–266*). Major efforts are required to understand the interplay of junctional complexes with other biological processes at mucosal surfaces.

### 1.3.3. Establishment of cell polarity

The establishment and maintenance of polarization relies on a finely tuned interplay between integrins, adherens junction, tight junction and cell polarity complexes. The three major polarity complexes are the PAR polarity complex promoting the establishment of the apical-basal membrane border, the Crumbs complex required to establish the apical membrane, and the Scribble complex defining the basolateral plasma domain (*267*).

To establish polarity, epithelial cells determine their orientation with their basal surface through the adhesion of integrin receptors to the extracellular matrix (*268*). Subsequently, epithelial cells extend membrane protrusions, known as filopodia, to contact neighboring cells (*268*). Normally, cell-to-cell contacts then initiate the polarization program. Adhesion proteins nectin recruits JAM-A through afadin with the help of ZO-1. Subsequently, JAM-A recruits PAR3 to initial tight junctions, establishing the apicobasal border. PAR3 serves as a scaffold protein recruiting a number of tight junctions, adherens junction and signaling protein, thereby enabling a number of coordinated steps that will lead to cell polarization. Basically, the PAR complex is responsible to separate adherens junction from tight junction proteins at the initial intercellular adhesion sites, allowing for formation of the adherens junction belt and mature tight junctions. The Scribble complex localizes with adherens junctions promoting basolateral membrane identity, and Crumbs signaling proteins accumulate at the apical membrane to induce differentiation and maturation of junctional complexes. Along this process, the cytoskeleton undergoes major rearrangement, resulting in an asymmetric distribution within the cells and tight anchoring to junctional complexes. After being established, apical-basolateral polarity is maintained through mutual antagonism or negative feedback regulation between the apical and cellular components. (*269*, *270*)

## 1.4. Cell-to-cell variability and the population context

### 1.4.1. Cell-to-cell variability

Cell-to-cell variability can be described as single cell heterogeneity within a population of genetically identical (isogenic) cells growing under the same conditions, *i.e.*, the deviation of individual cells from the population average (Fig. 15). The seminal work for this concept was performed by Elowitz et al. and Ozbudak et al. who employed fluorescent proteins and clearly demonstrated that expression levels can vary between identical cells (*271*, *272*). These papers marked the beginning of quantitative single cell biology, and over the past decades, single-cell measurements revealed large variations among individual cells and identified it as a fundamental property of cellular systems (*273–275*).

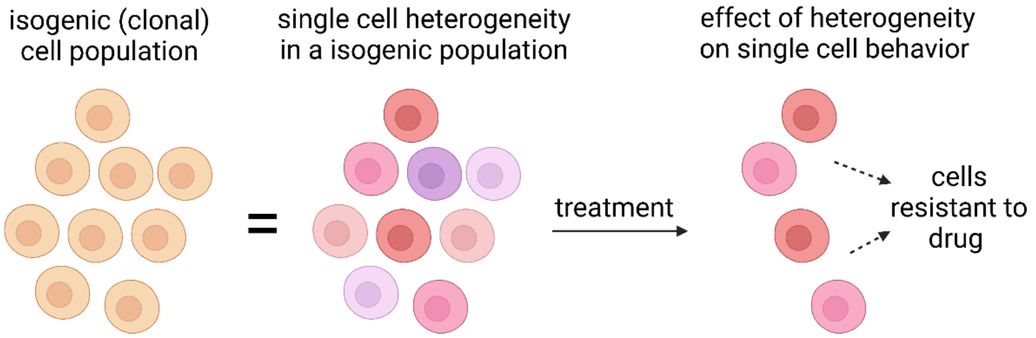

**Fig. 15. Cell-to-cell variability in isogenic populations.** Single cells in an isogenic (genetically identical/clonal) population are heterogeneous. This is called cell-to-cell variability. Cell-to-cell variability occurs at the gene expression, protein and metabolite level, leading to a single-cell heterogeneity in signaling pathways and cellular behavior. This can have strong implications during treatment of isogenic cells with drugs, as some cells might be resistant while others not.

Cell-to-cell variability is present at various levels, and was comprehensively reviewed by Symmons and Raj (*275*). Some examples are summarized in the table below. Shortly, the most studied area in single cell heterogeneity is at the mRNA level including abundance, half-life, and intracellular localization of mRNA transcripts. Cell-to-cell variation in transcription factor abundance, localization, and binding, as well as chromatin organization and modifications are important factors to consider in mRNA expression analyses. Cell-to-cell variability is also known to be dependent on abundance, modifications, and localization of proteins and metabolites. Finally, single-cell heterogeneity at the mRNA, protein and metabolite levels drives single-cell heterogeneity in signaling pathways, which has a direct influence on cellular behavior.

| **Cell-to-cell variability** | **Level** | **Reference** |
|---|---|---|
| Transcript abundance quantified by GFP in the cell via fluorescence microscopy or flow cytometry. | mRNA (gene expression) | Elowitz et al. (2002) (*271*), Ozbudak et al. (2002) (*272*), Taser and O'Shea (2004) (*276*) |
| Number of mRNA per cell measured by *in-situ* hybridization in fixed and living cells. Measurements were also done across hundreds of genes in a large number of cells simultaneously. | mRNA (gene expression) | Levsky et al. (2002) (*277*), Raj et al. (2006) (*278*), Raj et al. (2008) (*279*), Golding et al. (2005) (*280*), Chen et al. (2015) (*281*), Lubeck et al. (2014) (*282*) |
| Single cell differences in the entire transcriptome of individual cells measured by single-cell RNA-sequencing | mRNA (gene expression) | Grün et al. (2014) (*283*), Marinov et al. (2014) (*284*), Wu et al (2014) (*285*) |
| Location of mRNA in cells measured by single cell spatial transcriptomics. | mRNA (gene expression) | Achim et al (2015) (*286*), Junker et al (2014) (*287*), Satija et al. (2015) (*288*) |
| Transcription factor binding and localization in single cells using microscopy and probing technologies. | mRNA (gene expression) | Elf et al. (2007) (*289*), Hammar et al. (2012) (*290*), Sah and Tyagu (2013) (*291*) |
| Single cell differences in the proteome of individual cells measured by single-cell cytometry. | Protein | Bjornson et al. (2013) (*292*) |
| Single cell differences in the metabolome of individual cells measured by single-cell metabolomics. | Metabolites | Zenobi et al. (2013) (*293*) |

Cellular heterogeneity can be explained by deterministic and/or stochastic contributions. Processes are regarded as deterministic if different cells get different instructions therefore having a variable outcome, while stochasticity described different outcomes for cells that received the same instructions (*274*, *275*). A deterministic source of cell-to-cell variability is when the pre-existing state or activity of a cell, and hence the molecular machinery, regulate/drive the single cell heterogeneity. However, historically, cell-to-cell variability has been attributed to originate from stochastic events, based on the chemical nature of biological reactions (*271*, *275*). Indeed, stochasticity is the more widely accepted explanation behind heterogeneity in isogenic populations within the field. Stochastic events arise from ‘noise’, a term describing some randomness of molecular interactions in the cellular environment, resulting from low copy number of molecules and their random collision (*275*, *294*).

Crucially, a significant distinction exists between 'intrinsic' and 'extrinsic' noise when looking at stochastic events, a concept that was introduced by Elowitz et al. (*271*). In their experiments, Elowitz and colleagues quantified the variability in the expression from a promoter in *E. coli*. They introduced two copies of the same promoter into the *E. coli* genome, one driving the expression of cyan fluorescent protein (CFP) and one driving the expression of yellow fluorescent protein (YFP). Expression of the fluorescent proteins was analyzed by fluorescence microscopy (Fig. 16 A). Within this configuration, extrinsic noise affects the expression of both fluorescence reporters equally (Fig. 16 B). Extrinsic noise is determined by cell-to-cell variation in the concentration of cellular biomolecules such as ribosomes, enzymes, metabolites, overall proteins, and nucleic acids (Fig. 16 C). Intrinsic noise results from the probabilistic nature of molecular processes and the randomness inherent to transcription and translation (Fig. 16 C). As such, intrinsic noise affects the expression of the fluorescence reporters independently (Fig. 16 B).

There is a fundamental problems in separating stochasticity from determinism when studying cellular heterogeneity (*274*, *295*). Since the regulation of most cellular processes is highly complex and poorly understood, it is challenging to experimentally demonstrate that an event is solely stochastic, as opposed to the possibility of a yet unknown factor being responsible for the cell-to-cell variability. Indeed, as tools become more sophisticated, we can now often find the “cause” for a particular probabilistic-seeming event (*274*, *295*).

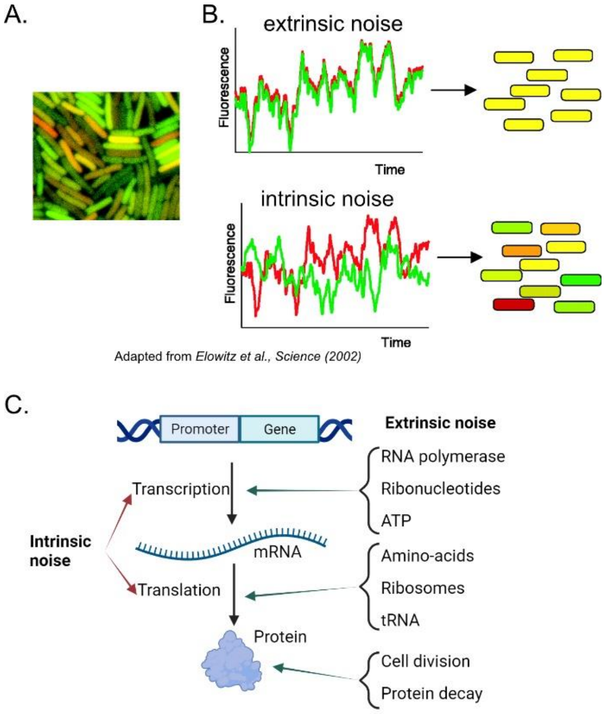

Adapted from *Elowitz et al., Science (2002)*

**Fig. 16. Intrinsic and extrinsic noise during stochastic events.** (A, B) Intrinsic and extrinsic noise was measured in *E. coli* by the expression of YFP (red) and CFP (green) under control of the same promoter. (A) Fluorescence image of individual *E. coli* displaying marked cell-to-cell variability in the expression of two identically regulated fluorescent proteins YFP and CFP. (B) Schematic depiction of the temporal behaviors of extrinsic noise and intrinsic noise. Extrinsic noise affects the expression of both fluorescence reporters equally, leading yellow fluorescence in bacteria. Intrinsic noise affects the expression the expression of the fluorescence reporters independently. (A, B) Adapted from (*271*). (C) Extrinsic noise is determined by cell-to-cell variation in the concentration of cellular biomolecules such as ribosomes, enzymes, metabolites, overall proteins, and nucleic acids. Intrinsic noise results from the probabilistic nature of molecular processes and the randomness inherent to transcription and translation.

### 1.4.2. The population context

As soon as cells are not single but part of a group, they possess a population context. The population context is constantly sensed by single cells and translated into a specific behavior. A widely studied example for this are bacteria, which develop a complex pattern of multicellular behavior to improve the overall fitness of the population (*296*). To accomplish this, bacteria engage in so-called *quorum sensing*, wherein they communicate, form cell-to-cell contacts and sense the local cell density through secreted signaling molecules (*297*). Given that the primary focus of this thesis are epithelial tissues, the description of the population context will be limited to eukaryotic adherent cells. The population context of non-adherent eukaryotic or prokaryotic cells will not be explored here.

The population context is the physical microenvironment in which an adherent cell is embedded in relation to neighboring cells. The parameters that constitute the population context of an individual cell are the local cell density, cell-to-cell contacts, and relative location within the population (*274*) (Fig. 17). Various molecular mechanisms sense these parameters and translate them to a population-dependent behavior including changes in polarization state, proliferation rate, sensitivity to apoptosis, metabolic state, and cell motility (*274*). Importantly, cell confluence, being a central parameter of the population context, induces major changes at the molecular level. Studies demonstrated that cell grown at high density exhibit a different lipid composition (*298*) or protein expression (*299*) as compared to cells grown at low density.

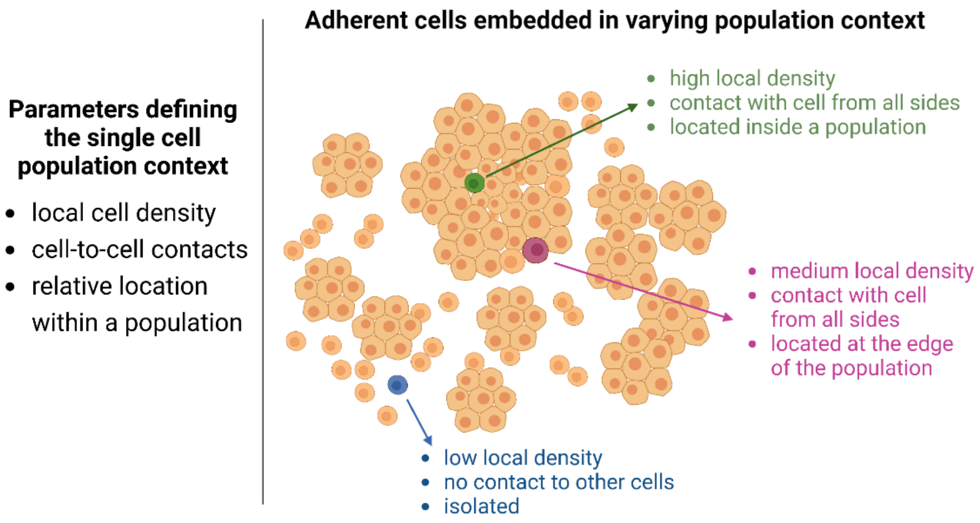

**Fig. 17. The population context of adherent cells.** The population context is the physical microenvironment in which an adherent cell is embedded in relation to neighboring cells. The population context is defined by the cell density, cell-to-cell contacts, and relative cell location within the population. Schematic shows examples of cells (in green, pink and blue) embedded in different population context.

The Hippo pathway is a key sensor of the cellular environment and population context, and it integrates diverse biochemical and biomechanical cues to modulate behavior (Fig. 18) (*300*). After sensing the cellular environment, the Hippo pathway plays a central role in regulating cell proliferation and cell fate. Activation of the Hippo pathway (Hippo ON) induces a kinase cascade in which Mammalia STE20-like kinase 1/2 (MTS1/2) phosphorylate and activate the large tumor suppressor 1/2 (LATS1/2). Activated LATS1/2 phosphorylate Yes-associated protein 1 (YAP) and transcriptional coactivator with PDZ-binding motif (TAZ). This leads to 14-3-3 mediated YAP/TAZ cytoplasmic retention and recruitment of the SCF E3 ubiquitin ligase. SCF-mediated ubiquitination induces YAP/TAZ degradation. To sum up, activation of the Hippo pathway results in the inhibition of YAP and TAZ (*301*). When the Hippo pathway is inactive (Hippo OFF), YAP and TAZ are activate and translocate to the nucleus (*301*). There they interact with the TEAD transcription factor family, inducing the expression of a wide set of genes associated with cell proliferation, survival, and migration (*301*).

Cell-to-cell contacts promote Hippo signaling (*302*, *303*). Within this context, components of junctional complexes, such as tight and adherens junctions, play a pivotal role supporting Hippo pathway activation (*304*, *305*). For example, junctional complexes incorporate and hijack the key transcriptional coactivator YAP, thereby controlling YAP effector function and downstream signaling (*306–308*). Conversely, disruption of cellular polarity correlates with reduced Hippo pathway signaling (*309*). Cell density also regulates the Hippo pathway, mostly through biomechanical cues dependent on the F-actin cytoskeleton structure, tensions within the cytoskeleton, and the influence these tensions have on junctional complexes (*300*). Moreover, the Hippo pathway is controlled by other pathways, such as metabolic pathways and multiple G protein coupled receptor signaling pathways (*300*).

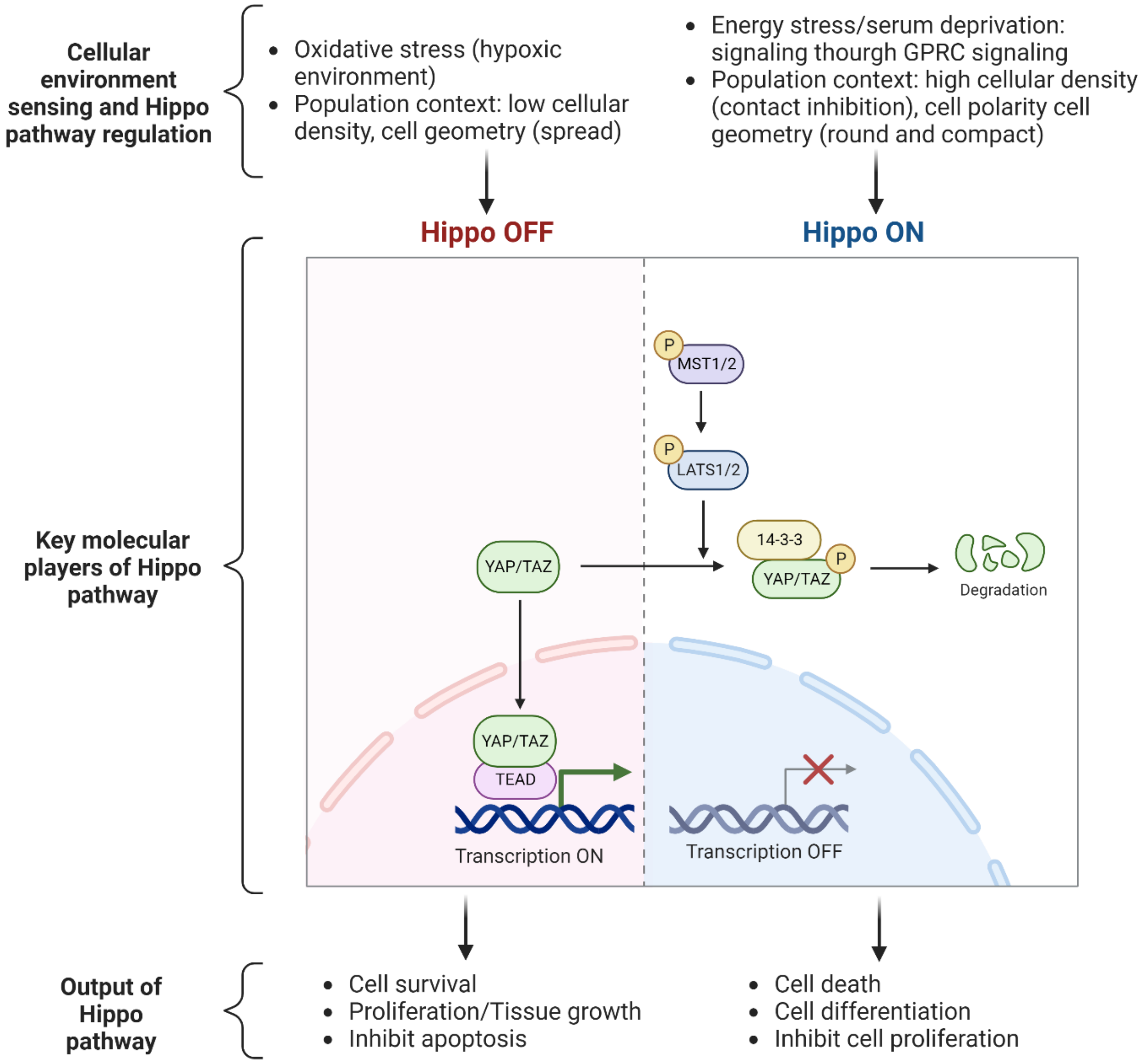

**Fig. 18. The Hippo pathway.** Schematic showing environmental factors regulating the Hippo pathway, the key molecular players and the output of the Hippo pathway.

### 1.4.3. Population context as a determinant of cell-to-cell variability

Snijder et al. (*274*) propose the population context as a deterministic factor driving cell-to-cell variability in isogenic cells. They argue that the population context creates a large spectrum of microenvironmental properties to which cells adapt, leading to a wide distribution of single-cell phenotypes. This notion is underscored by analyzing cells grown on micropatterns: When single cells were forced to adopt identical size and shape, effectively controlling for the population context and ensuring homogeneity, the normally heterogeneous subcellular distributions of intracellular organelles was strikingly consistent and not randomly distributed (*310*). Moreover, a study by Snijder et al. (*311*) demonstrated a correlation between cell-to-cell variability during endocytic events and the population context. They observed a heterogeneous pattern during virus infection (rotavirus, dengue virus, mouse hepatitis virus and SV40), CME and the amount of GM1 within colonies of both cancer- (HeLa and A431) and non-cancer-derived (MCF10A) cells. GM1, dengue virus infection and SV40 infection occurred mostly in large spread out cells localized at the edge of colonies, while mouse hepatitis virus infection and CME were highest in crowded areas localized in the center of cellular colonies. Using data-driven modelling approaches they demonstrate that the parameters defining the population context, particularly population size, local cell density, position of a cell within the colony and cell size, contributed to the cell-to-cell variability of endocytic events and lipid composition (*311*). Future studies integrating the spatial information using imaging and transcriptomic approaches will offer insights into how the population context impacts cell-to-cell variability.

### 1.4.4. Cell-to-cell variability in IFN-dependent signaling

Cell-to-cell heterogeneity is a prevalent characteristic of IFN-dependent signaling. A pioneering study by Rand et al. (*312*) directly addressed the heterogeneous response to IFNs. They treated murine fibroblasts NIH 2T2 with IFNβ and observed distinct ISG expressing and non-expressing subpopulation (Fig. 19), where the expressing subpopulation increased with extracellular IFNβ concentration. The prevalent cell-to-cell variability in the population was supported by the fact that IFN treatment of the non-responder population induced response at later time (after sorting and reculturing) in the same heterogeneous patterns as naïve cells (Fig. 19). Importantly, the non-responder population was permissive to virus infection, while the responder population was protected (Fig. 19). Similar follow-up studies supported a heterogonous response to IFNs, including to IFNβ (type I), IFNα (type I) and IFNλ3 (type III), in a variety of cell types (A549, Huh7.5, primary human hepatocytes, and murine intestinal epithelial cells) (*313–316*). Using live cell microscopy and a fluorescent A549 reporter cell line, Schmid et al. (*313*) demonstrated that the IFN responder population also exhibited a broad heterogeneity in the timing of ISG induction. Moreover, they observed that a fraction of cells was refractory to IFNα stimulation, even when treating with saturating IFN concentrations. Altogether, studies support a profound heterogeneity in (i) mounting a response to IFNs and (ii) the timing in which a cell responds.

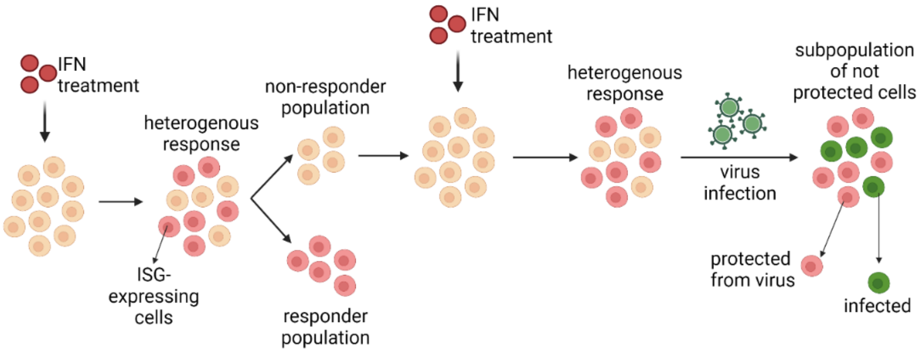

**Fig. 19. Cell-to-cell variability during IFN-dependent signaling.** IFN treatment of isogenic cells induces a heterogeneous response. This is characterized by cell-to-cell variability in ISG expression,

leading to a responder and non-responder population. IFN re-treatment of the non-responder population with IFNs induces the same heterogeneous response, with both, an ISG expressing (responder) and non-expressing (non-responder) population. Only the responder population is protected against virus infection.

A big discussion in the field is whether the heterogeneous response displays a unimodal or bimodal pattern. Bimodal means that the ISG expression follows a digitalized all-or-none principle, leading to a clear separation of the responder and non-responder population (*312*, *314*, *317–319*). However, several studies indicated that ISG induction follows a graded (unimodal) pattern meaning that gene expression is gradually induces by IFNs (*315*, *320*, *321*). Discrepancies in the conclusion may arise from differences in the ISG chosen in the experiments, differences in the ISG promoter architecture, the specific cell line utilized, and variations in IFN treatment concentrations and timing.

Rand et al. (*312*) developed a mathematical model and demonstrated that cell intrinsic stochasticity is responsible for a heterogeneous response to IFNβ in murine fibroblasts. A stochastic origin of cell-to-cell variability was supported with experimental data (stimulation of Huh7.5 with IFNα) and mathematical modelling simulations conducted by Maier et al. (*315*). Moreover, while analyzing the origin of stochasticity in the IFN response with the mathematical models, Maier et al. observed low intrinsic noise coming from molecule abundance and random collision, but high extrinsic noise at the receptor level and during the formation of the transcription factor ISGF3 in the JAK-STAT signaling pathway. However, the extrinsic noise seemed to be heavily regulated, therefore having a minor role in the heterogeneous response to IFNs. Another source for the heterogeneous response could be a reported stochastic IFN receptor expression (*322*). While many studies report a stochastic origin of cell-to-cell variability in IFN response, to the best of my knowledge only one study showed that the heterogeneous response has a deterministic origin: Bhushal et al. (*314*) demonstrated that epigenetic modulation and polarization status determined the responsiveness to type III IFNs of murine intestinal epithelial cells. Considering that the variability in cell-to-cell responses during IFN signaling dictates whether a cell within a population is protected from viral infection or remains susceptible, there is a need for in-depth investigation into the underlying origin of this heterogeneous response.

## 1.5. Objectives

Self-organization of identical cells into higher order structures is a central feature of organism development and tissue homeostasis. A turning point is the transition from single cells to cells as part of a population, which comes along with major changes in the population context. The population context is the physical microenvironment in which an adherent cell is embedded in relation to neighboring cells, and is determined by the local cell density, cell-to-cell contacts, and relative location within the population. Consequently, to efficiently self-organize, cells must have molecular mechanisms to sense their population context and interpret it to respond accordingly.

Epithelial tissues are large highly organized multicellular structures at the surfaces of all organs, thereby acting as a barrier between compartments or to the outside environment. Especially at mucosal surfaces with constant exposure to commensal and pathogenic microbes, it is critical that cells mount an adequate immune response ensuring protection from pathogens while preventing damage. The aim of this thesis was to elucidate how the population context and multicellular organization of epithelial cells affects virus infection and IFN-dependent immune signaling.

To investigate the influence of population context on epithelial surfaces, I developed two systems: A density-based approach, in which cells are seeded as small clusters or individual cells at low density, or as a confluent monolayer at high density similar to their physiological organization at epithelium surfaces. By employing this approach, cells are placed in contrasting microenvironments, enabling me to identify how significant changes in the population context impact molecular features and signaling pathways such as IFN-signaling and susceptibility to viral infection. The second method involves a micropatterning system, which I established to generate uniformly shaped circular clusters of epithelial cells. This technique permits the quantification of events occurring within a uniformed, controlled and reproducible cellular population, allowing for a precise assessment of how different cellular processes are spatially distributed. I used these approaches together with cell model systems (epithelial and fluorescent reporter cell lines), bio-molecular methods and high-content data bioinformatics analyses (RNA-sequencing analysis and fluorescent imaging pipelines) to drive the following research objectives:

(1) Assess the cell-to-cell variability during IFN sensing and signaling in human intestinal epithelial cells, and determine how this variability is influenced by the population context.
(2) Investigate the impact of the population context on basal IFN-dependent signaling.
(3) Study how the population context impacts virus infection of human epithelial cells.

In light of the COVID-19 pandemic, significant endeavors were necessary to decipher how the immune response of the host can limit the spread of SARS-CoV-2 infection, allowing for the development of effective treatments. Throughout the peak time of the COVID-19 pandemic, my lab has been extensively involved in SARS-CoV-2 related research. Work from our laboratory demonstrated that SARS-CoV-2 was sensitive to IFNs when infecting human intestinal epithelial cells. During my thesis, for a period of ten months, I focused my research effort on SARS-CoV-2 and worked on the following objective:

(4) Gain a comprehensive understanding on the kinetics of type I and type III IFN signaling controlling SARS-CoV-2 infection in IECs.

# 2. Results

## 2.1. Population context drives cell-to-cell variability during repponse to interferon treatment in epithelial cells

### 2.1.1. Response to IFNs is influenced by single cell location of cells within a population

Previous studies demonstrated that within an isogenic (genetically identical) cell population, a fraction of the cells do not respond to IFNs, even though they possess a fully functional IFN signal transduction pathway (*312–316*). To investigate whether the population context, specifically the location of a cell within the population, can influence IFN-mediated signaling in epithelial cells, I utilized a previously described human-colon carcinoma T84 cells expressing a fluorescent protein (fp) under the transcriptional control of the interferon-stimulated gene (ISG) MX1 promoter (T84-prom-Mx1-fp) (*160*), which was generated by the former student Patricio Doldan from our lab. This reporter system allows to visualize the response of each individual cell within the population, as only cells that respond to IFNs will fluoresce (Fig. 20 A). T84-prom-Mx1-fp cells were seeded at medium density (100,000 cell/cm$^2$ to allow for formation of cellular colonies of various sizes as well as very dense and sparsely seeded regions. Cells were either mock treated or treated with type I (IFNβ1) and type III (IFNλ1-3) IFNs for 24 hours, before being fixed and analyzed by fluorescence microscopy. Interestingly, mostly isolated cells without neighbors and cells located at the edge of a cellular colony responded to IFNs (Fig. 20 B, yellow arrows). In contrast, cells in the center of a colony remained unresponsive (Fig. 20 B, red arrows).

To quantify in an unbiased manner how the location of a cell within a population impacts its response to IFNs, I used the DBSCAN-CellX App developed by our collaborator Frederik Graw, Bioquant Heidelberg (URL: https://github.com/GrawLab/DBSCAN-CellX/). DBSCAN-CellX is a density-based clustering algorithm that determines the spatial distribution and positioning of single cells in a 2D plane. My analytical pipeline first quantified the fluorescent signal within each individual cell and then registered its XY-coordinates. These XY-coordinates were then analyzed using DBSCAN-CellX, which determines whether a cell is located at the edge or the center of a colony, or whether it is a single isolated cell (Fig. 20 C). Moreover, DBSCAN-CellX calculates the 'edge degree' of each cell, which represents the distance of a cell from the edge of its colony: the higher the edge degree, the larger the distance from the edge, with cells at the edge defined by an edge degree of 1, while an edge degree of 0 represents single cells that have no neighbors (Fig. 20 C).

Analysis of the location of the IFN-responsive cells within the cell population revealed that, regardless of whether the cells were treated with type I or type III IFNs, a significantly higher percentage of cells located at the edge of a cellular colony responded to IFNs compared to cells located in the center (Fig. 20 D). Upon examining the relationship between the count of cells inducing IFN signaling and their edge degree, I found that the group with the highest percentage of responder cells consisted of single cells lacking neighbors (edge degree 0) (Fig. 20 E). With increasing edge degree and hence, as cells grew further away from the colony edge, less cells expressed the IFN reporter after treatment (Fig. 20 F). Importantly, I observed a significant ($p<0.0001$) negative correlation between the edge degree and the percentage of positive cells ($r=-0.8471$ for IFNβ1 and $r=-0.7991$ for IFNλ1-3 treatment) (Fig. 20 F), further reinforcing that cells located inside a population are less responsive to both type I and type III IFNs (Fig. 20 E). Analyzing only the percentage of positive cells does not provide information about how strongly cells respond to IFNs. To address the magnitude of responsiveness, I correlated the normalized expression of the IFN fluorescent reporter (normalized fluorescence) with the edge degree. Type I IFN treatment showed a gradual decrease of the normalized fluorescence as the edge degree increased, supporting that also the overall magnitude of response is decreasing in cells grown inside a colony (Fig. 20 G). Interestingly, while type III IFN treatment showed a similar pattern until edge degree 4, the normalized fluorescence increased for edge degree 5-7, reaching values similar to edge degree 1 (Fig. 20 G). This suggests that after type III IFN treatment, the responder cells in the center of a colony induce signaling leading to an overall high normalized fluorescence.

Altogether, my findings suggest a heterogeneous immune response to IFNs within an isogenic IEC population, where cells at the edge of cellular colonies are overall more responsive than cells located inside the colony. This phenotype is especially prominent for type I IFN treatment, in which the number of responder cells as well as the magnitude of response steadily decreases as the cells grow further inside a colony. Very interestingly, while the number of responder cells was higher at the edge as compared to the center of a colony, responder cells located in the center of a colony appeared to have a high magnitude of IFN signaling after type III IFN treatment.

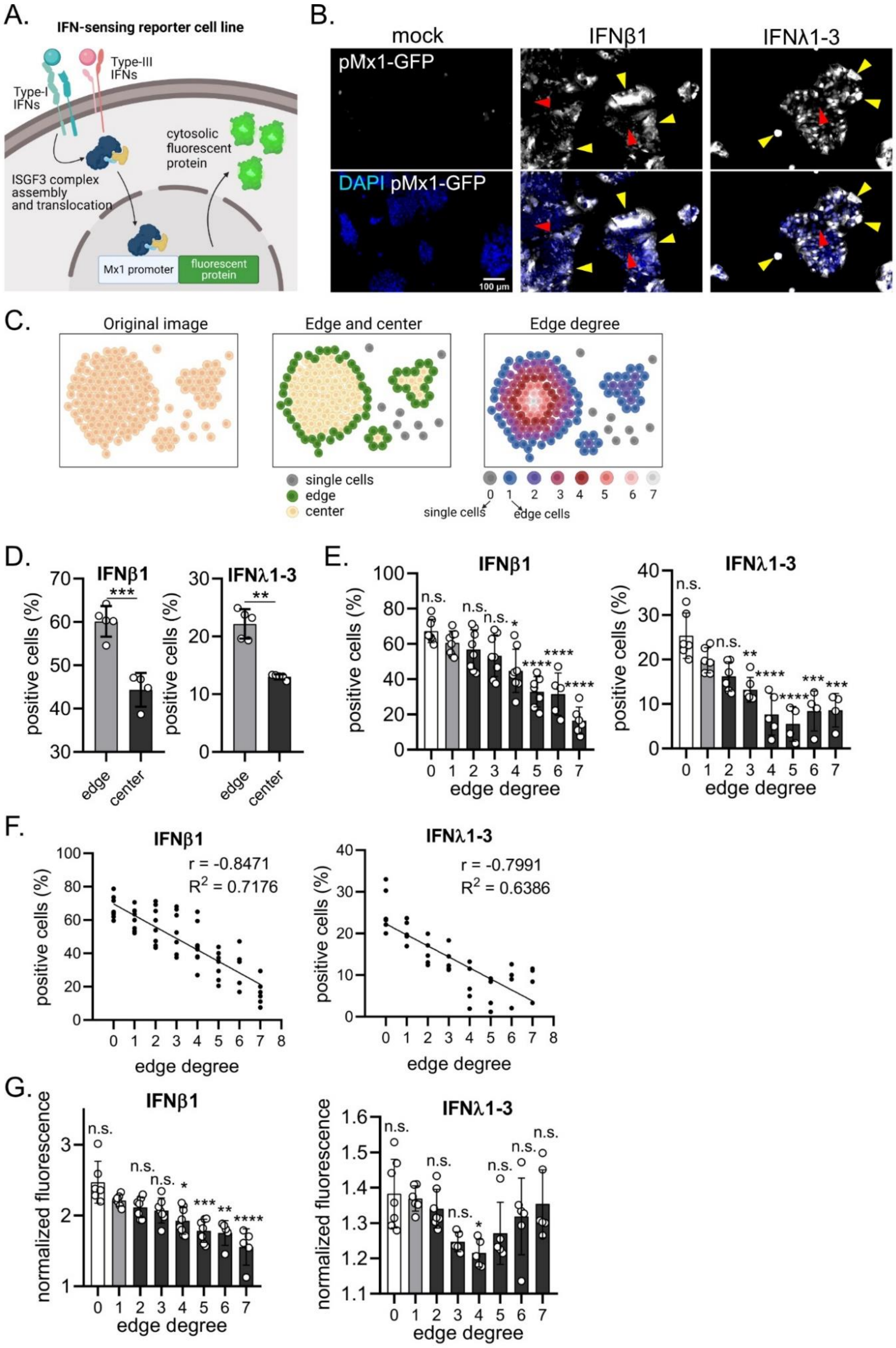

**Fig. 20. Location of a cell within a population determines its responsiveness to IFN treatment.** (A) Schematic depicting the T84 prom-Mx1-fp reporter cell line. Upon interaction of IFNs with their receptor, downstream signaling induces nuclear translocation of the transcription complex ISGF3. This

leads to expression of the fluorescent protein under control of the ISG Mx1 promoter. The fluorescent protein accumulates in the cytosol and can be visualized by fluorescence microscopy. (B-G) T84-prom-Mx1-GFP seeded at medium density were mock treated or treated with 2000 IU/mL IFNβ1 or 300 ng/mL IFNλ1-3 for 24 h. Cell nuclei were stained with DAPI and fluorescence microscopy was performed. (B) Representative images of cells (nuclei stained with DAPI are blue) expressing the fluorescent reporter (white). Yellow arrows point at IFN responder single cells or cells located at the colony edges. Red arrows point at non-responder cells in the colony center. (C) Correlation between single cell location and IFN-responsiveness was assessed using DBSCAN-CellX. Schematics depicting how the tool annotates cells according to their location at the edge or at the center of a cluster, or according to their edge degree are shown. An edge degree of 0 define single cells (no neighbors) and edge degree 1 are cells at the border of a colony. The higher the edge degree, the larger the distance from the edge. (D, E) Quantification of the percentage of positive fluorescent cells as compared to mock-treated cells: (D) edge vs. center cells and (E) percentage of positive fluorescent cells dependent on the edge degree. (F) Linear regression and coefficient of correlation (r) calculated for (E). (G) Normalized intensity of cells dependent on the edge degree. (D, E, G) Error bars indicate standard deviation. n ≥ 3 biological replicates, error bars indicate the standard deviation. n.s. =not significant. $P<0.05$ *, $P<0.01$ **, $P<0.001$ ***, $P <0.0001$ **** as determined by (D) Unpaired t test with Welch's correction, and (E, G) ordinary one-way ANOVA with Dunnett's multiple comparison test using edge degree 1 as reference.

### 2.1.2. Micropatterning is a powerful approach to investigate the spatial distribution of immune signaling in IEC populations

To explore the correlation between single cell location and its response to IFN, I exploited a micropatterning method that enables the generation of cell populations of defined and uniform sizes. For a more detailed explanation and characterization of the method refer to Annex section 5.1. This innovative approach allowed me to study cells under identical population context, facilitating a standardized analysis. In brief, a surface is micropatterned using UV light. Cells seeded on the micropatterned surface grow as uniform populations, which were treated and imaged by fluorescence microscopy. I then developed an imaging analysis pipeline, which segments the cell population into an edge region (outer ring) and center region (inner circle), allowing me to quantify the spatial segregation of fluorescence within the population. (Fig. 21 A)

To investigate the response of IECs within a population, T84-prom-Mx1-fp cells were seeded on micropatterned glass and treated with type I and type III IFNs for 0, 12, and 24 h, before analysis by fluorescence microscopy. Predominantly, cells situated at the edge of the patterned population exhibited a robust response to IFNβ1 treatment (Fig. 21 B). This observation was further supported by quantifying the mean fluorescent intensity (MFI) of cells at the edge and center of the population. Edge cells displayed significantly higher fluorescence levels after type I IFN treatment compared to center cells. Intriguingly, center cells maintained MFI values similar to mock-treated cells (Fig. 21 C), suggesting that in the center of a population IECs barely respond to type I IFN treatment. Similarly, IFNλ1-3 treatment also induced a more pronounced response at the edge relative to the center of the population (Fig. 21 B-C). In contrast to IFNβ1 treatment, center cells exhibited responsiveness to IFNλ1-3, albeit significantly lower than edge cells (Fig. 21 B-C).

Collectively, my data strongly suggest that IECs situated at the edge of a cell population are more responsive to IFNs as compared to cells embedded within the population. This attributes a spatial component to the immune response in IECs. Interestingly, this phenotype was less pronounced for type III IFN treatment, as center cells also induced a small but significant immune response, unlike treatment with type I IFNs.

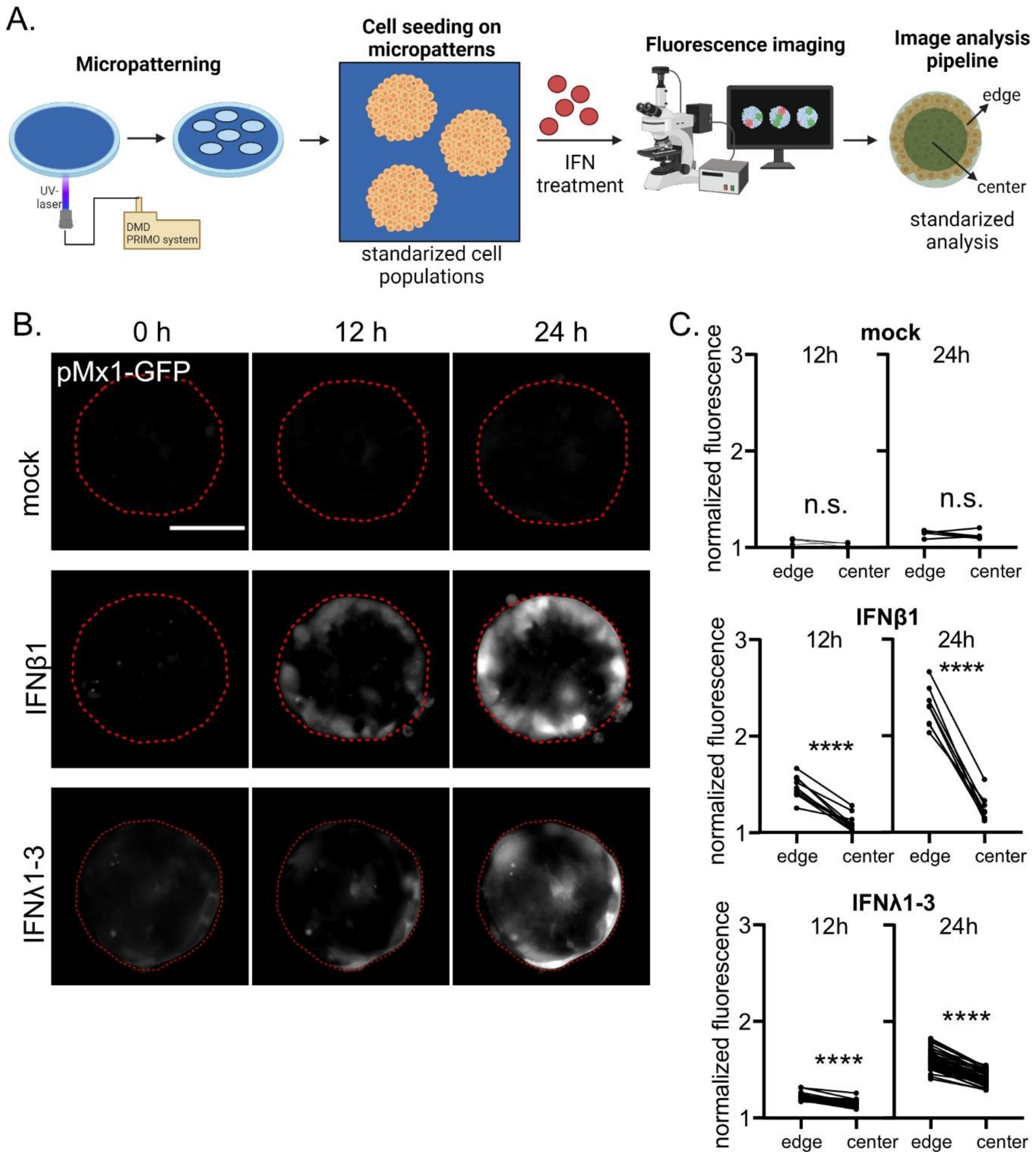

**Fig. 21. Cells located in the center of a cellular colony are less responsive to IFNs.** (A) Schematic depicting the micropatterning method, cell seeding as populations and analysis pipeline after fluorescence imaging (B, C) T84-prom-Mx1-GFP cells seeded on circular micropatterns (200 µm diameter) were mock treated or treated with 2000 IU/mL IFNβ1 or 300 ng/mL IFNλ1-3. Fluorescent imaging was performed at 0 h, 12 h, and 24 h post treatment. (B) Representative images. The red line represents the edge of the patterns. Expression of the fluorescent reporter is depicted in white. Scale bar = 100µm. (C) The reporter expression for each single population was quantified by measuring the mean fluorescence intensity (MFI) at the edge and the center of a population at 12 h or 24 h post

treatment, and normalizing it to the corresponding population 0 h post treatment. Each dot is one cell population (seeded on one micropattern), lines connect edge and center of the same cell population. n ≥ 3 biological replicates, error bars indicate the standard deviation. n.s. =not significant, P <0.0001 **** as determined by Paired t test.

### 2.1.3. Cellular density significantly influences the response of IECs to IFN

To understand which part of the IFN-mediated signaling pathway is impaired in cells located at the center of a population, I compared the response to IFN between T84 cells seeded at high (205,000 cells/cm$^2$) and low (27,000 cells/cm$^2$) density. At high density, cells form a continuous intact monolayer where every cell is in contact with some neighboring cells, thereby representing the center of a population (Fig. 22 A). Conversely, at low cell density, most cells can be considered "edge" cells as they are either isolated or part of small colonies with at least one side lacking a neighbor (Fig. 22 A). IECs at high and low density were treated with IFNβ1 or IFNλ1-3, and the expression of the ISGs IFIT1, Mx1, and Viperin was measured over time using reverse transcriptase quantitative PCR (RT-q-PCR) (Fig. 22 B). Analysis of ISG expression revealed that cells at low density induced significantly higher ISG transcription compared to cells seeded at high density, with minimal transcriptional upregulation of ISGs in cells seeded at high densities at all measured timepoints (Fig. 22 B).

After binding of IFN to its receptor, JAK is induced, which in turn phosphorylates STAT1/STAT2 (*117*). To address whether cell density can impact the phosphorylation of STATs following IFN stimulation, T84 cells seeded at low and high densities were treated with IFNβ1 or IFNλ1-3 for 1 h. The phosphorylation status of STAT1 was addressed by Western Blot analysis. Results show that IECs seeded at low density treated with either type of IFN induced significantly higher STAT1 phosphorylation as compared to cells seeded at high density (Fig. 22 C-D). Interestingly, the difference in STAT1 phosphorylation (Fig. 22 C-D) and ISG expression (Fig. 22 B) between high and low density after type III IFN treatment was not as prominent as the differential induction upon type I IFN treatment. These findings align with the outcomes from IEC populations seeded on micropatterns (Fig. 21), where type III IFNs also elicit a small immune response in the center of the cell populations seeded on micropatterns.

To underline the differential IFN-dependent immune response at high and low density in a more dynamic manner, I seeded T84 prom-Mx1-fp cells expressing an H2B-turquoise plasmid (to visualize cell nuclei) at high and low density, and treated them with increasing concentrations of IFNβ1 or IFNλ1-3. Live fluorescence imaging for 24 hours showed a dose-dependent response to IFN treatment in cells seeded at low density, but not in cells seeded at high density (Fig. 23). Importantly, cells seeded at high density only exhibited minimal response to IFN treatment (Fig. 23). These results are in agreement with the intrinsic ISG expression levels measured using RT-q-PCR (Fig. 22 B), further demonstrating that the population context significantly impacts the response of IECs to IFN treatment.

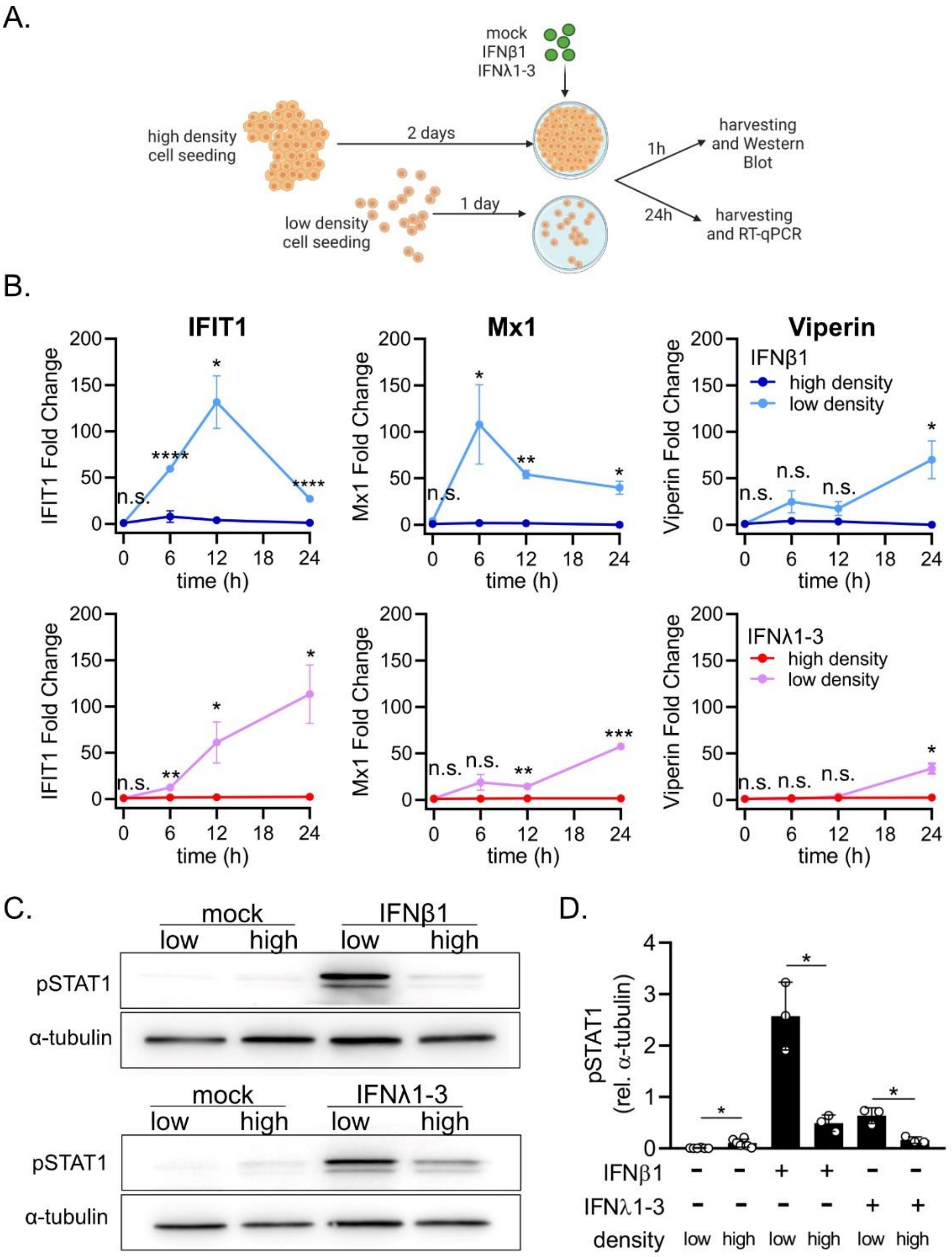

**Fig. 22. Cell density negatively correlates with IFN-dependent signaling.** T84 cells seeded at high and low density were mock treated, or treated with 2000 IU/mL IFNβ1 or 300 ng/mL IFNλ1-3. (A) Schematic depicting the experimental setup. (B) 24 h post IFN treatment, RNA was harvested to evaluate the transcription of the representative ISGs IFIT1, Mx1, and Viperin using q-RT-PCR. ISG relative expression was normalized to the mock-treated cells of the respective time-point (fold change). (C) 1 h post treatment, cellular protein extracts were collected to assess the phospho-STAT1 (pSTAT1) abundance by Western Blot. pSTAT1 was quantified relative to the housekeeping protein α-tubulin. (B, C) n = 3 biological replicates, error bars indicate the standard deviation. n.s. =not significant. P<0.05 *, P<0.01 **, P<0.001 ***, P <0.0001 **** as determined by Unpaired t test with Welch's correction between high and low density (for each time-point).

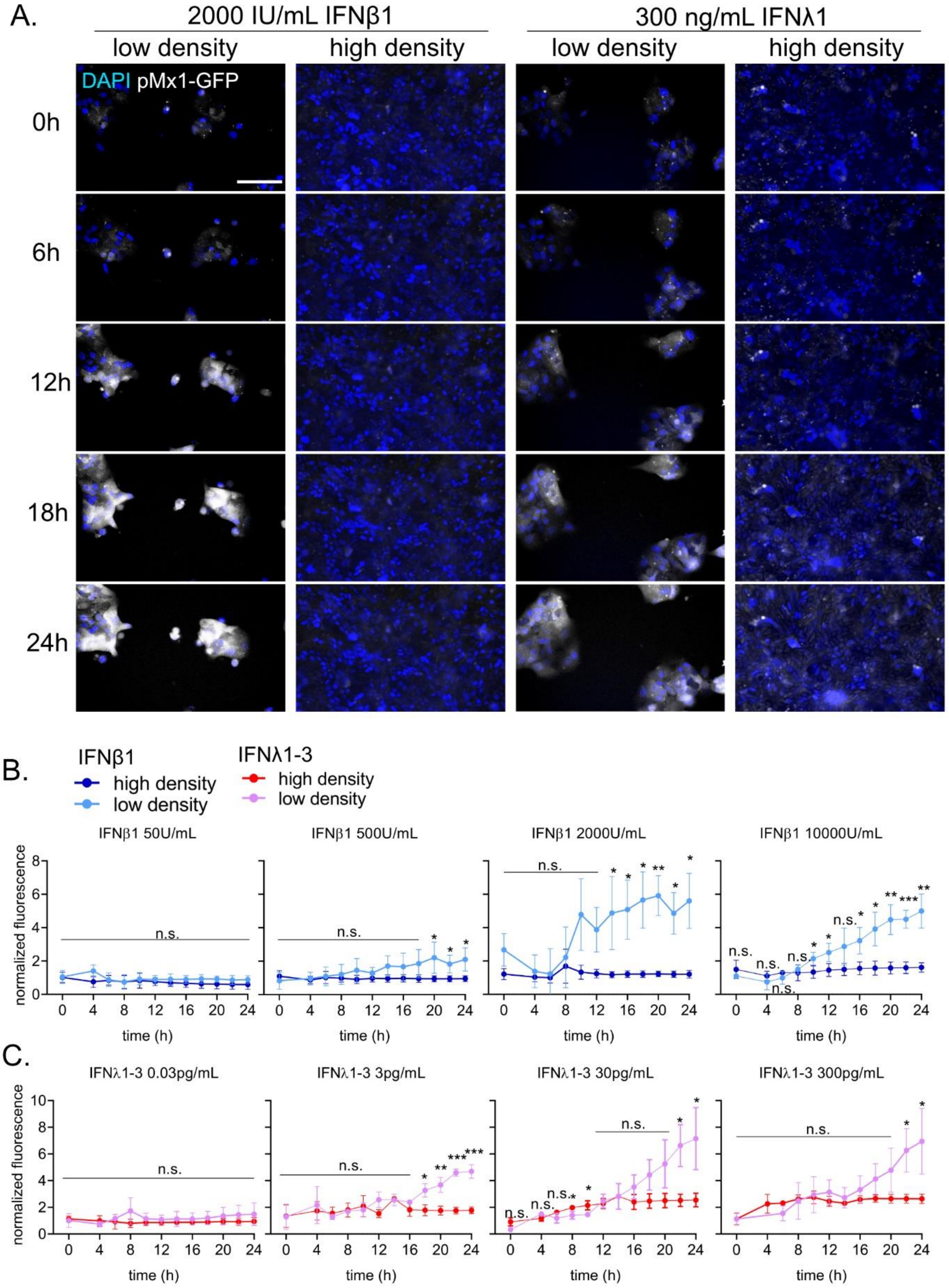

**Fig. 23. Temporal response of cells at high and low density to IFN treatment.** T84-prom-Mx1-GFP cells at high or low density were treated with increasing concentrations of IFNβ1 and IFNλ1-3. Live cell fluorescence imaging was performed at an interval of 2 h for 24 h. (A) Representative images for selected time-points. (B, C) The mean fluorescence intensity (MFI) of the reporter expression within each cell was averaged for each density and normalized to the mock MFI of each time-point (fold change) for (B) IFNβ1 and (C) IFNλ1-3. n = 3 biological replicates, error bars indicate the standard deviation. n.s =not significant. P<0.05 *, P<0.01 **, P<0.001 ***, P <0.0001 **** as determined by Unpaired t test with Welch's correction between high and low density for each time-point.

In conclusion, my findings indicate a negative correlation between IEC density and the response to IFNs. Confluent cells at high density display minimal responsiveness to IFNs, while sparse cells exhibit elevated levels of STAT1 phosphorylation and downstream ISG expression upon IFN treatment. These results highlight the significance of cellular density in shaping the cellular immune response, and how the spatial context plays a crucial role in IFN-mediated signaling.

### 2.1.4. Basolateral treatment of IECs with IFN suppresses the spatial heterogeneity in IFN-mediated signaling

When IEC form a confluent monolayer they polarize, and possess an apical and basolateral membrane (Fig. 14). The basolateral side is in contact with the cell culture vessel *in vitro* and the lamina propria *in vivo*, while the apical side faces the cell culture medium *in vitro* and the gut lumen *in vivo*. One plausible explanation for the limited to non-responsiveness of IECs to IFNs when located in the center of a population or seeded at high density could be that the IFN receptors are predominantly localized on the basolateral membrane. Within this scenario, IFNs cannot access the basolateral membrane (where the receptors are localized) for cells at the center of a population or in a confluent monolayer when seeded on glass or plastic surfaces. Hence, when seeded on plastic/glass surfaces, these center cells will not induce IFN-dependent signaling. Conversely, IFNs can stimulate cells located at the edge of a colony since these cells lack polarization and do not exhibit an asymmetric basolateral distribution of their receptors (*323*). To test this model, I seeded T84 cells on transwell inserts to establish a polarized cell monolayer (Fig. 24 A). First, I confirmed the polarization status and formation of a semi-permeable epithelial monolayer of cells seeded on transwell inserts. Epithelial cells formed a tight junction belt between individual epithelial cells as seen by immunostaining the tight junction protein ZO1 (Fig. 24 B). Tight junctions are intercellular adhesion complexes in epithelia controlling paracellular permeability. Moreover, I observed the establishment of a characteristic trans-epithelial electrical resistance (TEER) over-time (Fig. 24 C), and the formation of a tight monolayer that prevents diffusion of molecules between cells as assessed by paracellular diffusion of FITC-Dextran from the apical to the basolateral transwell compartment (Fig. 24 D).

To test my hypothesis that the IFN receptors are enriched to the basolateral membrane, I treated polarized IECs on transwell inserts with IFNs from either the apical or basolateral side for 24 h (Fig. 24 A). q-RT-PCR analysis of the expression of the ISG IFIT1 demonstrated that basolateral treatment induced a significantly higher response compared to apical treatment for both type I and type III IFNs (Fig. 24 E), strongly suggesting an enrichment of IFN receptors at the basolateral side of polarized T84 cells.

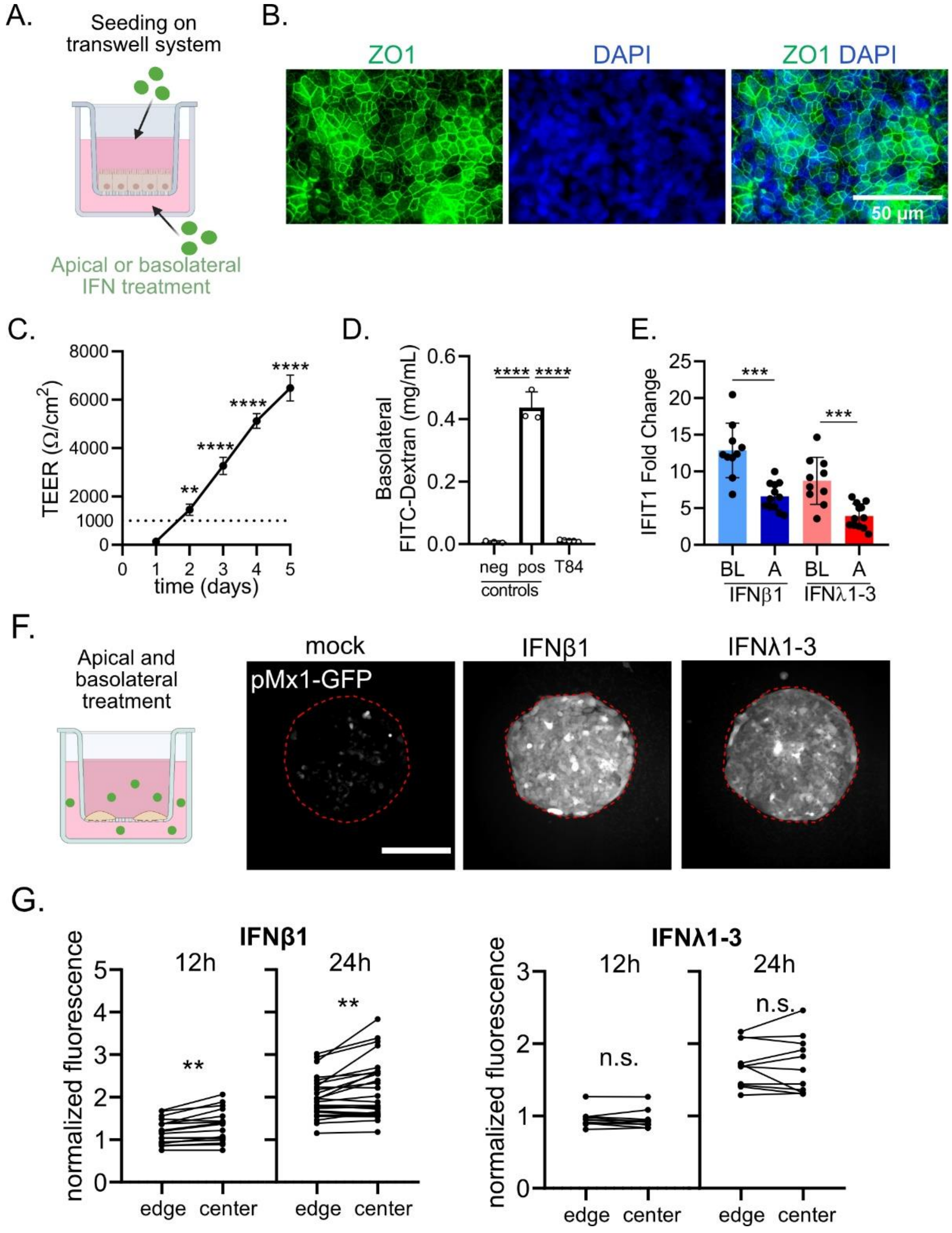

**Fig. 24. T84 cells better respond to IFN when stimulated on their basolateral side.** (A-E) T84 cells were seeded on transwell inserts to allow for a polarized monolayer formation. Then cells were mock treated, or treated from the apical (A) or basolateral (BL) side with 2000 IU/mL IFNβ1 or 300 ng/mL IFNλ1-3. (A) Schematic depicting the transwell system and treatment. (B) 5 days post seeding, cells were fixed, and indirect immunofluorescence was performed against the junctional complex protein ZO1 (green). Nuclei were stained with DAPI (blue). Scale bar=50 µm. (C) Formation and integrity of the monolayer was followed by measuring the transepithelial electrical resistance (TEER) (Ω/cm$^2$) over 5 days. Values > 1000 Ω/cm2 (dotted line) shows that cells established a polarized monolayer formation. (D) 5 days post seeding, after reaching a polarized monolayer, the integrity of the monolayer was confirmed by the FITC-Dextran permeability assay. Diffusion of FITC-Dextran from the apical to the basolateral compartment was measured and expressed as concentration (mg/mL) of FITC-Dextran in the basolateral compartment after 3h incubation. Positive control (pos) was the maximum diffusion possible and the negative control (neg) was medium only without FITC-Dextran. (E) 24 h post IFN treatment, RNA was harvested, and q-RT-PCR was used to evaluate the expression of the ISG IFIT1. Data is normalized to mock (fold change). (F, G) T84 prom-Mx1-GFP cells were seeded on micropatterned transwell membranes. Cells were mock treated, or treated simultaneously from the

apical and basolateral side with 2000 IU/mL IFNβ1 or 300 ng/mL IFNλ1-3. Cells were fixed at 0 h, 12 h, and 24 h post treatment and fluorescent imaging was performed. (F) Schematic depicting the method (left), and representative images showing treated T84 cell populations (right). The red line represents the edge of the patterns. Expression of the fluorescent reporter is depicted in white. Scale bar=100µm. (G) The reporter expression was quantified by measuring the mean fluorescence intensity (MFI) at the edge and the center of a population at 12 h or 24 h post treatment, and normalizing it to the corresponding 0 h post treatment at the edge and center, respectively. Each dot is one cell population (seeded on one micropattern), lines connect edge and center of the same cell population. (C-E, G) n ≥ 3 biological replicates, error bars indicate the standard deviation. n.s. =not significant, P<0.05 *, P<0.01 **, P<0.001 ***, P <0.0001 **** as determined by (C, D) Ordinary one-way ANOVA with Dunnett's multiple comparison test using day 1 of the TEER measurement or the positive control of the FITC-Dextran permeability assay as reference, (E) Unpaired t test with Welch's correction, and (G) Paired t test.

To further investigate whether basolateral treatment could render cells grown in the center of a population responsive to IFNs, I micropatterned transwell inserts (described in Annex section 5.1 and Fig. 67) and seeded the T84-prom-Mx1-fp reporter cell line on them to allow for formation of standardized cell populations which are now accessible from the basolateral side. In this setup, T84-prom-mx1-fp cells were simultaneously treated with IFNs from the apical and basolateral sides for 24 h (Fig. 24 F, left schematic). Fluorescent microscopy analysis revealed that the prom-Mx1-fp reporter expression was no longer restricted to edge cells but was also observed at the center of the cell populations after type I and III IFN treatment (Fig. 24 F). Quantification of the fluorescent signal relative to mock-treated cells showed that center cells induced strong ISG levels which were slightly higher compared to edge cells following type I IFN treatment (Fig. 24 G, left panels). These observations are contrary to the response observed when micropatterned cells were stimulated with IFNs only from their apical side (Fig. 21 A-B), where only edge cells were responsive. Similarly, Type III IFN treatment also induced ISG expression in center cells during simultaneous apical and basolateral treatment (Fig. 24 G, right panels), which was significantly higher as compared to the ISG expression observed in cell populations that were treated solely from their apical side (Fig. 21 A-B). Taken together, my data demonstrates that the spatial restriction of the immune response following IFN treatment can be bypassed by stimulating cells from their basolateral side.

### 2.1.5. IFNAR2 and IL10RB are predominantly localized at the basolateral membrane of polarized T84 cells

In collaboration with Francesco Muraca from my lab and Benno Kuropka (Christian Freund Group at the Freie Universität Berlin, Institute of Chemistry and Biochemistry), I directly investigated the localization of the IFN receptor in polarized epithelial cells. T84 cells were grown as a polarized monolayer on transwell inserts. The apical or basolateral membrane proteins were labeled with non-permeable NHS-biotin (Fig. 25 A). Subsequently, biotinylated proteins were pulled-down using streptavidin beads and identified using mass spectrometry (Fig. 25 A). Mass spectrometry results showed a significant enrichment of biotinylated surface proteins, while any nonspecific binding to the beads was negligible (Fig. 25 B), thereby confirming the efficiency of the pulldown. To ensure the specificity of the assay, I verified the correct localization of well-known apical markers (ALPP and ALPPL2, dots in orange) and basolateral markers (ATP1B1 and ATP1A1, dots in blue) in polarized IECs (Fig. 25 C). Finally, mass spectrometry data of the surface proteome revealed that both IFNAR2 and IL10RB were detectable on the surface of T84 cells, exhibiting a specific distribution of 75% on the basolateral side and 25% on the apical side (Fig. 25 C). Notably, IFNAR1 and IFNLR1 were not detectable using mass spectrometry, likely due to their low expression levels.

This distribution pattern of IFNAR2 and IL10RB is consistent with my earlier findings, where I stimulated T84 cells with IFNs from either the apical or basolateral membrane (Fig. 24). Together my data strongly suggest a model where the spatial restriction of IFN response to cells located at the edge of a cellular colony is due to the predominant distribution of the IFN receptor to the basolateral membrane of polarized T84 cells.

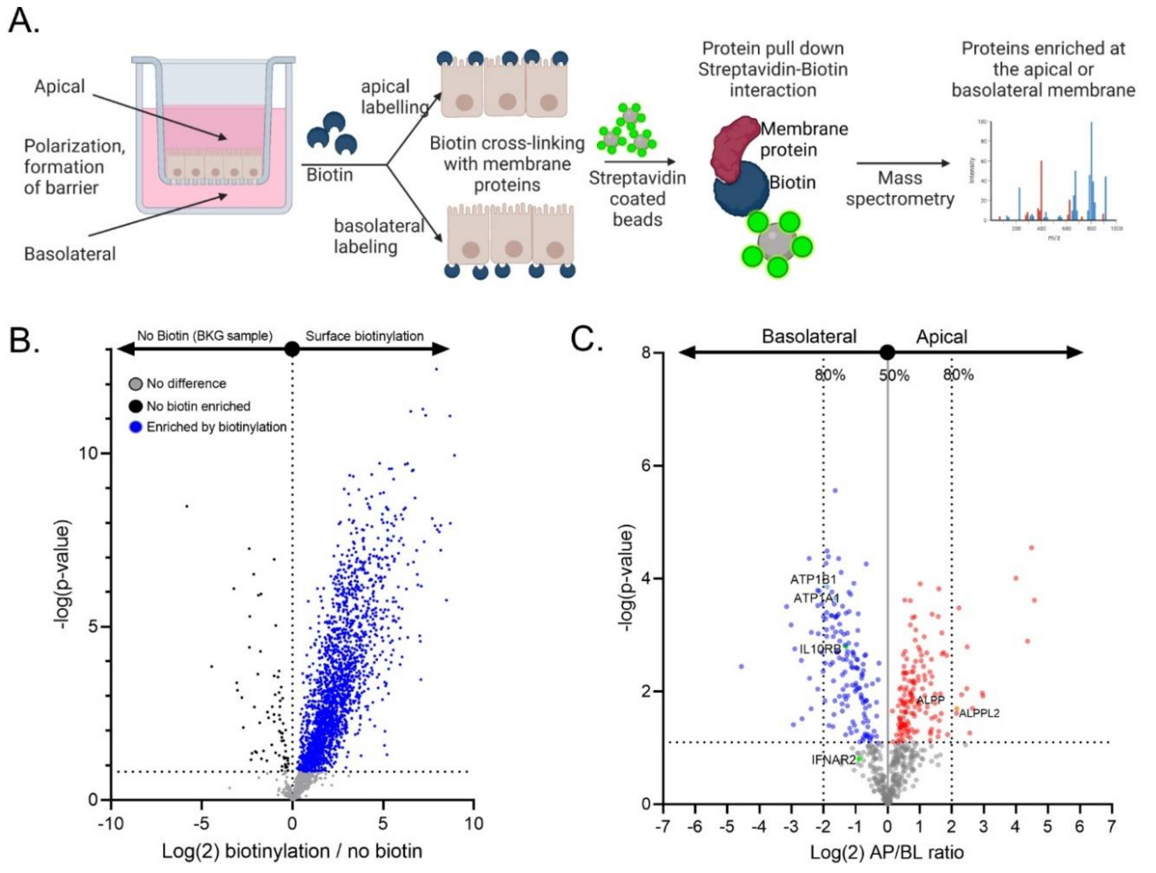

**Fig. 25. Mass spectrometry of the apical and basolateral proteome confirms the polarized localization of IFN receptors.** T84 WT cells were grown as a polarized monolayer on transwell inserts. Apical or basolateral surface proteins were biotinylated by addition of cell non-permeable reactive NHS-biotin to the apical or basolateral compartment of the transwell insert, respectively. Biotinylated proteins were pulled down using streptavidin beads and identified using mass spectrometry. (A) Schematic showing the method. (B) Volcano plot showing enrichment via biotinylation of the surface proteome. (C) Volcano plot showing apical/basolateral log2 ratios for detected surface proteins in T84 cells (right). IFNAR2 and IL10BR are both present on the basolateral side of polarized T84 cells (n = 6, p-value calculated using FDR <0.01). Known apical and basolateral markers of polarized gut epithelial cells are also highlighted. (B, C) n = 6 biological replicates. Data shown in panels (B) and (C) were generated by Francesco Muraca.

### 2.1.6. Tight junctions in polarized IECs cells restrict IFN access to their basolateral receptors

Tight junctions control paracellular permeability, and ZO1 has a central role as a scaffold protein within junctional complexes (*258*). To investigate whether tight junctions prevent the diffusion of IFN to the basolateral side of polarized cells, I used a T84 ZO1 knock-out (KO) cell line in which the tight junction integrity is disrupted. This cell line was generated by a former lab member, Patricio Doldan. Tight junction disruption allows for uncontrolled paracellular diffusion between cells, potentially enabling IFN access to basolateral receptors when treating cells from the apical side (Fig. 26 A). The successful knock-out of ZO1 was validated at the protein level through Western blot analysis (Fig. 26 B) and immunofluorescent staining (Fig. 26 C). Moreover, the deletion of ZO1 resulted in impaired formation of a tight monolayer, as evidenced by delayed establishment of trans-epithelial electrical resistance (TEER) compared to WT cells (Fig. 26 D). After 5 days post-seeding, T84 WT cells reached a TEER of 6500 $\Omega/cm^2$ while ZO1 KO cells TEER was significantly lower at 1500 $\Omega/cm^2$ (Fig. 26 D).

When subjected to IFN treatment from the apical side, sparse T84 WT cells displayed significantly higher ISG expression as compared to confluent T84 WT cells (Fig. 26 E). In striking contrast, the response to IFNs at low vs. high density was indistinguishable in T84 cells depleted of ZO1 (Fig. 26 E). These findings support that the tight junction protein ZO1 serves to restrict the paracellular diffusion of IFN between polarized T84 cells. This statement, however, needs to be supported by an IFN-diffusion assay across a monolayer of T84 WT vs. T84 ZO1 KO cells. Altogether, access of IFN to the basolateral membrane of a polarized T84 cellular monolayer emerges as a pivotal determinant in inducing an IFN-mediated response.

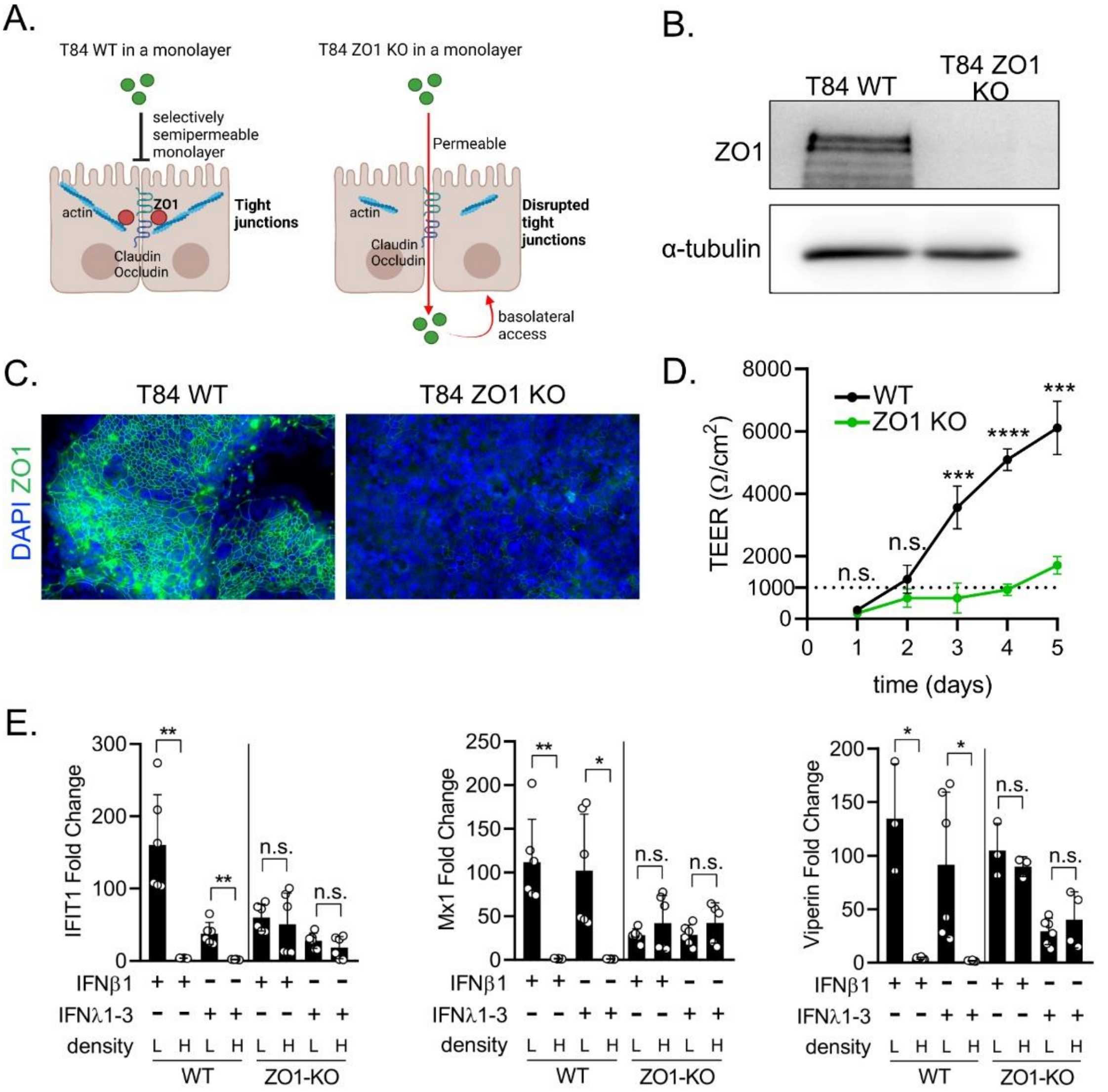

**Fig. 26. Disruption of tight junctions allows for IFN response in cells at high density.** (A) Schematic depicting hypothethical paracellular diffusion in a monolayer of T84 WT and T84 ZO1 KO cells with disrupted junctional complexes. (B) T84 WT and T84 ZO1 KO cell protein extracts were harvested to control the absence of ZO1 protein in the KO cells by Western Blot. α-tubulin served as a housekeeping protein. (C) T84 WT and T84 ZO1 KO cells were fixed and indirect immunofluorescence was performed against the junctional complex protein ZO1 (green). Nuclei were stained with DAPI (blue). (D) T84 WT and T84 ZO1 KO cells were seeded on transwell inserts and grown as a polarized monolayer. Transepithelial electrical resistance (TEER) was measured over a period of 5 days. Dotted line shows a TEER of 1000 Ω/cm$^2$ corresponding to the resistance formed by confluent polarized T84 cells. (E) T84 WT and T84 ZO1 KO cells at high (H) and low (L) density were treated apically with 2000 IU/mL IFNβ1 or 300 ng/mL IFNλ1-3. 24 h post treatment, RNA was harvested, and q-RT-PCR was used to evaluate the expression of the ISG IFIT1. Data is normalized to mock (fold change). (D, E) n ≥ 3 biological replicates, error bars indicate the standard deviation. n.s. = not significant, P<0.05 *, P<0.01 **, P<0.001 ***, P <0.0001 **** as determined by (D) ordinary one-way ANOVA with Dunnett's multiple comparison test using the positive control as reference, and (E) Unpaired t test with Welch's correction.

### 2.1.7. IEC density significantly affects the IFN-induced protection from virus infection

In traditional two dimensional cell culture experiments, 50-70% cell confluency is often chosen as a “good” cell density to study various cellular processes. When working with epithelial model systems, cells are grown at higher density to mimic the physiological conditions (they naturally form an epithelium cellular monolayer) and to induce cell polarization. Given the localization of IFN receptors to the basolateral side of IEC, I questioned whether cellular density could influence the outcome of viral infection during IFN treatment.

To explore this, T84 cells were seeded at high and low density and pre-treated with IFNβ1 and IFNλ1-3 for 24 h (Fig. 27 A). Subsequently, cells were infected with Vaccinia virus (VV) or Mammalian Reovirus (MRV) for 16 hours, and infection levels were assessed through immunofluorescence microscopy (Fig. 27 A). In line with my hypothesis, T84 cells seeded at low cell density and pre-treated with IFNs demonstrated better control over VV infection as compared to pre-treated cells at high density (Fig. 27 B). Upon quantification of VV-infected cells, infection levels without IFN treatment were approximately 50% for both cells grown at high and low cell density (Fig. 27 C). IFNβ1 pre-treatment of sparse cells substantially reduced the number of VV infection to about 5%, and IFNλ1-3 significantly reduced it to around 20% (Fig. 27 C). In contrast, for cells seeded at high density, IFN pre-treatment showed no significant effect on VV infection levels when compared to mock-treated infected cells (Fig. 27 C). Similar observations were made for MRV infection, wherein IFN pre-treatment of cells at low density significantly reduced the number of infected cells compared to non-treated cells, while no protective effect of IFN pretreatment was seen for cells seeded at high density (Fig. 27 D).

These results demonstrate that the accessibility of IFN receptors influences the antiviral response of T84 cells. Notably, cells at low confluency, where an antiviral state was induced after IFN treatment, effectively restricted virus infection. Conversely, cells at high confluency with limited receptors accessible on the apical side exhibited a weaker response to IFN pre-treatment and thus were not protected from virus infection.

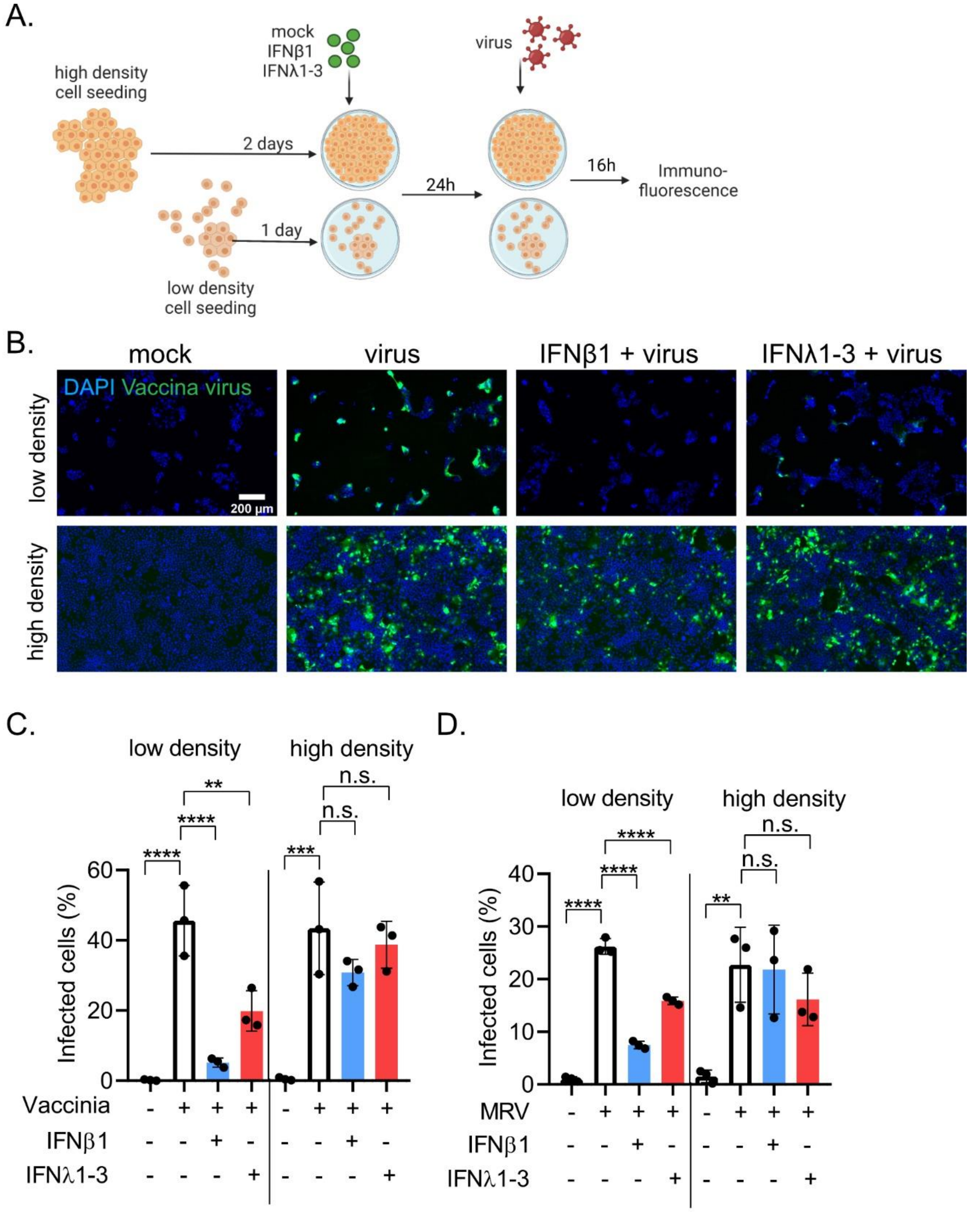

**Fig. 27. Polarized IFN receptor localization affects induction of an antiviral state in confluent cells.** T84 cells seeded at high and low density were mock-treated or pre-treated with 2000 IU/mL IFNβ1 or 300 ng/mL IFNλ1-3. 24 h post treatment, cells were infected with Vaccinia virus-eGFP (VV) or Mammalian Reovirus (MRV) at an MOI of 1 (as determined in T84 WT cells). Infection media was supplemented with the respective IFN. 16 h post infection, cells were fixed, immunostained for viral protein and fluorescence imaging analysis was performed. (A) Schematic of the experimental setup. (B) Representative images showing Vaccinia virus eGFP (green) infected cells. Nuclei were stained with DAPI (blue). Scale bar=200µm. (C, D) Quantification of the number of (C) Vaccinia virus eGFP infected cells and (D) MRV infected cells. n = 3 biological replicates, error bars indicate the standard deviation. n.s. = not significant, P<0.01**, P<0.001***, P <0.0001**** as determined by ordinary one-way ANOVA with Dunnett's multiple comparison test. Test was performed within high or low density groups, using only virus infected cells (no pretreatment) as reference.

### 2.1.8. Heterogeneity in IFN-signaling in other epithelial and non-epithelial cells

Using the human intestinal epithelial T84 cell line I demonstrated a significant cell-to-cell variability during IFN signaling, depending on the cell population context and the basolateral IFN receptor localization. In order to assess whether this phenomenon is consistent across different epithelial tissues that line mucosal surfaces, I cultured the human intestinal epithelial cell line CaCo2 and the human airway epithelial cell line Calu3 at high and low cell density, and treated them with type I and III IFNs from the apical side. Cells at low densities exhibited a more robust immune response to IFNs compared to cells at high density (Fig. 28 A), which aligns with the findings observed in T84 cells (Fig. 22). Additionally, when treating Calu3 cells cultured as polarized monolayers on transwell membranes, it was evident that IFNs coming from the basolateral membrane induced a more pronounced immune response compared to IFNs coming from the apical membrane (Fig. 28 B). This observation indicates that the variation in immune response between high and low cell densities can also be attributed to the basolateral IFN receptor localization in Calu3 cells.

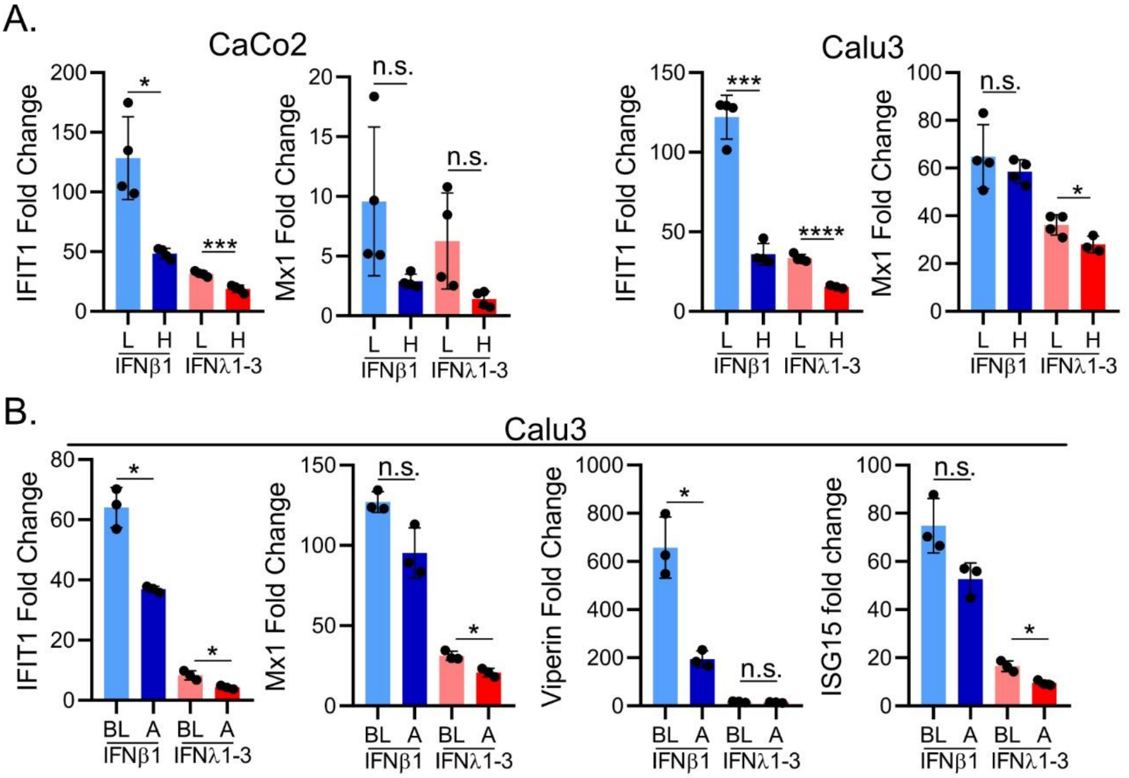

**Fig. 28. IFN-dependent signaling and the population context in mucosal epithelial cell lines.** (A) CaCo2 and Calu3 cells were seeded at high (H) and low (L) density. (B) Calu3 cells were seeded on transwell inserts and cultured until formation of a polarized monolayer. (A, B) Cells were mock treated, or treated with 2000 IU/mL IFNβ1 or 300 ng/mL IFNλ1-3. For (B) cells were treated from the apical (A) or basolateral (BL) side of the transwell compartment. 24 h post IFN treatment, RNA was harvested to evaluate the transcription of the representative ISGs IFIT1, Mx1, Viperin and ISG15 using q-RT-PCR. ISG relative expression was normalized to the mock-treated cells (fold change). n ≥ 3 biological replicates, error bars indicate the standard deviation. n.s. =not significant. P<0.05 *, P<0.01 **, P<0.001 ***, P <0.0001 **** as determined by Unpaired t test with Welch's correction.

Similar results were obtained for primary human intestinal epithelial cells. Apical treatment of ileum- and colon-derived organoids induced ISG15 protein expression mostly at the edges of clusters (white arrows), while cells embedded in the dense monolayer were less responsive to IFNs (red arrows) (Fig. 29 A-B). Moreover, basolateral IFN treatment of ileum-derived organoids induced more prominent ISG expression as compared to apical treatment (Fig. 29 C), underlining that the IFN receptor is preferentially localized to the basolateral membrane.

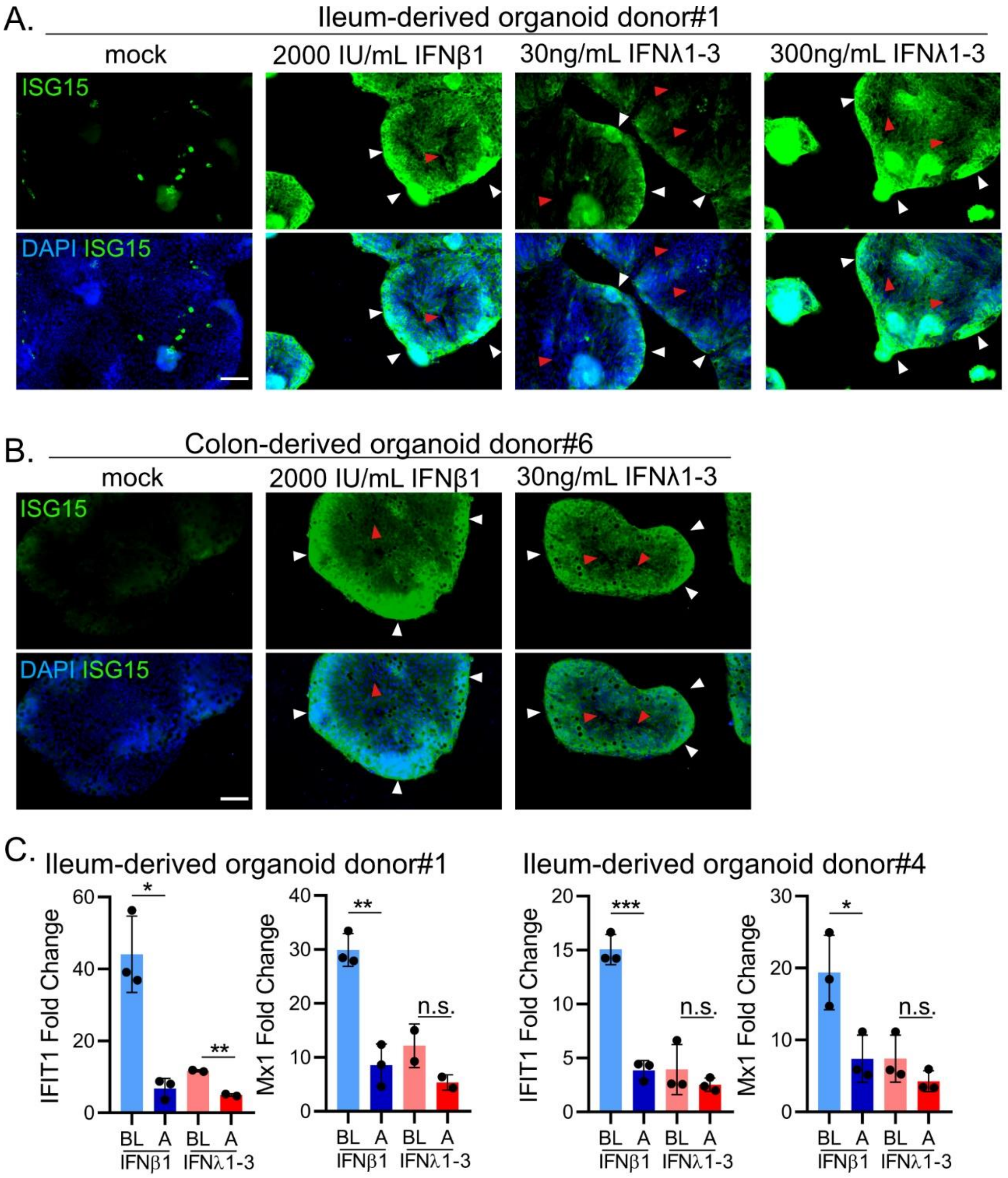

**Fig. 29. IFN-dependent signaling and the population context in human gut-derived organoids.** (A, B) Ileum- (A) and colon- (B) derived organoids were seeded in 2D aiming for medium density, and were mock treated or treated with 2000 IU/mL IFNβ1, 30 ng/mL IFNλ1-3 or 300 ng/mL IFNλ1-3 for 24 h. Indirect immunofluorescence was performed against ISG15 (green). Nuclei were stained with DAPI (blue). Scale bar=100 µm. Yellow arrows point at IFN responder single cells or cells located at the colony edges. Red arrows point at non-responder cells in the colony center. (C) Ileum-derived organoids were

seeded on transwell inserts and cultured until formation of a polarized monolayer. Cells were mock treated, or treated with 2000 IU/mL IFNβ1 or IFNλ1-3 (30 ng/mL for donor#1 and 300 ng/mL for donor#4) from the apical (A) or basolateral (BL) side of the transwell compartment. 24 h post IFN treatment, RNA was harvested to evaluate the transcription of the representative ISGs IFIT1 and Mx1 using q-RT-PCR. ISG relative expression was normalized to the mock-treated cells (fold change). n ≥ 2 biological replicates. n.s. =not significant, error bars indicate the standard deviation. P<0.05 *, P<0.01 **, P<0.001 ***, as determined by Unpaired t test with Welch's correction.

I finally tested whether this spatial heterogeneity in immune response also applies to other cell lines. For human kidney tubule epithelial cell line HK2 and fibroblast hamster kidney cell line BHK21, confluent cells were less responsive to apical IFN treatment as compared to sparse cells (Fig. 30 A-B). As a note, BHK21 do not respond to type III IFNs because they are fibroblasts and do not express the IFNLR1 (Fig. 30 B). Interestingly, the human hepatocyte-derived cellular carcinoma epithelial-like cell line Huh7 showed differential IFN-dependent signaling for cells at high at low density (Fig. 30 C). However, for Huh7, sparse cells expressed more IFIT1 than confluent cells, while confluent cells expressed more Mx1 than sparse cells (Fig. 30 C). These results support that cell-to-cell variability also occurs during IFN response in other cell lines of epithelial and non-epithelial origin. This variability is regulated by cell confluence and hence influenced by the single cell population context. Whether it also depends on a polarized IFN receptor localization, or which molecular factors play a role, needs to be further addressed.

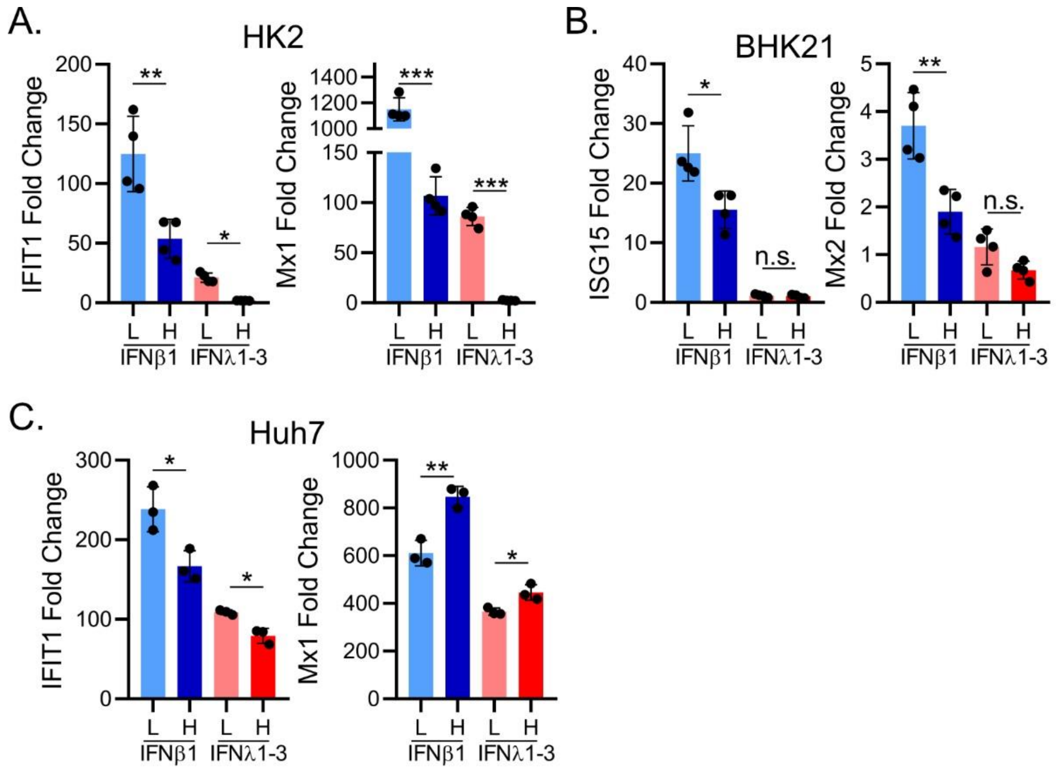

**Fig. 30. IFN-dependent signaling and the population context in other epithelial and non-epithelial cell lines.** HK2 (A), BHK21 (B) and Huh7 (C) cells were seeded at high (H) and low (L) density. Cells were mock treated, or treated with 2000 IU/mL IFNβ1 or 300 ng/mL IFNλ1-3. 24 h post IFN treatment, RNA was harvested to evaluate the transcription of the representative ISGs IFIT1, Mx1, ISG15 and Mx2

using q-RT-PCR. ISG relative expression was normalized to the mock-treated cells (fold change). n ≥ 3 biological replicates, error bars indicate the standard deviation. n.s. =not significant. P<0.05 *, P<0.01 **, P<0.001 ***, as determined by Unpaired t test with Welch's correction.

In conclusion, my findings reveal that epithelial cells lining mucosal surfaces (gut and airway epithelium) respond differently to IFNs depending on their population context. Isolated cells and cells at the edge of a cellular colony exhibit a much stronger response to IFNs compared to cells within the colony. This spatial restriction of IFN-mediated signaling is attributed to the basolateral location of IFN receptors in epithelial cells. Within a cellular colony, center cells with only their apical plasma membrane accessible, respond poorly to IFN treatment. Importantly, this differential response to IFNs based on the population context critically determines whether mucosal epithelial cells are protected from viral infection after IFN treatment. My study underscores the significance of considering the population context when investigating cell susceptibility to viral infection and the efficacy of antiviral strategies, as the cell location within a population and the level of confluency can significantly impact experimental outcomes.

## 2.2. Basal IFNλ3 expression is controlled by the population context in epithelial cells

### 2.2.1. Cell density system to study different states of the single cell environment

Growth and function of epithelial surfaces requires single cells to spatially organize with neighboring cells. Consequently, understanding how the population context and the single-cell environment influence physiological outcomes becomes crucial. Previous studies have shown that protein expression, lipid composition, endocytic events and virus infection are influenced by the population context (*298*, *299*, *324*). Moreover, me (Results section 2.1.) and a study by Bhushal et al. (*325*) demonstrated that cellular density, a central feature of the population context, impacts the response to IFNs in epithelial cells. I aimed to address whether also basal IFN expression is affected or even regulated by the environment in which a cell is embedded.

IFNs are produced in a cell under sterile conditions, leading to basal IFN-dependent signaling without any pathogenic or damage-associated trigger (*222*). This basal IFN-dependent expression and downstream signaling is required to maintain homeostasis and immune responsiveness, and needs to be tightly regulated to avoid autoimmunity (*222*). To study the impact of the population context on basal IFN expression and signaling, I established a density-based system to represent the two extreme environments in which a cell can be embedded (also described in Results section 2.1.3.). At high density, cells form a monolayer, promoting cell polarization and tight junctional connections with adjacent cells. This resembles the physiological state of epithelial surfaces. In contrast, at low density, cells either grow individually or form small clusters, resulting in heterogeneous populations with limited cell polarization and fewer inter-cellular complexes and interactions.

### 2.2.2. RNA-sequencing reveals a basal activation of the IFN-signaling pathway for epithelial cells at high density

I first wanted to gain an overall understanding of the molecular differences exhibited by IECs under high and low density conditions, particularly in terms of their immune signatures. To achieve this, I employed RNA sequencing to obtain a comprehensive overview of the transcription profiles of IECs grown at high and low cell density. The intestinal epithelial T84 cell line was seeded at high and low density, and RNA was extracted and sequenced. Principal Component Analysis (PCA) clustered replicates from each density group together, indicating minimal variability and high dataset reproducibility (Fig. 31 A). Differential gene expression analysis of cells grown at high vs low density revealed that many genes were significantly upregulated or downregulated at high density as compared to low density (Fig. 31 B, red dots are genes that are significantly differentially expressed between the two growth conditions). This observation demonstrates that density exerts a profound impact on cellular behavior. Analysis of the 50 most differentially regulated genes between high and low cell density (Fig. 32 C) revealed that many interferon-stimulated genes (ISGs), such as IFI44L, Mx2, OAS2, and IFI6 were more expressed in cells grown at high density (Fig. 31 C). These findings suggest an upregulation of the IFN signaling pathway in confluent cells compared to sparsely seeded cells. A list of the most up- and down-regulated genes in cells seeded at high vs. low density can be found in Annex section 5.2., and Tables 11 and 12.

To address whether the IFN pathway was globally altered at high cell density compared to low cell density, I employed Gene Set Enrichment Analysis (GSEA) (*326*, *327*) to shed light into molecular pathways and biological processes that are modulated by confluency. GSEA systematically examines predefined gene sets to identify enriched pathways in differentially expressed genes between high and low density conditions. My analysis revealed that cells at low density exhibited molecular signatures associated with transcription, translation and cell division (Fig. 32 A). In contrast, cells at high density displayed significant enrichment in biological processes involved in protection against virus infection and IFN-dependent signaling (Fig. 32 B). I further validated these findings using PROGENy analysis (*328*), which inferred pathway activities from transcriptomic data. The PROGENy analysis confirmed the activation of immune signaling pathways in cells at high density compared to low-density cells, particularly of the JAK-STAT pathway which is induced by IFN-signaling (Fig. 32 C). Collectively, my results strongly suggest that the cellular microenvironment and population context (precisely cellular density) significantly influence innate immune pathways, leading to the steady-state activation of the IFN-dependent pathway in cells at high density.

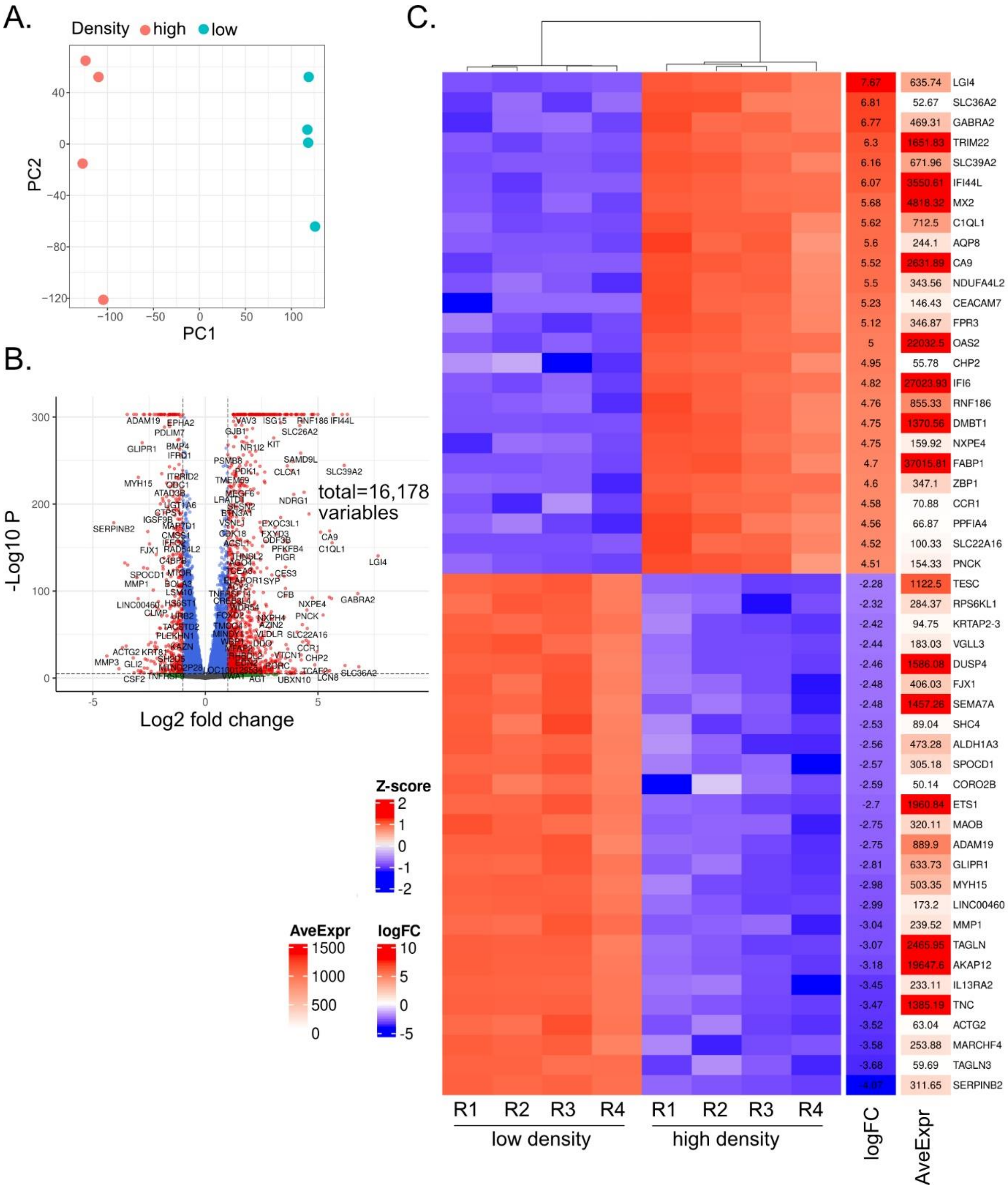

**Fig. 31. Bulk RNA-Sequencing of T84 cells at high and low density.** T84 WT cells were seeded at high and low density, and bulk RNA sequencing was performed. (A) Principal component analysis depicting all replicates of samples at high and low density used for RNA-sequencing analysis. (B, C) Differential gene expression analysis of cells grown at high vs. low density. (B) Volcano plot showing 16,178 variables (genes). Grey dots = non-significant differential gene expression, green dots = significant Log$_2$ Fold change (> 1) difference in gene expression, blue dots = significant p-value/probability (> 5) of difference in gene expression, red dots = differentially expressed genes at high vs. low (Log$_2$ Fold change > 1 and p-value/probability > 5). (C) Heat map clustering the 50 most differentially regulated genes between high and low density across the different replicates. Z-score within the replicates, Average Expression (AveExpr) and logFC is depicted for each of these genes.

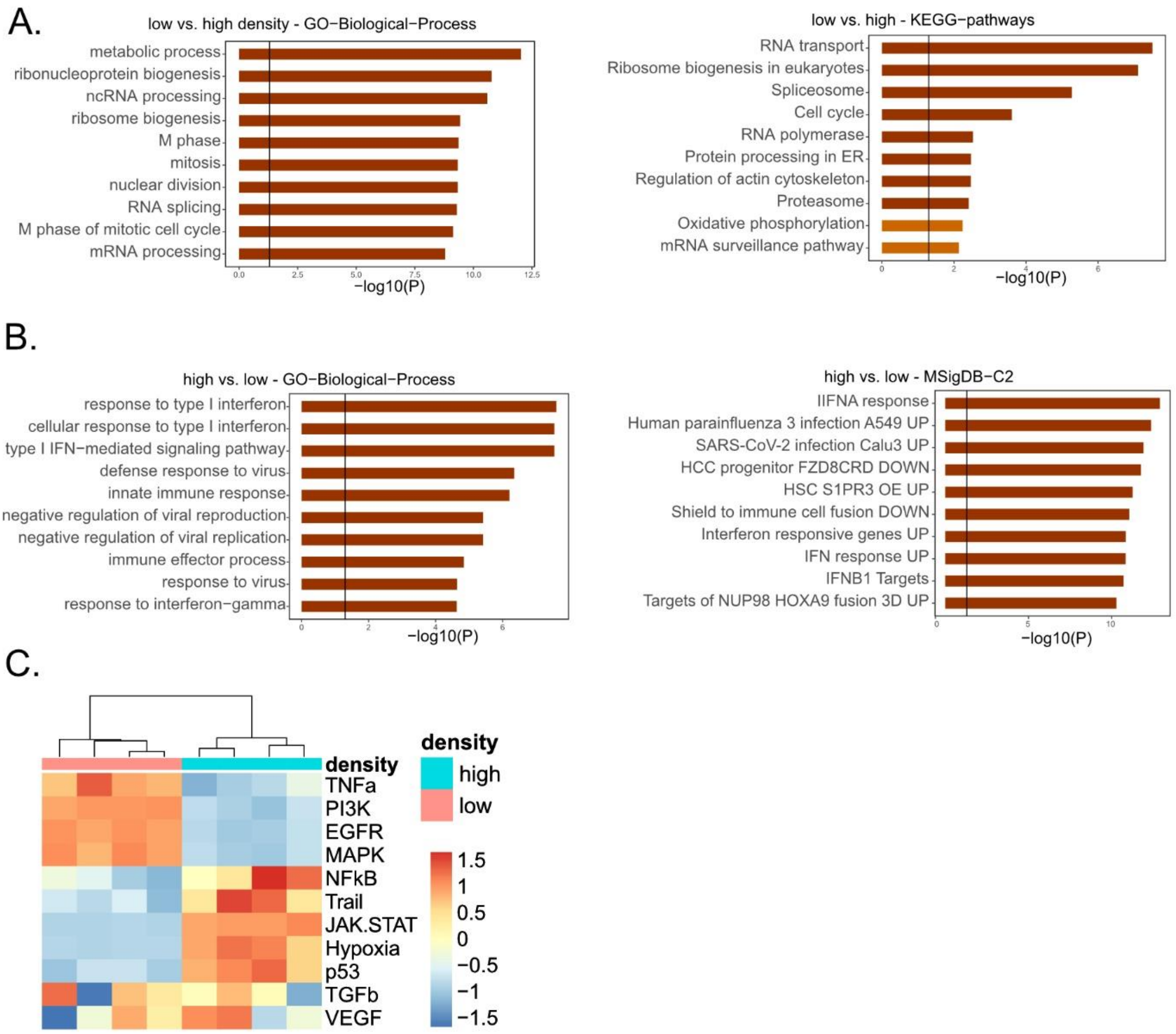

**Fig. 32. RNA-Sequencing reveals and up-regulation of the IFN-dependent pathway in cells at high density as compared to cells at low density.** (A, B) Gene Set Enrichment Analysis (GSEA) of (A) low vs. high and (B) high vs. low seeding conditions. The –log10(P) shows values calculated by using the q value (adjusted p value). Red bars are significant when calculating with the p-value (p-value > 1.5) and orange bars are non-significant when calculated with the p-value (p-value < 1) (C) Heat-map showing pathway activities obtained after PROGENy analysis.

To validate my RNA-sequencing results, I analyzed the expression of ISG transcripts using RT-q-PCR in T84 WT cells seeded at high and low density. Additionally, to address that the differential expression of genes related to immune response between low and high density cells was dependent on the IFN-signaling pathway, I used a T84 IRF3 KO cell line which is deficient in inducing IFN transcription. I previously generated the T84 IRF3 KO cell line during my Master’s thesis in this lab. Supporting the RNA-sequencing data, T84 WT cells showed significantly higher ISG expression in confluent cells as compared to sparse cells (Fig. 33 A). This difference was abolished in T84 IRF3 KO cells (Fig. 33 A), in which the ISG expression at high and low density was similar or less as compared to the ISG expression in T84 WT cells at low density. Importantly, cytokines that are not regulated through IRF3 and for which expression is not dependent on IFN signaling, were either not differentially expressed in T84

WT cells at high and low density (IL-1β, IL-6 and IL-18) or even upregulated in sparse cells as seen for IL-8 (Fig. 33 B).

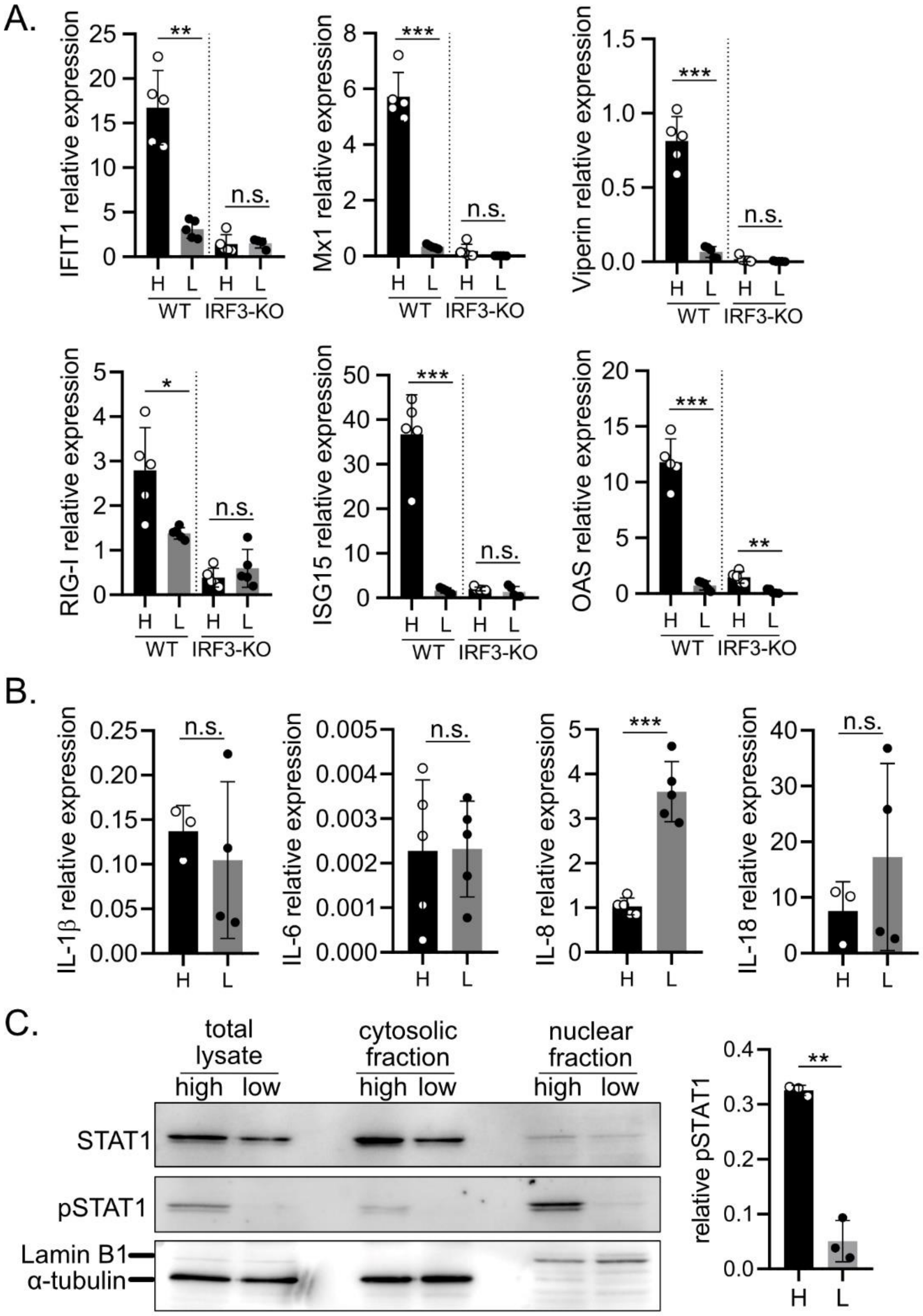

**Fig. 33. Basal activation of the IFN-dependent pathway in confluent epithelial cells.** T84 WT and T84 IRF3 KO cells were seeded at high and low density and treated with culturing media (to address basal signaling). (A, B) 24 h post treatment, RNA was harvested to evaluate the transcription of (A) representative ISGs IFIT1, Mx1, Viperin, RIG-I, ISG15 and OAS, and (B) pro-inflammatory cytokines IL-1β, IL-6, IL-8 and IL-18 using q-RT-PCR. (C) 1 h post treatment, cells were collected and cellular fractioning was done to assess the phospho-STAT1 (pSTAT1) abundance in the total cell, the cytosol or the nucleus by Western Blot. pTBK1 in the cytosolic fraction from. α-tubulin served as a housekeeping protein for the cytosolic fraction, and Lamin B1 served as a housekeeping protein for the nuclear fraction. pSTAT1 was quantified relative to the housekeeping protein α-tubulin from the total lysate fraction. (A-C) n ≥ 3 biological replicates, error bars indicate the standard deviation. n.s. =not significant. P<0.05 *, P<0.01 **, P<0.001 ***, P <0.0001 **** as determined by Unpaired t test with Welch's correction.

The signaling of IFNs occurs via the JAK/STAT pathway (Fig. 9). After expression, secreted IFNs interact with their receptor inducing activation of the JAK family. JAKs phosphorylate STAT1 and STAT2, which then associate with IRF9 and form the ISGF3 complex to induce transcription of ISGs. To finally prove that density induces IFN-dependent signaling, I conducted Western Blot analysis to assess total STAT1 protein abundance and phosphorylated STAT1 levels. As expected, the inactive STAT1 form is mostly enriched in the cytosolic fraction of cells (Fig. 33 C). Interestingly, total STAT1 levels are slightly higher in cells at high density as compared to cells at low density (Fig. 33 C). This is in agreement with the RNA-Sequencing data, in which STAT1 transcript levels were significantly upregulated in confluent cells as compared to sparse cells. STAT1 is an ISG, and it is reasonable to speculate that its transcript levels are induced by the increasing basal IFN-dependent signaling as cells become confluent. This induction of STAT1 expression could support a positive feedback loop, potentially amplifying the IFN signaling response in confluent cells. As anticipated, the Western Blot analysis revealed that phosphorylated STAT1 is predominantly enriched in the nuclear fraction (Fig. 33 C). This localization is consistent with the active form of STAT1, which is known to assemble into the ISGF3 complex to induce transcription of ISGs. Most Importantly, pSTAT1 levels were significantly higher in cells at high density (Fig. 33 C). Together with the ISG expression level, this confirms my transcriptomic analysis of cells grown at high vs low density, and supports the notion that cellular density regulates basal IFN-dependent signaling.

To address whether this differential regulation of IFN signaling at high vs. low cell density is also conserved in other mucosal cell types, I measured the expression of various ISG levels by RT-q-PCR in the human intestinal epithelial cell lines CaCo2 and HT29, and the human airway epithelial cell lines Calu3 and A549. Results showed that, while not all ISGs had their expression regulated by cell density in all tested cells, most ISGs were upregulated in high density cells compared to low density cells (Fig. 34 A). Not only mucosal surfaces, but every surface within the body is covered with epithelial cells. To test whether also other epithelial cell types elicit a basal IFN-dependent immune response, I measured the ISG expression at high and low density in the human kidney tubule epithelial cell line HK2 and the human hepatocyte-derived cellular carcinoma epithelial-like cell line Huh7. With one exception (Mx1 in HK2 cells), no differential IFN-dependent immune activation was seen for cells seeded at different densities (Fig. 34 B). Finally, I assessed the basal immune activation in the fibroblast (non-epithelial) cell line hamster kidney cell line BHK21, and observed that Mx2 and ISG15 were differentially regulated by cellular density, while Mx1 and OAS3 not (Fig. 34 C). For conclusive results in non-epithelial tissues, the basal IFN-dependent immune response must be determined in other fibroblasts from human origin.

Collectively, the results indicate an upregulation of the IFN-signaling pathway in T84 cells when they reach confluence (high density) compared to when they are sparse (low density). Moreover, my findings also suggest that this cell density-dependent regulation of IFN signaling is conserved across epithelial tissues that line mucosal surfaces and are in direct contact with the outside environment. In non-epithelial cells and in epithelial cells lining inner organs, there are some variabilities in basal ISG expression, and further experiments are required to clearly address the role of confluence on steady-state IFN-signaling.

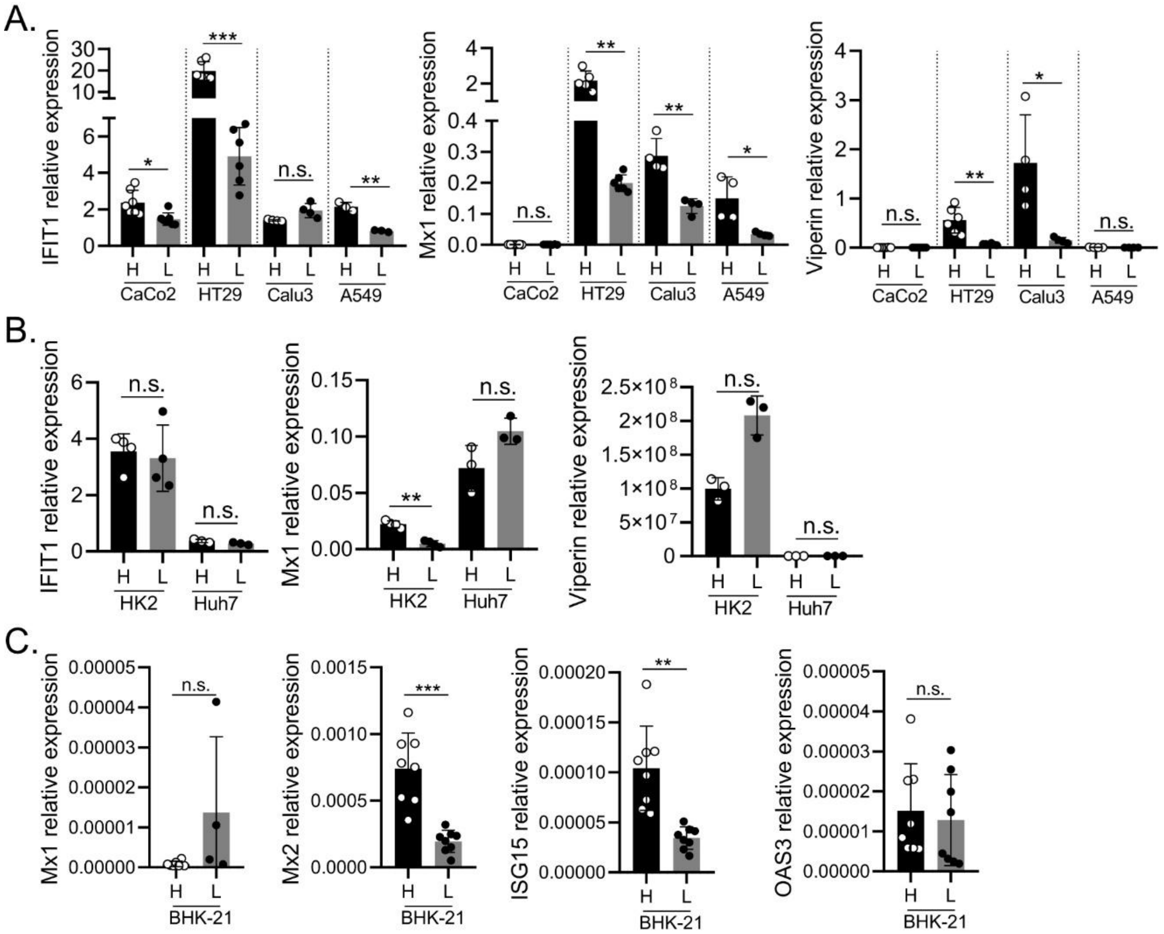

**Fig. 34. Basal activation of the IFN-dependent pathway in epithelial and non-epithelial cell lines. Epithelial cells lining mucosal surfaces.** (A), epithelial cells lining inner organs (B) and fibroblasts (C) were seeded at high and low density. Cells were treated with culturing media (to address basal signaling) and 24 h post treatment, RNA was harvested to evaluate the relative expression of ISGs IFIT1, Mx1, Mx2, Viperin, RIG-I, ISG15 and OAS3 using q-RT-PCR. n ≥ 3 biological replicates, error bars indicate the standard deviation. n.s.=not significant. P<0.05 *, P<0.01 **, P<0.001 ***, P <0.0001 **** as determined by Unpaired t test with Welch's correction.

### 2.2.3. IFN-sensing reporter cell line allows to follow the density-dependent induction of IFN signaling in a dynamic manner

Assessing the cell density-dependent regulation of IFN signaling in cells at low or high density only offers a static view of this process. In order to comprehensively explore the basal immune response in a more dynamic fashion and definitively confirm that cellular density serves as the determinant for the induction of IFN signaling at high density, I utilized the T84 prom-Mx1-GFP cell line. First, I confirmed that this IFN-sensing reporter cell line behaves similarly to the WT T84 cells by measuring the basal ISG expression at high and low density with RT-q-PCR. Similar to WT T84 cells, ISG expression in T84 prom-Mx1-mCherry was also significantly higher in confluent cells as compared to sparse cells (Fig. 35 A).

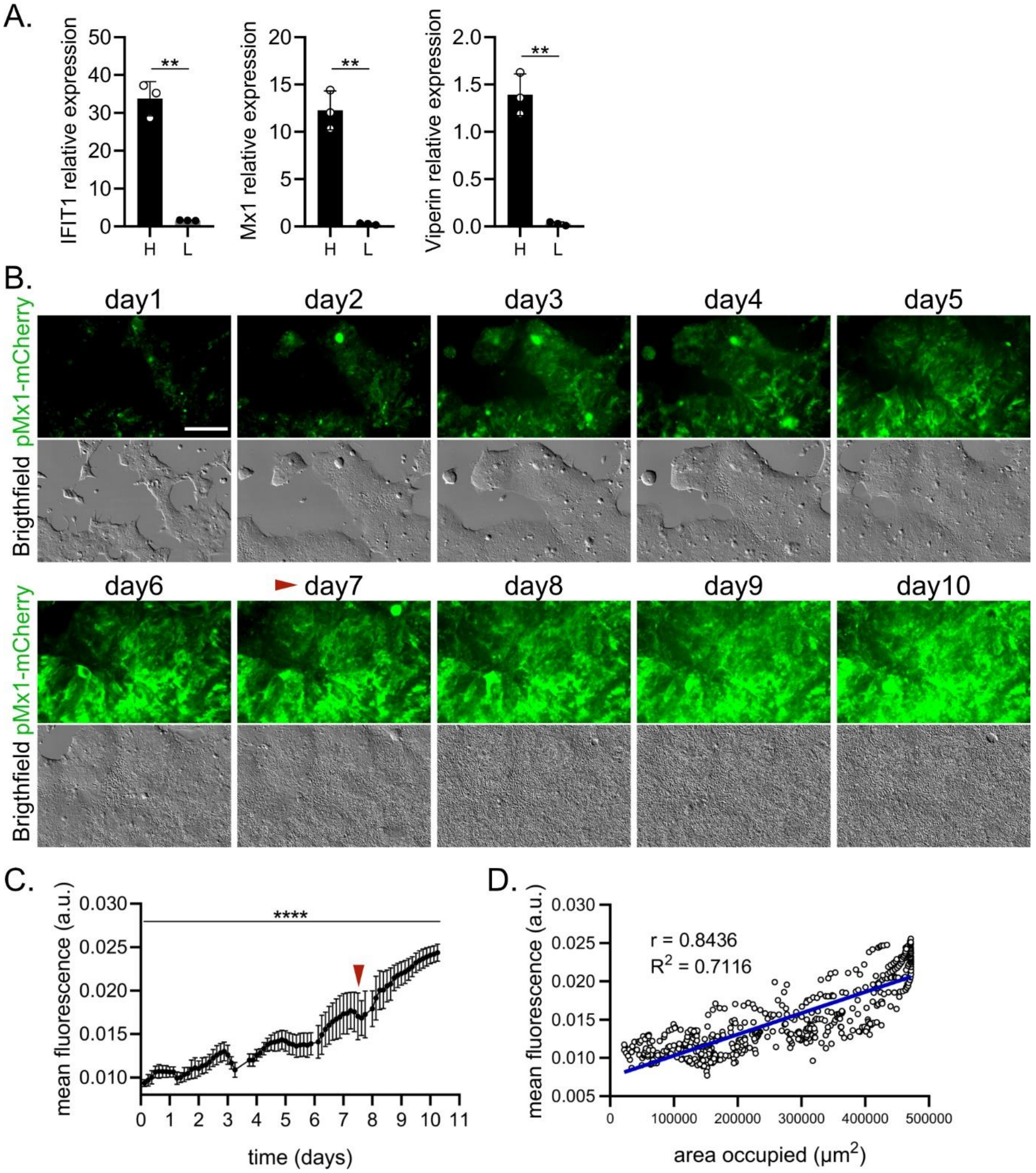

**Fig. 35. IFN-sensing reporter cell line allows to follow the density-dependent induction of IFN signaling in a dynamic manner.** (A) T84 prom-Mx1-mCherry cells were seeded at high and low density, and treated with culturing media (to address basal signaling). 24 h post treatment, RNA was harvested to evaluate the relative expression of ISGs IFIT1, Mx1, and Viperin using q-RT-PCR. (B-D)

T84 prom-Mx1-mCherry cells were seeded low density in 8-well imaging chamber slides (Ibidi) and one-day post-seeding cells were imaged over a period of 10 days to visualize the expression of the fluorescent reporter encoding mCherry under the control of the MX1 promoter region (pMx1-mCherry). Red arrow marks the time-point in which cells formed a confluent monolayer. (B) Representative images showing expression of pMx1-mCherry (green) every day for 10 days. Brighfield images visualize the cells and their growth into a monolayer. (C) Quantification of the pMx1-mCherry mean fluorescence intensity over time within the area with growing cells. (D) Linear regression and coefficient of correlation (r) calculated for the mean fluorescence from (C) and the area occupied by cells. (A, C) n ≥ 3 biological replicates, error bars indicate the standard deviation. $P<0.01$ **, $P <0.0001$ **** as determined by (A) Unpaired t test with Welch's correction, and (C) Ordinary one-way ANOVA.

To directly monitor how cell density impacts the basal IFN response in T84 cells, the reporter cell line was seeded in 8-well imaging chamber slides (Ibidi) and, one-day post-seeding cells were imaged over a period of 10 days to visualize the expression of my fluorescent reporter encoding GFP under the control of the ISG MX1 promoter region (pMx1-mCherry) (Fig. 35 B). At day 1, cells grew as isolated single cells or in small and medium sized clusters, and expressed low levels of the fluorescent reporter (Fig. 35 B-C). Throughout time, the cell clusters grew together and the cellular density increased, until at day 7 they formed a confluent monolayer. Notably, after the formation of a confluent monolayer at day 7 (Fig. 35 B-C, red arrow signalizes day of formation of a monolayer), the fluorescent signal continued to show a slight increase up to day 10, probably because the cells still continued proliferating leading to a higher cell density. Increase in the area occupied by the cells and hence cellular density directly correlated with a steady increase of pMx1-mCherry mean fluorescence (Fig. 35 D). Taken together, visualizing the expression of the IFN-sensing reporter over time confirms that the cellular density in T84 cells induces the activation of the basal IFN dependent pathway.

### 2.2.4. Density-dependent immune activation is dependent on TBK1, leading to IFNλ3-dependent ISG expression

To identify the molecular players responsible for this basal immune activation, I capitalized from various T84 knock-out cell lines previously generated in my lab (see Table 6 at the Material section 4.1.4.) which are deficient for central molecules of the IFN-dependent pathway. T84 WT cells serve as a positive control, where cells at high density exhibit markedly elevated ISG expression in comparison to cells at low density (Fig. 36 A). On the other hand, IRF3 KO cells function as a negative control, where IFN induction is non-functional, resulting in the absence of basal ISG expression in cells at high density (Fig. 36 A). Knock-out of the type I IFN receptor IFNAR1 (IFNAR KO) showed a similar ISG expression pattern as WT cells (Fig. 36 A), suggesting that type I IFNs are not responsible for the basal immune activation. On the contrary, knock-out of the type III IFN receptor IFNLR1 (IFNLR KO) lead to inhibition of the basal ISG expression at high density, similar to ISG expression levels in IRF3 KO cells (Fig. 36 A). This demonstrated that type III IFN signaling plays a crucial role in regulating the basal immune response in confluent cells. That conclusion was further supported by the ISG expression pattern in T84 IFNAR1 IFNLR1 double knockout cells (IFNR dKO), which exhibited no basal ISG transcripts at high cell density (Fig. 36 A).

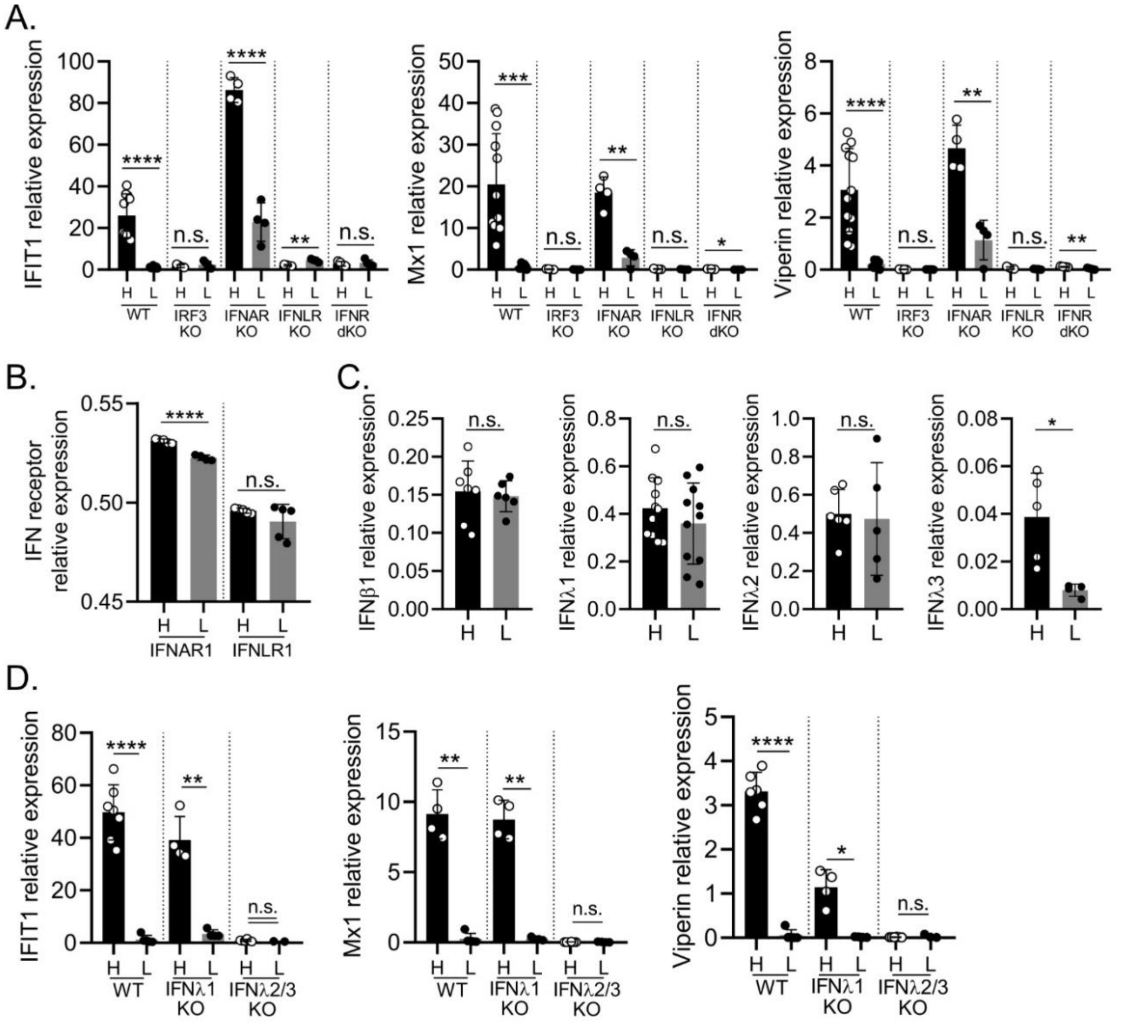

**Fig. 36. IFNλ3 expression and signaling is responsible for the basal immune activation at high cell density.** T84 WT and knock-out (KO) cells were seeded at high and low density, and treated with culturing media (to address basal signaling). 24 h post treatment, RNA was harvested to evaluate the relative expression of various genes using q-RT-PCR. (A) Relative expression of ISGs IFIT1, Mx1 and Viperin in T84 WT, IRF3 KO, IFNAR KO, IFNLR KO and IFNAR IFNLR double KO (IFNR dKO) cells. (B) Relative expression of IFNAR1 and IFNLR1 in T84 WT cells. (C) Relative expression of IFNβ1, IFNλ1, IFNλ2 and IFNλ3 in T84 WT cells. (D) Relative expression of ISGs IFIT1, Mx1 and Viperin in T84 WT, IFNλ1 KO and IFNλ2/3 KO cells. (A-D). n ≥ 3 biological replicates, error bars indicate the standard deviation. n.s.=not significant. P<0.05 *, P<0.01 **, P<0.001 ***, P <0.0001 **** as determined by Unpaired t test with Welch's correction.

To address whether the difference in immune signaling is rooted in the IFN receptor abundance, I measured the IFN receptor expression by RT-q-PCR in T84 WT cells at high and low density. No correlation between receptor abundance and induction of IFN signaling at high density was observed (Fig. 36 B). Of note, IFNAR1 expression level was slightly higher in high density cells as compared to low density cells (Fig. 36 B). However, as demonstrated above (Fig. 36 A, IFNAR KO cells), the type I IFNs are not responsible for the basal immune signaling at high density. Finally, I assessed whether IFNs are differentially expressed upon confluence in T84 WT cells by RT-q-PCR. Excitingly, while IFNβ1, IFNλ1 and IFNλ2 were expressed at similar levels in high and low density, IFNλ3 was significantly higher in confluent as compared to sparse cells (Fig. 36 C). To confirm this data and address in more detail which IFN is relevant for the basal immune activation, I exploited the T84 IFNλ1 knock-out (created by Yagmur Keser) and IFNλ2/3 knock-out (created by Dorothee Reuss) cell lines. Knock-out of IFNλ2/3, and not IFNλ1, depleted the density-dependent basal ISG expression (Fig. 36 D). Together this data suggests that, when epithelial cells grow confluent, IFNλ3 is significantly induced leading to downstream ISG expression.

To identify the factors that regulate the induction of IFNλ3 at high confluency, I analyzed the activity of key molecules upstream of IFN transcription (Fig. 8). The reduced ISG (Fig. 37 A, Fig. 36 A) and IFNλ2/3 (Fig. 37 A) expression levels observed in confluent T84 IRF3 KO cells as compared to confluent WT cells demonstrates that IRF3 is a key transcription factor required to induce IFNλ3 transcription at high cell density. This is underlined by the observation that active phosphorylated IRF3 levels are higher in the nuclear fraction of confluent cells as compared to sparse cells, while total IRF3 protein levels were not differentially expressed between cells at high and low density (Fig. 37 B). TBK1 is a central kinase in innate immune sensing and activation, and directly phosphorylates IRF3. Total TBK1/NAK (NF-κB activating kinase) protein levels were similar in cells at high and low cell density (Fig. 37 B). However, the active phosphorylated form of TBK1/NAK in the cytoplasm was significantly higher in confluent cells as compared to sparse cells (Fig. 37 B-C). Moreover, inhibition of TBK1/IKKε by the inhibitor BX297 significantly reduced IFNλ2/3 and ISG Mx1 transcript levels in T84 WT cells at high density, while it did not have an effect in cells at low density (Fig. 37 D).

Altogether this data shows that, in confluent epithelial cells, TBK1 is activated and in turn phosphorylates IRF3. IRF3 translocates to the nucleus inducing the transcription of basal IFNλ3. IFNλ3 signals through the IFNLR, inducing the activation of the JAK/STAT signaling cascade and transcription of ISGs under homeostatic conditions.

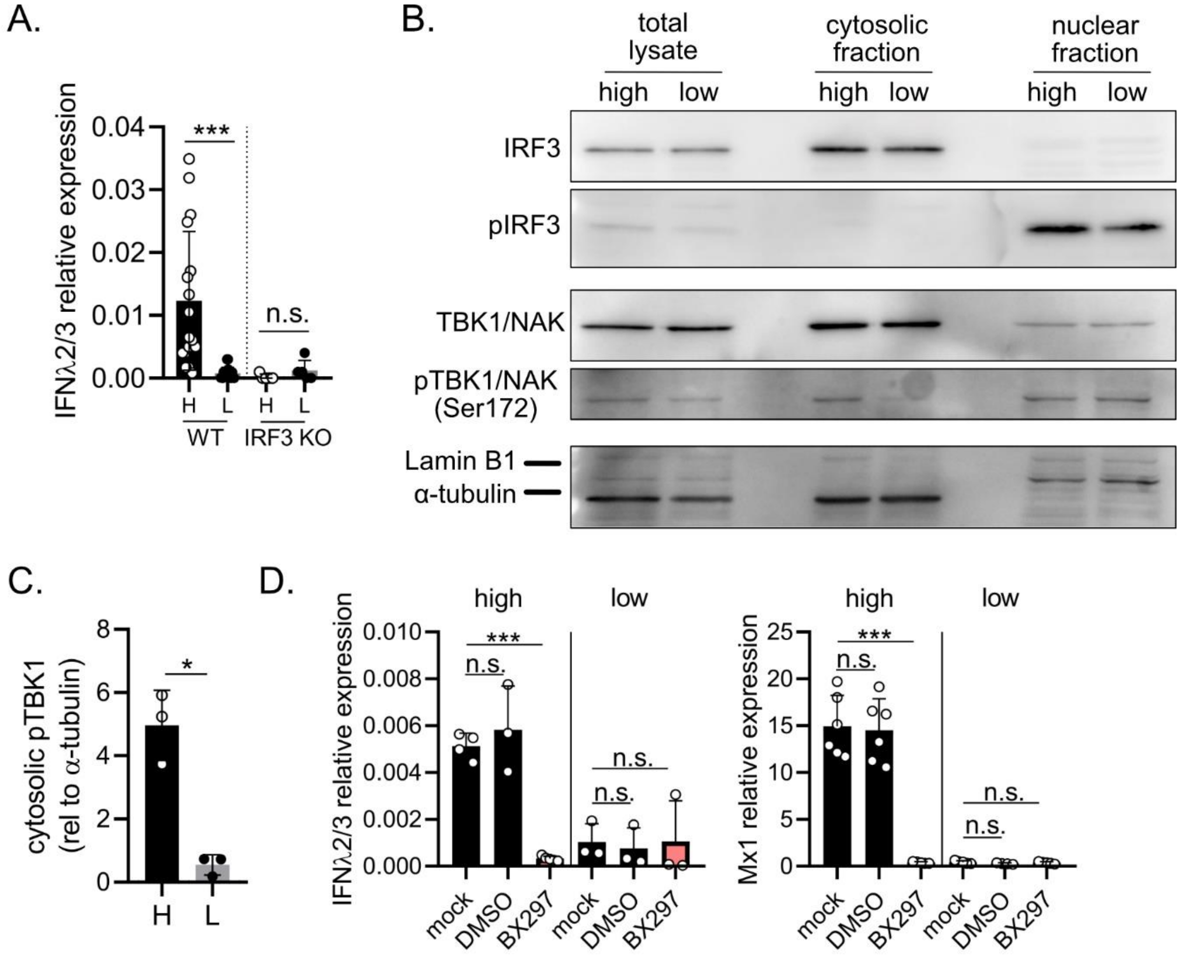

**Fig. 37. In confluent cells, TBK1 is responsible to induce IRF3 and basal IFN expression.** (A) T84 WT and IRF3 KO cells were seeded at high and low density, and treated with culturing media (to address basal signaling). 24 h post treatment, RNA was harvested to evaluate the IFNλ2/3 relative expression using q-RT-PCR. (B) T84 WT cells seeded at high and low density were collected, and cellular fractioning was done to assess IRF3, phospho-IRF3 (pIRF3), TBK1/NAK and phosphoTBK1/NAK (pTBK1/NAK) protein abundance in the total cell lysate, the cytosolic fraction or the nuclear fraction by Western Blot. α-tubulin served as a housekeeping protein for the cytosolic fraction, and Lamin B1 served as a housekeeping protein for the nuclear fraction. (C) pTBK1 in the cytosolic fraction from (B) was quantified relative to the housekeeping protein α-tubulin. (D) T84 WT cells were seeded at high and low density, and either mock (culturing media)- or DMSO-treated, or treated with 1 µM TBK1-inhibtor BX297 (exact treatment is explained in the methods section 4.2.5.2). After treatment, RNA was harvested to evaluate the relative expression of IFNλ2/3 and Mx1 using q-RT-PCR. (A, C, D) n ≥ 3 biological replicates, error bars indicate the standard deviation. n.s.=not significant. P<0.05 *, P< 0.01 **, P<0.001 ***, P <0.0001 **** as determined by Unpaired t test with Welch's correction.

### 2.2.5. Mitochondrial DNA induces the cGAS-STING pathway at high cell density

The activation of IFN signaling typically occurs in response to the recognition of pathogenic elements by pattern recognition receptors (PRRs). However, when investigating the basal immune response, no exogenous pathogens are present in the cells. Interestingly, it has been widely reported that the PRR cGAS also recognizes cellular endogenous DNA from mitochondrial or nuclear origin (*91*). After cellular-derived DNA sensing, cGAS produces the second messenger 2'3'-cGAMP, which binds to STING under sterile conditions. This leads to

STING relocalization to the Golgi apparatus, where it phosphorylates TBK1 and IRF3 (*91*). As such, the cGAS-STING pathway is a promising candidate for inducing the density-dependent basal IFN-dependent immune response in epithelial cells.

To investigate the potential involvement of this pathway in the differential immune response at high and low density, I employed well-characterized inhibitors targeting STING. I first validated the efficacy of the inhibitors in my system. T84 WT cells were seeded at high and low density, and treated with the STING agonist diABZ. These treatments were performed in the presence or absence of the STING inhibitors, allowing me to evaluate the inhibitory effect of the drugs. Immune activation was determined by expression of IFNλ2/3 and the ISG Mx1 using RT-q-PCR. At high density, the STING agonist diABZ induced a strong immune response, which was efficiently downregulated by the STING inhibitors H151 and STING IN-2 (Fig. 38 A). These observations validate that the STING and cGAS inhibitors are active in T84 cells. Interestingly, in sparse cells diABZ did not lead to a notable induction of IFNλ2/3 expression, and only induced low levels of Mx1 transcripts (Fig. 38 A). This suggests that STING signaling is impaired at low cell density and cannot be activated by the STING agonist diABZ. Altogether, the results confirm efficient inhibition of STING signaling by the tested drugs in my system.

To directly address the role of the STING pathway during homeostatic IFN signaling, T84 WT cells were seeded at high and low confluence, and treated with the STING inhibitors. Basal IFN signaling was measured by expression of IFNλ2/3 and the downstream ISG Mx1 using RT-q-PCR. In T84 cells seeded at high density, the inhibition of STING significantly decreased the basal immune activation (Fig. 38 B). On the contrary, at low density no major effect could be seen by treatment with STING inhibitors (Fig. 38 B). These results strongly suggest that the STING pathway mediates basal activation of IFN signaling at high density. To validate these findings, I established a T84 cell line in which STING expression is silenced by shRNA as confirmed by Western Blot analysis (Fig. 38 C). Supporting the results obtained from the STING inhibitor treatment, at high cell density the basal IFNλ2/3 and downstream ISGs transcript levels were notably lower in T84 STING knock-down (KD) cells as compared to the control T84 scrambled (scr) shRNA cells (Fig. 38 D). I previously demonstrated that the basal ISG expression in confluent cells is dependent on IFNλ3 expression, and not IFNλ1 or IFNλ2 (Fig. 36 C-D). To investigate the specific role of the STING pathway in inducing the transcription of IFNλ3, the IFNλ1 transcript levels were measured in T84 WT cells treated with the STING inhibitor H151 and in the T84 STING KD cell line. T84 cells with impaired STING signaling exhibited minimal alterations in IFNλ1 expression (Fig. 38 E), indicating that the density-dependent activation of the STING pathway predominantly influences IFNλ2/3 expression.

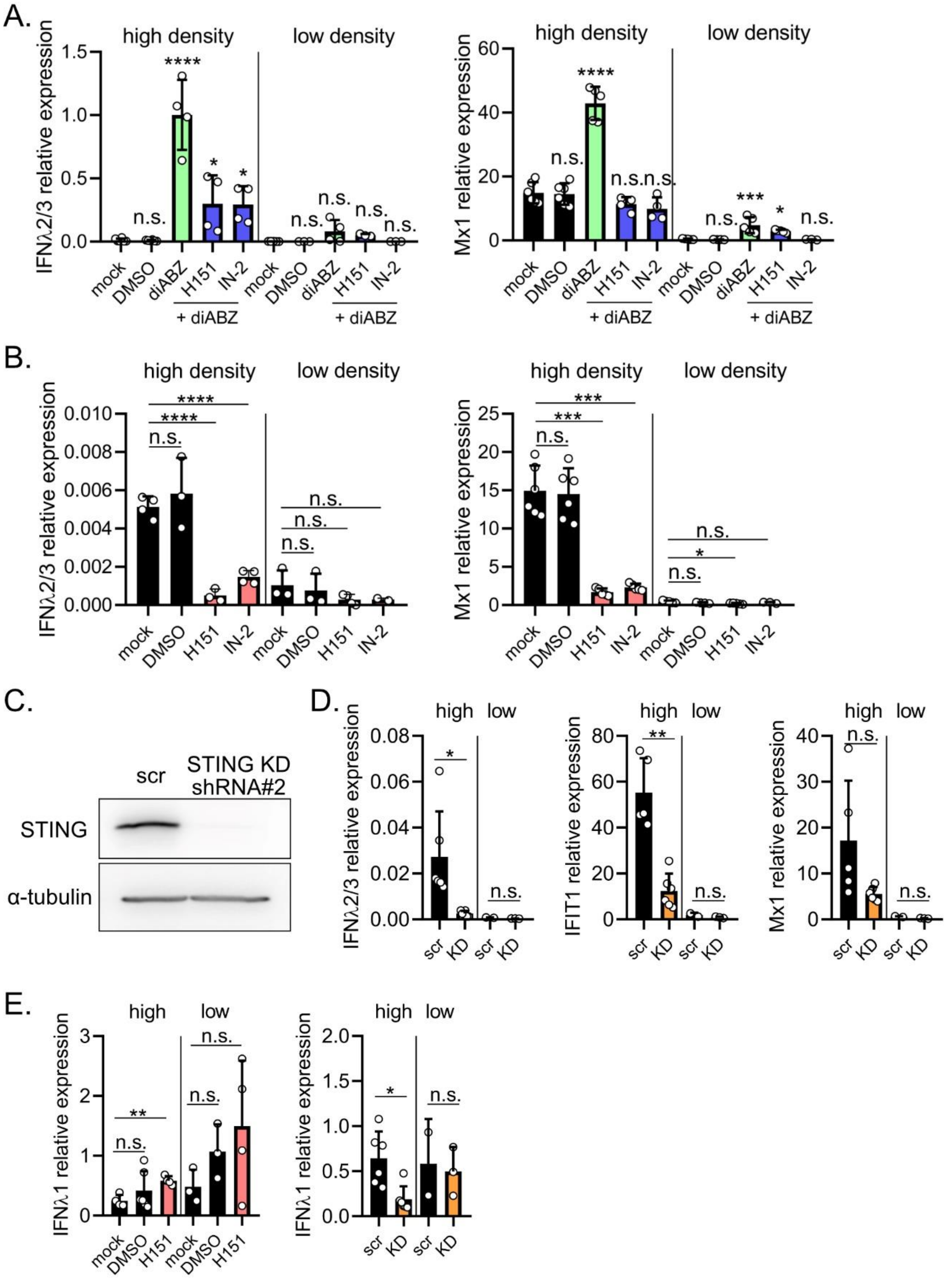

**Fig. 38. STING is responsible for inducing basal IFNλ2/3 expression in confluent epithelial cells.** (A, B) T84 WT cells were seeded at high and low density, and either mock (culturing media)- or DMSO-treated, or treated with 20 µM STING-inhibitor H151 or 2 µM STING-inhibitor STING-IN2 in combination with 10 µM STING-agonist diABZ (A) or without diABZ (B) (exact treatment is explained in the methods section 4.2.5.2). After treatment, RNA was harvested to evaluate the relative expression of IFNλ2/3 and Mx1 using q-RT-PCR. (C) I created a cell line with silenced STING by shRNA (STING knock-down (KD)). T84 scrambled (scr) control cellular protein extracts were collected to assess the STING abundance. α-tubulin served as a housekeeping protein. (D) T84 scrambled control (scr) and T84 STING KD cells were seeded at high and low density, and treated with culturing media (to address basal signaling). 24 h post treatment, RNA was harvested to evaluate the IFNλ2/3, IFIT1 and MX1 relative

expression using q-RT-PCR. (E) T84 WT depleted of STING either by treatment with 20 µM STING-inhibitor H151 or by STING knock-down were seeded at high and low density. Appropriate controls (mock- and DMSO-treatment, and T84 scrambled control (scr) cells) were also used. RNA was harvested to evaluate the IFNλ1 relative expression using q-RT-PCR. (A, B, D, E) n ≥ 3 biological replicates, error bars indicate the standard deviation. n.s.=not significant. P<0.05 *, P<0.01 **, P<0.001 ***, P <0.0001 **** as determined by (A) ordinary one-way ANOVA with Dunnett's multiple comparison test using the mock as reference, and (B, D, E) Unpaired t test with Welch's correction.

Given that STING activation is orchestrated by cGAS, I aimed to corroborate the dependence of basal IFN expression on cGAS using the inhibitors G150 and RU521. For these experiments I exclusively seeded cells at a high density, as only confluent cells trigger basal immune activation and are susceptible to STING inhibition (Fig. 38). Similar to before with the STING inhibitors, I first validated the efficacy of the drugs targeting cGAS in my system. T84 cells at high density were infected with Vaccinia virus, in absence or presence of the inhibitors. Vaccinia virus is a double stranded DNA virus that replicates in the cytoplasm and is therefore sensed by cGAS, serving as an agonist for this PRR (*329*). Cell infection resulted in a significant induction of IFNλ2/3 expression, which was effectively inhibited by the cGAS inhibitors G150 and RU521 (Fig. 39 A). However, despite the induction of IFNλ2/3 expression, the downstream ISG Mx1 was not upregulated after infection (Fig. 39 A), probably due to the Vaccinia virus proficiency in counteracting the cellular immune response (*329*). To address the role of cGAS on basal IFN expression and signaling, confluent T84 WT cells were treated with the cGAS inhibitors, and basal IFNλ2/3 and Mx1 expression was measured using RT-q-PCR. Inhibition of cGAS significantly decreased the basal immune activation (Fig. 39 B), supporting that cGAS mediates STING activation during homeostasis.

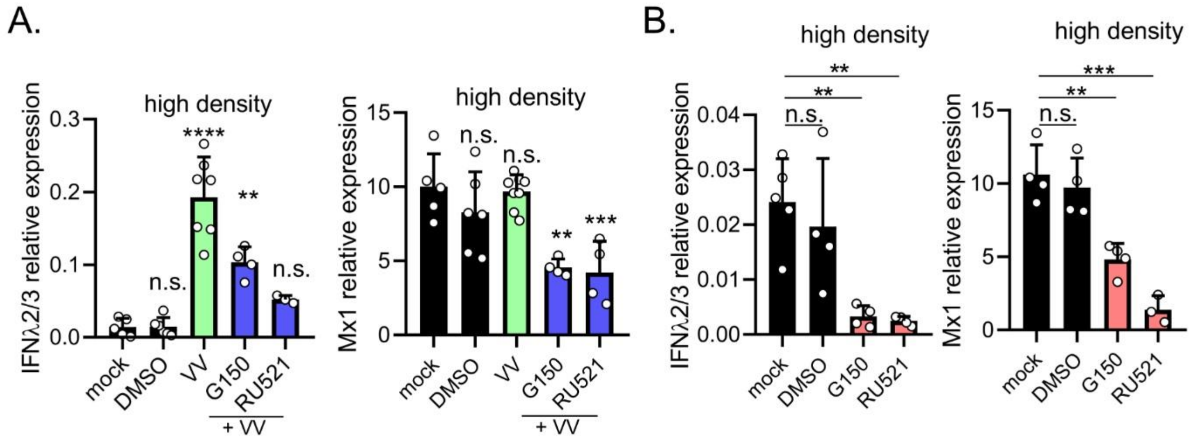

**Fig. 39. The PRR cGAS leads to activation of basal IFN-signaling in confluent epithelial cells.** T84 WT cells were seeded at high, and either mock (culturing media)- or DMSO-treated, or treated with 10 µM STING-inhibitors G150 and RU521 in combination with cGAS-agonist Vaccinia virus (VV) (A) or without virus (B) (exact treatment is explained in the methods section 4.2.5.2). After treatment, RNA was harvested to evaluate the relative expression of IFNλ2/3 and Mx1 using q-RT-PCR. n ≥ 3 biological replicates, error bars indicate the standard deviation. n.s.=not significant. P<0.05 *, P<0.01 **, P<0.001 *** as determined by (A) ordinary one-way ANOVA with Dunnett's multiple comparison test using the mock as reference, and (B) Unpaired t test with Welch's correction.

A key following question is: what factor does activate cGAS in confluent epithelial cells? It has been demonstrated that leaked mitochondrial DNA (mtDNA) in the cytoplasm can be sensed by cGAS, leading to the initiation of immune signaling even under homeostatic sterile conditions (*234*). To investigate whether leaked mtDNA triggers the cGAS-STING pathway at high cell density, I depleted T84 WT cells from total mtDNA by prolonged treatment with low concentrations of Ethidium Bromide (EtBr) or 2'-3'-dideoxycytidine (ddC). Low concentration of EtBr selectively reduce mtDNA without affecting nuclear DNA (*330*), and ddC is an inhibitor of mitochondrial DNA polymerase γ and does not affect the function of nuclear DNA polymerases (*331*). qPCR analysis measuring mtDNA abundance relative to nuclear DNA revealed an efficient depletion of mtDNA after treatment (Fig. 40 A). Of note, mtDNA levels were significantly higher in sparse cells as compared to confluent cells (Fig. 40 A). Basal IFN-signaling of mtDNA-depleted cells was then assessed by measuring IFN and ISG expression levels by RT-q-PCR. While IFNλ1 expression was not influenced by the absence or presence of mtDNA in the cell, IFNλ2/3 and Mx1 transcript levels were significantly decreased in mtDNA-depleted cells at high density (Fig. 40 B).

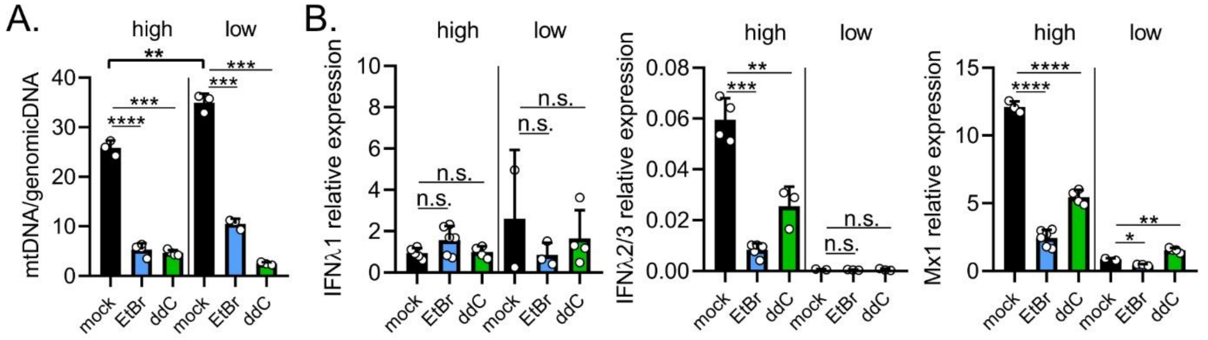

**Fig. 40. Mitochondrial DNA induces the cGAS-STING pathway at high dell density.** T84 WT cells were seeded at high and low density were depleted of mitochondrial DNA (mtDNA) by 6 days treatment with 300 ng/mL Ethidium Bromide (EtBr) or 100 µg/mL 2'-3'-dideoxycytidine (ddC). (A) Total cellular DNA was harvested and ratio of mtDNA to genomic DNA was calculated by quantitative PCR using primers targeting the mitochondrial gene nd2 and the nuclear gene S18. (B) RNA was harvested to evaluate the relative expression of IFNλ1, IFNλ2/3 and Mx1 using q-RT-PCR. n ≥ 3 biological replicates. n.s.=not significant. P<0.05 *, P<0.01 **, P<0.001 ***, P <0.0001 **** as determined by Unpaired t test with Welch's correction.

Collectively, these data present compelling evidence supporting a model where activation of the IFN-signaling in confluent epithelial cells is mediated by mtDNA, probably leaked into the cytoplasm. In this model, mtDNAs is recognized by cGAS, leading to the activation of STING, which in turn phosphorylates TBK1, resulting in the induction of IFNλ3 expression and subsequent downstream signaling.

### 2.2.6. Cell density sensing through the Hippo pathway is a determinant for basal immune signaling in epithelial cells

The findings presented above demonstrate that mtDNA induces the cGAS-STING pathway and basal IFN-dependent immune response at high cell density, but not at low cell density. One possible explanation is that at high cell density, there is a higher abundance of mtDNA, which can potentially leak into the cytoplasm. However, I observed that total mtDNA abundance is slightly, yet significantly, higher in sparse cells compared to confluent cells (Fig. 40 A). This leads me to hypothesize that the activation of the cGAS-STING pathway or downstream signaling may be actively inhibited in cells at low density. Supporting this model, I observed that treating cells at low density with the STING agonist diABZ does not induce downstream IFN signaling (Fig. 38 A). This strongly suggests that a cellular factor at low confluency may inhibit STING signaling, and this factor's activity appears to depend on cellular density or other environmental cues.

The Hippo pathway is a crucial signaling cascade involved in regulating cell growth, proliferation, and tissue homeostasis by sensing various cellular environmental factors, including cell density, oxygen availability, and substrate stiffness. The key targets of the Hippo pathway are the transcriptional co-activators YAP and TAZ, which promote the expression of genes involved in cell proliferation and survival. When the Hippo pathway is active, YAP and TAZ are degraded and prevented from entering the nucleus to stimulate gene expression (Fig. 18). Conversely, when the pathway is inactive, YAP and TAZ can enter the nucleus and activate genes that promote cell growth and proliferation (Fig. 18). Interestingly, previous studies established a link between the Hippo pathway and IFN signaling, in which YAP/TAZ antagonize the innate antiviral response. Zhang et al. (*332*) demonstrated that at low cellular density, YAP/TAZ hijack TBK1, preventing its activation upon pathogen detection by the cells (Fig. 41 A). In contrast, they proved that at high density the Hippo pathway is activated, leading to the degradation of YAP/TAZ and facilitating unhindered TBK1 signaling upon pathogenic infection (Fig. 41 A) (*332*). Moreover, another study (*333*) demonstrated that YAP associates with IRF3 and represses its dimerization, thereby also inhibiting immune signal transduction. Whether the YAP/TAZ pathway can participate in regulating basal immune response in cells in sterile conditions has not investigated to date. Given the function of YAP/TAZ in repressing the immune response upon pathogen challenges, I aimed to investigate whether the YAP/TAZ-dependent inhibition of TBK1 or IRF3 also regulates the cell density-dependent induction of basal IFN-dependent signaling in the context of mtDNA-induced cGAS-STING signaling.

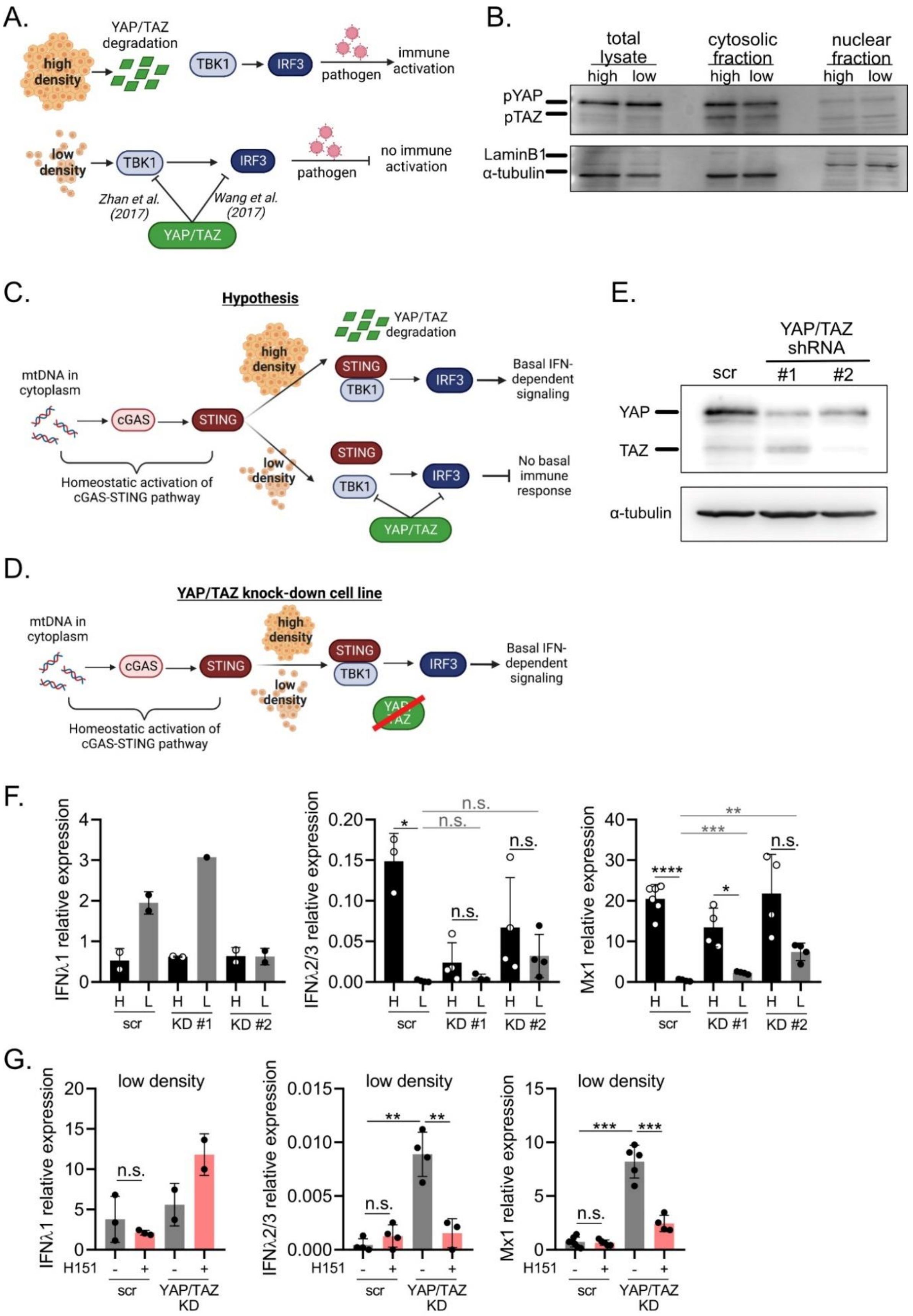

**Fig. 41. Cell density sensing through the Hippo pathway determines basal immune signaling in epithelial cells.** (A) YAP/TAZ (effector molecules of the Hippo pathway) are degraded in cells at high density, and accumulate in cells at low density. Studies by Zhang et al. (*332*) and Wang et al. (*333*) demonstrated that YAP/TAZ inhibit TBK1 and IRF3 activation during virus infection, thereby restricting

an efficient immune response in cells at low density. (B) T84 WT cells seeded at high and low density were collected, and cellular fractioning was done to assess phospho-YAP (pYAP) and phospho-TAZ (pTAZ) protein abundance in the total lysate, the cytosolic fraction or the nuclear fraction by Western Blot. α-tubulin served as a housekeeping protein for the cytosolic fraction, and Lamin B1 served as a housekeeping protein for the nuclear fraction. (C) I hypothesize that in T84 cells, mitochondrial DNA (mtDNA) leaked into the cytoplasm is always inducing a homeostatic activation of the cGAS-STING pathway. Cell density is sensed by the Hippo pathway. At low density, YAP/TAZ accumulate and inhibit the cGAS-STING-dependent immune activation. At high density, however, YAP and TAZ are degraded, allowing for STING to induce basal IFN expression and signaling. (D) A YAP/TAZ knock-down cell line would confirm the hypothesis in (C), as YAP/TAZ would be depleted at both high and low cell density. Without YAP/TAZ, STING-dependent activation of basal IFN-signaling would occur under both seeding conditions. (E) I created T84 cell lines with silenced YAP/TAZ using two shRNAs (#1 and #2). T84 scrambled control (scr), YAP/TAZ knock-down (KD) #1 and YAP/TAZ KD#2 cell protein extracts were collected to assess the YAP/TAZ abundance by Western Blot. α-tubulin served as a housekeeping protein. (F) T84 scrambled control (scr), YAP/TAZ KD #1 and YAP/TAZ KD#2 cells were seeded at high and low density, and treated with culturing media (to address basal signaling). 24 h post treatment, RNA was harvested to evaluate the relative expression of IFNλ1, IFNλ2/3 and Mx1 using q-RT-PCR. (G) T84 scrambled control (scr) and YAP/TAZ KD #1 cells seeded at low density where either mock-treated (culturing media) or treated with 20 µM STING-inhibitor H151. RNA was harvested to evaluate the relative expression of IFNλ1, IFNλ2/3 and Mx1 using q-RT-PCR. (F, G) $n \geq 3$ biological replicates, error bars indicate the standard deviation. n.s.=not significant. $P<0.05$ *, $P<0.01$ **, $P<0.001$ ***, $P<0.0001$ **** as determined by Unpaired t test with Welch's correction.

As cells reach confluency, the Hippo pathway is activated, leading to a kinase cascade that ultimately results in phosphorylation of cytoplasmic YAP/TAZ (Fig. 18). Phosphorylation of YAP/TAZ marks them for ubiquitination and subsequent proteasome-dependent degradation (*300*). To first address whether in my system YAP and TAZ proteins are regulated by confluence, I analyzed their phosphorylation at high and low density by Western Blot. Higher abundance of phosphorylated protein is noticeable in the cytosolic fraction of cells at high density as compared to cells at low density, which is particularly pronounced for phosphorylated TAZ (pTAZ) (Fig. 41 B). These results suggest that also in my system the Hippo pathway is activated at high density and induces phosphorylation and subsequent degradation of YAP/TAZ.

This allows me to hypothesize on a molecular working model in which sensing of the cellular environment leads to differential immune signaling under homeostatic sterile conditions. At steady state, leaked mtDNA activates the cGAS-STING pathway (Fig. 41 C). In confluent cells, when YAP/TAZ are being degraded due to density dependent activation of the Hippo pathway, STING induces phosphorylation and activation of TBK1. This leads to IRF3 dimerization and transcription of basal IFNλ3 (Fig. 41 C). However, at low density, cytoplasmic YAP/TAZ hijack TBK1 or IRF3, impeding their interaction with STING and downstream signaling (Fig. 41 C). To test this hypothesis, I decided to knock-down (KD) YAP and TAZ. If my hypothesis was true, in the T84 YAP/TAZ KD cell line I would expect that the homeostatic activation of the cGAS-STING pathway induces basal IFN expression in both, high and low density conditions, since YAP/TAZ are absent and cannot hijack TBK1 or IRF3 (Fig. 41 D). To generate the knock-down cell lines, two different shRNAs targeting YAP and TAZ were stably transduced into T84 cells. The Western Blot analysis revealed that shRNA #1 was more efficient in down-regulating YAP alone, while shRNA #2 efficiently silenced both, YAP and TAZ (Fig. 41 E).

T84 cells expressing control scrambled (scr) shRNA and T84 cells with knocked-down YAP/TAZ (KD) were cultured at both high and low cell densities. To investigate basal immune signaling activation, I examined the IFN and ISG Mx1 expression using RT-q-PCR. I found that YAP/TAZ silencing did not affect the transcript levels of IFNλ1 (Fig. 41 F, left panel), suggesting that IFNλ1 and the Hippo pathway do not interact. In the control scrambled shRNA cells, a significantly higher IFNλ2/3 and Mx1 expression was observed in confluent as compared to sparse cells (Fig. 41 F, right panels). However, these differential expression levels between cells at high and low density was less prominent for the YAP/TAZ KD cell lines (Fig. 41 F, right panels). Notably, the YAP/TAZ KD cells at low density displayed increased IFNλ2/3 expression and significantly higher Mx1 transcript levels as compared to the scrambled shRNA control cells under the same low-density conditions (Fig. 41 F, right panels). These results provide evidence that YAP/TAZ exert an inhibitory effect on IFN-dependent immune signaling when IECs grow at low density. To point out, the increased basal immune signature at low density was especially notable in knock-down cells expressing the shRNA #2, which efficiently silenced both YAP and TAZ (as confirmed by Western Blot analysis, Fig. 41 E). On the contrary, YAP/TAZ silencing by shRNA #1, which mostly down-regulated YAP, only induced a minimal increase of basal IFN-signaling. This suggests that mostly TAZ, and not YAP, is responsible for inhibiting basal immune signaling at low confluence.

To address whether the increase in basal immune signaling in the YAP/TAZ KD cells is dependent on cGAS-STING activation, T84 control scrambled (scr) shRNA cells and T84 YAP/TAZ KD cells (expressing the shRNA #2) were seeded at low cell density, and treated with the STING inhibitor H151. While the mock-treated YAP/TAZ KD cells displayed significantly higher IFNλ2/3 and Mx1 expression compared to the control scrambled shRNA cells, this enhanced immune response was effectively suppressed when STING was inactive (Fig. 41 G). These results further support an orchestrated regulation of cGAS-STING signaling by the Hippo pathway.

As a complementary approach, I overexpressed YAP and TAZ in T84 cells using various constructs, and efficiently generated one YAP and one TAZ over-expressing cell line (Fig. 42 A). If my hypothesis is correct, namely that YAP/TAZ sequesters TBK1/IRF3 thereby disrupting basal immune signaling (Fig. 41 C), efficient YAP/TAZ over-expression should inhibit basal IFN-dependent signaling at high density. However, cells over-expressing YAP or TAZ at high density did not show any reduction in basal IFNλ2/3 and ISG transcript abundance (Fig. 42 B). While these data do not support my model, it remains to be controlled whether the YAP and

TAZ proteins from the over-expressing constructs act in the same manner as endogenous YAP and TAZ proteins.

Finally, I adopted an indirect approach, focusing on how the cell translates its immediate microenvironment into signaling events. As epithelial cells reach confluence, they undergo changes in their transcriptional profile and physiology, including cell polarization and the formation of junctional complexes between neighboring cells. ZO1, a central scaffold protein involved in the efficient assembly of junctional complexes, plays a key role in signaling to the cell that confluence has been achieved. ZO1 activation induces the Hippo pathway and sequesters YAP/TAZ proteins to the junctional complexes, inhibiting YAP/TAZ signaling (*301*). Consequently, the absence of ZO1 would be expected to enhance YAP/TAZ activity. Interestingly, ZO1 knock-out significantly reduced basal ISG expression at high cell density compared to wild-type cells (Fig. 42 C). In fact, ZO1 knockout resulted in a decrease in ISG transcript levels at high density comparable to those observed at low density (Fig. 42 C). These results strongly suggest that formation of junctional complexes in confluent cells promote the IFN response by inhibiting YAP/TAZ, which normally act as a negative regulator of basal IFN expression. Moreover, it indirectly supports the notion that cell environment sensing regulates basal immune signaling.

My data using YAP/TAZ knock-down cell lines indicates that sensing the cellular environment through the Hippo pathway plays a significant role in modulating immune signaling. There are still inconsistencies in the results when analyzing basal immunity in the YAP/TAZ overexpression cell lines, and further efforts are required to fully confirm the interaction between the Hippo pathway and basal IFN expression in epithelial cells. However, based on my data, I suggest the following working model: At low cell density, YAP/TAZ proteins act to inhibit the homeostatic activation of the cGAS-STING pathway. Importantly, the results suggest that TAZ, rather than YAP, predominantly mediate the inhibitory effect. Conversely, as cells reach confluence, the Hippo pathway is activated, partially through YAP/TAZ sequestration by the junction complexes. This leads to the cytosolic degradation of YAP/TAZ, thereby facilitating cGAS-STING-dependent activation of IFN signaling. My findings highlight the critical role of cellular density as a determinant for basal sterile immune response.

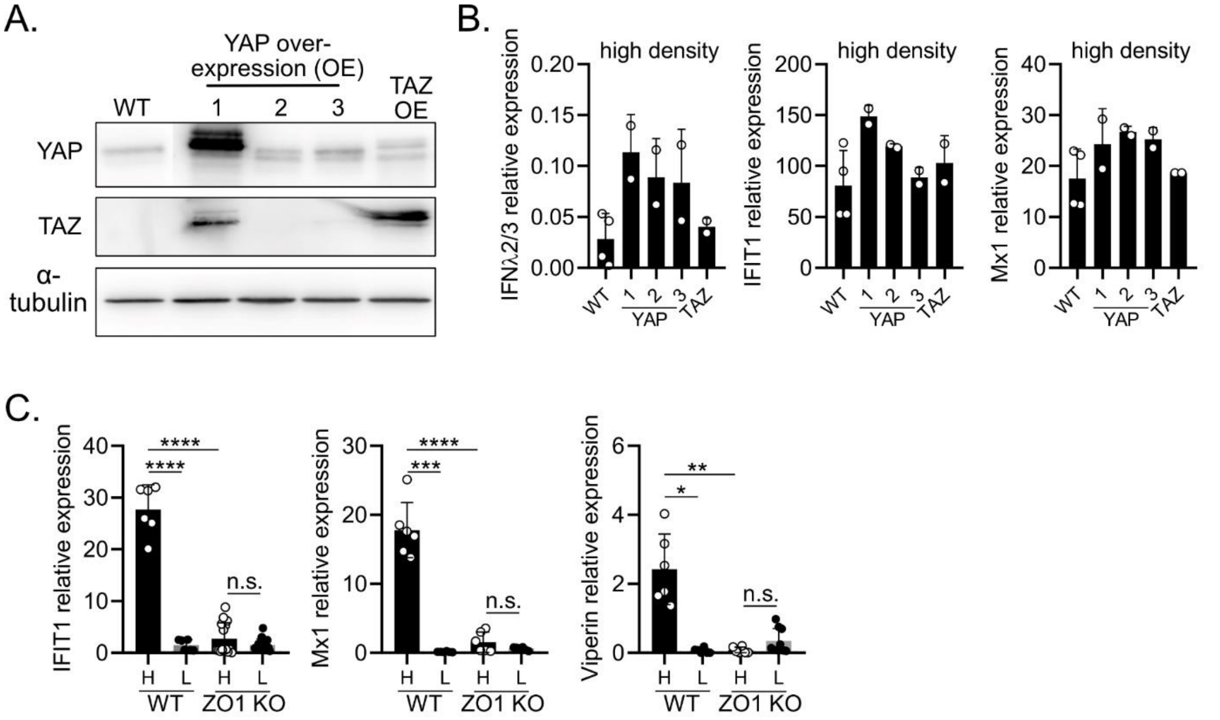

**Fig. 42. Depletion of ZO1, but not over-expression of YAP/TAZ, ablates basal IFN-dependent signaling at high density.** (A) T84 cell lines over-expressing YAP and TAZ were created by transduction of plasmids encoding for YAP/TAZ proteins. Proteins were harvested from T84 WT, YAP over-expressing (OE) and TAZ OE cell lines to assess the YAP/TAZ abundance by Western Blot. α-tubulin served as a housekeeping protein. (B) T84 WT, YAP OE and TAZ OE cell lines were seeded at high density and treated with culturing media (to address basal signaling). 24 h post treatment, RNA was harvested to evaluate the relative expression of IFNλ2/3, IFIT1 and Mx1 using q-RT-PCR. n ≥ 2 biological replicates. (C) T84 WT and ZO1 knock-out (KO) cells were seeded at high and low density, and treated with culturing media (to address basal signaling). 24 h post treatment, RNA was harvested to evaluate the relative expression of the ISGs IFIT1, Mx1 and Viperin using q-RT-PCR. n ≥ 3 biological replicates, error bars indicate the standard deviation. n.s.=not significant. P<0.05 *, P<0.01 **, P<0.001 ***, P <0.0001 **** as determined by Unpaired t test with Welch's correction.

### 2.2.7. Basal IFN-dependent signaling is also regulated by density in primary intestinal organoids

To address whether primary human IECs also exhibit a basal immune response dependent on their cellular environment, my colleague Zina Maria Uckeley seeded human ileum-derived organoids in two-dimensions at various cell densities. 2 days post seeding, I assigned to each well a density level ranging from 1 to 4 (Fig. 43 A). At density level 1, cells were sparsely seeded in 2D, resembling T84 cells at low density. To point out here, growing gut-derived organoids sparsely proved challenging, resulting in fewer replicates for this density level. As the density level increased, the cells grew more confluent, eventually leading to the development of 3D dome structures at level 4 due to the limited space available for monolayer expansion. Basal IFN-dependent signaling was assessed by IFN and ISG expression using RT-q-PCR. Similarly to results in T84 and other epithelial cell lines, confluency is positively correlated with IFNλ2/3 and ISG expression (Fig. 43 B). Of note, IFNλ1 transcript levels also increased with gut-derived organoid cell density (Fig. 43 B). This was not observed in the T84 cell line, in which confluence specifically induced IFNλ3 transcription (Fig. 36 C).

To use a more physiological model resembling *in vivo* conditions, ileum-derived organoids were cultured in 3D, allowing the development of crypt-villi structures. Zina Maria Uckeley seeded human ileum- and colon-derived organoids in matrigel at a 'low density', forming initial clusters of 1-4 cells. Over the course of 10 days after seeding, the organoids grew as 3D structures, gradually increasing in size, cell number, and cell density. I assessed the basal immune signaling by RT-q-PCR over that period, and observed that IFN and ISG transcription significantly increased as organoids grew (Fig. 43 C). Together, the ileum-derived organoid data revealed that, also in a more physiological model, basal IFN-signaling depends on the cellular microenvironment. It remains to be understood what role IFNλ1 plays in organoid density-dependent immune response.

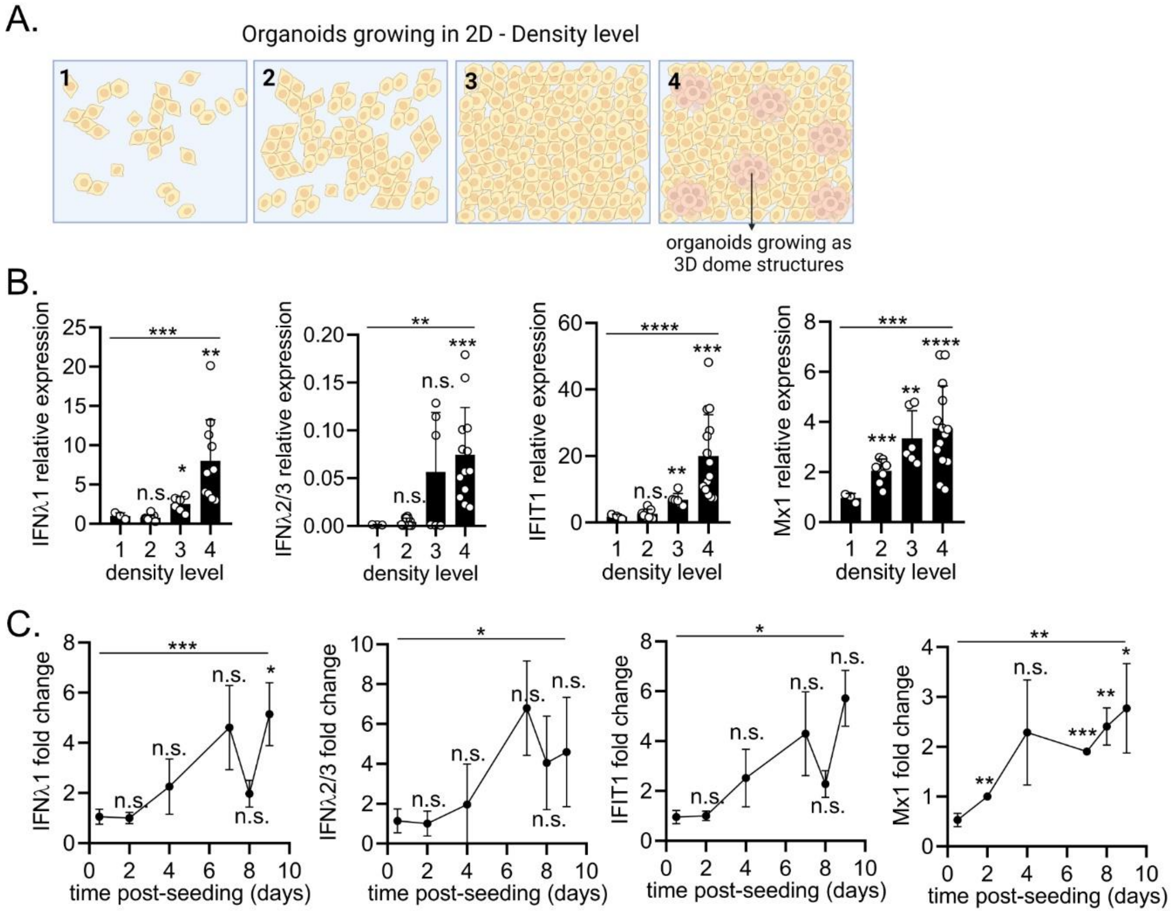

**Fig. 43. Density-dependent basal IFN expression in human-derived gut organoids.** (A, B) Ileum-derived organoids were grown in 2-dimensions (2D) at increasing cellular density, ranging from level 1-4. (A) Schematic depicting the 2D organoid seeding at different density levels. At density level 3, the organoids form a uniform monolayer of cells. At density level 4, organoids form a monolayer with regions at which cells form 3-dimensions (3D) dome structures. (B) Cells were treated with culturing media (to address basal signaling), and 24 h post treatment RNA was harvested to evaluate the relative expression of IFNλ1, IFNλ2/3, IFIT1 and Mx1 using q-RT-PCR. (C) Ileum-derived organoids were seeded in matrigel as single cells or cells clustered in small groups (2-4 cells). Cells were cultured over a period of 10 days, allowing for organoids to grow into 3D structures, eventually forming crypt-villi

structures. RNA was collected along the time-course to evaluate the relative expression of IFNλ1, IFNλ2/3, IFIT1 and Mx1 using q-RT-PCR. (B, C) n ≥ 3 biological replicates, error bars indicate the standard deviation. n.s.=not significant. $P<0.05$ *, $P<0.01$ **, $P<0.001$ ***, $P<0.0001$ **** as determined by ordinary one-way ANOVA. For (B) a Dunnett's multiple comparison test was done additionally, using density level 1 as reference.

The results of this project provide valuable insights into how the population context and the cellular environment regulate basal immune signaling in epithelial cells. The data reveal that confluency leads to IFNλ3 transcription and downstream ISG expression in various human epithelial cell lines lining mucosal surfaces. Moreover, human gut-derived organoids cultured in 2D and 3D also exhibited a density-dependent increase in IFN-dependent signaling, which demonstrates the physiological relevance of this basal IFN expression. Interestingly, under homeostatic conditions, the cGAS-STING pathway appears to be activated by leaked mtDNA into the cytoplasm, thereby mediating the density-dependent immune response. Remarkably, the Hippo pathway emerges as the link between IFN signaling and the cellular environment, particularly through its regulation of YAP/TAZ. At low density, YAP/TAZ inhibit homeostatic STING signaling, while at high density, activation of the Hippo pathway leads to YAP/TAZ degradation, enabling STING to trigger the IFN-dependent response. Additional experiments are necessary to fully demonstrate that YAP/TAZ or another molecular factor inhibit basal immune signaling in low density cells. Collectively, these findings highlight the role of cellular density as a crucial factor governing basal immune signaling in epithelial cells, which may have implications for understanding tissue homeostasis and host defense mechanisms.

## 2.3. Spatial heterogeneity during virus infection in epithelial cells

### 2.3.1. Efficient virus replication is restricted to the edges of epithelial cell populations

The cell localization within a population has notable effects on basal immune signaling (Results 2.2.) and on response to IFNs (Results 2.1.) in epithelial cells. Moreover, previous research has highlighted the substantial influence of the cell population context on endocytic events and virus infection (*324*). Therefore, the goal of this project is to investigate and characterize whether the population context impacts virus infection of epithelial cells.

As described in 2.1 and 2.2 of my result sections, in order to create a diverse array of cellular micro-environments and position cells in different population context, the intestinal epithelial T84 cells were seeded at varying densities, ranging from sparsely distributed (25,000 cells/cm$^2$) to highly confluent (260,000 cells/cm$^2$). Cells were then infected with virus for 24 h, and harvested to assess infection levels by immunofluorescence staining or by RT-q-PCR detecting viral genome. Cells grown at low density were more permissive to MRV infection as compared to denser seeded cells, while in confluent cells almost no infection could be detected (Fig. 44 A). Quantification of MRV infected cells (Fig. 44 B) and MRV genome (Fig. 44 C) exhibited a negative correlation between virus infection and cellular density. Indeed, at higher cell density (160,000 and 260,000 cells/cm$^2$) no significant increase in infection was observed as compared to mock infection. The same results were observed for Human Astrovirus (HAstV) infection (Fig. P3-F1 D-E), reinforcing that this observation is not exclusive to MRV and holds true for other viral infections.

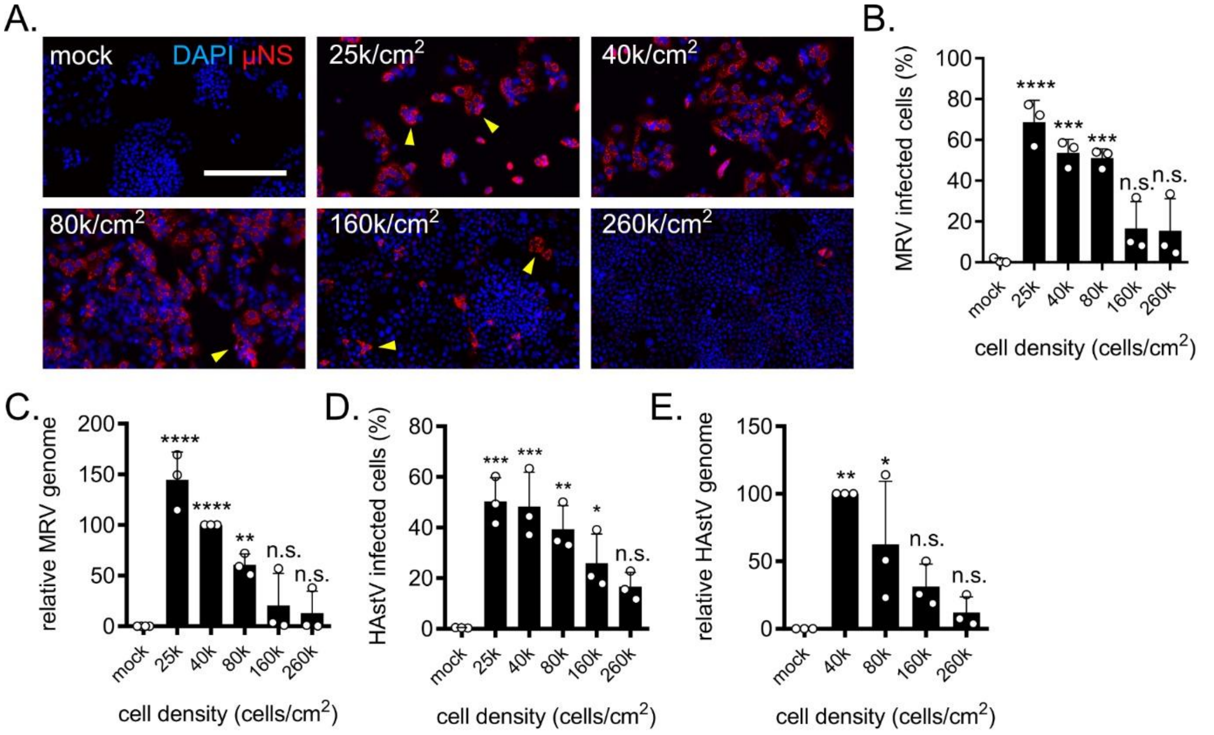

**Fig. 44. T84 cell density negatively correlates with virus infection.** T84 WT were seeded at increasing cell density and infected with (A-C) Mammalian Reovirus (MRV) and (D, E) Human Astrovirus (HAstV). (A, B, D) 16 hpi, cells were fixed and indirect immunofluorescence was performed against viral proteins. (A) Representative images showing MRV infection (antibody directed against µNS protein, in red) in cells seeded at different densities. Nuclei were stained with DAPI (blue). Scale bar=100 µm. Yellow arrows point at infection occurring in sparse cells and cells at the edges of colonies. (B, D) Using images from the immunofluorescence staining, the number of infected cells at the different seeding conditions were quantified for (B) MRV and (D) HAstV. (C, E)16 hpi, RNA was harvested to evaluate the relative (C) MRV and (E) HAstV genome expression using q-RT-PCR. (B-E) n = 3 biological replicates. n.s.=not significant, error bars indicate the standard deviation. $P<0.05$ *, $P<0.01$ **, $P<0.001$ ***, $P <0.0001$ **** as determined by Ordinary one-way ANOVA with Dunnett’s multiple comparison test, using mock-infected cells as reference.

When analyzing the spatial distribution of infected cells, I noticed that mostly single cells or cells at the edges of colonies were permissive for MRV (Fig. 44 A, yellow arrows), while cells embedded in a confluent monolayer remained uninfected. To better understand the spatial heterogeneity during virus infection, I used the micropatterning approach (refer to Annex section 5.1 for detailed description of the method), which allowed me to create standardized epithelial cell populations with a defined edge and center. T84 cells were seeded on micropatterned glass, and infected with different viruses for 16 h before immunostaining and imaging by fluorescence microscopy. Infection with the enteric viruses MRV and HAstV, the airway pathogen SARS-CoV-2 and the arbovirus Germinston virus (GERV), lead to a strongly heterogeneous distribution of infected cells, with the edge being significantly more infected than the center of the cell population (Fig. 45 A).

To quantify the location of the infected cells in a standardized manner, I established an analysis pipeline using CellProfiler 3.1.9 (Fig. 45 B). First, using the DAPI signal, unique masks were created for each population to segregate them into an edge and a center area. This pipeline then measured the integrated intensity at both the edge and the center of each cell population. Subsequently, the integrated intensities at the edge and center were normalized first to the total intensity and then to the occupied area. The resulting outcome is represented as infection values at the edge and center, relative to each other. When infection levels are comparable at the edge and center, the relative infection value will be close to 1. Conversely, if there are differences between edge and center, the values will deviate from 1. If a point is above 1, it means that the infection is higher as compared the corresponding counterpart region of the population (edge/center from the same population), and if a point is below 1 it indicates that the infection is lower as compared to the corresponding counterpart region (edge/center from the same population) (Fig. 45 B).

The differential distribution of virus infection between edge and center were quantified for infection with various viruses (Fig. 45 C). As expected, mock treated T84 cell populations did not show a differential distribution of fluorescent signal and values were close to 1. For all tested viruses, edge cells of a T84 population were more infected than center cells. To test these findings in other epithelial cell types, intestinal epithelial CaCo2 and airway epithelial Calu3 cells were seeded on micropatterned glass and similarly infected with different viruses for 16 h. Both in CaCo2 (Fig. 45 D) and Calu3 (Fig. 45 E) populations, infection was enriched in edge cells. Altogether, I observed a heterogeneous distribution of virus infection within epithelial cell populations, in which the edge cells are more infected than the center.

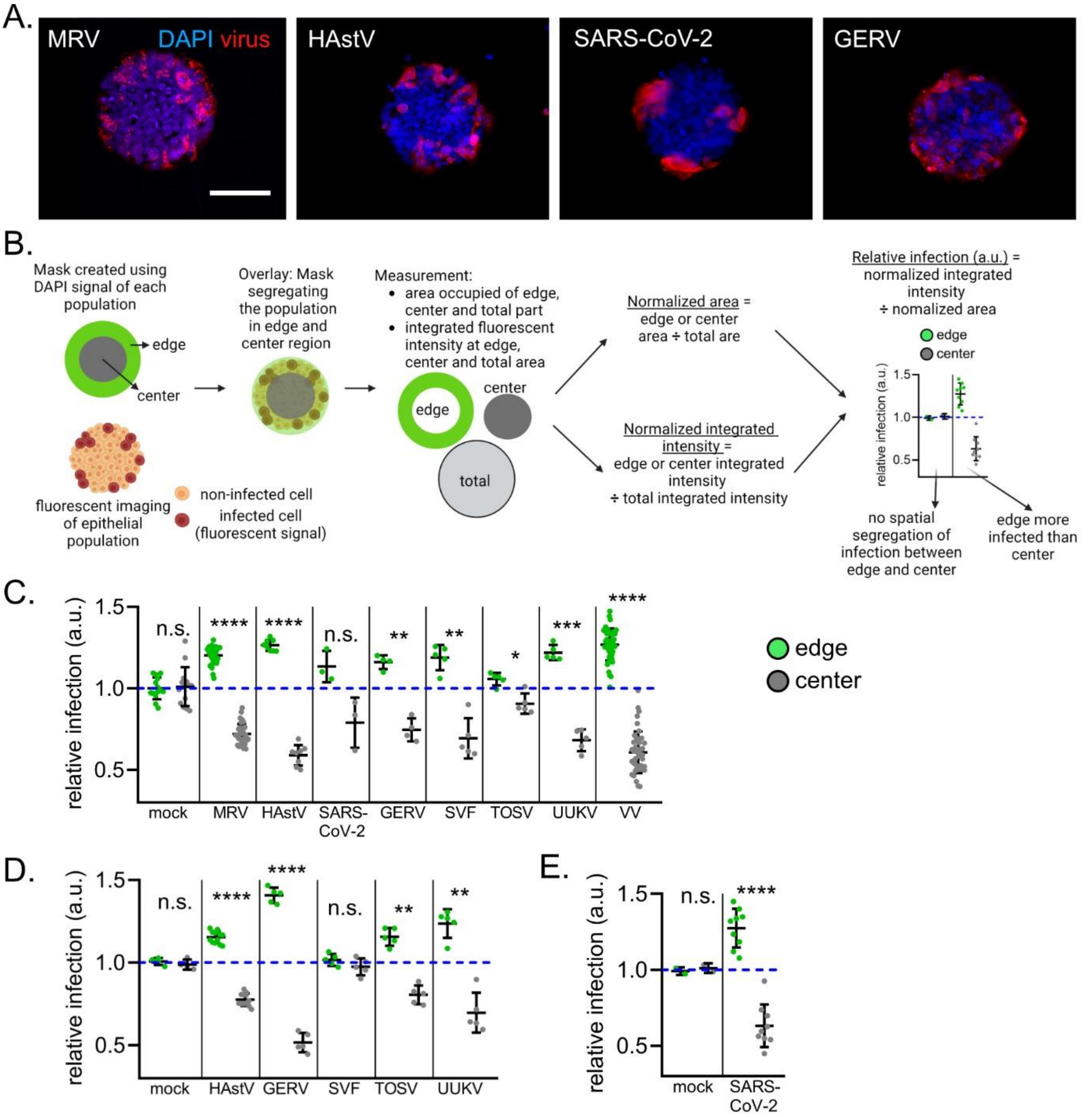

**Fig. 45. During apical infection, edge cells in epithelial populations are more infected than center cells.** Epithelial cells were grown as populations on micropatterned glass and infected from the apical side with a variety of viruses. 16 hpi, cells were fixed and indirect immunofluorescence was performed against viral proteins to visualize location of virus infection. (A) Representative images showing virus infected T84 cell populations. Virus is in red and nuclei were stained with DAPI (blue). Scale bar=100 µm. (B) An analysis pipeline was developed to measure the spatial segregation of virus infection in epithelial cell populations. Schematic depicts how the 'relative infection' at the edge and the center of a population were calculated. (C-E) Quantification of the relative infection levels at the edge and center of (C) T84, (D) CaCo2 and (E) Calu3 populations infected with a palette of viruses. n ≥ 3 biological replicates, error bars indicate the standard deviation. n.s.=not significant. $P<0.05$ *, $P<0.01$ **, $P<0.001$ ***, $P<0.0001$ **** as determined by Paired t test. Abbreviations: Mammalian Reovirs (MRV), Human Astrovirus (HAstV), Severe acute respiratory syndrome coronavirus type 2 (SARS-CoV-2), Germinston Virus (GERV), Semliki Forest Virus (SFV), Toscana Virus (TOSV), Uukuniemi Virus (UUKV), Vaccinia virus (VV).

Seeding on glass or plastic exposes only the apical side of the cells to the cell culture medium, while the basal side remains inaccessible in contact with the plastic or glass vessel surface (Fig. 46 A, left). Therefore, in my experimental setup, when epithelial cells grow at different densities or as defined populations on glass/plastic, the center cells of a cluster will only encounter the virus from the apical side. This is problematic, especially considering that epithelial cells polarize upon interaction with other cells, leading to distinct apical or basolateral membrane compositions. As such, it is possible that virus endocytosis in epithelial tissues is preferred from the basolateral side. The lack of access to the basolateral side could therefore result in the observed heterogeneous infection pattern (Fig. 44 and Fig. 45). To challenge this model and gain accessibility to the basal side, I utilized the transwell system, where cells are grown on a semipermeable membrane allowing them to be treated from both the apical and basal sides (Fig. 46 A, right). T84 WT cells were seeded at increasing densities on transwell membrane inserts, and infected simultaneously from both sides with different viruses for 16 h. Quantification of MRV infected cell numbers by immunostaining and virus genome by RT-q-PCR revealed a negative correlation between cell density and MRV infection (Fig. 46 B), as similar to apical infection (Fig. 44). To test whether simultaneous apical and basolateral infection was also restricted to the edges, accounting for the negative correlation between infection and density, T84 cells were grown as populations on micropatterned transwell inserts. Infection from both sides with several unrelated viruses, specifically MRV, HAtsV, Rotavirus, SARS-CoV-2, GERV and Vaccinia virus (VV), resulted in significantly higher relative infection levels at the edge as compared to the center of the population (Fig. 46 C-D). These results indicate that virus replication is only supported by the edge cells of a cellular colony. Importantly, the infection pattern in epithelial populations is heterogeneous regardless of the side of infection (apical or basal infection), ruling out that the apical area of the cell restricts virus infection.

My experiments clearly demonstrate that center cells in a population are not permissive for virus infection, and therefore possess a different molecular phenotype than permissive edge cells. To test whether center cells can behave as edge cells if they change their location, I used a Picosecond Laser Detachment Assay in collaboration with the Motomu Tanaka Research Group (Institute for Physical Chemistry, Heidelberg University). This method allowed me to create a new edge in the center of a T84 population. Briefly, a picosecond laser pulse was led through an inverted microscope into the culture medium (Fig. 47 A). The laser pulse induced a shock wave which detached the cells in a controlled manner, leading to a new edge where before an intact monolayer was growing (Fig. 47 B, yellow dotted line). Following the creation of the new edge in the center of the population, T84 cells were immediately infected with HAstV for 16 h, and the infection was analyzed by immunofluorescence microscopy. Surprisingly, cells situated at the newly formed edge were also infected with the virus, showing similar behavior to the outer edge cells (Fig. 47 C). In contrast, cells embedded within the intact monolayer exhibited minimal infection levels. These results indicate that as soon as cells localize to the edge of a colony, they become susceptible to viral infection.

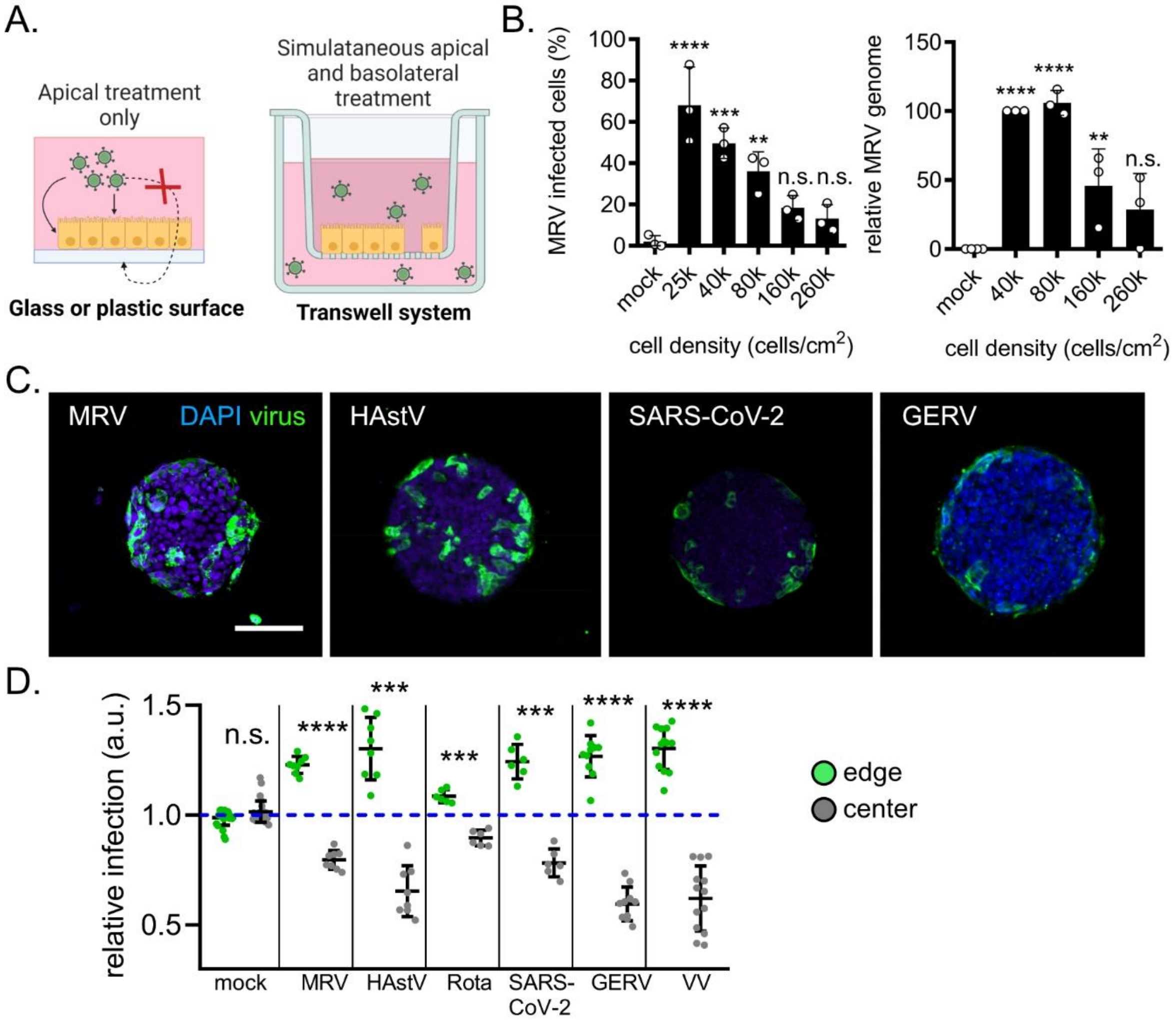

**Fig. 46. Virus mostly localizes to edge cells of epithelial populations during simultaneous apical and basolateral infection.** (A) When epithelial cells are seeded on glass or plastic surfaces, only the apical side faces the infection media while the basolateral side of the cell is not accessible. To gain accessibility to the basolateral side, cells are seeded on semipermeable membranes of transwell inserts. (B) T84 cells seeded at increasing density on transwell inserts were infected with MRV. 16 hpi, indirect immunofluorescence was performed against µNS protein and the percentage of infected cells was quantified. (C, D) T84 cells were grown as populations on micropatterned transwells and infected simultaneously from the apical and basolateral side with a variety of viruses. 16 hpi, cells were fixed and indirect immunofluorescence was performed against viral proteins to visualize location of virus infection. (C) Representative images showing virus infected T84 cell populations. Virus is in green and nuclei were stained with DAPI (blue). Scale bar=100 µm. (D) Quantification of the relative infection levels at the edge and center of populations infected with a palette of viruses. n ≥ 3 biological replicates, error bars indicate the standard deviation. n.s.=not significant. $P<0.05$ *, $P<0.01$ **, $P<0.001$ ***, $P<0.0001$ **** as determined by (B) Ordinary one-way ANOVA with Dunnett's multiple comparison test using mock-infected cells as reference, and (D) Paired t test.

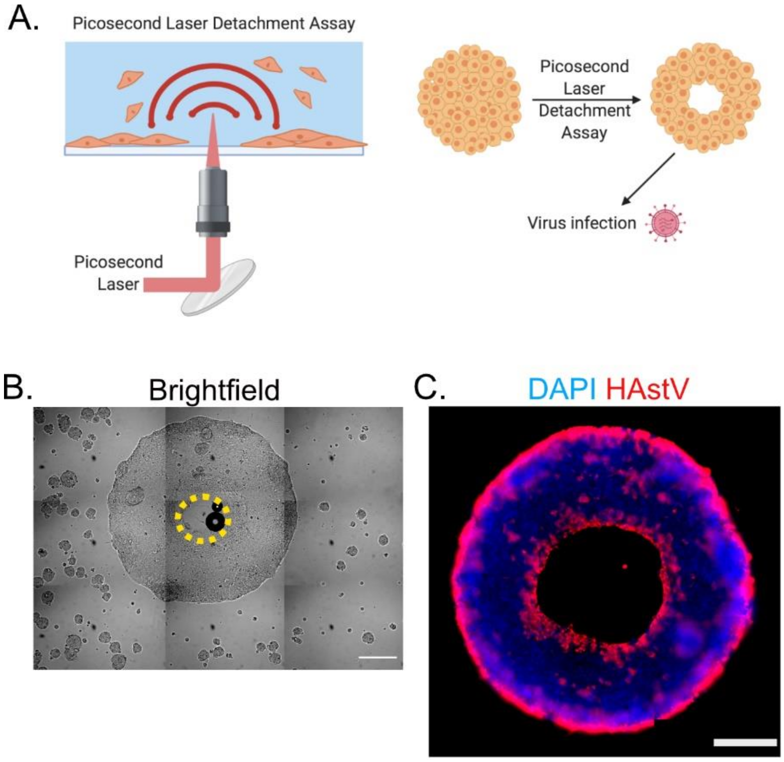

**Fig. 47. Creation of a new edge in the center and virus infection.** T84 cells were seeded on 1000 µm diameter micropatterns on glass. To create a new edge in the center of a population the Picosecond Laser Detachment Assay was used. A picosecond laser pulse was led through an inverted microscope which induced a shock wave. The shock wave detached cells in a controlled manner positioning center cells at a new edge within second. Immediately, cells were infected with Human Astrovirus (HAstV) fors 16 h. Infection was visualized by immufluorescent staining against the viral protein. (A) Schematic of the Picosecond Laser Detachment Assay and the subsequent infection. (B) Representative brightfield image showing the micropattern after the Picosecond Laser Detachment Assay. Yellow dotted line marks the new edge in the population center. Scale bar=200 µm. (C) Representative images showing HAstV infection (red) after creation of the new edge. Nuclei were stained with DAPI (blue). Scale bar=200 µm.

### 2.3.2. Virus binding is enriched at the edges and the basal side of epithelial cell populations

Center cells of populations are less infected than edge cells (Fig. 44 to Fig. 47). Many viral factors or cellular mechanisms playing a role along the viral infection cycle can lead to this spatial heterogeneity. The first event in the viral infection cycle is virus binding to the cellular membrane and subsequent endocytosis of the viral particle. To address whether these initial events are different between edge and center cells in a population, consequently leading to the spatial heterogeneity of infection levels, I adjusted a previously described binding and endocytosis assay protocols (*334*, *335*) to cells seeded on micropatterned surfaces. For this I used GERV particles labeled with a fluorescent dye in conditions that do not significantly impair their infectivity (kindly provided by Zina Maria Uckeley from the Pierre-Yves Lozach Group, University Hospital Heidelberg)

To monitor the efficacy of virus binding, fluorescently labeled GERV particles were incubated with cells seeded on micropatterns for 1.5 h at 4°C (Fig. 48 A i). This temperature allows virus particles to interact with cellular receptors and membrane components without undergoing internalization. Bound particles were then visualized by fluorescence microscopy. Similarly, in order to study virus endocytosis, fluorescently labeled GERV particles were initially incubated with cells on micropatterns at 4°C for 1 h to promote binding. Unattached particles were subsequently removed through washing, and endocytosis was enabled by incubating cells for 1 h at 37°C (Fig. 48 A ii). To differentiate between surface bound and internalized particles, samples were treated with trypan blue before imaging. Trypan blue quenches Atto488 from particles attached to the cell membrane, but does not affect already internalized GERV-Atto488 particles (*4*). I did Z-stack imaging using high resolution spinning disc microscopy (Fig. 48 B). This allowed me to determine not only the spatial distribution of particles within the population (edge and center), but also to see whether virus particles localize preferentially to the apical or basal membrane of cells. The apical view is a Z-project of the Z-stack and visualizes the localization of the viral particles across the population (*i.e.*, XY-axis, edge vs. center). The side view visualizes the particle localization across the Z-axis (apical-basal axis).

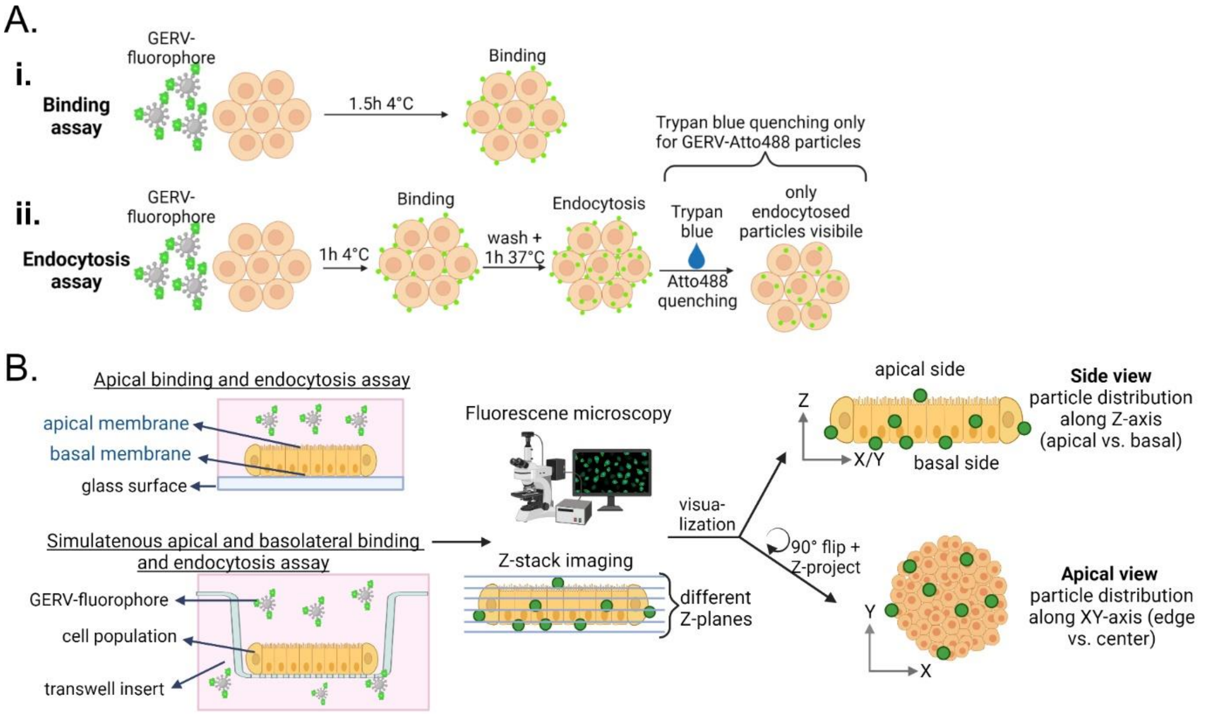

**Fig. 48. Virus binding and endocytosis assay.** (A) Schematic of the (i) binding and (ii) endocytosis assay using Germinston virus (GERV) particles coupled to a fluorophore. (B) Schematic of the binding and endocytosis assay performed on cell population seeded on glass (only apical treatment) or transwell inserts (simultaneous apical and basal treatment). Confocal fluorescence imaging was performed by recording different Z-planes to analyze the virus particle distribution along the apical-basal Z-axis (apical view) and the edge-center XY-axis (side view).

To address how the virus interacts with the apical membrane of cells, I performed the binding assay on T84 cells seeded on glass micropatterns. The apical view revealed that GERV-Atto488 particles were mostly bound to the edges of the epithelial cell population (Fig. 49 A, yellow arrows), suggesting that virus particles did not bind cells efficiently from their apical membrane (in the center of a population). Enrichment of bound particles to the edge is in agreement with the significantly higher levels of virus infection at the edge as compared to the center of a population (Fig. 44 and Fig. 45).

To test if the viruses can bind and enter the cell from the basal membrane, GERV-Atto647 binding and endocytosis was assessed on T84 populations seeded on micro patterned transwells (Fig. 49 B). The side view supported that virus particles were not able to bind center cells in a population from the apical side (side view). Surprisingly, GERV-Atto647 particles did attach to the basal membrane of center cells (side view, yellow arrows). These results visualize a heterogeneous enrichment of virus along the apical-basal cell axis. I then determined the spatial distribution of bound and endocytosed particles throughout the XY-axis of the population using the apical view. Interestingly, viral particles were distributed across the entire population independent of the cell localization, with an enriched amount of particles at the edges (apical view).

When using GERV-Atto647 it is difficult to discern between bound or endocytosed particles. Therefore, I repeated the assays on T84 cell populations seeded on micropatterned transwells using GERV-Atto488 and trypan blue treatment to quench bound but not endocytosed particles (Fig. 49 C). Similar to results using GERV-Atto647, GERV-Atto488 particles were mostly bound to the basal membrane of the population (side view, yellow arrows). Moreover, the endocytosis assay using trypan blue treatment made clear that viral particles were also endocytosed by the cells (side view, yellow arrows). The apical view supported that bound and endocytosed particles were homogeneously distributed within the population, without any noticeable segregation at the edge or the center region.

Altogether, I showed that virus particles are capable of attaching to all cells within a cell population. However, virus binding occurs predominantly from the basal side or the population's edges, with minimal occurrences from the apical side. Additionally, I demonstrated that basally bound particles are efficiently endocytosed by the cell.

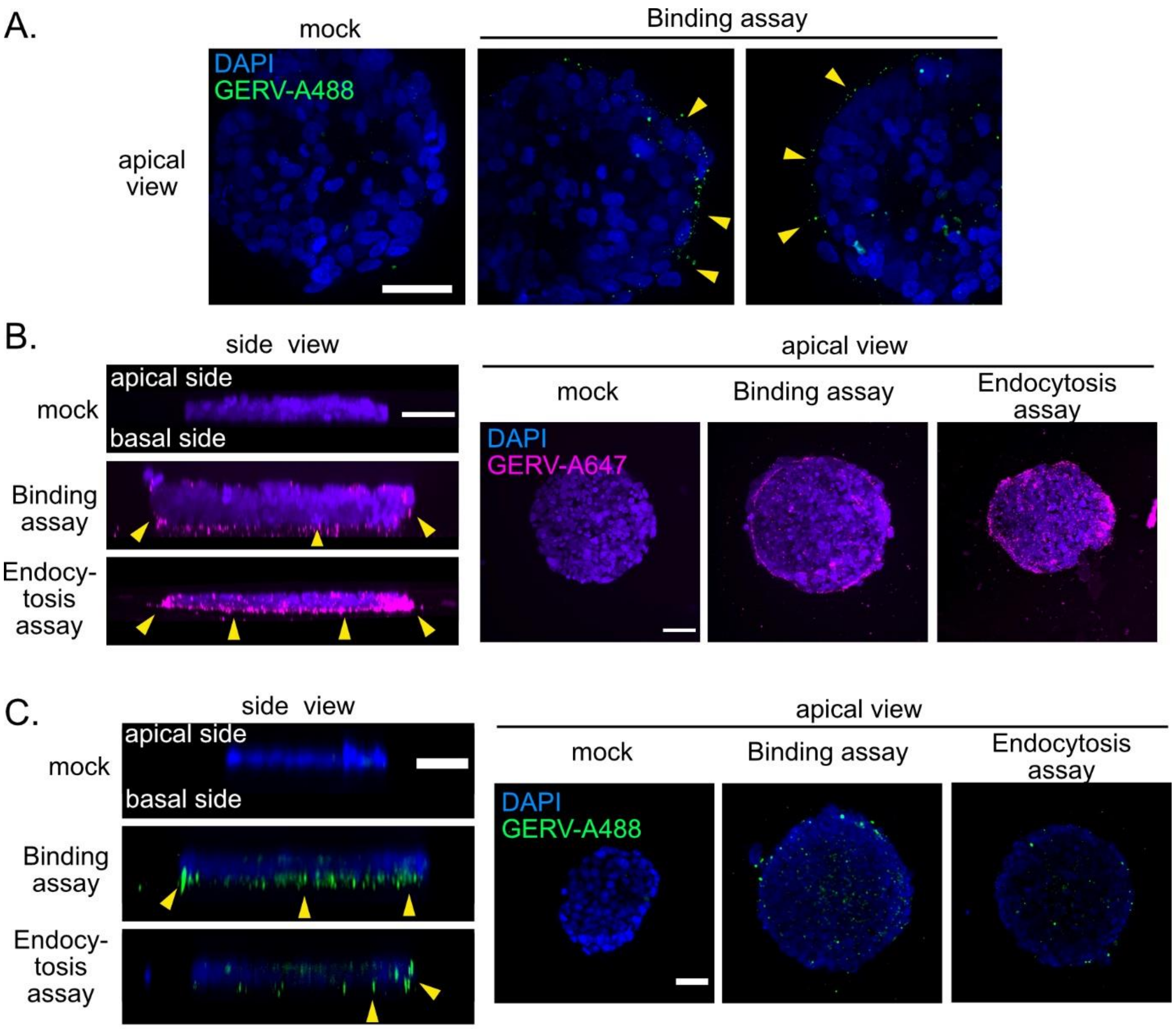

**Fig. 49. Virus binding is enriched at the edges and the basal side of epithelial populations.** T84 cells were grown as populations on micropatterned glass or transwell inserts. Cell populations underwent binding and endocytosis assays, and the virus particle location was analyzed by spinning disc fluorescence microscopy. Representative images of cell populations seeded on (A) glass or (B, C) transwell inserts that underwent the binding and endocytosis assay. The assays were performed with (A, C) GERV-Atto488 (green) or (B) GERV-Atto647 (magenta) virus particles. Nuclei were stained with DAPI (blue). Scale bar=50µm. Yellow arrows signalize virus particle localization to the edge cells of populations, or the basal side of cells.

To address whether this basolateral favored endocytosis of virus particles is specific to viruses or if it is also occurring to other cargo, I monitored clathrin-mediated endocytosis (CME) at the apical and basal membrane of epithelial cells. During CME, all molecular players subsequently assemble at the membrane, inducing membrane bending and the formation of clathrin-coated pits loaded with cargo (*336*). Clathrin-coated pits then internalize and detach from the membrane, to be transported as vesicles inside the cell (*336*). To visualize CME at cellular membranes, I used cells stably expressing σ2 linked to GFP (σ2-GFP). σ2 is one of the four subunits forming the multimeric adaptor protein 2 (AP2), which localizes to clathrin-coated pits and acts at cell membranes to internalize cargo during CME (*336*). Fluorescence microscopy images revealed that σ2 was only localized at discrete positions (dots) at the basal membrane and not to the apical membrane in T84 cells seeded as colonies on glass (Fig. 50 A). Moreover, immunostaining of clathrin-heavy chain (CHC) showed formation of small pits mostly at the basal side of T84 cell populations (Fig. 50 B, yellow arrows). Also CaCo2 σ2-GFP cells seeded as population on micropatterned glass formed clathrin-coated pits at the basal but not the apical membrane (Fig. 50 C). Carmon Kee generated ileum-derived organoids stably transduced with σ2-GFP and seeded them in matrigel as 3D structures, in which the apical side of the cells faces inwards and the basal side faces outwards in direct contact with medium (Fig. 50 D, DIC channel). I imaged the organoids and, similar to what I observed in the cell lines, clathrin-coated pits (marked by discrete localization of σ2-GFP) were enriched at the basolateral membrane of the cells (Fig. 50 D, yellow arrows), while at the apical few to no pits could be seen.

Together, this data suggests that CME is occurring more frequently at the basal side of a polarized epithelial cell as compared to the apical side. This can impact virus infection. Importantly, more experiments and functional assays are required to fully support this observation, and to test whether this is true for other cellular endocytic mechanisms.

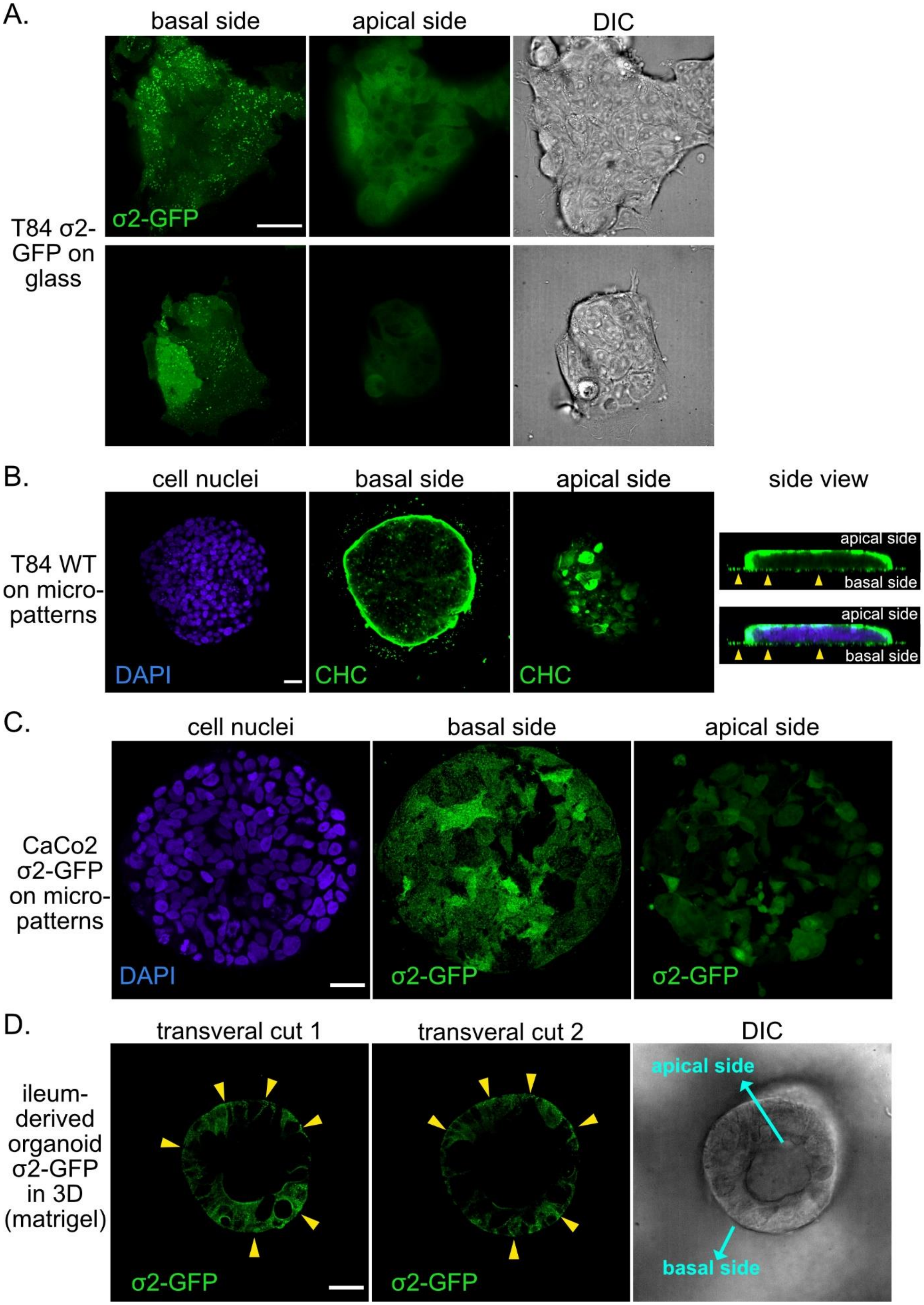

**Fig. 50. Clathrin-mediated endocytosis (CME) occurs more frequently at the basal membrane of T84 cells.** (A-C) Visualization of clathrin-coated pits at membranes: cells seeded as colonies and either (A, C) expressing σ2 linked to GFP (σ2-GFP), or (B) immunostained for clathrin-heavy-chain (CHC), were imaged using spinning disc microscopy. Only the apical or basal membrane was imaged. Representative images of (A) T84 σ2-GFP (green) seeded on glass as colonies, (B) T84 WT cells

seeded on micropatterned transwell inserts as populations and immunostained for CHC (green), and (C) CaCo2 σ2-GFP (green) seeded on micropatterned glass as populations. Nuclei were stained with DAPI (blue). Scale bar=30 µm. (D) Human ileum-derived organoids expressing σ2 linked to GFP (σ2-GFP) were seeded as 3D structures in matrigel and imaged using spinning disk microscopy. Representative images of a Z plane with σ2-GFP in green. The brightfield visualizes the outline of the organoids. Scale bar=30 µm. (A-D) Yellow arrows point to the basal localization of clathin-coated pits.

### 2.3.3. Polyamines and virus infection in epithelial populations

My results support that virus binding in epithelial cell populations occurs mostly from the basolateral side, with few to no binding taking place at the apical side. A study by Kicmal et al. (*337*) demonstrated that polyamine depletion reduced the attachment of various RNA viruses to the cell. Interestingly, when I characterized the epithelial cell populations seeded on micropatterns, spatial metabolomics data revealed that the polyamines spermine and analogues were enriched at the edges while being almost absent in the center (Fig. 69 B). As a result, it is plausible that viruses cannot attach to the apical side of center cells in a population because they lack polyamines.

To examine whether adding exogenous polyamines will allow for virus binding in the center of a population and subsequent efficient infection, T84 populations seeded on micropatterned glass were mock-treated or treated for 16 h with polyamines (PA). Cells were then infected with MRV for 16 h in presence or absence of PA, and localization of infected cells was assessed by immunofluorescence staining. Polyamine treated populations showed no difference compared to non-treated infected cell populations, with MRV infection occurring mostly at the edges (Fig. 51 A). Concluding, such increasing polyamines concentrations do not render cells located in the center of a population more susceptible to virus infection.

In a complementary experiment, to investigate how reduced polyamine presence in edge cells impacts virus infection, T84 cell populations were treated with Difluoromethylornithine (DFMO) followed by infection with MRV. DFMO is an irreversible inhibitor of ornithine decarboxylase, an enzyme catalyzing the primary step in polyamine biosynthesis (*338*). Fluorescence imaging showed an unusual morphology of T84 cell populations for mock treated, MRV infected and DFMO treated samples (Fig. 51 B). The populations did not form a tight monolayer in the center, but several areas within the population had no cells grown on them, thereby forming holes and new edges (Fig. 51 B). This phenomenon is attributable to cellular starvation, given that DFMO treatment must be performed in absence of FBS. If polyamines would support virus endocytosis, DFMO treated cells depleted of polyamines should show less infection. However, fluorescence imaging revealed that DFMO treated cells were infected with MRV at similar levels to non-treated infected cells (Fig. 51 B). The results suggest that inhibiting polyamines does not inhibit virus binding under my conditions.

The addition or inhibition of polyamines does not appear to influence the heterogeneous infection pattern within epithelial cell populations (Fig. 51). Therefore, polyamines probably do not impact the spatial heterogeneity during infection. Nevertheless, in order to firmly substantiate this conclusion, it would be essential to conduct binding and endocytosis assays, and to use varying concentrations and treatment time of the different compounds.

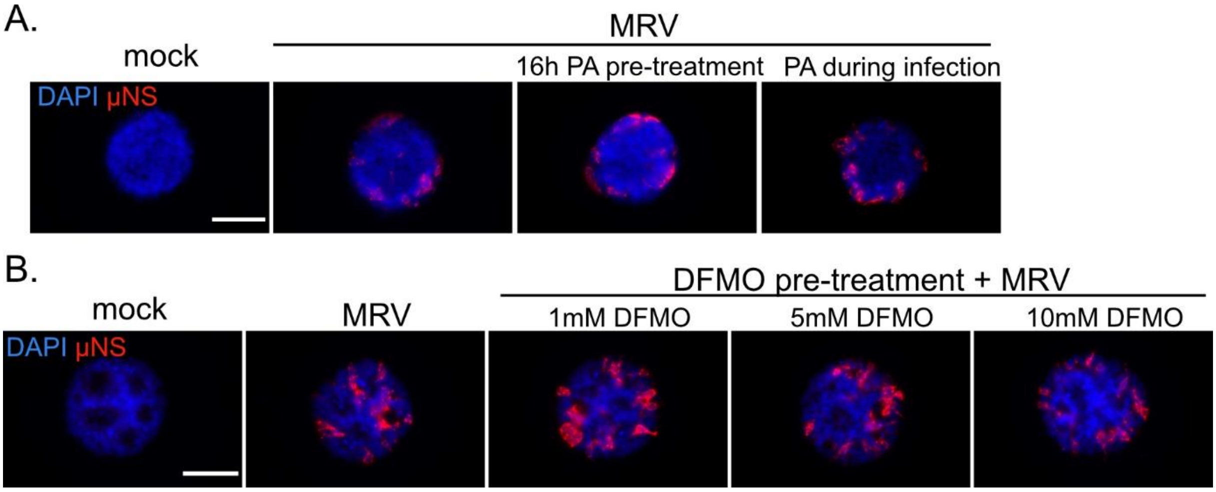

**Fig. 51. Polyamines and virus infection in epithelial populations.** T84 cells were seeded as populations on micropatterned glass. (A) 16 h prior to infection or at the moment of infection, cells were treated with 300 µM polyamine mix (1:1:1 Spermine, Spermidine and Putrescine). Cells were infected with MRV in media supplemented with 300 µM polyamine mix. (B) Cell populations were pre-treated with different concentrations of DFMO for 96 h in media containing 2% FBS. Cells were then infected with MRV in media supplemented with DFMO and containing 2% FBS. (A, B) 16 h post infection, cells were fixed and immunostained for viral µNS protein. Representative images show virus in red. Nuclei were stained with DAPI (blue). Scale bar=100 µm.

### 2.3.4. Treatment of epithelial cell populations with trypsin from the basolateral side abrogates spatial heterogeneity during infection

While studying the spatial heterogeneity during infection in epithelial cells, I also tested rotavirus infection levels in cell populations. The activation of rotavirus involves trypsin-dependent proteolytic cleavage of its outer-capsid proteins, resulting in the formation of highly infectious particles (*339*). Consequently, I conducted rotavirus infections in the presence of trypsin in the culture media. T84 cells were seeded on micropatterned glass or transwell membranes, allowing treatment either from the apical side only or from simultaneous apical and basolateral side, respectively. The cell populations were infected with rotavirus for 16 h in the presence of trypsin, and the location of infection was assessed by fluorescence microscopy. Similar to all other tested viruses (Fig. 45), apical infection resulted in a heterogeneous pattern, with rotavirus-infected cells localized mostly to the edge of the population (Fig. 52 A). However, when treating T84 populations from both sides, also center cells were permissive to rotavirus infection as similar to edge cells (Fig. 52 B). This was the first virus showing a homogenous infection level across the cell population (no apparent difference between edge and center).

To assess the role of trypsin on this abrogation of spatial heterogeneity, I infected T84 cell populations with MRV in absence or presence of trypsin. Previously, I demonstrated that MRV predominantly infects cells located at the periphery of a cell population, regardless of the infection originating from the apical or basal side of the cell (Fig. 45 and Fig. 46). Those experiments were conducted without trypsin in the media. When subjecting cell populations to apical infection along with trypsin treatment, there were no discernible differences in the viral distribution compared to infections performed without trypsin, with mostly edge cells being permissive for MRV (Fig. 52 B). However, the spatial segregation of MRV infection was abolished when I simultaneously performed infection and trypsin treatment from both the apical and basolateral side. In this scenario, both, edge and center of the population showed similar infection levels (Fig. 52 C). Conversely, in the absence of trypsin within the culture medium, MRV infection remained constrained to cells positioned at the population's edge (Fig. 53 C). The effect of trypsin was further underlined by the quantification of relative MRV infection, in which only simultaneous apical and basolateral treatment did induce similar infection levels between edge and center cells (Fig. 52 D).

These results demonstrate that treatment of trypsin from the basal membrane renders center cells in an epithelial population susceptible to virus infection, as demonstrated for MRV and rotavirus. Further investigation is required to determine whether this increased susceptibility is due to the virus entering the cell from the lateral membrane or if it is because of changes in the cell phenotype. The reason why apical trypsin treatment does not impact the spatial localization of infections remains unclear.

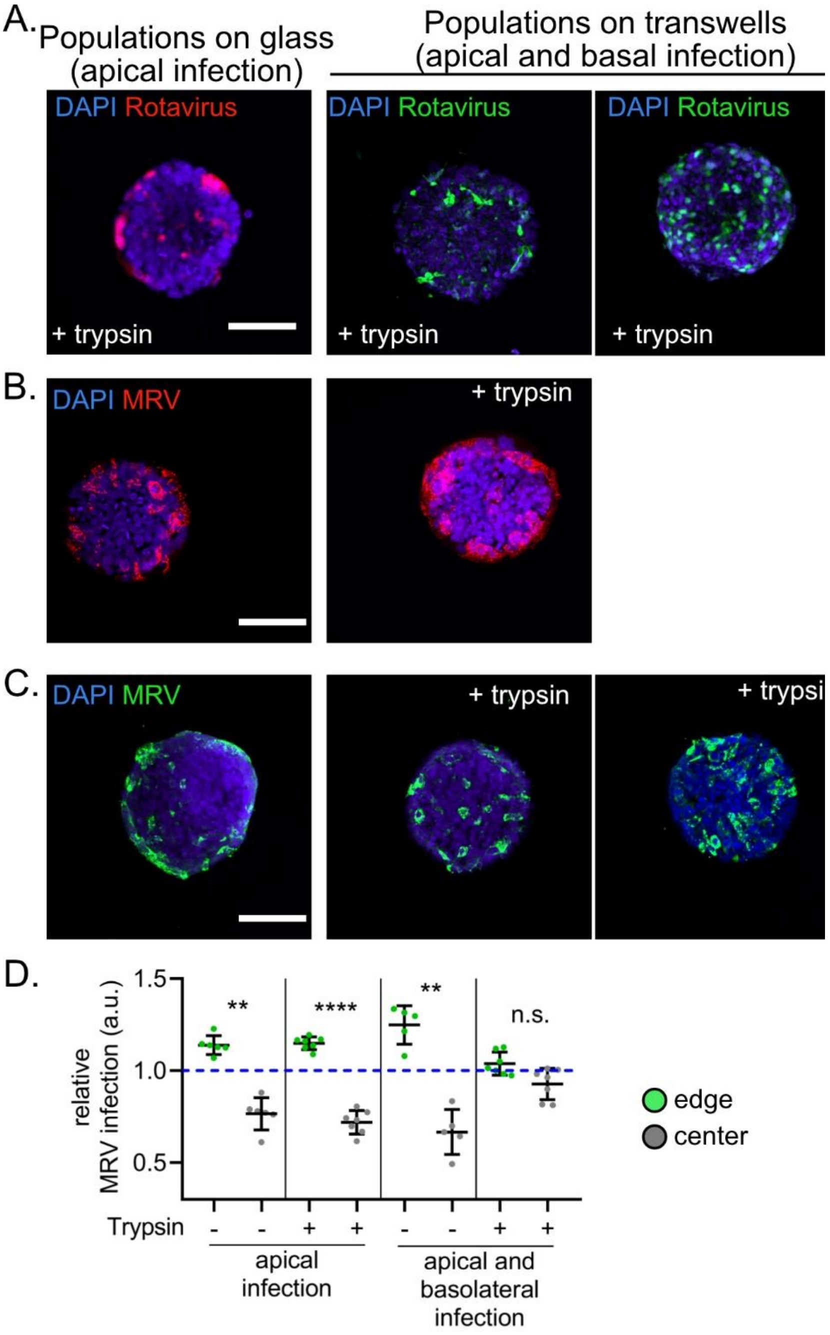

**Fig. 52. Basolateral trypsin treatment of epithelial cell populations abrogates the spatial heterogeneity during infection.** T84 WT cells were either seeded on micropatterned glass or transwell inserts as populations. Cell populations were then infected from the apical side only or simultaneously from the apical and basal side with Rotavirus dUnaG. The media was without or supplemented with 2 µg/mL trypsin during the infection. 16 h post infection, cells were fixed, MRV infected cells were immunostained for viral µNS (Rotavirus dUnaG infections are fluorescent and do not need immunostaining), and visualized by fluorescence microscopy. (A-C) Representative images of (A) Rotavirus dUnaG infected cell populations, (B) cell populations seeded on glass and infected with MRV from the apical side only, and (C) cell populations seeded on transwell inserts and infected with MRV from the apical and basolateral side. Cell nuclei were stained with DAPI (blue). Scale bar=100 µm. (D) Quantification of the relative MRV infection at the edge or the center of a population during apical infection only or simultaneous apical and basolateral infection, in presence or absence of 2 µg/mL trypsin. n ≥ 3 biological replicates, error bars indicate the standard deviation. n.s.=not significant. P<0.01 **, P <0.0001 **** as determined by Paired t test.

### 2.3.5. Role of IFN signaling in the spatial segregation of virus infection

My results indicate that virus binding and internalization can take place from the basal membrane of all cells regardless of their position within the population (Fig. 49). Nevertheless, the presence of viral protein indicating active virus replication is observed exclusively in edge cells of an epithelial population (Fig. 46). This contrasting observation, where virus internalization happens in all cells but virus replication is restricted to the edge cells, points toward the possibility of a cellular mechanism that actively suppresses virus replication/production following its entry into cells located at the center of a population. I demonstrated that the cellular environment and the population context determine basal immune signaling in epithelial cells (Results 2.2.). As cells grow confluent, activation of the cGAS-STING pathway by mtDNA induces TBK1 and IRF3 activation. IRF3 in turn acts as a transcription factor for IFNλ3. Basal IFNλ3 expression and secretion induces JAK/STAT signaling leading to ISG transcription in homeostatic sterile conditions. Consequently, a reasonable hypothesis is that center cells in a population exhibit density-dependent basal IFN-signaling, which has the potential to effectively hinder virus replication after virus entry. In the subsequent experiments, my objective was to understand the interplay between basal IFN signaling and its role in providing protection against viral infections in cells located within a population.

T84 WT cells or T84 cells exhibiting a disrupted IFN signaling pathway were seeded on micropatterned glass. Cell populations were then infected apically with HAstV for 16 h and analyzed by immunofluorescence staining. Inhibition of JAK/STAT by the compound Pyridine 6, knock-out of IRF3, IFNAR1 and IFNLR1 double knock-out (IFNR dKO) or knock-out of IFNλ2/3 lead to the same edge infection as in WT cells with intact IFN-signaling (Fig. 53 A-B). The probable reason for this observation is that cells localized in the center of a population only bind and take up virus from the basal membrane (Results part 2.3.2. and Fig. 49).

To gain accessibility to the basal membrane, I seeded T84 WT, IRF3 KO, IFNλ1 KO and IFNλ2/3 KO cells on transwell inserts. Under these conditions, single cells are embedded in an intact monolayer, similar to cells localized in the center of a micropattern-population. Formation of a polarized semipermeable monolayer resembling physiological epithelial surfaces was confirmed by a TEER measurement above 1000 Ω/cm$^2$. Surprisingly, while all cell lines reached a TEER above 1000 Ω/cm$^2$ within 3 days after seeding, IFNλ2/3 never reached values above 360 Ω/cm$^2$ (Fig. 53 C) although cells formed a monolayer as seen by microscopy images (Fig. 53 D).

Cell seeded on transwell inserts were then simultaneously infected from the apical and basal side with Vaccinia virus (VV) for 16 h, and infection was visualized by fluorescence microscopy. Only low levels of infection occurred in the intact monolayer of T84 WT cells (Fig. 53 C). This mirrors results from T84 WT cells seeded on micropatterned transwells, in which VV did not infect the center of a population (Fig. 46). Similarly, VV replication was not observed in the monolayer formed by IRF3 KO and IFNλ1 KO cells (Fig. 53 C). In contrast, the IFNλ2/3 KO cell monolayer was strongly infected by VV (Fig. 53 C), suggesting that IFNλ2/3 has a pivotal role in protecting against this virus. MRV and HAstV infections of T84 IFNλ2/3 KO cells seeded on transwell inserts were also higher than in T84 WT cells confirming the importance of IFNλ2/3 for protection against other viruses (Fig. 53 D).

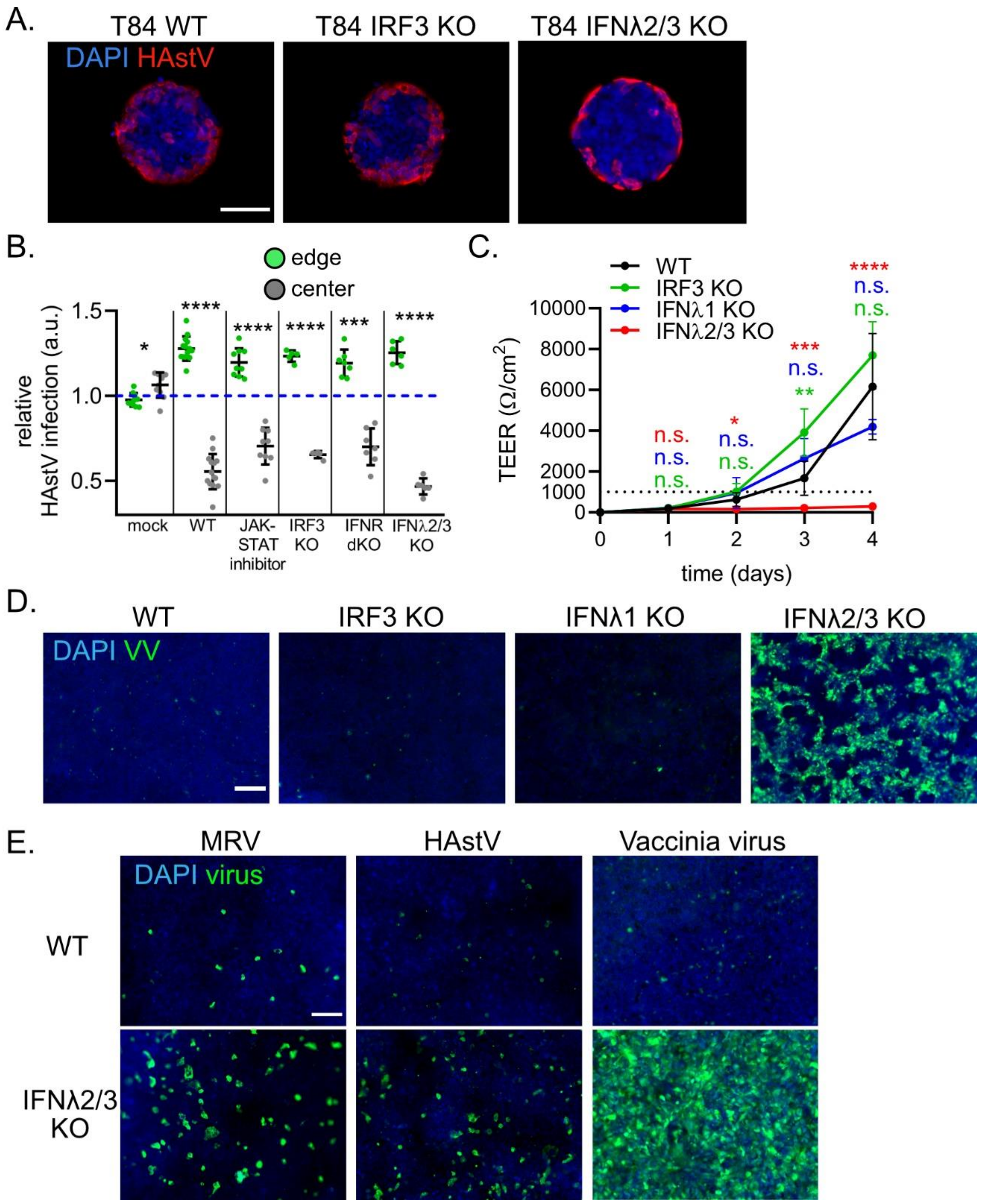

**Fig. 53. Role of IFN signaling during spatial segregation of virus infection.** (A, B) T84 WT, IRF3 knock-out (KO), IFNAR1 IFNLR1 double KO (IFNR dKO) and IFNλ2/3 KO cell lines, were grown as populations on micropatterned glass. Prior to infection, one group of T84 WT cells was treated with 2 µM Pyridine for 50 min to inhibit JAK/STAT signaling. Cells were infected from the apical side with Human Astrovirus (HAstV), without or supplemented with 2 µM Pyridine. 16 h post infection, cells were fixed and HAstV protein was immunostained to image by fluorescence microscopy. (A) Representative images of T84 WT and KO cells apically infected with HAstV (green). Cell nuclei were stained with DAPI (blue). Scale bar=100 µm. (B) Quantification of the relative HAstV infection at the edge or the center of a population during apical infection of T84 WT and KO cell lines. n ≥ 3 biological replicates, error bars indicate the standard deviation. P <0.0001 **** as determined by Paired t test. (C-E) T84 WT, IRF3 KO, IFNλ1 KO and IFNλ2/3 KO cells were seeded on transwell inserts and grown until formation of a polarized monolayer. Cells were then infected simultaneously from the apical and basal side of the transwell compartment with Vaccinia virus eGFP (VV), Mammalian reovirus (MRV) and HAstV. 16 h post infection, cells were fixed, MRV and HAstV infected cells were immunostained for viral proteins (VV eGFP infections are fluorescent and do not need immunostaining), and visualized by fluorescence

microscopy. (C) Assessment of cell polarization by measurement of the TEER over time. n ≥ 3 biological replicates, error bars indicate the standard deviation. n.s.=not significant. P<0.05 *, P<0.01 **, P <0.0001 **** as determined by Unpaired t test with Welch's correction between the T84 WT and the knock-out cell lines (color coding corresponds to the respective KO cell as compared to WT cells). (D, E) Representative images showing (D) VV eGFP infection (green) in T84 WT, IRF3 KO IFNλ1 KO and IFNλ2/3 KO cells and (E) MRV, HAstV and VV eGFP infection in T84 WT and IFNλ2/3 KO cells. The nuclei from of the confluent monolayer seeded on transwells was stained with DAPI (blue). Scale bar=200 µm.

This project studied the intricate interplay between the population context and virus infection in epithelial cells. I demonstrated that virus binding and endocytosis can occur in all cells from the basal or lateral membrane, but active virus replication is predominantly confined to edge cells within cell populations. This intriguing pattern points to the existence of a mechanism in center cells that actively suppresses virus production post-entry, potentially linked to density-dependent basal IFN-signaling. Overall, these findings emphasize the pivotal role of population context in shaping virus infection dynamics, highlighting the importance of cellular location and density-dependent IFN-signaling.

### 2.4. Type III Interferons potently control SARS-CoV-2 infection in human intestinal epithelial cells

I worked on this project jointly with my colleagues Carmon Kee and Patricio Doldan. We published this project together as shared first authors in the Journal of Virology (*159*).

#### 2.4.1. Endogenous type III IFNs control SARS-CoV-2 replication and spread in human intestinal epithelial cells better than endogenous type I IFNs

SARS-CoV-2 can infect the intestinal epithelium, contributing to disease pathogenesis and virus spread (*161*, *185*, *189*, *192*). To develop effective treatments, it is crucial to grasp how the immune system in the gut controls virus infection. Earlier studies from my laboratory demonstrated that, when SARS-CoV-2 infects IECs, it triggers a protective immune response dependent on IFN signaling (*161*). The aim of this study was to thoroughly comprehend the role of type I and type III IFN signaling in controlling SARS-CoV-2 infection in the gut.

To build on my lab earlier findings (*161*), first I confirmed the induction of IFN expression and downstream signaling by SARS-CoV-2 in the human colon cell line T84. RT-q-PCR analysis revealed that virus infection induced significant transcription of type I (IFNβ1) and type III (IFNλ2/3) IFNs as compared to mock infected cells (Fig. 54 A). Moreover, HEK-Blue assay confirmed secretion of type I and type III IFNs into the supernatant after SARS-CoV-2 infection (Fig. 54 B). Finally, phosphorylation of STAT1 was determined by Western Blot, showing that virus-induced IFN expression leads to downstream JAK-STAT pathway activation (Fig. 54 C).

These results support that SARS-CoV-2 infection in IECs triggers an IFN-dependent immune response.

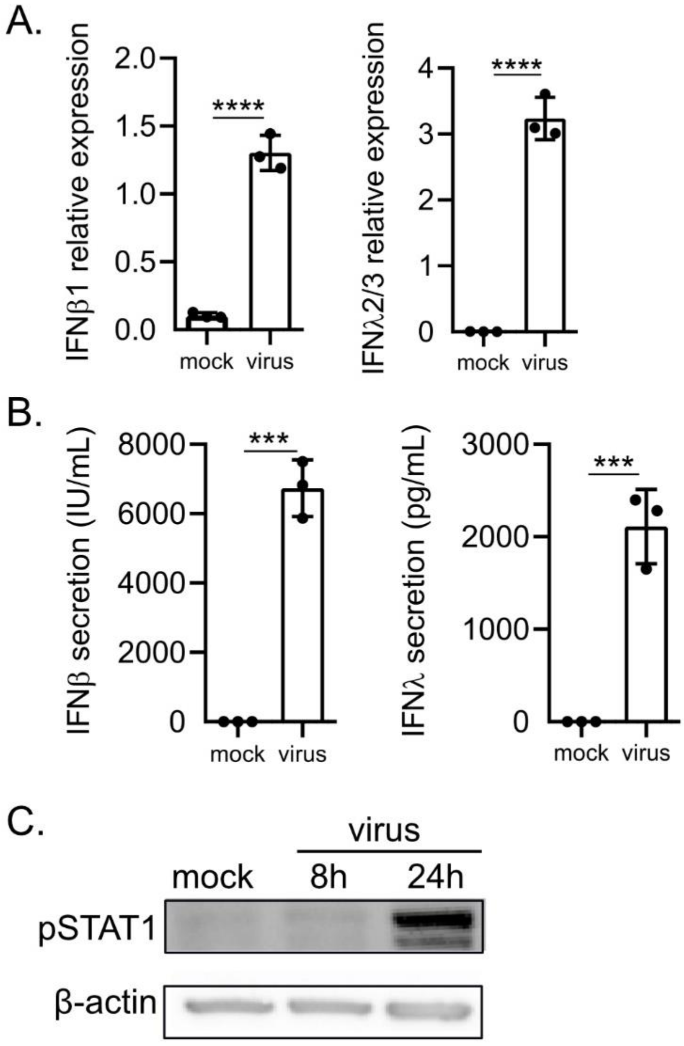

**Fig. 54. SARS-CoV-2 induces an IFN expression and signaling.** T84 WT cells were mock treated or infected with SARS-CoV-2 using an MOI of 0.04 (as determined in Vero cells). Cells were harvested at different times post-infection, and the expression of IFNs and the activation of IFN- signaling were determined. (A) At 24 hpi, RNA was harvested to assess the IFNβ1 and IFNλ2/3 relative expression using RT-q-PCR. (B) At 24 hpi, the supernatants of infected cells were harvested, infectious virus in the supernatant was inactivated, and the secretion of type I and III IFNs was assessed by the HEK-Blue assay. (C) At 8 and 24 hpi, the cells were lysed, and the activation of the JAK-STAT pathway was determined by STAT phosphorylation using Western blotting. (A, B) n = 3 biological replicates, error bars indicate the standard deviation. n.s.=not significant. P<0.05 *, P<0.01 **, P<0.001 ***, P <0.0001 **** as determined by a two-tailed unpaired t test with Welch's correlation. Data shown in this Figure were generated by me together with Carmon Kee and Patricio Doldan.

While the induction of both type I and type III IFNs is observed in response to SARS-CoV-2 (Fig. 54), this does not imply that both types of IFNs control the virus with the same efficiency. To address the dynamic interplay of type I and type III IFNs in constraining virus replication and dissemination, T84 WT cells, or cells lacking the type I IFN receptor (IFNAR KO), the type III IFN receptor (IFNLR KO), or both receptors (IFN receptor double knock-out (dKO)) were infected with SARS-CoV-2. At different times post infection, cells were immunostained for the viral nucleocapsid protein (Fig. 55 A). During the early phases of infection (4 and 8 h post-infection, hpi), IFNAR KO and IFN receptor dKO cells displayed a slightly higher degree of infection as compared to WT and IFNLR KO cells (Fig. 55 B). In stark contrast, as infection progressed (at 12 and 24 hpi), cells lacking the type III IFN receptor exhibited increased susceptibility to infection compared to cells lacking the type I IFN receptor (Fig. 55 B). These results validate the significance of both the type I and type III IFN systems in controlling SARS-

CoV-2 infection in IECs and suggested that type III IFN might be more important than type I IFN to control SARS-CoV-2 in T84 cells.

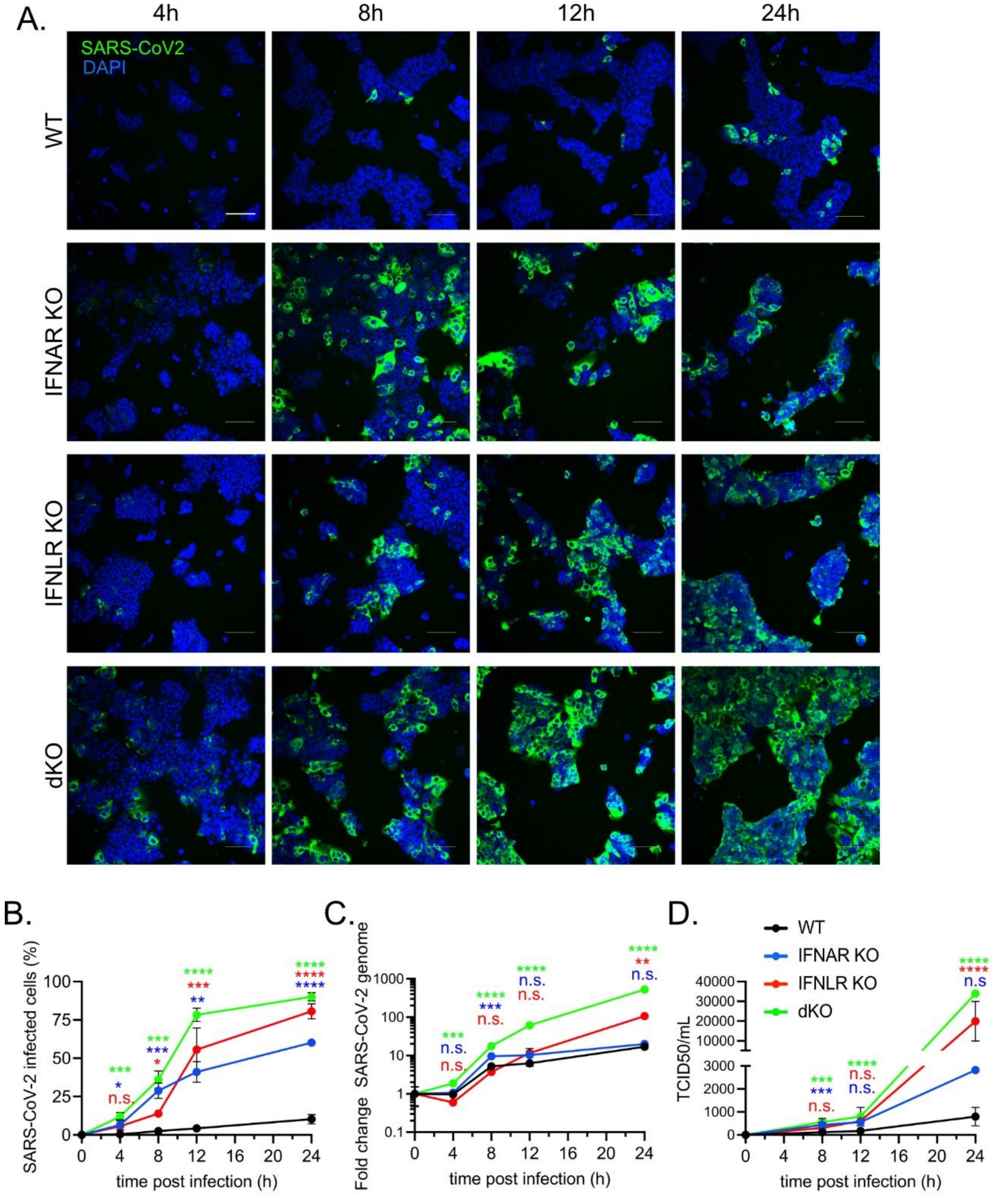

**Fig. 55. Kinetics of SARS-CoV-2 infection in human intestinal epithelial cells.** (A-D) T84 WT cells and T84 cells depleted of type I IFN receptor (IFNAR KO), type III IFN receptor (IFNLR KO), or both IFN receptors (dKO) were infected with SARS-CoV-2 at an MOI of 0.04 (as determined in Vero cells). At 0, 4, 8, 12, and 24 hpi, the cells were harvested to assess virus infection, replication, and *de novo* particle release. (A) Indirect immunofluorescence was performed against the viral nucleocapsid protein (green). Nuclei were stained with DAPI (blue). Representative images are shown. Scale bar=100 µm. (B) The percentage of SARS-CoV-2-positive cells was quantified from (A). (C) RNA was harvested, and RT-q-PCR was used to evaluate the copy number of the SARS-CoV-2 genome. The data are normalized to input (fold change). (D) T84 WT supernatants for 0, 8, 12, and 24 hpi were harvested and titrated on Vero cells. After 24 h, Vero cells were fixed, and the TCID50/mL of newly produced particles was determined by in-cell Western analyses using an antibody against the viral nucleocapsid. (B-D) n = 3 biological replicates, error bars indicate the standard deviation. n.s.=not significant. P<0.05 *, P<0.01

**, $P<0.001$ ***, $P<0.0001$ **** as determined by Ordinary one-way ANOVA with Dunnett's multiple-comparison test using WT T84 cells as reference. The color of the significance stars represents the cell line that is being compared to WT T84 (green for dKO, red for IFNLR KO, and blue for IFNAR KO). Data shown in this Figure were generated by me together with Carmon Kee and Patricio Doldan.

I then analyzed the impact of virus replication in IECs lacking the IFN receptor by RT-q-PCR. For all time points, virus genome was significantly higher in IFN receptor dKO cells, underlining the importance of IFN signaling to control virus genome replication (Fig. 55 C). Importantly, similar to the pattern observed for infected cell counts (Fig. 55 B), cells lacking the type III IFN receptor exhibited elevated levels of viral genome copies in comparison to both WT and IFNAR KO at later stages post-infection (Fig. 55 C). Intriguingly, at 24 hpi, cells IFNAR KO cells displayed a replication level of SARS-CoV-2 similar to the one observed in WT cells (Fig. 55 C).

To test how the absence of IFN signaling impacted the production of *de novo* virus particles, WT and IFN receptor KO cells were infected with SARS-CoV-2. Supernatants were collected at 8, 12, and 24 hpi, and titrated on naive Vero cells to obtain the viral 50% tissue culture infective dose(s) (TCID50)/mL present in the T84 cell supernatant. Results show that the production and release of *de novo* viral particles were markedly influenced by intrinsic IFN signaling (Fig. 55 B-C). Similar to my previous results regarding the number of infected cells and the levels of viral replication (Fig. 55 B-C), IFNLR KO and IFN receptor dKO cells exhibited higher levels of newly produced infectious viral particles in the supernatant as compared to WT and IFNAR KO cells (Fig. 55 D).

Altogether, my results confirm that the absence of IFN signaling favors SARS-CoV-2 infection, replication and *de novo* particle production. Importantly, endogenous type III IFN expression and signaling appears more important compared to type I IFN to protect T84 cells against SARS-CoV-2.

### 2.4.2. IFNs inhibit SARS-CoV-2 infection in a concentration-dependent manner

My findings underscore the pivotal role of endogenous type III IFN-mediated signaling in inhibiting SARS-CoV-2 infection in IECs, while suggesting a less protective role played by endogenous type I IFNs. To circumvent the potential influence of different kinetics in IFN expression and secretion upon virus infection as the underlying cause for the variation in protective effects between type I and III IFNs, I chose to synchronize the IFN-mediated response using exogenous treatment.

To evaluate both IFN antiviral activity efficiency against SARS-CoV-2 and explore potential differences between type I and type III IFNs, T84 WT cells were treated with increasing concentrations of either IFN-β1 (type I) or IFN-λ1/2/3 (type III) for 12 or 24 h before SARS-CoV-2 infection. At 24 hpi, infection levels were analyzed by immunofluorescence staining for

SARS-CoV-2 nucleoprotein, RT-q-PCR for the virus genome, and measurement of released infectious particles. Immunofluorescence staining demonstrated that both type I and type III IFNs exhibited dose-dependent reduction in SARS-CoV-2 infected cells (Fig. 56 A-B). Interestingly, a more pronounced inhibition of SARS-CoV-2 infection was observed for cells treated for 12h with low concentrations of type I IFNs (1 and 10 U/mL) as compared to higher concentrations (100 U/mL) (Fig. 56 B). The underlying molecular basis for this inverted dose-dependent response remains unclear, although it is possible that low IFN concentrations induce a robust antiviral state while minimizing activation of negative regulatory feedback loops. This could result in a stronger antiviral effect compared to treatment with higher concentrations. Intriguingly, higher doses (>2000 U/mL) of type I IFN were required to achieve <10% of infected cells, while type III IFNs were effective in curbing virus infection even at the lowest tested concentration (0.003 ng/mL), achieving infection rates below 5% of infected cells (Fig. 56 B).

Analysis of the number of released infectious viral particles into the cell supernatant also revealed a dose-dependent reduction in the amount of newly generated virus, further confirming a link between IFN-signaling and inhibition of *de novo* virus production (Fig. 56 C). Moreover, both type I and type III IFNs led to dose- and time-dependent decreases in viral replication, as evidenced by the measurement of the relative amount of SARS-CoV-2 genome (Fig. 56 D). Interestingly, as also observed upon quantification of infected cells (Fig. Fig. 56 A-B), efficient inhibition of viral replication was reached with low type III IFN concentrations, while higher type I IFN concentrations were required to attain the same inhibitory effect (Fig. 56 D).

These outcomes show that exogenous IFN treatment of IECs prior to SARS-CoV-2 infection interferes with virus infection, replication, and generation of *de novo* infectious virus particles in a time- and dose-dependent manner. Furthermore, small amounts of type III IFNs can completely inhibit virus infection, whereas the tested lower type I IFNs concentrations were not as effective in controlling infection.

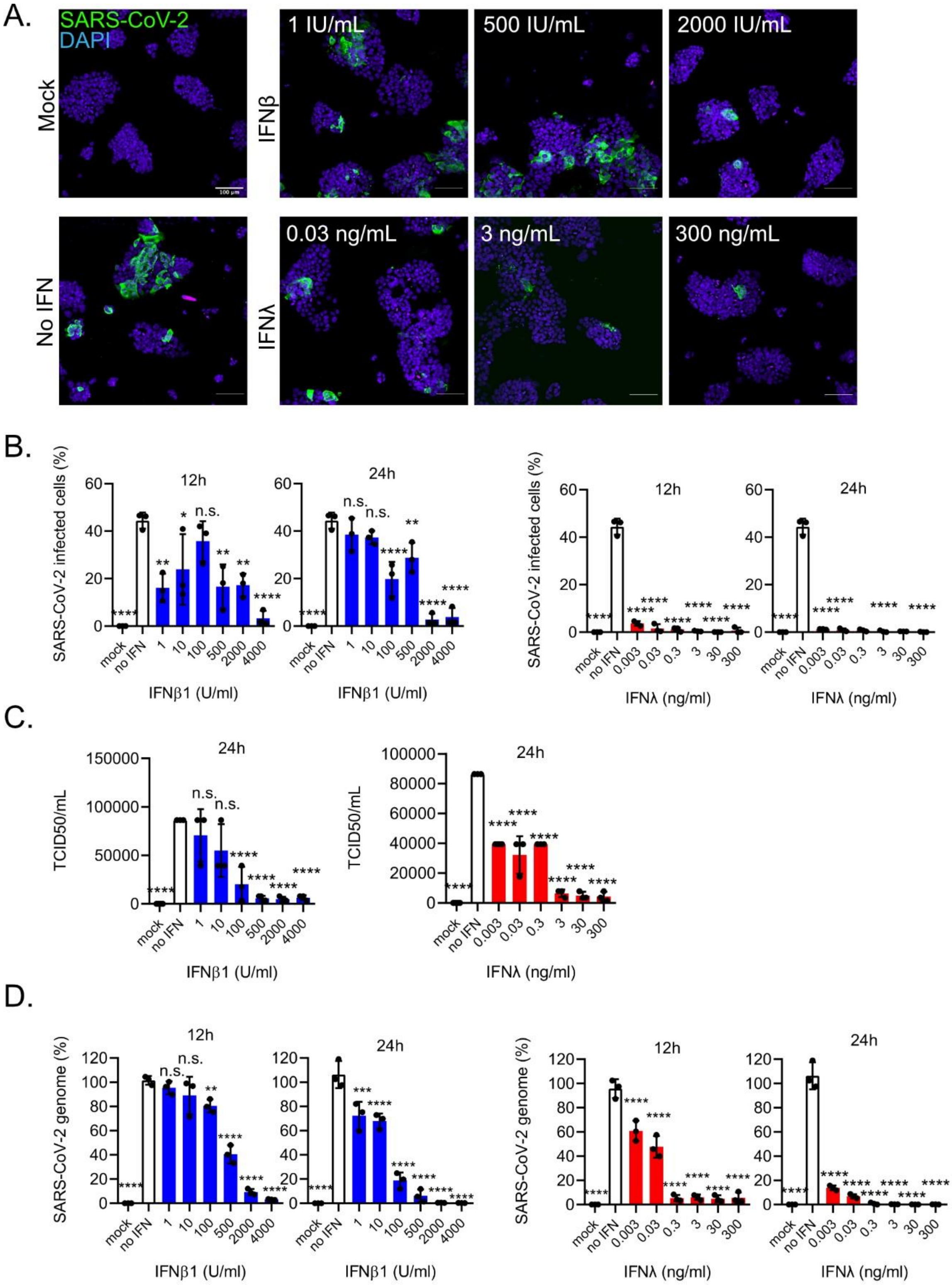

**Fig. 56. Exogenously added type I and III IFNs inhibit SARS-CoV-2 infection of hIECs in a concentration-dependent manner.** T84 WT cells were mock treated or pretreated with increasing concentration of type I (IFN-β1) and type III (IFN-λ1/2/3) IFNs for 12 or 24 h prior to infection. Cells were infected with SARS-CoV-2 using an MOI of 0.04 (as determined in Vero cells). At 24 hpi, the cells were harvested to assay virus infection and replication. (A) Cells were fixed, and indirect immunofluorescence analysis was performed against the viral nucleocapsid (green). Nuclei were stained with DAPI (blue). Representative images are shown. Scale bars=100 µm. (B) The percentage of SARS-CoV-2-positive cells was quantified from (A). (C) Supernatants of 24-h-IFN-pretreated and infected T84 WT cells were harvested and titrated on Vero cells. After 24 h, the Vero cells were fixed, and the TCID50/mL of newly produced particles was determined by in-cell Western blotting with an antibody against the viral

nucleocapsid. The data are expressed as percentages, setting non-IFN-treated cells to 100%. (D) RNA was harvested, and RT-q-PCR was used to evaluate the replication of the SARS-CoV-2 genome using primers that target nucleocapsid transcript. The data are normalized to input and expressed as percentages, setting non-IFN-treated cells to 100%. (C-E) n = 3 biological replicates, error bars indicate the standard deviation. n.s.=not significant. P<0.05 *, P<0.01 **, P<0.001 ***, P <0.0001 **** as determined by Ordinary one-way ANOVA with Dunnett's multiple-comparison test using non-treated infected cells as a reference. Data shown in this Figure were generated by me together with Carmon Kee and Patricio Doldan.

IFN-β1 is expressed as antiviral activity (U/mL) and IFN-λ1/2/3 is expressed by weight (ng/mL). This means that I cannot directly compare the effect of "low" type I IFN concentration with "low" type III IFN concentrations on SARS-CoV-2 infection, as the units of measurement are different. To circumvent this problem, I tested the antiviral effect of these cytokines on another virus. Vesicular stomatitis virus (VSV) is often used as a standard to study how IFNs affect viral infections. Therefore, I performed the same pretreatment experiment using increasing IFN concentrations as for SARS-CoV-2 (Fig. 56), but with VSV expressing luciferase (VSV-Luc). T84 WT cells were pre-treated with type I and III IFNs for 12 or 24 hours and then infected with VSV-Luc. At 8 hpi, a luciferase assay was performed to measure virus infection levels. Surprisingly, even though low levels of type III IFNs were effective against SARS-CoV-2 (Fig. 56), they did not significantly inhibit VSV-Luc infection (Fig. 57 B, 0.003 ng/mL). On the other hand, type I IFN seemed to induce a stronger antiviral state against VSV as compared to SARS-CoV-2 (Fig. 57 A and Fig. 56 B, respectively). Comparing the antiviral activities of type I and type III IFNs on VSV and SARS-CoV-2 suggest that SARS-CoV-2 is particularly sensitive to type III IFNs.

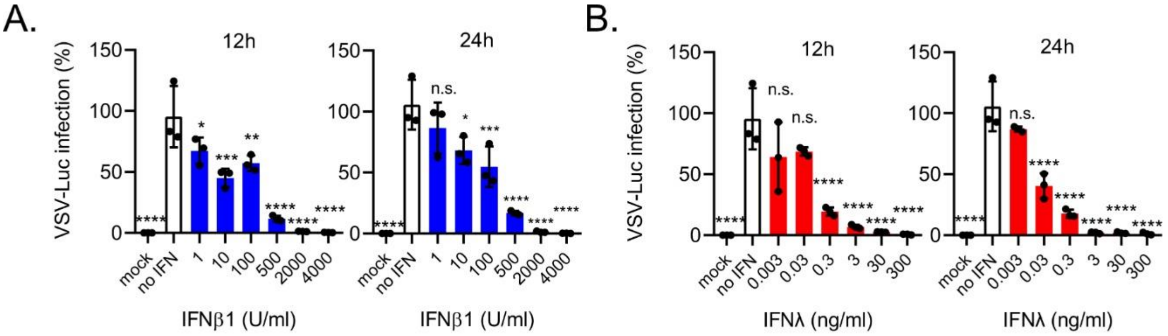

**Fig. 57. Exogenously added type I and III IFNs inhibit VSV-Luc infection of hIECs in a concentration-dependent manner.** WT T84 cells were mock treated or pretreated with increasing concentrations of (A) type I (IFN-β1) and (B) type III (IFN-λ1/2/3) IFNs for 12 and 24 h prior to infection. The cells were infected with VSV-Luc using an MOI of 5 (as determined in T84 wild type). At 8 hpi, the cells were harvested to assay virus infection with a luciferase assay. The VSV-Luc infection was quantified, and the results are expressed as percentages, setting non-IFN-treated cells to 100%. n = 3 biological replicates, error bars indicate the standard deviation. n.s.=not significant. P<0.05 *, P<0.01 **, P<0.001 ***, P <0.0001 **** as determined by Ordinary one-way ANOVA with Dunnett's multiple-comparison test using non-treated infected cells as a reference. Data shown in this Figure were generated by me together with Cuncai Guo.

When analyzing in more detail the dose- and time-dependent antiviral effect of IFN on SARS-CoV-2, I observed that longer pre-treatment time and higher IFN concentrations were required to significantly reduce the viral genome in IECs (Fig. 56 D) as compared to the time and concentrations required to significantly reduce the number of infected cells (Fig. 56 B). This disparity between virus genome replication and number of infected cells was particularly notable at lower IFN concentrations. To explore these differences, T84 WT cells were treated with 1 U/mL of IFNβ1 or 0.003 ng/mL of IFN-λ1-3 for 12 h before SARS-CoV-2 infection. Cells were harvested 24 hpi, and immunostained with antibodies targeting the SARS-CoV-2 nucleocapsid protein to visualize virus protein expression or targeting double-stranded RNA (J2) to monitor viral genome replication (Fig. 58 A). This approach enabled me to investigate potential discrepancies in virus genome replication and nucleocapsid translation at the single cell level.

Quantitative analysis revealed that about 16% of the non-treated infected cells were positive for both, double-stranded RNA (J2) and nucleocapsid protein. 15% of cells exhibited virus genome replication without protein translation as evidenced from J2 positive cells, while only 3% were positive for Nucleocapsid protein alone (Fig. 58 B). These numbers are in agreement with the viral replication cycle. Interestingly, IFN treatment did not affect the percentage of double-stranded RNA (J2) and Nucleocapsid positive cells, however it significantly decreased the number of double positive cells (Fig. 58 B). This strongly suggests that viral genome replication is occurring at similar rates between untreated and treated infected cells, however nucleocapsid protein translation appears inhibited or delayed upon IFN treatment. Intriguingly, this decline in the number of double-positive cells was more pronounced in IFN-λ1-3-treated cells (Fig. 58 B).

Altogether, analyzing virus genome replication and nucleocapsid translation at a single cell level suggest that a central mechanism through which IFNs restrict SARS-CoV-2 spread is by inhibiting viral nucleocapsid protein translation. Type III IFNs appear to more potently inhibit infection though this mechanism.

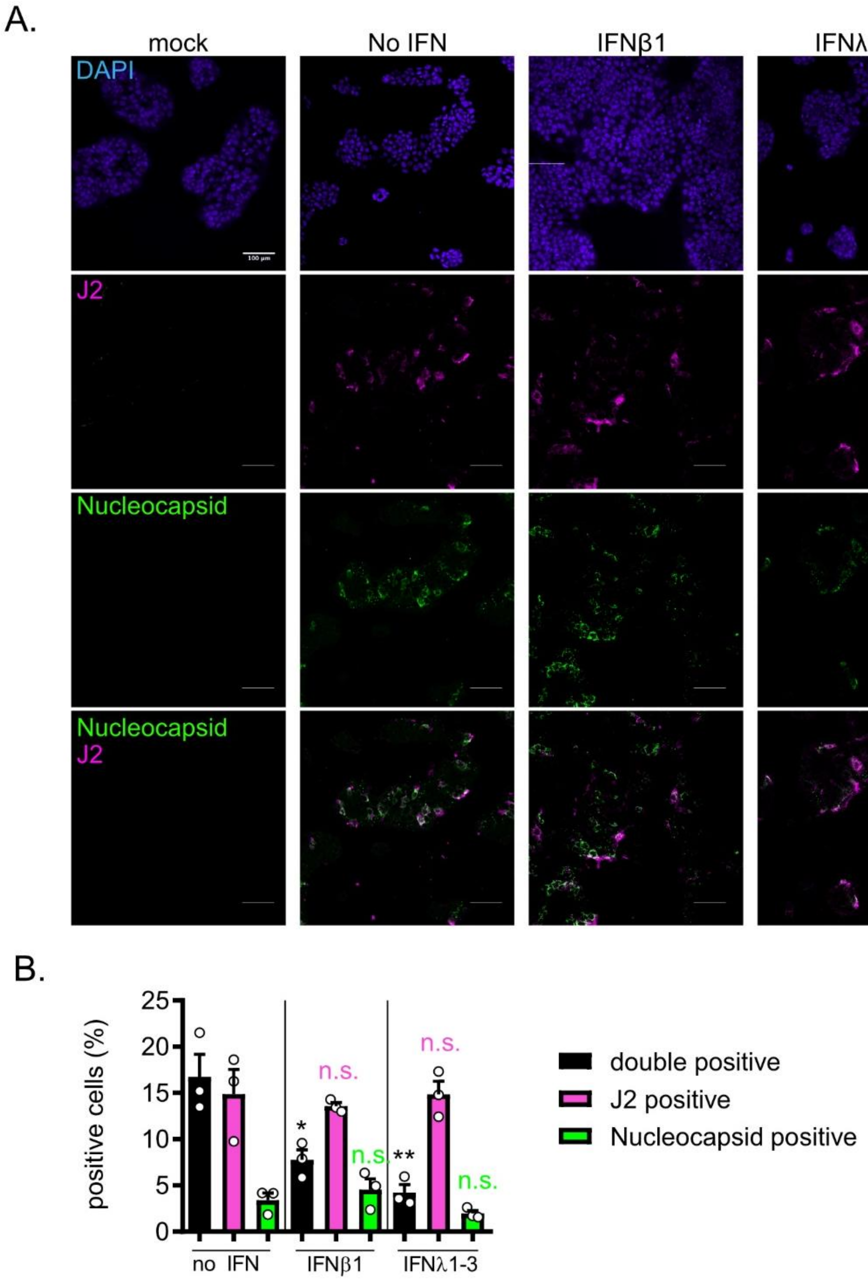

**Fig. 58. Type I and type III IFNs induce an antiviral state to protect against SARS-CoV-2 in hIECs by interfering with nucleocapsid expression.** WT T84 cells were mock treated or pretreated with type I and III IFN at low concentrations (1 U/mL IFN-β1 or 0.003 ng/mL IFN-λ1/2/3) for 12 h prior to infection with SARS-CoV-2 using an MOI of 0.04 (as determined in Vero cells). The cells were harvested at 24 h after SARS-CoV-2 infection. (A) Cells were fixed, indirect immunofluorescence was performed against the viral nucleocapsid protein (green) and dsRNA (J2) (magenta), and nuclei were stained with DAPI (blue). Representative images are shown. Scale bar=100 µm. (B) The percentages of both nucleocapsid-positive and J2-positive cells (double-positive cells), J2-positive-only cells and nucleocapsid-positive-only cells were quantified from (A). n = 3 biological replicates, error bars indicate the standard deviation. n.s.=not significant. $P<0.05$ *, $P<0.01$ ** as determined by ordinary one-way ANOVA with Dunnett's multiple-comparison test using the non-treated infected cells as a reference. Data shown in this Figure were generated by me together with Carmon Kee and Patricio Doldan.

### 2.4.3. Pretreatment with type III IFNs mediates a faster antiviral response against SARS-CoV-2 than pretreatment with type I IFNs

To determine whether both type I and type III IFNs require the same time to achieve protection against SARS-CoV-2 in IECs, T84 WT cells were pre-treated with IFNs at different time-points (from 24 to 3 h) prior to infection with SARS-CoV-2. During virus infection, the IFNs were maintained in the media. 24 hpi, the viral genome load and the count of virus-infected cells were assessed using RT-q-PCR and immunofluorescence assay, respectively (Fig. 59 A). First, I tested concentrations of 4000 IU/mL for IFNβ1 and 3 ng/mL for IFNλ1-3 as they completely inhibit virus replication after 24 h pretreatment (Fig. 56 E). Both type I and type III IFNs manifest similar kinetics of antiviral activity at high concentrations (Fig. 59 B). A 3 h pretreatment with either IFN was effective in entirely mitigating SARS-CoV-2 infected cells, as evidenced by nucleocapsid immunostaining (Fig. 59 B, left panels). Viral genome levels were also substantially diminished by a 3 h pretreatment with either IFN, albeit only by 60% in comparison to non-treated infected cells (Fig. 59 B, right panels). This data demonstrates that at high concentrations, type I and III IFNs do not show differential kinetics in protection against SARS-CoV-2, probably because cells are exposed to saturating levels of the cytokines.

Given the complete suppression of virus infection by high IFN concentrations, I aimed to determine whether lower concentrations would influence the kinetics of the antiviral response against SARS-CoV-2. IFN concentrations resulting in a 50% reduction in genome replication were selected (Fig. 56 E). T84 WT cells were treated with either 500 U/mL of IFNβ1 or 0.03 ng/mL of IFNλ1-3 for different time points prior to SARS-CoV-2 infection. Results demonstrate that a 24 h pretreatment with a low dose of type I IFN is necessary to significantly diminish the counts of SARS-CoV-2-infected cells and viral genome copies, while shorter exposure times do not have a significant effect (Fig. 59 C). In contrast, shorter pre-treatment with type III IFNs efficiently inhibits SARS-CoV-2 infection (Fig. 59 C). A 24 h pretreatment with 0.03 ng/mL of IFN-λ1-3 leads to complete elimination of cells positive for nucleocapsid protein and significant reduction in virus genome copies (Fig. 59 C). These results strongly suggest that type III IFN requires less time to establish an antiviral effect against SARS-CoV-2 compared to type I IFNs.

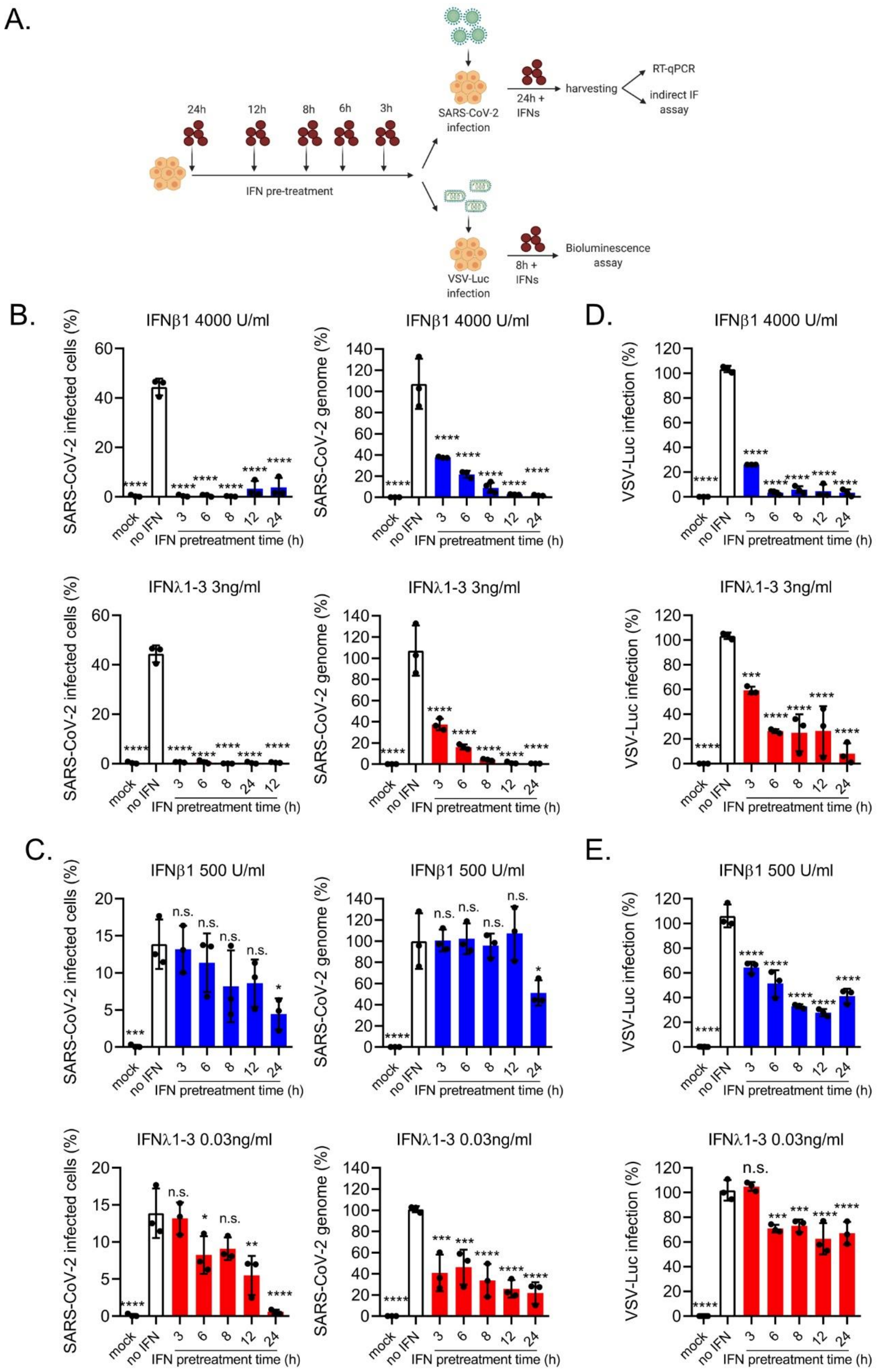

**Fig. 59. Differences between type I and type III IFNs in providing antiviral protection in hIECs against SARS-CoV-2 and VSV.** WT T84 cells were mock treated or pretreated with type I and III IFN at high (4,000 U/mL IFN-β1 or 3 ng/mL IFN-λ1/2/3) or low (500 U/mL IFN-β1 or 0.03 ng/mL IFN-λ1/2/3)

concentrations for different time points prior to infection. The cells were infected with either SARS-CoV-2 at an MOI of 0.04 (as determined in Vero cells) or vesicular stomatitis virus expression firefly luciferase (VSV-Luc) at an MOI of 5 (as determined in wild-type T84 cells). At 24 hpi (for SARS-CoV-2) or 8 hpi (for VSV-Luc), the cells were harvested to assay virus infection. (A) Schematic of infection setup. (B, C) The percentages of SARS-CoV-2-positive cells were quantified by immunofluorescence (left panels), and viral replication was assessed by RT-q-PCR (right panels). RT-q-PCR data are normalized to input (fold change) and expressed as percentages, setting non-IFN-treated cells to 100%. (D, E) VSV-Luc infection was assayed by measuring the luciferase activity at 8 hpi. The luciferase activities for IFN-treated samples were normalized to the luciferase activity of the mock-treated sample, which corresponds to 100%. (B-E) n = 3 biological replicates, error bars indicate the standard deviation. n.s.=not significant. $P<0.05$ *, $P<0.01$ **, $P<0.001$ ***, $P<0.0001$ **** as determined by ordinary one-way ANOVA with Dunnett's multiple-comparison test using non-treated infected cells as a reference. Data shown in panels (B, C) were generated by me together with Carmon Kee and Patricio Doldan, and data shown in panel (D, E) were generated by me together with Cuncai Guo.

The intriguingly rapid kinetics of antiviral defense induced by type III IFNs contradict previous findings, which indicated a longer period for type III IFNs to establish an antiviral state (*123*). To ascertain that the rapid antiviral effect induced by type III IFNs against SARS-CoV-2 is virus-specific, I pre-treated T84 WT cells with high and low IFN concentrations for different times prior to with VSV-Luc infection. Consistent with prior studies, 8 h pretreatment with high type I IFN concentrations is required for 90% reduction in VSV infection, whereas type III IFN requires 24 h to achieve a comparable decrease in infectivity (Fig. 59 D). Similarly, experiments using low IFN concentrations further supported that type I IFNs exert faster control over VSV infection compared to type III IFNs (Fig. 59 E). These findings confirm that type III IFNs require more time to establish an antiviral state against VSV-Luc as compared to type I IFNs. Notably, when comparing the antiviral activities at low concentration for type I and III IFNs (Fig. 59 C vs. E), I see that SARS-CoV-2 is more resistant to type I IFNs while more sensitive to type III IFNs as compared to VSV.

Collectively, these results suggest that type I IFNs require longer to establish an antiviral state in IEC against SARS-CoV-2 than type III IFNs. The potency of type III IFNs in inducing an antiviral state appears specific for SARS-CoV-2, and not observed against VSV-Luc.

### 2.4.4. IFN post- and pre-treatment protect IECs against SARS-CoV-2 spread

I determined that type III IFNs confer better protection against SARS-CoV-2 compared to type I IFNs when IECs are treated prior to infection. To investigate whether IFNs can exert their effects after viral infection, I infected T84 WT cells with SARS-CoV-2 and treated them with either 4000 U/mL of IFN-β1 or 3 ng/mL of IFN-λ1-3 at various time points post-infection (Fig. 60 A). At 24 hpi the relative viral genome was evaluated by RT-q-PCR. Both type I and III IFNs were able to inhibit viral replication when added up to 4 h after infection (Fig. 60 B). For type I IFNs this inhibition was noticeable even when added 8 hpi (Fig. 60 B). The antiviral effect was even more pronounced for *de novo* virus particle production (Fig. 60 C). Even when adding at 8 hpi, no infectious viral particles were detectable in the cell supernatants for type I IFN treatment, and a significant 15-fold reduction in the release of viral particles compared to untreated cells was seen for type III IFNs (Fig. 60 C). To validate these findings in primary intestinal epithelial cells, human ileum-derived organoids seeded in 2D were infected with SARS-CoV-2 and treated with IFNs at various times post-infection (Fig. 60 A). Similar to the results obtained in T84 cells, virus replication (Fig. 60 D) and *de novo* virus release (Fig. 60 D) was significantly impaired by IFN post-treatment in ileum-derived organoids.

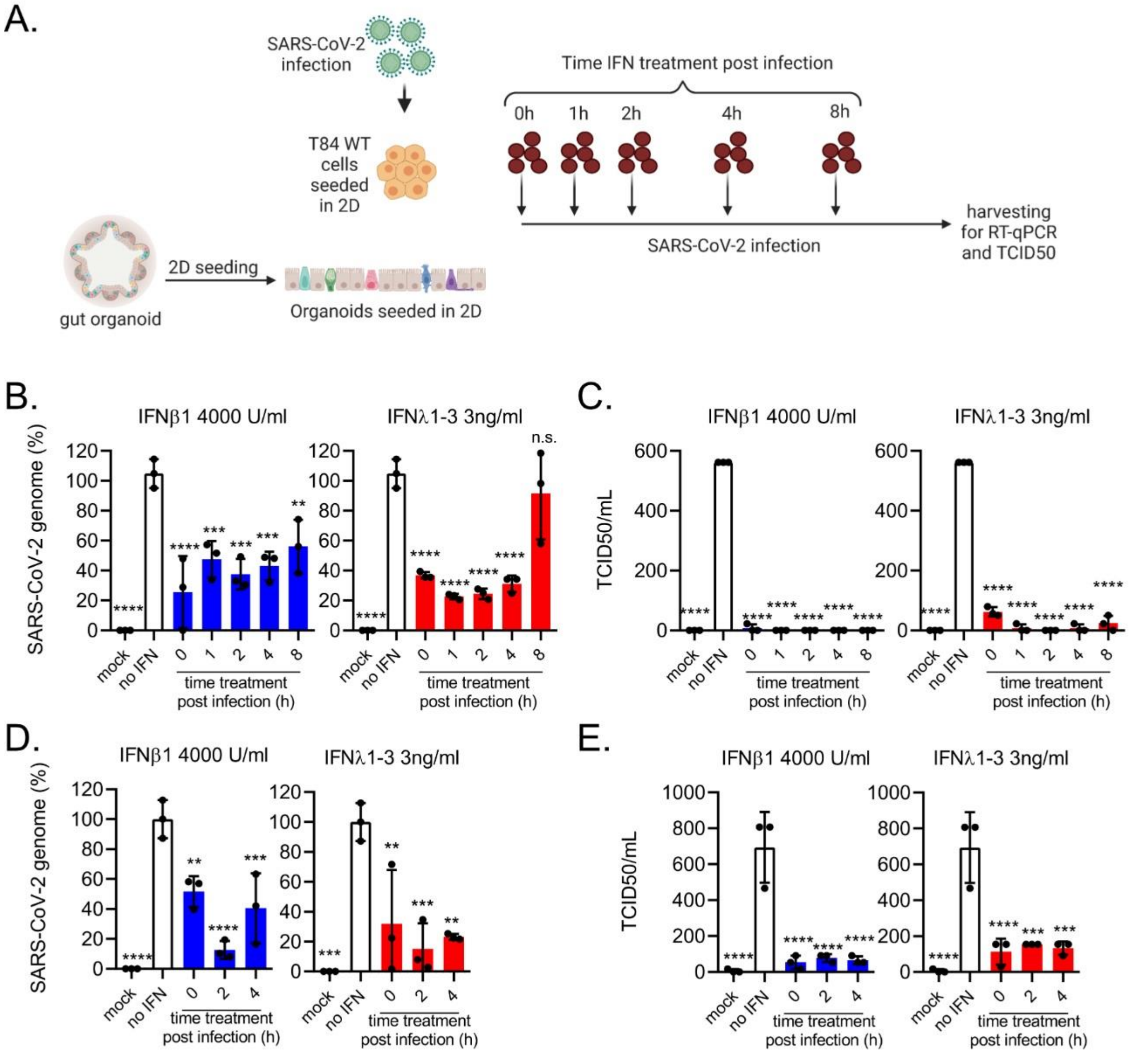

**Fig. 60. Kinetics of type I and III IFNs establishment of an antiviral state against SARS-CoV-2 in hIECs.** T84 WT cells or ileum-derived organoids seeded in 2D were infected with SARS-CoV-2 at an MOI of 0.04 (as determined in Vero cells). At 0, 1, 2, 4, or 8 hpi, 4,000 U/mL of IFN-β1 or 3 ng/mL of IFN-λ1/2/3 was added. (A) Schematic of experiment setup. (B, D) At 24 hpi, RNA was harvested from (B) T84 WT and (D) ileum-derived organoids to assess virus replication levels using RT-q-PCR. Data are normalized to the input (fold change) and expressed as percentages, setting non-IFN-treated cells to 100%. (C, E) At 24 hpi, (C) T84 WT cells and (E) and ileum-derived organoid supernatants were harvested and titrated on Vero cells. After 24 h, Vero cells were fixed, and the TCID50/mL of newly produced particles was determined by in-cell Western blotting with an antibody against the viral nucleocapsid. (B-E) n = 3 biological replicates, error bars indicate the standard deviation. n.s.=not significant. $P<0.05$ *, $P<0.01$ **, $P<0.001$ ***, $P<0.0001$ **** as determined by Ordinary one-way ANOVA with Dunnett's multiple-comparison test using non-treated infected cells as a reference). Data shown in this Figure were generated by me together with Carmon Kee and Patricio Doldan.

To address how long the IFN-mediated antiviral state persists in IECs, T84 WT cells were treated with 4,000 U/mL of IFNβ1 or 3 ng/mL of IFNλ1-3 for 24 h. Cells were then washed, and a medium exchange was done by adding fresh medium without IFNs. At various time-points after the medium exchange, WT T84 cells were infected with SARS-CoV-2 (Fig. 61 A). At 8 hpi, the virus genome copy number was quantified using RT-q-PCR, revealing that the antiviral state induced by both type I and III IFNs persisted for up to 72 h (Fig. 61 B). Importantly, the protective effect induced by type I IFN markedly diminished over time (Fig. 61 B). In contrast, type III IFNs triggered a longer-lasting and more robust antiviral state (Fig. 61 B). Even at 48 h after the medium exchange, virus replication was inhibited by 75% with type III IFN treatment, and 72 h after the medium exchange the genome virus was reduced to 50% as compared to non-treated infected cells (Fig. 61 B). IFN-treatment effect on the release of infectious particles was assessed 24 hpi (Fig. 61 A). In alignment with viral replication levels (Fig. 61 B), the release of infectious viral particles was more effectively controlled upon treatment with type III IFNs as compared to type I IFNs in T84 cells (Fig. 61 B).

The persistence of the antiviral state induced by type I and III IFNs was also assessed in human ileum-derived organoids (Fig. 61 A). Similar to the findings in T84 cells, both types of IFNs exhibited a sustained antiviral effect that persisted for up to 48 hours after treatment in organoids (Fig. 61 C). Notably, 72 h after medium exchange, only type III IFNs reduced the viral genome load by half compared to non-treated organoids (Fig. 61 C). Furthermore, at 48 and 72 hours after medium exchange, type III IFNs better controlled *de novo* particle release into the supernatant as compared to type I IFNs (Fig. 61 C). These results underscore the long-lasting protective capacity of type III IFNs against SARS-CoV-2 infection in comparison to type I IFN treatment.

To investigate whether the prolonged antiviral effect induced by IFNs in IECs was specific to SARS-CoV-2, T84 WT cells were infected with VSV-Luc after IFN washout (Fig. 61 A). Intriguingly, both, type I and type III IFNs, were less protective against VSV-Luc as compared to SARS-CoV-2 in T84 cells (Fig. 61 D). Notably, type I IFNs induced a longer antiviral state against VSV-Luc as compared to type III IFNs, significantly reducing VSV-Luc infection even 24 h after the medium exchange (Fig. 61 D). In contrast, type III IFNs were unable to significantly reduce VSV-Luc infection at any time point after the medium exchange in IECs (Fig. 61 D), underscoring the virus-specific sensitivity of SARS-CoV-2 to type III IFNs.

Collectively, while both types of IFNs inhibit viral replication and spread even when administered after SARS-CoV-2 infection, priming (pre-treatment and wash-out) with type III IFNs results in a more potent and prolonged antiviral state against SARS-CoV-2, surpassing the effects of type I IFNs.

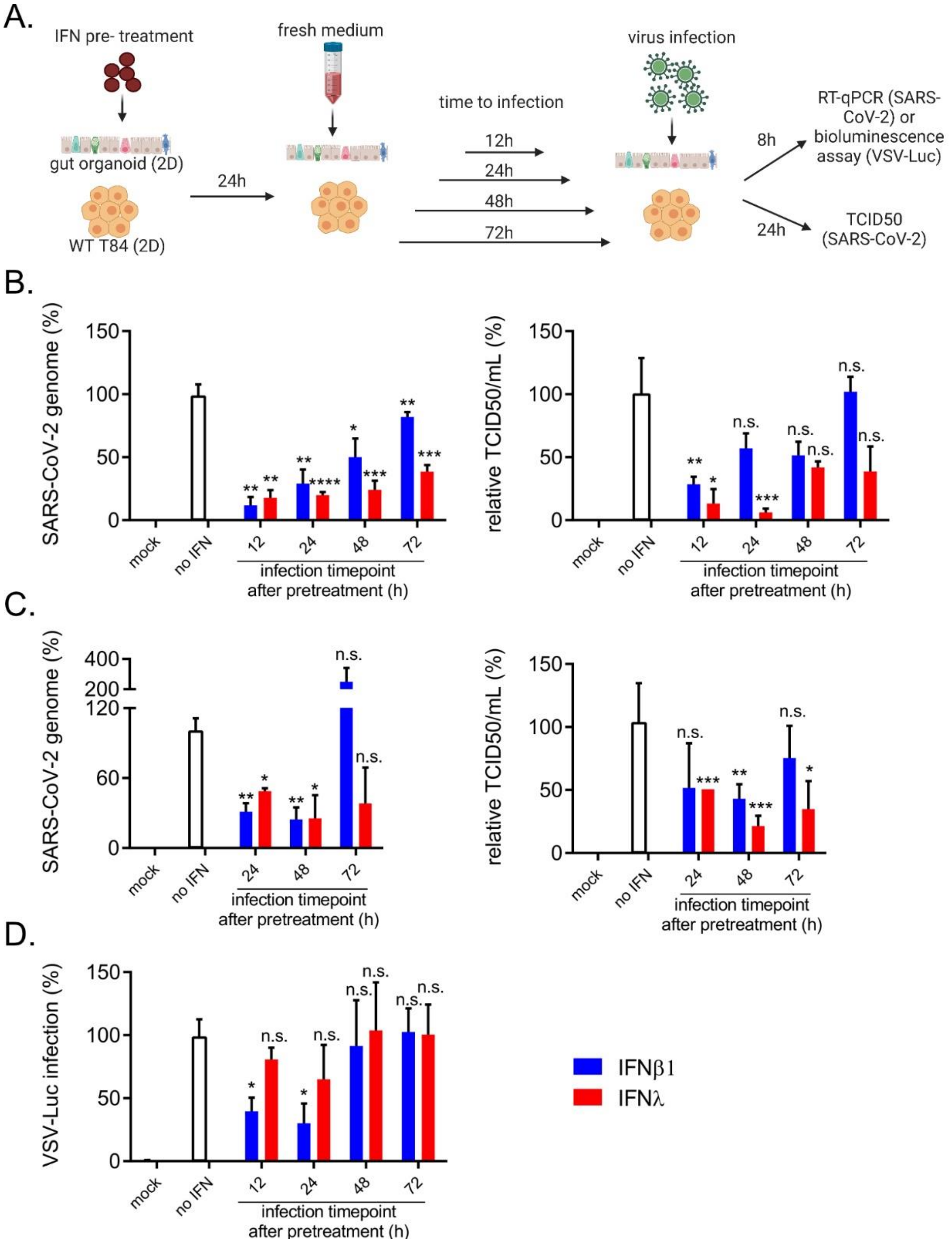

**Fig. 61. Type III IFNs induce a longer lasting antiviral state in hIECs against SARS-CoV-2 infection compared to type I IFN.** T84 WT cells or ileum-derived organoids were mock treated or pretreated with 4,000 U/mL IFN-β1 or 3 ng/mL IFN-λ1/2/3. At 24 h after treatment, fresh medium was added to the cells. At 12, 24, 48, or 72 h after medium exchange, the cells were infected with SARS-CoV-2 or VSV-Luc. (A) Schematic of experiment setup. (B, C) Infection with SARS-CoV-2 using an MOI of 0.04 (as determined in Vero cells). Left panels: At 8 hpi, RNA was harvested to assess virus replication levels in (B) T84 WT cells and (C) ileum-derived organoids using RT-q-PCR, and the virus genome was normalized to the input (fold change). Right panels: At 24 hpi, supernatants of (B) T84 WT cells and (C) ileum-derived organoids were harvested and titrated on Vero cells. After 24 h, Vero cells were fixed, and the TCID50/mL of newly produced particles was determined by in-cell Western blotting with an antibody against the viral nucleocapsid. (D) Infection with VSV-Luc using an MOI of 5 (as determined in the T84 wild type). At 8 hpi, a luciferase assay was performed to determine virus infection levels. (B-D) SARS-CoV-2 genome copy number, TCID50/mL of newly produced particles, and VSV-Luc infection levels were normalized to the non-treated infected cells at the respective time point. n = 3 biological replicates, error bars indicate the standard deviation. n.s.=not significant. P<0.05 *, P<0.01 **, P<0.001 ***, P

<0.0001 **** as determined by a two-tailed unpaired t test with Welch’s correlation, using non-treated infected cells for the respective time points as a reference). Data shown in panels (B, C) were generated by me together with Carmon Kee and Patricio Doldan, and data shown in panel (D) were generated by me together with Cuncai Guo.

In this study, I investigated the role of IFNs in controlling SARS-CoV-2 infection in the intestinal epithelial cells. I confirmed the induction of both type I and type III IFNs upon SARS-CoV-2 infection in human IECs, and demonstrated their critical roles in inducing an antiviral immune response. Using receptor knockout cells, I showed that endogenous type III IFNs exhibit a stronger protective effect than type I IFNs. Experiments with synchronized IFN treatment provided in *trans* revealed that low type III IFN concentrations efficiently inhibit SARS-CoV2 infection and spread, but not VSV infection. Moreover, pre-treatment with type III IFNs resulted in a faster antiviral response against SARS-CoV-2 and induced a longer lasting antiviral effect as compared to type I IFNs. My study contributes to the understanding of the differential roles of type I and type III IFNs in combating SARS-CoV-2 infection in the gut, and highlights the importance of type III IFNs to control virus infection.

# 3. Discussion

## 3.1. The population context and response to IFNs

Cell-to-cell variability is a central feature of genetically identical (isogenic) cell groups. This study aimed to investigate how the cell population context influences the cell-to-cell variability during IFN-dependent signaling in epithelial cells. Using single-cell and population analysis approaches, I revealed that both type I and type III IFNs trigger a heterogeneous response in isogenic epithelial cells. This heterogeneity was characterized by a spatial component, in which cells at the edge of a cellular colony mount a significantly higher immune response as compared to cells localized in the center of the cell colony. I identified that the source of this cell-to-cell variability lies in the polarized distribution of IFN receptors toward the basolateral side of epithelial cells (Fig. 62 A). Cells localized in the center of a colony form a polarized monolayer, and IFNs coming from the cell culture medium (apical side) cannot access the basolateral receptors (Fig. 62 B). Conversely, cells at the colony's edge lack polarization, and their receptors are distributed all around the cell, allowing interaction with IFNs present in the cell culture medium (Fig. 62 B). Consistent with this observation, basolateral IFN treatment induced a spatially homogenous response in which all cells, independently of their location within a population (center or edge of colony), respond to IFNs. Importantly, I demonstrated that this polarized localization of IFN receptors can significantly influence the outcome of infection. Pre-treating confluent epithelial cells with IFNs offered limited protection against viral infection, while pre-treating sparse cells induced a strong antiviral state. This finding highlights the importance of considering the population context when studying host/pathogen interactions and when addressing the potency of the antiviral function of IFNs in epithelial cells.

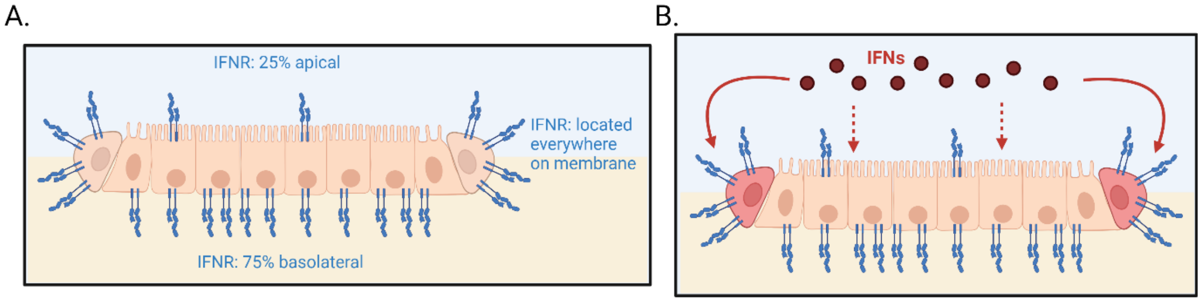

**Fig. 62. The population context influences the response to IFNs in epithelial cells.** (A) IFN receptor distribution along the apical-basal axis in polarized epithelial cell populations. (B) The response to apical IFN treatment in an epithelial cell population is heterogeneous because of the polarized receptor localization.

### 3.1.1. Heterogeneous response of cells within a population to IFN treatment

Cell-to-cell variability during the IFN-dependent response in clonal cell populations has been widely observed. Isogenic cells in a population respond at different times post-type I IFN treatment (*313*, *315*). Moreover, type I IFN treatment induces a heterogeneous pattern of ISG expression in fibroblast and epithelial cell groups, leading to responder and non-responder subpopulations (*313*–*316*, *340*). Importantly, whether a cell responds or not to IFNs, is not terminally imprinted as demonstrated by re-stimulation experiments. In these experiments, after the first round of IFN treatment, the non-responder population was sorted and re-treated with IFNs as before, which lead to the same heterogeneous pattern of ISG expression characterized by responder and non-responder cells (*313*, *340*). This excludes the existence of a stable fraction of unresponsive clones and indicates that all populations contain both responders and non-responders. Using *in-silico* modeling and single cell data, the cell-to-cell variability during IFN-dependent signaling was explained by stochastic events rooted in "biochemical noise" (*315*, *340*), rather than deterministic events tightly regulated by the molecular machinery.

In line with previous studies, I also observed that an isogenic population of adherent epithelial cells treated with either type I or type III IFNs from the apical side results in heterogeneous signaling, ranging from highly responding to non-responder subpopulations (Fig. 20 and Fig. 21). By using tools that integrate spatial components and ISG expression patterns, I identified the population context, precisely the local cell density and position within a population, as a deterministic factor for the cell-to-cell variability. Cells densely packed in a monolayer (center of a population) will polarize and the IFN receptors will be localized to the basal membrane, while edge cells are not polarized and the receptor will be distributed along the entire membrane. Therefore, in addition to stochastic events, I propose that the basolateral IFN receptor localization in confluent epithelial cells constitutes a deterministic explanation for the heterogeneity during IFN signaling. Interestingly, a study by Bhushal et al. (*314*) also demonstrated that cellular density affects responsiveness to type III IFNs. In this study, they observed a non-responsive subpopulation upon type III IFN treatment in murine IECs, which decreased in number when cells reached confluence. They further demonstrated that cell polarization and the epigenetic status determines the size of the non-responder population. Bhushal et al, demonstrated that the heterogeneous response to type III IFNs in mouse IECs is partially regulated by the molecular machinery. This and our study highlight the role of cell confluence and the population context during IFN sensing and signaling, which can be incorporated as a deterministic factor when studying cell-to-cell heterogeneity.

Altogether, it is evident that IFNs induce a heterogeneous response in clonal cell populations. However, there are discrepancies in explaining whether the origin for this cell-to-cell variability are stochastic or deterministic events, or to which extent either type of event (stochastic or deterministic) affects single-cell responses. These discrepancies can arise from the differences in quantifications techniques (flow cytometry vs. fluorescence imaging) and biological systems (cell types and ISGs measured). Overall, understanding the molecular basis for cell-to-cell heterogeneity is only at its infancy. There is currently an ongoing debate over whether cell-to-cell variability is genuinely random (stochastic) or if the differences between cells arise from molecular factors that are presently unknown (*275*). Indeed, within the past years, examples of stochastic behavior have been revealed to be far more deterministic than initially thought (reviewed in (*275*, *341*)). To globally address the origin of cell-to-cell variability during IFN sensing, previous analyses, single-cell data at a high spatio-temporal resolution and modelling approached need to be systematically integrated.

### 3.1.2. Cell-to-cell variability and the population context during IFN signaling in different cell lines

I used the intestinal epithelial cell line T84 as a model system to study cell-to-cell variability in epithelial cells. Using this model system, I concluded that the population context and the basolateral IFN receptor localization in polarized epithelial cells strongly determines single cell response to IFN treatment. To validate my results, I employed the human intestinal epithelial cell line CaCo2, the human airway epithelial cell lines Calu3, non-transformed human-derived mini-gut organoids, epithelial cell lines from non-mucosal origin (human-derived HK2 and Huh.7) and, as a negative control for cells that do not polarize, the hamster derived fibroblast BHK21 cell line. For all epithelial cells from mucosal origin (CaCo2, Calu3 and human-derived mini-gut organoids) the same pattern of cell-to-cell heterogeneity during IFN treatment was observed as for T84 cells (Fig. 22 and Fig. 24). Interestingly, the epithelial cell lines of non-mucosal origin showed mixed results, sometimes similar and sometimes contrary to those in T84 cells. Together these results suggest that the polarized IFN-receptor localization determines the responsiveness in epithelial cell of mucosal origin, and, to some extent, in epithelial cells of non-mucosal origin. Finally, the fibroblast cell line also elicited a differential immune response at high vs. low density, being much more responsive at low density, which was similar to results seen in T84 cells. This is contrary to my expectations, since fibroblasts do not polarize, and hence should not elicit a polarized membrane composition and receptor localization. It is probable that other factors influence the responsiveness at high vs low density in these fibroblast cells.

### 3.1.3. Techniques to study spatio-temporal cell-to-cell heterogeneity

Studying heterogeneity in isogenic populations has benefited from techniques such as single-cell transcriptomics and flow-cytometry. However, these methods do not integrate both the spatial and temporal determinants that may characterize cell-to-cell variability. In contrast, high content imaging enables the collection of spatially and temporally resolved data at single cell resolution. Here, I used two high-content fluorescent imaging approaches to address how the population context impacts cell-to-cell variability during IFN-mediated signaling in adherent cells: (a) a bioinformatics method (DBSCAN-CellX) (Fig. 20) and (b) a micropatterning method (Fig. 21 and Fig. 24). Using the recently developed DBSCAN-CellX approach (https://github.com/GrawLab/DBSCAN-CellX/), I determined the relative location of individual cells with respect to their neighboring cells (Fig. 20), providing me with a tool to address single cell behavior in their population context. This allowed me to identify a spatially-dependent heterogeneous response pattern, in which significantly more cells at the edge of a population induced ISG expression as compared to cells in the center of a population. The spatial segregation of immune events was confirmed using a micropatterning approach. I created cell populations in which all population context parameters (population size, local density, polarization status) were controlled (Fig. 21 and Fig. 24), enabling me to study cell population behavior in an unbiased and reproducible manner. Using these tools in combination with high content imaging pipelines will improve our understanding of single cell heterogeneity and its implications.

### 3.1.4. The population context impacts the cell ability to mount an antiviral response after IFN treatment

It is evident that cell-to-cell variability significantly impacts the single cell phenotype, behavior, and responses to diverse stimuli. Notably, single-cell heterogeneity provides a mechanism for generating diversity and to increase the population range of responses to changing environmental conditions (*273*, *275*). For instance, a study identified the presence of small subpopulations within genetically identical bacterial colonies, which were able to survive stress such as drug treatment (*342*). Importantly, they demonstrated that survival was linked to a preexistent heterogeneity in bacterial populations rather than to the presence of resistant mutants, because cells regrown from such persistent bacteria remained sensitive to the drug (*342*). This is especially relevant for pharmaceutical companies, as a developed antibiotic might not completely clear a bacterial infection. Also treatment strategies against cancer can be impacted by this phenomenon. Cancer is a highly heterogeneous disease, which is apparent when building accurate clinical models based on population-averaged measurements to guide diagnosis and treatment of the disease (*343*). Even when using clonal cancer populations in controlled laboratory conditions, response and sensitivity of cancer cells to drugs varied widely (*344*–*346*). For example, epidermal growth factor receptor tyrosin kinase inhibitors (EGFR TKIs) have been first-line therapy options against non-small cell lung cancer harboring *EGFR* sensitive mutations (*347*). Importantly, after EGFR TKI treatment of drug-sensitive human tumor cell lines, a small subpopulation of reversibly “drug tolerant” cells was consistently found (*344*). This subpopulation was a results of the intrinsic heterogeneity within the cancer cell population (*344*), which ultimately can protect a tumor from eradication by different treatment strategies. Therefore, it is crucial to understand cell-to-cell variability and its origin in cell culture systems, to better tackle technical problems raising from heterogeneous responses in isogenic cells.

When analyzing the origin of cell-to-cell variability during IFN signaling in isogenic epithelial cells, I identified cellular density, which comes in hand with cell location, as deterministic factors leading to a heterogeneous response within a population. Both cell density and cell location are central features of the population context in which a cell is embedded. Importantly, I demonstrated that cell confluence can greatly impact whether cells sense IFNs and therefore induce a protective antiviral state. I apically pre-treated cells with IFNs at both high and low cell densities before exposing them to viruses and then assessed the number of infected cells (Fig. 27). The conclusions that are drawn from these two different experimental setups (high vs. low cell density) are opposing: Results obtained from low density suggest that IFNs induce a strong antiviral state against the tested viruses. On the contrary, results from confluent cells show that IECs cannot be protected from viruses by IFNs. These experiments underscore the critical importance of considering cell density and the population context when designing experimental setups, particularly in the context of the intestinal epithelium and the antiviral immune response.

Prior research has shown that cell density plays a substantial role in fundamental cellular molecular pathways, influencing aspects such as lipid composition (*298*), endocytic events (*324*) and the expression of central molecules including autophagy markers p62 and LC3II, lysosomal cathepsin D as well as nuclear proteins HDAC1 and Lamin B1 (*299*). Trajkovic et al. (*299*) treated cells with widely used compounds (brefeldin A, nocodazole, Ly294002 or YM-201636) that significantly decrease cell density over-night. After over-night incubation, the treated cells were imaged and were matched to controls based on the new reduced density. In a Western Blot analysis in which cell density-responsive proteins pS6, p62 and Lamp1 were quantified, treated cells were compared to non-density matched (initial seeding density) or density matched controls. Comparison to these different controls lead to ambiguous results: using the non-density matched control as opposed to a density-matched control created, erased, inverted, or affected significance of a difference in protein expression levels (*299*). This demonstrated that cell density is a potent experimental variable, and Trajkovic et al. (*299*) emphasize that a rational experimental design including cell density controls will minimize erroneous interpretation of cell culture data. Furthermore, it is crucial to recognize that cell density is often associated with drug resistance. Several studies have demonstrated that cells forming a confluent monolayer are significantly less susceptible to drug treatments (*348*, *349*). This has profound implications in the field of drug screening and development within the biomedical industry. In light of these observations and my data, I propose that cell density has been underestimated in the evaluation of research results and should be more proactively considered when planning experiments. Additionally, collaborative efforts should be made to better understand the population-related factors that influence biological processes.

### 3.1.5. Polarized distribution of IFN receptors and ISG response

The mass spectrometry analysis of the surface proteome revealed a distinct distribution pattern for the type I IFN IFNAR2 and the type III IFN IL10RB receptor subunits, with approximately 75% located on the basolateral membrane and 25% on the apical membrane of polarized IECs (Fig. 25). Consistent with this distribution, treatment with type I IFN did not trigger a strong immune response in cells located in the center of a population or in a densely packed cell monolayer during apical treatment. Moreover, type I IFN treatment of a cell monolayer seeded on transwell inserts induced substantially higher ISG expression levels during basolateral than during apical treatment. In contrast, type III IFN treatment did not induce such a differential phenotype and did not align with the 75% basolateral to 25% apical receptor localization pattern. Intriguingly, when examining the immune activation triggered by type III IFN in relation to the cells' proximity to the colony edge (edge degree), I observed that the normalized fluorescence of cells decreased as they were located farther away from the edge, but then increased in cells located deeper within the center of the colony (Fig. 20). Apical type III IFN treatment of cell populations showed that, overall, cells located at the edge are more responsive than center cells. However, and contrary to type I IFN treatment, the cells located in the very center of the population still elicited a response to type III IFNs (Fig. 21). Additionally, type III IFN treatment of epithelial cells seeded on transwell inserts induced higher ISG levels from the basolateral side, however the difference was not as pronounced as with type I IFN treatment (Fig. 24 E). Altogether, the data suggests that cells located in the center of a population in a highly confluent micro-environment are responsive to apical type III IFNs, although the IL10RB receptor subunit is mostly localized at the basolateral membrane. Bhushal et al. (*314*) demonstrated in mouse IECs that cell polarization increases the sensitivity to IFNλ3 treatment. It is possible that also in our system cell polarization makes cells more responsive to type III IFNs. Cells localized in the center of a population are highly polarized. Therefore, apical type III IFNs would bind to the few IFNLR localized to the apical membrane, and induce an immune response. Conclusive experiments need to be performed to support this hypothesis.

My findings reveal that both type I and type III IFN receptor subunits exhibit an enrichment on the basolateral membrane of polarized IECs. While previous research has reported polarized localization of IFN-alpha (*350*) and IFN-gamma (*351*) receptors on the basolateral membrane of airway epithelial cells, to the best of my knowledge, no prior report has specifically focused on the localization of IFN receptors in the gut. This polarized receptor localization may carry physiological significance since, *in vivo*, IECs are in direct contact with the *lamina propria* from the basolateral side, where immune cells are also situated. In contrast, the apical membrane of IECs faces the gut lumen, which contains the commensal microbiota. Sensing IFNs from the sterile basolateral side could be a mechanism to selectively sense IFNs provided by immune cells (Fig. 63). Additionally, IECs have the capacity to express and secrete IFNs, which can act in an autocrine and paracrine manner, thereby contributing to the propagation of an antiviral immune response. Interestingly, and in line with my results, it has been demonstrated that, following virus infection of polarized human IECs *in vitro*, IFNλ is predominantly secreted to the basolateral side (*352*). Under physiological conditions in the gut this is logical, as apical IFNs would be secreted into the lumen and washed away during the peristaltic movement of the intestinal tract. Further studies must address whether IFN secretion *in vivo* by IECs occurs on the apical or basolateral side, and how this is relevant in the context of a basolateral IFN receptor localization.

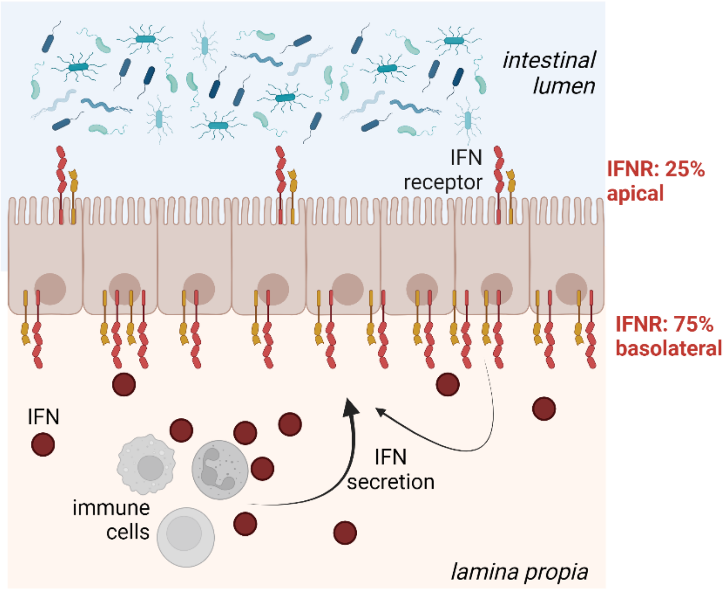

**Fig. 63. Enriched basolateral IFN receptor localization in the intestinal epithelium.**

With this project I provide a novel approach to understand the origins of heterogeneity in isogenic populations. I demonstrated that the spatial heterogeneity during IFN response in polarized epithelial cells of mucosal origin is partially originated by a basolateral receptor localization (Fig. 62 and Fig. 63). The population context determined cell-to-cell heterogeneity can have wide-ranging effects on the experimental outcome, and I suggest that experiments need to be planned accordingly to obtain accurate results.

### 3.2. The population context and homeostatic immune signaling

Epithelial surfaces are multicellular tissues in which individual cells are required to spatially organize with neighboring cells to react adequately to stimuli. This is particularly crucial in mucosal epithelial tissues, which act as a barrier between the host and the external environment, and are in continuous contact with the microbiota. Therefore, epithelial cells need to maintain responsiveness towards pathogens, without inducing an exacerbated immune activation which could harm the tissue or the commensal microbiota. Achieving and maintaining this delicate equilibrium requires tight regulation of immune signaling pathways. In this project I aimed to understand how the population context of epithelial cells regulates immune signaling under homeostatic conditions (steady state). I established a density-based system to represent the two extreme environments in which an epithelial cell can be embedded. At high density, cells form a monolayer, promoting cell polarization and tight junctional connections with adjacent cells. This resembles the physiological state of epithelial surfaces. In contrast, at low density, cells either grow individually or form small clusters, resulting in heterogeneous populations with limited cell polarization and fewer inter-cellular complexes and interactions. RNA-sequencing data revealed that at steady epithelial cells at high and low density have very distinct transcription profiles (Fig. 31). Notably, pathway enrichment analysis showed that the IFN-signaling pathway was highly upregulated without a pathogenic trigger in confluent cells (Fig. 32). Using epithelial knock-out cell lines and compounds targeting various signaling molecules, I dissected the molecular mechanisms driving this upregulation (Fig. 64). I found that mitochondrial DNA activates the cGAS-STING pathway under homeostatic conditions. This induces TBK1 and IRF3, leading to basal IFNλ3 and downstream ISG expression in confluent cells. The basal immune activation is controlled by the Hippo pathway, which senses cellular confluence and adjusts the cell behavior to its microenvironment. Importantly, I demonstrated that the density-dependent basal immune activation occurs in epithelial cell lines and in primary epithelial cells lining mucosal surfaces (airway and intestinal epithelium).

It is widely reported that type I IFNs are constitutively expressed under homeostatic conditions, leading to downstream IFN-dependent signaling (*221*, *222*). Basal type I IFN expression is thought to maintain immune homeostasis and responsiveness (*222*). However, less is known about the upstream factors involved in inducing and regulating basal type I IFNs, and, to the best of my knowledge, no study focused on the expression of basal type III IFNs. In this project I report that type III IFNs are also expressed at a basal level in epithelial cells, and that the expression is regulated by the population context. Moreover, I delineate the key molecular players involved in the signaling cascade. My results show that the type III IFN-pathway is intrinsically activated in cells located within an intact epithelium. This points towards an additional layer of protection used by mucosal epithelia, in which cells within an intact epithelium express high levels of antiviral ISGs to deter potential challenge by viruses.

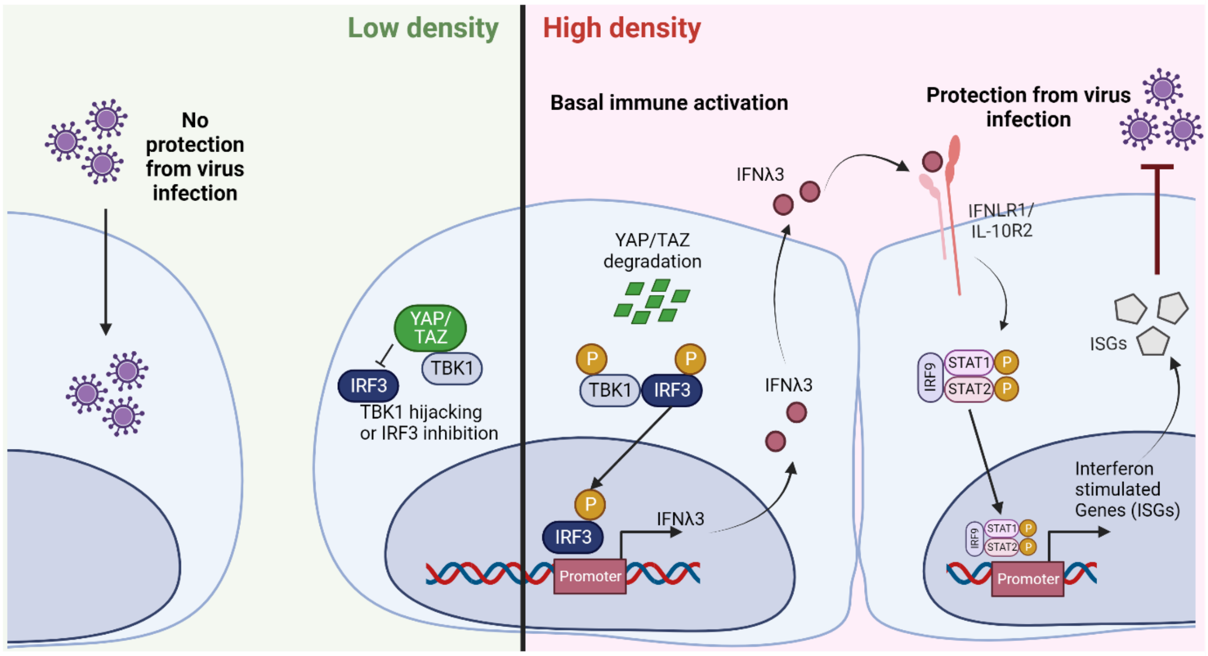

**Fig. 64. Density-dependent expression of IFNλ3 and downstream type III IFN signaling.**

### 3.2.1. Mitochondrial DNA as the trigger of basal IFNλ3 expression

I demonstrated that at steady state in confluent human epithelial cells the cGAS-STING pathway induces phosphorylation and activation of TBK1 and the transcription factor IRF3, which in turn leads to basal IFNλ3 expression. Two previous studies performed in mouse cells also show that the cGAS-STING pathway is constitutively signaling, inducing basal type I IFN production (*233*, *234*). However, if type III IFN expression is affected by constitutive cGAS-STING activation was never addressed before.

One notable characteristic that distinguishes the cGAS-STING pathway from other innate immune signaling pathways is that its activation is initiated by a fundamental component of life, namely DNA. For this reason, the PRR cGAS senses a broad repertoire of DNA species of both foreign and self-origin that are localized in the cytosol (*353*). I identified mitochondrial DNA (mtDNA) as one major ligand inducing the density-dependent basal type III IFN expression. This is in line with results from Tu et al. (*234*), which found satellite DNA, mtDNA, and retroelement DNA but not genomic DNA bound to cGAS at resting state in mouse cells. Importantly, in my study I determined mtDNA as the trigger for basal immune signaling, but I did not quantify the abundance of mtDNA in the cytosol. After cellular fractioning the mtDNA copy number in the cytosol can be measured by RT-q-PCR as described in (*90*). This approach will provide valuable insights into the differences of leaked cytosolic mtDNA levels between cells at high and low density.

mtDNA is a well described ligand for cGAS, however it is mostly associated to cellular stress acting as a DAMP (*354*). Extensive studies have shown that mtDNA is released under pathological conditions, such as oxidative stress, genotoxic stress, high levels of proinflammatory factors, viral infection and mitochondrial dysfunction, subsequently activating the cGAS-STING pathway (*354*). mtDNA needs to trespass the inner and outer mitochondria membranes to escape into the cytosol, which makes mtDNA release a complex event tightly regulated during cellular stress (*354*, *355*). A great example of such an event is cellular apoptosis (*356*). In response to apoptotic stimuli the Bcl-2 family of proteins, BCL2 antagonist/killer (BAK) and BCL2-associated X (BAX), induce permeabilization of the mitochondrial outer membrane (MOM) leading to Cytochrome C release, which is required to initiate the apoptotic cascade (*356*). During this process, BAK/BAX oligomerize at the MOM and form macropores (*357*, *358*). The mitochondrial inner membrane (MIM) then herniates through the BAK/BAX macropores, releasing mitochondrial matrix components including mtDNA (*357*, *358*). Voltage-dependent anion channels (VDACs) also form macropores at the MOM, and require mitochondrial permeability transition pore (mPTP) opening for permeabilization of the MIM and mtDNA release (*359*). Crucially, unlike BAK/BAX pores, VDAC oligomers can form in non-apoptotic cells on stressed mitochondria (*359*). While the mechanisms of mtDNA release during cellular stress are widely studied, the release of mtDNA during homeostasis (without cellular stress) and the mechanisms by which it escapes from the mitochondria need to be further explored.

### 3.2.2. Regulation of basal IFNλ3 expression by the population context

Aberrant activation of the cGAS-STING pathway supports the development of diverse pathologies, as evidenced by autoinflammatory and autoimmune diseases. Gain-of-function mutations in STING can lead to a severe autoinflammatory syndrome named STING-associated vasculopathy with onset in infancy (SAVI), which is characterized by recurrent fevers, ulcerative skin lesions, vasculitis and interstitial lung disease (*232*, *360*, *361*). The cGAS-STING pathway is also involved in systemic lupus erythematosus (SLE), the prototypic chronic systemic autoimmune disease, and other autoimmune diseases such Sjögren syndrome, scleroderma and dermatomyositis (*86*). Approximately, 15% of a total cohort of 41 SLE patients displayed elevated levels of cGAMP in their serum, strongly suggesting activation of the cGAS pathway (*362*). Moreover, loss of TREX1 (three prime exonuclease 1) activity in humans and mice causes SLE and the interferonopathy Aicardi–Goutieres (*363*, *364*). In healthy individuals, TREX1 degrades cytosolic DNA and prevents the activation of the cGAS-

STING pathway (*363*, *364*). Therefore, cGAS-STING signaling needs to be tightly regulated to maintain cellular and organismal homeostasis.

cGAS and STING are modulated by a wide range of post-translational modifications (*354*). For example, protein kinase B (also known as Akt) phosphorylates cGAS at the Ser305 residue, thereby suppressing cGAMP synthesis (*365*). Ring finger 5 (RNF5) and RNF90 ubiquitinate STING, inducing proteasome-dependent degradation and reduction in cellular antiviral response (*366*, *367*). Conversely, Pokatayev et al. (*368*) identified TOLLIP as a STING stabilizer at the resting state that is important for establishing tissue immune homeostasis. STING trafficking is also heavily regulated. STING activation requires trafficking from the ER to the Golgi through the ER-Golgi intermediate compartment (ERGIC) (*369*, *370*). At the Golgi, STING recruits and activates TBK1 and IRF3 (*369*, *370*). Recent human genetic studies have revealed a mechanism that operates at steady state and actively retrieves STING from the Golgi back to the ER to suppress cellular activation. Specifically, the adaptor protein SURF4 interacts with STING at the Golgi to facilitate STING's encapsulation into COPI vesicles for retrograde transport (*371*, *372*). After interaction with TBK1 and IRF3, STING continues trafficking to post-Golgi vesicles and lysosomes, leading to rapid STING degradation and dampening of IFN signaling (*373*). It was shown that trans-Golgi coiled coil protein GCC2 and several RAB GTPases regulate STING post-Golgi trafficking, and interruption of post-Golgi STING trafficking induces basal interferon signaling (*234*). Further modulation of STING signaling is attained by regulation of TBK1 and IRF3 through post-translational modifications and non-coding microRNAs (*374*, *375*). After STING-mediated phosphorylation, IRF3 translocates to the nucleus inducing the transcription of IFNs. STING-dependent signaling can therefore also be controlled by direct regulation of IFN gene expression. One important transcriptional repressor of IFN transcription during steady state is IRF2, which binds to a positive regulatory element in the IFNα and IFNβ promoters competing with positive regulators (*376*). Altogether, various mechanisms have been identified which regulate cGAS-STING signaling under homeostatic or pathogen-mediated conditions, avoiding an exacerbated immune response while maintaining basal activation.

In this project I propose a novel mechanism that controls immune activation at steady state. I suggest that the population context plays a regulatory role in governing homeostatic cGAS-STING activation and the downstream IFN signaling. I observed that epithelial cells at high density show significantly higher basal type III IFN expression as compared to cells at low density. I reasoned that a pathway sensing the cellular density and the population context mediates the differential basal immune activation. The Hippo pathway senses the cellular environment by integrating diverse biochemical and biomechanical cues to modulate cell behavior (*300*). Interestingly, recent studies linked the Hippo pathway to pathogen-mediated

IFN-signaling (*332*, *333*). These studies demonstrated that the effector molecules YAP/TAZ, which accumulate in cells at low density, inhibit TBK1 or IRF3 activation during pathogenic stimulation (*332*, *333*). My results strongly suggest that YAP/TAZ proteins also inhibit STING downstream signaling at steady state (Fig. 64), explaining why no basal IFN expression was detected in sparse cells. In contrast, in confluent cells, activation of the Hippo pathway triggers the degradation of YAP/TAZ proteins. This, in turn, permits STING to activate TBK1 and IRF3, ultimately resulting in the basal expression of type III IFNs (Fig. 64). It is worth emphasizing that YAP and TAZ may have distinct roles in the regulation of basal immune signaling. This is evident from my results, where knock-down cell lines with silenced YAP alone or with the silencing of both YAP and TAZ proteins displayed varying phenotypes in terms of basal type III IFN and ISG expression (Fig. 41). Although YAP and TAZ share high protein sequence similarity, previous research has highlighted significant structural and functional differences between the two proteins (*309*, *377*). Conclusive experiments are required to determine the unique contributions of YAP and TAZ on density-dependent basal immune signaling.

A large number of upstream signals have been identified to regulate the Hippo kinase cascade, and can be classified into five groups: cell density, mechanical cues, cell polarity, soluble factors and stress signals (comprehensively reviewed in (*378*)). The first three groups play a key role in density-dependent basal immune activation. Cell density is sensed by various proteins, including E-cadherin (*379*) and annexin A2 (*380*), which transmit the information to the Hippo pathway. Mechanical cues are important signals by which cells sense their microenvironment. Cytoskeleton tension and cell-to-cell attachment are examples of mechanical forces exerted on the cells, and several regulator proteins transmit that information to the Hippo pathway. For example, the regulator protein Rho participates in the cell-attachment induced YAP activation (*381*). Precisely, during cell attachment the cytoskeleton is rearranged. Rho family GTPases play a key role in actin cytoskeleton organization, and Rho is activated during cell attachment. This leads to inhibition of Lats1/2, and allows for activation and nuclear translocation of YAP (*381*). Epithelial cells polarize on their apical-basolateral axis when they grow as a confluent monolayer. A wide array of proteins located at both the apical and basal domains, as well as within cell junctional complexes, have been documented as upstream regulators of the Hippo pathway (*378*). The tight junction scaffold protein ZO1 was shown to co-localize with YAP at the cell membrane, thereby hijacking YAP and inhibiting its effector function (*382*). Knock-out of ZO1 exhibited a reduction of YAP at cell junctions and an increase of nuclear YAP (*382*). Very interestingly, and in agreement with that study, knock-out of ZO1 in epithelial cells also showed an effect on basal immune signaling. ZO1 knock-out cells seeded at high density did not induce basal IFN signaling and the ISG levels were similar to those in sparse cells (Fig. 42). To which extent the ablation of basal immune signaling was due to ZO1-YAP interaction or other regulatory mechanisms must be addressed in the future.

Altogether, my results strongly suggest that the population context of cells, which encloses changes in cell density, mechanical cues and cell polarity, is sensed by the Hippo pathway. After sensing of the population context, the downstream YAP/TAZ effector proteins of the Hippo pathway are degraded or interact with immune factors, modulating basal immune activation. Importantly, the Hippo pathway is not necessarily known for its interplay with innate immunity, but for its crucial role in the regulation of numerous biological processes such as proliferation and cell differentiation. The Hippo pathway is important in maintaining normal intestinal epithelium homeostasis, characterized by a stem cell niche in the crypt, and cell differentiation towards the villi (*383*). Various studies demonstrated that YAP/TAZ promote stem cell properties in the intestine, and their protein expression is restricted to the stem cell niche at the bottom of crypts (reviewed in (*383*)). How the accumulation of YAP/TAZ protein in intestinal stem cells affects their basal immune activation and response to virus infection needs to be further addressed.

The Hippo pathway and its signaling is not limited to the maintenance of stem cells and cell differentiation in the intestinal epithelium, but is also involved in sensing the oxygen levels. The human intestinal epithelium exhibits a steep oxygen gradient along the crypt-villi axis, with the tip of the villi being in a hypoxic environment (~1% $O_2$) and the crypts being in a normoxic environment (~21% $O_2$) (*384*). Hypoxia is a stress signal that regulates the Hippo pathway and induces accumulation of YAP/TAZ proteins (*385*). Interestingly, in epithelial ovarian cancer cells, hypoxia downregulated YAP phosphorylation but upregulated TAZ phosphorylation, suggesting that hypoxic conditions could differentially mediate the activities of YAP and TAZ (*386*). The regulation of the Hippo pathway by hypoxia is mediated by Zyxin (*387*), SIAH2 ubiquitin E3 ligase (*385*), and hypoxia-inducible factor 1 subunit alpha (HIF-1α) (*388*). Current work in my laboratory is investigating how the hypoxic conditions within the gut influence both basal and pathogen-triggered immune signaling. We have found that confluent IECs exposed to hypoxia exhibit reduced IFN signaling under steady state conditions and mount a weaker IFN response following viral infection as compared to IECs in normoxia. Consequently, IECs in a hypoxic environment are more susceptible to virus infection. Currently, the mechanisms responsible for this ablated immune response in IECs under hypoxic conditions are being analyzed, and whether the Hippo pathway is also responsible for this observed phenotype is being studied in my laboratory.

### 3.2.3. Role of basal IFNλ3-dependent signaling in confluent cells

I demonstrated that IFNλ3 is constitutively expressed at steady state in confluent epithelial cells from mucosal origin (airway and intestinal epithelium), resulting in the transcription of downstream ISGs. However, basal induction of IFNλ3 is actively suppressed in sparse epithelial cells. This observation raises questions regarding the functional significance of the basal immune activation in confluent cells and the reasons behind its absence in sparsely seeded cells. Under healthy physiological conditions, epithelial tissues lining mucosal surfaces form a confluent monolayer of polarized cells. Within these epithelial tissues, single cells have a similar population context as compared to cells in my experimental system seeded at high density. Given that confluent cells mirror the characteristics of a healthy epithelium, I suggest that basal immune signaling plays a role in supporting the barrier function of mucosal epithelial tissues. Conversely, cells at low density exhibit a population context akin to a disrupted or pathological epithelium.

#### *3.2.3.1. Antiviral effect of basal IFN expression*

Activation of type III IFN signaling in dense cells induces ISG expression, which could suffice to control incoming pathogen infection. Previous studies demonstrated that basal type I IFN expression and signaling has a direct anti-pathogenic function. IFNε is a type I IFN constitutively expressed along the female reproductive tract, which is essential to protect from bacterial (chlamydia) (*225*) and viral (HSV2 and Zika) (*225*, *226*) infections. Basal type I IFN-signaling was also shown to control hepatitis virus C and hepatitis E virus infection in Huh7.5 human liver cells (*227*), rotavirus infection in human intestinal epithelial cells (*228*) and MV-Edmonston infection in mouse neurons (*389*). To determine whether basal type III IFN expression also confers protection against virus infection in confluent epithelial cells, the supernatant of densely seeded cells can be used to treat sparse cells prior to virus infection.

#### *3.2.3.2. Type III IFN signaling and inflammatory responses in epithelial surfaces*

The continuous exposure of mucosal epithelial surfaces to both commensal and pathogenic microbes underscores the need for a delicate equilibrium between protective and pathological immune responses. The type III IFNs response has lower potency, slower kinetics and is less inflammatory as compared to the type I IFN response (reviewed in (*390–393*)). Therefore, type III IFNs provide front-line non-inflammatory protection at sites in frequent contact with microbes. Basal type III IFN expression in confluent epithelial cells can serve as a finely-tuned mechanism to maintain the barrier function of mucosal surfaces, while preventing an inflammatory immune response that might damage the tissue.

Interestingly, I found a direct negative correlation between type III IFN signaling and inflammatory responses. Confluent epithelial cells expressed significantly more IFNλ2/3 than sparse cells, while sparse cells expressed significantly higher IL-8 than dense cells (Fig. 33). IL-8 (also named C-X-C motif ligand 8 (CXCL8)) is a member of the CXC chemokine family which is expressed during inflammatory processes as a consequence of tissue injury (*394*). IL-8 transcription is induced by the transcription factors NF-κB, AP1 and C/EBPβ (also known as NF-IL-6) (*395*). Transcription factors C/EBP homologous protein (CHOP) (*396*) and cAMP response element binding protein (CREB) (*397*) can also bind the IL-8 promoter. After expression and secretion, IL-8 interacts with the G-protein coupled seven transmembrane receptors CXCR1 and CXCR2 to induce downstream signaling (*398*). The major property of IL-8 is chemotaxis of target cells, such as neutrophils and T cells, to the site of inflammation (*394*). Moreover, IL-8 stimulates cells to carry out phagocytosis, enhancing tissue repair (*394*). Importantly, many studies reported elevated IL-8 levels in the lung of cystic fibrosis patients, contributing to the pathology (*399–402*).

Induction of type III IFNs in confluent epithelial cells and IL-8 in sparse epithelial cells points towards a mechanism in which the population context not only controls IFN expression but also inflammatory cytokines. Interestingly, a crosstalk between the Hippo pathway and the inflammatory NF-κB pathway has been demonstrated. The Hippo-pathway kinase MST1/2 is active in cells at high density, and was reported to attenuate NF-κB-dependent inflammatory gene expression induced by TNFα (*403*). The role of YAP and TAZ on inflammatory responses is controversial. YAP was shown to inhibit inflammatory responses mediated by NF-κB signaling (*404–406*). Conversely, TAZ promoted liver inflammation and tumor development, and over-expression of TAZ in mouse livers increased the secretion of proinflammatory cytokines (*407*). Moreover, Mooring et al. (*408*) showed that hepatocyte-specific expression of a constitutive active form of YAP in mice for a week potently activated the expression of inflammatory factors including TNFα, IL-1β. In line with this, mice with specific knockouts of YAP or YAP/TAZ in hepatocytes showed reduced inflammation (*408*). To sum up, previous research demonstrated that the Hippo pathway interacts with the NF-κB and acts as a positive or negative regulator of inflammatory immune responses. To which extent the Hippo pathway controls not only basal type III IFN expression at high density, but also basal inflammatory cytokine expression at low density needs to be further studied.

Epithelial junctions also regulate inflammatory processes, and even an intact epithelial barrier with partially disturbed junctional complexes or junctions lacking certain components is sufficient to trigger inflammatory signaling pathways (*258*). It has been broadly reported that ablation of p120-catenin, a core component of adherens junctions, results in activation of the NF-κB pathway and increased expression of pro-inflammatory cytokines in murine epidermis, human skin cells, and in human airway epithelial cells (*263–265*). This phenomenon was explained through the inhibitory role of p120 on RhoA: in the absence of p120, RhoA becomes activated, subsequently leading to the activation of NF-κB (*263*, *265*). A related study found that conditional α-catenin ablation in the skin epidermis results in up-regulation of the activated NF-κB and its pro-inflammatory target genes (*409*). Hemidesmosomes, the junctional complexes that anchor the epithelial cells to the extracellular matrix, were also shown to function as integral components of the innate defense system within epithelial tissues. Loss of major hemidesmosomes components is associated with skin inflammatory defects (*410–412*) and caused inflammation in murine epithelial cells (*413*, *414*). Ablation of hemidesmosome core receptor integrin α6 in mouse IECs quickly induced pro-inflammatory cytokine expression, and this immune response was proposed to result in chronic gut inflammation and subsequent tumor formation (*414*). Taken together, these discoveries point to an indispensable role of junctional complexes in suppressing inflammatory responses in epithelial tissues. This helps to explain the association between defective adherens junctions and the development of inflammatory disorders such as intestinal ulcerative colitis and Crohn's disease (*258*). A genetic analysis found a causal link between cadherins (adherens junction proteins) and Crohn's disease (*415*). Also, mutations of hemidesmosome-associated keratin 8 is considered to increase the risk of inflammatory bowel disease (*416*, *417*). It is therefore essential to understand the link between epithelial junctions and regulation of innate signaling pathways.

Based on my data and a comprehensive review of the literature, I propose an antagonistic relationship between type III IFN signaling and inflammatory responses in mucosal epithelial surfaces. This interplay is intricately controlled by the cellular population context, and it plays a pivotal role in preserving homeostasis while also enabling an effective response to disruptions in the epithelial barrier. In healthy conditions, mucosal surfaces are formed by a dense monolayer of polarized epithelial cells. This specific micro-environment is sensed by single cells, ultimately leading to basal IFNλ3 expression. Type III IFN dependent signaling in the intact epithelium serves as a non-inflammatory immune activation, that supports barrier function. The epithelium can be disrupted from infection, trauma, neoplasm, and autoimmune disease. Upon disruption of the epithelium, the population context of cells changes, resembling the one of cells seeded at low density within my experimental system. Under those conditions, type III IFN signaling is reduced while an inflammatory immune response is activated. The inflammatory immune response serves to clear infection and promote repair during pathology, but dysregulation can support inflammatory diseases such as Crohn's disease.

#### *3.2.3.3. Barrier function of basal IFNλ3 expression*

Beyond their antiviral function, IFNs have been associated with roles in regulating the physical barrier formation at epithelial surfaces. In a mechanism independent of STAT1 signaling, both type I and III IFNs were shown to induce cell junction tightening in brain microvasculature endothelial cells (*172*, *173*). This in turn reduced the blood brain barrier permeability, protecting mice from virus neuroinvasion (*172–174*). Type I IFNs in the airway epithelium induced the production of tight junctions thereby preventing bacteria transmigration (*175*), and counteracted tight junction dissociation during rhinovirus infection (*176*). Similarly, type III IFNs enhanced intestinal barrier formation, protecting human IECs from bacteria (*177*) and *Cryptosporidium parvum* (*178*) infection. Contrary to this, recent studies demonstrated that sustained IFNλ treatment disrupts the airway epithelial barrier, thereby predisposing the host to bacterial superinfections (*171*, *179*). Similarly, it was reported that both type I and III IFNs disrupt airway epithelial repair during recovery from viral infections (*180*). To date there is a controversial view on whether IFNs support or disrupt epithelial tissues. While assessing the formation of a polarized cell monolayer of cells growing in transwell inserts, a compelling observation came to light when comparing T84 IFNλ2/3 KO cells with their T84 WT counterparts. Unlike T84 WT cells, T84 IFNλ2/3 KO cells never achieved a TEER exceeding 1000 Ω/cm² (maximum values were around 400 Ω/cm²) (Fig. 53). Importantly, this phenomenon was not attributed to a lack of cellular growth, as fluorescence imaging revealed that T84 IFNλ2/3 KO cells indeed grew into a confluent monolayer. Work from our partner lab has demonstrated that T84 IFNλ2/3 KO cells either do not form or form aberrant junctional complexes. Furthermore, they established that T84 IFNλ2/3 KO cells fail to establish a semipermeable barrier, in stark contrast to T84 WT cells. These collective findings suggest the possibility that basal IFNλ2/3 expression may play a supportive role in the formation of junctional complexes and the establishment of epithelial barriers.

In this project I demonstrate that IFNλ3 is expressed at basal levels in confluent mucosal epithelial cells, and I elucidate the mechanism responsible for initiating and controlling the type III IFN signaling during homeostatic conditions. Importantly, my results support the notion that the population context plays a crucial role in governing immune signaling processes. This knowledge should be further exploited, as it could provide a novel view to understand inflammatory pathologies and tissue homeostasis.

### 3.3. The population context and virus infection of epithelial cells

Mucosal epithelial tissues are the first physical barrier that pathogenic viruses encounter and need to trespass for an efficient infection of the host. Understanding the dynamics of virus attachment, entry and replication at these surfaces is essential to understand pathogenesis, and provides information to develop possible treatment methodologies at the initial site of infection. In this project I unraveled the profound influence of the population context of epithelial cells on virus infection, in which particularly the cell location within a colony plays a pivotal role. Sparse cells or those at the edges of a population displayed notably higher virus infection levels in comparison to cells embedded in a monolayer. The increased susceptibility of sparse or edge cells to infection was observed consistently across different unrelated viruses, regardless of whether they were enveloped or non-enveloped. Similarly, this spatial heterogeneity of viral infection did not seem to be viral genome dependent as I tested dsRNA

(MRV, Rotavirus), positive sense RNA (HAstV, SARS-CoV-2, SFV), negative sense RNA (GERV, TOSV, UUKV) and dsDNA (Vaccinia virus) viruses. Intriguingly, the spatially restricted infection of epithelial cells did not correlate with virus attachment. Virus particles did bind to all cells within an epithelial cell population, regardless of their location at the edge or the center. This stands in stark contrast with the heterogeneous pattern of effective virus replication, where infection is limited to cells located at the edges of the population. Importantly, virus binding and endocytosis only occurred from the basal membrane of polarized cells localized in the center of a population, and few to no particles did attach to the apical membrane. In summary, the positioning of cells within a population seems to exert an influence on multiple stages of virus binding, endocytosis, and replication, resulting in a pronounced spatial segregation of efficiently infected cells. Within the scope of this thesis the underlying molecular players causing this heterogeneity were not identified.

### 3.3.1. Virus attachment and entry from the basal membrane of polarized epithelial cells

To study the impact of the population context on virus infection, I used a micropatterning based system. Characterization of epithelial cells seeded as population on these micropatterns demonstrated that cells localized in the center are polarized, while edge cells are not (Fig. 68). Moreover, binding and endocytosis assays using one representative virus (GERV) revealed that virus particles only attach and enter from the basal membrane of cells localized in the center of populations. Collectively, these findings imply that the process of GERV attachment and entry exhibits a pronounced asymmetry and is enriched at the basal membrane of polarized epithelial cells. Importantly, previous studies demonstrated that entry of adenovirus (*418*), vesicular stomatitis virus (*419*, *420*), vaccinia virus (*421*, *422*), reovirus (*423*, *424*), porcine rotavirus (*425*, *426*), human cytomegalovirus (*427*) and semliki forest virus (*420*) is also enriched to the basolateral surface of cells. The polarized entry of viral particles may be attributed to the uneven distribution or accessibility of virus attachment factors, or to the asymmetrical distribution of endocytic pathways within the cell.

Surface distribution of virus receptors and attachment factors determines if a virus binds to the cells, and a polarized localization of these factors may restrict the uptake of a virus to a specific domain of the plasma membrane. The reovirus receptor JAM-A is localized at tight junctions and is only accessible from the basolateral side of the cell (*428*). Consistent with the JAM-A localization, reovirus was shown to bind and infect preferentially from the basolateral surface of intestinal and airway epithelia (*423*, *424*). The junctional proteins JAM-A, occludin and ZO1 have also been reported to play a role during rotavirus attachment and entry in MA104 cells (*15*), which would explain the preferential infection of porcine rotavirus through the basolateral surface of epithelial cells (*425*, *426*). The adenovirus receptors CAR and MHC-I were shown to be only present in the basolateral membrane of airway epithelial cells, making these cells partially resistant to apical adenovirus infection (*418*). The opposite distribution was observed for the SARS-CoV-2 receptor ACE2, which preferentially localizes to the apical membrane of polarized epithelial cells (*429*, *430*). Consequently, SARS-CoV-2 was shown to infect the airway epithelium only from the apical membrane (*431*). To study virus binding and endocytosis in epithelial cell populations, I used the orthobunyavirus GERV as a model system. For orthobunyaviruses, sulfation, heparin sulfates, and C-lectins are involved in particle binding to the cell surface (*46–48*), and the receptor DC-SIGN has been reported to promote infection (*49*). While no precise information is available about the localization of these membrane factors in polarized epithelial cells, it is conceivable that the asymmetrical GERV binding in epithelial cells is a result of the basolateral attachment factor localization. Importantly, not only the presence, but also the accessibility of the attachment factors is required for efficient virus binding. Mucosal epithelial surfaces secrete mucins to the apical luminal side to form a thick mucus layer *in vivo* (*432*, *433*). Also *in vitro* human epithelial cell lines, such as T84 and CaCo2, produce mucus (*434*, *435*). It is possible that epithelial cells seeded on micropatterns and located in the center of population secrete mucus to the apical side, and the mucus layer impedes GERV access and binding to the membrane. Degrading this mucus layer using commercially available reagents could give further insights on the underlying reason for the polarized GERV attachment.

Viruses capitalize from cellular endocytic processes to enter the host cells and many (if not most) viruses take advantage of clathrin-mediated endocytosis (CME). Indeed, all viruses which I used in this thesis can be internalized by CME (refer to the introduction section 1.1.2.), except for vaccinia virus which is too large to use this pathway. Intriguingly, I observed enriched CME at the basal membrane of polarized intestinal epithelial cells as determined by the formation of clathrin-coated pits (CCP), with almost no CCPs forming at the apical membrane (Fig. 50). This observation contradicts previous studies on polarized epithelial Madin–Darby canine kidney (MDCK) cells showing that CME takes place at both the apical and basolateral domains (*436–438*). The discrepancies in the results may be attributed to the different origin of the epithelial cells. Specifically, the cells were obtained from either canine (MDCK) or human (T84, CaCo2, and ileum-derived organoids) tissues. And, more importantly, MDCK cells are derived from the kidney epithelium, which constitutes an epithelial tissue lining inner organs. On the other hand, IECs reside on mucosal surfaces, constantly exposed to microbiota from the apical side. It is plausible that epithelial cells at mucosal surfaces have developed mechanisms to restrict viral entry from the luminal side, thereby preventing recurrent infections. It is worth noting that the primary function of the intestinal epithelium is nutrient absorption, raising the question of which mechanisms do IECs employ if CME is not involved. I have demonstrated that macropinocytosis occurs from the apical domain of polarized IECs localized in the center of a population (Fig. 70). Macropinocytosis allows internalization of large amounts of extracellular fluid and solutes (*439*), and could therefore be an efficient mechanism to take up nutrients from the luminal environment.

My findings indicate that GERV exclusively binds to and undergoes endocytosis from the basolateral membrane of polarized epithelial cells. However, it remains essential to fully investigate whether this phenomenon is due to the polarized localization of virus attachment factors or if it arises from limited access to the apical membrane. Additionally, it is crucial to explore whether this enriched basolateral particle binding extends to the other viruses that I used in this thesis. Previous research has already demonstrated a preference for basolateral entry in the case of some of these viruses, such as reovirus, rotavirus, and SFV. These observations lead to the speculation that epithelial cells at mucosal surfaces have evolved mechanisms to hinder pathogen entry from the luminal side, which is in constant contact with microbiota.

### 3.3.2. Spatial heterogeneity of virus infection in epithelial cell populations

All cells within an epithelial cell population, regardless of their location at the edge or the center, were capable of binding and endocytosing GERV particles (Fig. 49). However, efficient GERV replication, as assessed by immunostaining of expressed virus protein, was exclusively observed in cells positioned at the outer edge of cell colonies (Fig. 46). This spatial restriction of infection to the population periphery was consistently observed for several other tested viruses (MRV, HAstV, Rotavirus, SARS-CoV-2, Vaccinia virus, SFV, TOSV and UUKV) (Fig. 44, Fig. 45 and Fig. 46). These viruses were either enveloped or non-enveloped, had a different genome (RNA vs. DNA and double-stranded vs. single-stranded), and are known to use different endocytic pathways for cell entry. This observation rules out the possibility that the spatial heterogeneity during infection is dependent on the virus itself, and its morphology, entry, or replication cycle. Instead, these findings strongly support the existence of a cellular mechanism that restricts active virus replication specifically in cells located at the center of the colonies, while permitting replication in cells positioned at the colony edges.

#### *3.3.2.1. IFNλ2/3 and spatial restriction of virus infection*

Epithelial cells seeded as a confluent monolayer or cells located in the center of a colony are embedded in a population context characterized by high local cell density and cell-to-cell contacts from all sides. Conversely, sparse cells or cells located at the population edge are in a microenvironment of low local cell density with few cell-to-cell contacts, with at least one membrane not touching another cell. The population context is sensed by each cell, inducing a certain behavior. For example, sensing of the population context induces the polarization of epithelial cells that are embedded in a confluent monolayer. Importantly, I demonstrated that cells at high density elicit IFNλ3-signaling at steady state and downstream basal ISG expression (Results section 2.2). In contrary, sparse cells lack this basal IFN-dependent immune activation. It is possible that the basal IFNλ3 expression in densely seeded center cells of a population is sufficient to inhibit viral replication.

To test this, I took advantage of IECs depleted of effector molecules along the IFN pathway (Fig. 53 C-E). Infection of confluent T84 IFNλ2/3 KO cells resulted in high viral load distributed uniformly across the dense epithelial layer, with infection levels significantly higher than in T84 WT cells. This increased sensitivity to the pathogens was specifically linked to the absence of IFNλ2/3 expression, as evidenced by the fact that T84 IFNλ1 KO cells displayed a low viral load, akin to the infection levels observed in T84 WT cells. Within this experiment it is not possible to discern between the role of basal or virus-induced IFNλ2/3 expression. However, it outlines that IFNλ2/3 expression inhibits virus replication in confluent cells. I infer that the expression of basal IFNλ2/3 (as opposed to virus-induced IFNλ2/3 expression) likely plays a role in restricting virus infection.

As previously noted, IFNλ2/3 do not form complete tight junctions and are unable to establish a TEER. This raises two hypothesis explaining why a T84 IFNλ2/3 KO monolayer is more susceptible to virus infection than a T84 WT monolayer: (a) the basal or virus-induced IFNλ2/3 expression inhibits replication after virus entry, or (b) basal IFNλ2/3 expression supports the formation of junctional complexes within an epithelial monolayer. If junctional complexes between the cells that form the monolayer are not intact, viruses can easier infect the cells. These two possibilities can be addressed through (a) a supernatant transfer assay to determine if there is a different basal protection from the supernatant of IFNλ2/3 KO or WT cells, or (b) through the use of a ZO1 KO cell line to address the significance of intact junctional complexes for virus sensitivity.

I showed that IRF3 is the transcription factor driving basal IFNλ3 expression (Fig. 33, Fig. 36, Fig. 37). Consequently, knock-out of IRF3 should have a similar effect as knock-out of IFNλ2/3 on infection of epithelial monolayers. However, infection levels of a T84 IRF3 KO monolayer are comparable to the infection levels of a T84 WT monolayer, and much lower than of a T84 IFNλ2/3 KO monolayer (Fig. 53). This is counterintuitive and the molecular dynamics underlying this observation remain elusive. Work in our laboratory has shown that T84 IRF3 KO cells appear to form intact and functional tight junctions when they grow into a monolayer. This supports the hypothesis that tight junctions, rather than the antiviral effect of ISGs, are essential to impede virus infection of epithelial tissues.

### *3.3.2.3. Trypsin and virus infection of epithelial cell populations*

As extensively discussed, virus infection is restricted to the edge of epithelial cell populations. Interestingly, treatment of epithelial cell populations with trypsin from the basal side resulted in virus infection in the center cells and not only in the edge cells (Fig. 52). The serine protease trypsin cleaves proteins that anchor cells to the cell culture vessel or to each other. Hence, subjecting epithelial cell populations to trypsin treatment disrupts the intercellular complexes (tight and adherens junctions), which clearly makes cells more susceptible to virus infection. This observation supports the notion that junctional complexes play a pivotal role in inhibiting virus infection in a dense epithelial monolayer. Experiments in which junctional complexes are modulated will further support this notion. Many compounds that inhibit the formation or induce disassembly of intercellular complexes are commercially available and can be used for such experiments. Important to note here is that only basal trypsin treatment made center cells susceptible to rotavirus and MRV infection. Contrary to this, apical trypsin treatment did not show any effect and, as similar to experiments without trypsin treatment, only edge cells in a population were efficiently infected with rotavirus and MRV. It is possible that epithelial cells secrete a protective mucus layer on their apical side, which might hinder trypsin from reaching the cells and disrupting the junctional complexes.

Junctional complex disruption could result in center cells adopting a cellular environment (population context) more akin to that of edge cells, which lack direct connections to neighboring cells. As a consequence, viruses might gain access to the lateral side of the cell, similar to what occurs with edge cells, potentially enhancing virus binding, entry, and infection. Moreover, the disruption of intercellular connections might also induce a shift in the cellular phenotype from 'center' to 'edge', resulting in changes of basal type III IFN signaling and homeostatic immune activation. Significantly more research is needed to disentangle the causal relationship from the observed effect, and to elucidate the sequence of molecular events that lead to the observed phenotype.

This project studied the intricated interplay between the population context and virus infection in epithelial cells. I demonstrated that virus binding and endocytosis can occur in all cells from the basal membrane, but efficient virus replication is predominantly confined to edge cells within cell populations (Fig. 65 A). While numerous questions remain unanswered, the infection restricted to edge cells in epithelial cells holds significant physiological implications. It becomes evident that intact epithelial surfaces are protected from efficient virus infection (Fig. 65 B). However, when the epithelium is compromised due to diseases or other factors, microlesions may emerge, localizing cells to edges of the cell monolayer. Edge cells exhibit a heightened susceptibility to virus infection, thereby facilitating viral dissemination and inducing inflammatory processes (Fig. 65 B). This, in turn, can support the progression of diseases such as ulcerative colitis and Crohn's disease.

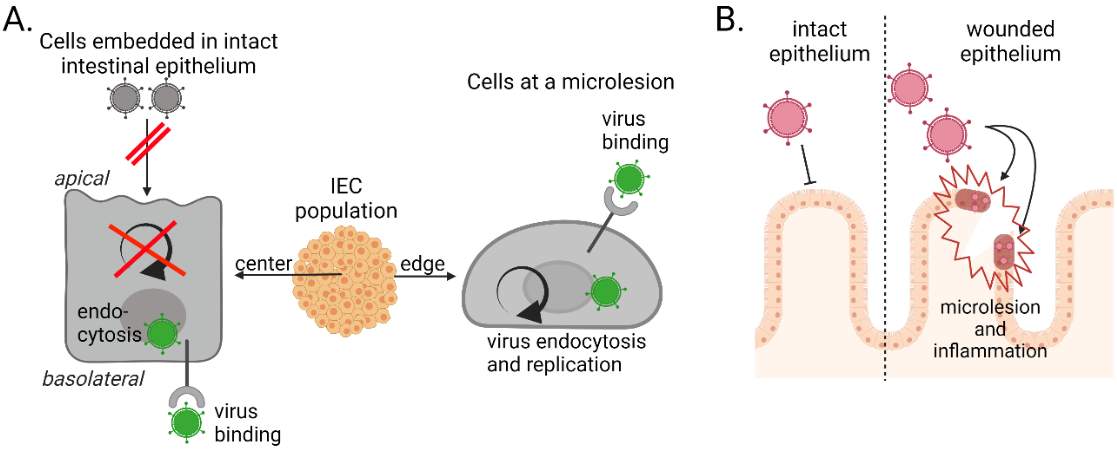

**Fig. 66. Spatial heterogeneity during virus infection.** (A) Virus binding, endocytosis and efficient replication in cells located at the edge and the center of an intestinal epithelial cell (IEC) population. (B) Hypothetical localization of virus infection within the intestinal epithelium. The intact epithelium is not permissive for viruses, and only cells located at microlesions can get infected by viruses supporting inflammatory processes at the wound side.

### 3.4. Type III IFNs control SARS-CoV-2 in intestinal epithelial cells

SARS-CoV-2 infects the gastrointestinal tract, and a major fraction of COVID-19 patients display gastrointestinal symptoms and shed viral genome within their feces (*183*, *185*, *187–190*, *192*). This underscores the importance of understanding how IECs control virus infection, allowing us to better characterize and treat the associated pathogenesis. In this study, I investigated the kinetics and differences of type I and III IFNs in establishing an antiviral program against SARS-CoV-2 in human IECs. My results show that SARS-CoV-2 induces an IFN-dependent immune response in IECs (Fig. 54), and that both type I and III IFNs are efficient in mounting a protective state against the virus (Fig. 55 and Fig. 56). However, over the course of infection, endogenous type III IFNs are essential in controlling virus spread, while endogenous type I IFNs play a minor role in restricting SARS-CoV-2 (Fig. 55). Additionally, only low concentrations and shorter pretreatment time with type III IFNs, as compared to type I IFNs, were sufficient to inhibit virus infection (Fig. 56 and Fig. 59). This increased sensitivity to type III IFNs was specific to SARS-CoV-2, as the same IFN concentrations and treatment time did not control VSV infection (Fig. 57 and Fig. 59). Importantly, type III IFNs induced a long-lasting antiviral state in IEC and inhibited SARS-CoV-2 infection, but not VSV infection, even at 72 h post-treatment (Fig. 61). Altogether my results indicate that type III IFNs, rather than type I IFNs, are better in clearing SARS-CoV-2 infection in the human intestinal tract.

#### 3.4.1. Comparing the antiviral effect of type I and type III IFNs against SARS-CoV-2 in human intestinal epithelial cells

Within this study I aimed to understand the kinetics of type I and type III IFN signaling to control SARS-CoV-2 infection in IECs. Comparing whether these IFNs have a more potent antiviral effect at the same concentration is intrinsically difficult, since the IFNs are commercially available at concentrations expressed in different units. Type III IFNs are available in protein concentrations (ng/mL), while type I IFN concentration is expressed as an antiviral activity (U/mL). To circumvent this issue, I decided to perform the same kinetic assays that I performed on SARS-CoV-2 but in VSV instead. VSV is considered a gold-standard model system to study IFN-dependent signaling, and a previous study from my lab determined that type III IFNs required a longer time to induce a protective state in human IECs against VSV as compared to type I IFNs (*123*). First, I could reproduce the previous results that type I IFN is more potent in inhibiting VSV infection (Fig. 57, Fig. 59). By comparing the effect of both type I and type III IFNs on VSV and SARS-CoV-2 infection (Fig. 56, Fig. 57 and Fig. 59), I demonstrated that low concentrations of type I IFN were able to control VSV infection, while having little to no effect on SARS-CoV-2 infection. Reciprocally, low concentrations of type III IFNs were able to control SARS-CoV-2, but with limited to no impact on VSV. The different efficiency in conferring antiviral protection against two different viruses within the same cell type implies that type I and III IFNs induce distinct antiviral states. These distinct states appear to exhibit greater potency against specific viruses. While there is limited evidence supporting the idea that type I and type III IFNs trigger the expression of different ISGs (*440*), recent findings demonstrated that both cytokines induce the same set of ISGs but with markedly different timing and magnitude (*115*, *123*, *125*, *441–444*), potentially leading to the formation of unique antiviral states.

Several studies support the importance of both type I and type III IFNs in controlling SARS-CoV-2 in the human gut (*194–196*, *445*), however the difference between the two type of IFNs had not yet been explored. My results demonstrate that there are major differences in the kinetics of antiviral properties induced by type I and III IFNs against SARS-CoV-2 in human IECs, and that type III IFNs are overall more efficient to restrict virus infection (lower dosage and shorter treatment times) in these cells than type I IFNs. Type I and III IFNs also act on airway epithelial cells, which represent the primary site of SARS-CoV-2 infection. However, only few studies demonstrate that type III IFNs induce a protective state against SARS-CoV-2 in the human lung epithelium (*206*, *208*, *211*). Moreover, a direct comparison between both IFNs against this virus has not been done for the lung epithelium. Inhibition of *de novo* infectious virus production in Calu-3 cells suggests that type I IFN would be more potent than type III IFNs (*208*). This underscores the need to investigate SARS-CoV-2 across diverse cellular models covering the broad virus tropism. Such an approach is essential due to potential organ-specific variations in the pathogen's susceptibility to distinct antiviral strategies.

### 3.4.2. IFN-dependent inhibition of SARS-CoV-2 structural protein translation

I showed by immunostaining of the virus nucleocapsid protein (N-protein) and by quantification of the viral genome that both type I and III IFNs restrict SARS-CoV-2 in a concentration-dependent manner (Fig. 56). Interestingly, inhibition of N-protein with a certain IFN concentration did not correlate with inhibition of the virus genome. Indeed, viral genome load was still measured in samples where no N-protein could be detected. To further investigate this discrepancy between the number of viral genome copies and the presence of N-protein-positive infected cells, I assessed whether single cells were positive for either N-protein alone, J2 alone, or both N-protein and J2. N-protein represented the translation of structural proteins, and J2 labelled double-stranded RNA (dsRNA) and represented virus RNA synthesis and genome transcription. In untreated SARS-CoV-2-infected cells, around 15% were positive for J2 only and 16% were positive for both (J2 and N-protein) (Fig. 58). This pattern is in agreement with the replication cycle, in which first viral RNA is synthesized and then viral structural proteins are translated (*197*). Interestingly, in IFN-treated cells, still 15% of cells were positive for viral dsRNA only, while cells positive for N-protein significantly decreased (Fig. 58). This observation was especially prominent in type III IFN-treated cells. These findings suggest that one potential mechanism by which IFNs restrict the spread of the virus is by inhibiting the translation of subgenomic RNA, particularly the translation of structural proteins. Immediately after entry, the genomic viral RNA undergoes an initial translation step leading to expression of the ORF1a/b polyprotein, which results in nonstructural proteins that form the viral replication and transcription complex (*197*). My results showing virus RNA synthesis in samples without N-protein expression suggests that the initial virus genome translation of nonstructural proteins is less affected by IFN treatment than the later translation of structural proteins.

Previous research has reported that type I IFN treatment during dengue virus and HIV infection can impact virus protein translation (*446*, *447*), but little is known about the type I and III IFN-mediated inhibition of coronavirus N-protein translation, especially concerning SARS-CoV-2 infection. Several ISGs have been identified as potentially inhibiting viral protein translation, which may play crucial roles in the IFN-dependent response to SARS-CoV-2. One well-studied ISG is PKR, which, upon activation, phosphorylates EIF2α to halt cellular translation (*448*). Also, members of the IFIT family demonstrated their ability to suppress viral protein translation through various mechanisms, such as binding to the eukaryotic translation initiation factor 3 (eIF3) and thereby interfering with the assembly of the preinitiation complex, or by directly sequestering viral mRNA (*449*, *450*). Moreover, ISG20 was shown to impair translation of virus protein without affecting cellular protein translation by discriminating self from non-self (*211*).

In conclusion, my observations suggest a possible mechanism of action for IFNs to limit SARS-CoV-2 spread in human IECs by inhibiting the production of N-protein (and possibly other viral proteins). This subsequently reduces the release of functional virus particles to neighboring cells. Further research is needed to uncover the intricate details of the mechanism underlying IFN-mediated inhibition of viral genome replication and translation.

### 3.4.3. Type III IFNs as a therapeutic candidate to inhibit SARS-CoV-2 in the human intestinal tract

Type III IFNs act primarily at mucosal barriers, including the lung and the intestinal epithelium, due to the restricted IFNLR1 receptor expression to epithelial and some immune cells (*94*, *391*). Crucially, a well-established model proposes that within the intestinal tract, type III IFNs serve as a safeguard against enteric infection of epithelial cells. They achieve this protection without triggering an exacerbated immune response and tissue damage, thus helping to maintain tissue homeostasis. In contrast, type I IFNs are known to elicit a more robust immune response and protect the underlying *lamina propria* when a pathogen spreads beyond intestinal epithelial cells (*181*, *392*). Importantly and as reviewed before (*451*), type I IFN treatment was shown to support development of autoimmune diseases and can induce tissue damage. This, together with the fact type III IFNs act fast, require lower concentrations, and have a longer-lasting effect against SARS-CoV-2 as compared to type I IFNs, positions type III IFNs as a suitable therapeutic candidate against SARS-CoV-2 infection in the gut.

In the past years, type I IFNs have been approved for use in treating virus infection and, in light of the recent pandemic, many studies and clinical trials focused on establishing efficient IFN-α-based therapies against SARS-CoV-2 (*452*, *453*). Moreover, pegylated IFNλ is undergoing phase 3 clinical trials as an early treatment against COVID-19 (*454*). However, studies on the effect of IFN-treatment on COVID-19 pathogenesis are still contradictory. Additionally, the timing of IFN treatment initiation, the duration of treatment, the IFN type used and other pivotal factors of IFNs are not yet well defined for a broad medical use against SARS-CoV-2 infection (*452*, *453*). Besides the therapeutic administration of IFNs, a major unanswered question in the field is whether IFNs serve protective or detrimental functions in COVID-19. While some studies support that defective IFN responses are in hand with severe COVID-19 pathogenesis (*455*, *456*), other studies reported that prolonged IFN production correlates with negative clinical outcomes (*216*, *218*). It has recently been demonstrated that IFN production impairs lung function and triggers severe disease in mouse models of lung viral infection (*171*, *180*). Interestingly, a study showed that IFN-λ1 and IFN-λ3 drive protective ISGs in the upper airways of mildly ill patients infected with SARS-CoV-2, while critical patients express IFN-αβ and IFN-λ2, and have low ISGs and high p53 expression (*457*). Taken together, while IFNs hold potential for use as treatment for SARS-CoV-2, research to fully characterize the kinetics and mode of action of IFNs in the different affected organs are required to choose adequate treatment timing, site of administration and dosage.

# 4. Material and Methods

## 4.1. Material

### 4.1.1. Chemicals and Reagents

**Table 1**: List of chemicals and reagents

| **Chemicals and Reagents** | **Manufacturer** | **Catalog number** |
|---|---|---|
| A83-01 (activin receptorlike kinase (ALK)-5 inhibitor) | Millipore Sigma | SML0788 |
| 30% Acrylamide/Bis-acrylamide solution (37.5:1) | Bio-Rad | 1610158 |
| Acetic acid | Sigma-Aldrich | 320099 |
| Acetone | Fisher Scientific | A18-4 |
| Advanced Dulbecco's Modified Eagle Medium: Nutrient Mixture F-12 (DMEM / F-12) (1:1) | Gibco | 12634010 |
| Agar | Fisher-Scientific | BP1423-500 |
| Ammonium Acetate | Sigma-Aldrich | 73594 |
| Ammonium Persulfate (APS) | AppliChem | A1142 |
| Ampicillin (100 mg/mL) | Roth | K029.2 |
| B27 | Fisher Scientific | 17504044 |
| Blasticidin | Invivogen | ant-bl-1 |
| Bovine Serum Albumin (BSA) | Sigma-Aldrich | A3294 |
| Bromphenol Blue | AppliChem | 131165 |
| Calcium Chloride (CaCl2) | Fisher | AC423525000 |
| Collagen from human placenta Type IV | Sigma-Aldrich | C5533-5MG |
| Collagen from rat tail | Sigma-Aldrich | C7661 |
| cOmplete protease inhibitor | Sigma-Aldrich | 11836170001 |
| 2′,3′-Dideoxycytidine (ddC) | Sigma-Aldrich | D5782 |
| DAPI solution | BD-Biosciences | 564907 |
| diABZ STING agonist (Compound 3) | Selleckchem | 217.00 |
| DirectPCR-Lysis Reagent Cell | PeqLab | 31-301-C |
| DMSO (Dimethl Sulfoxide) | Fisher Scientific | BP231-100 |
| DNase/RNase-Free Distilled Water (UltraPure™) | Thermo Fisher Scientific | 10977015 |
| Dublecco’s Modified Eagle Medium: Nutrient Mixture F-12 (DMEM/F12) (1:1) | Gibco | 31330 |
| Dublecco’s Modified Eagle Medium GlutaMax (DMEM/GlutaMax) | Gibco | 31965 |
| EDTA (disodium salt dihydrate) | Sigma-Aldrich | E5134 |
| EGF | Gibco | PMG8041 |
| Ethanol absolute (EtOH) | Sigma-Aldrich | 32205 |
| Ethidium bromide solution | MP Biomedicals | ETBC1001 |
| Fetal Bovine Serum (FBS) | Capricorn Scientific | FBS-11A |
| Fluorescein isothiocyanate–dextran (FITC)-labelled Dextran, 4 kDa | Sigma-Aldrich | 46944 |
| Gastrin | Sigma-Aldrich | G9145 |
| Glasgow Minimum Essential Medium (GMEM) | Fisher Scientific | 11710035 |
| Glo Lysis buffer | Promega | E2661 |
| GlutaMAX | Gibco | 35050061 |
| Glycerol | Sigma-Aldrich | G7757 |
| Glycine | Sigma-Aldrich | G7126 |

| | | |
|---|---|---|
| Guanidine thiocyanate | Fisher | 411110010 |
| HEPES | Sigma-Aldrich | H7523 |
| Human recombinant IFN-beta1a (IFNβ) | R&D SYSTEMS | 8499-IF-010 |
| Human recombinant IFNλ1 (IL-29) | R&D SYSTEMS | 1598-IL-025/CF |
| Human recombinant IFNλ2 (IL28 | R&D SYSTEMS | 1587IL025/CF |
| Human recombinant IFNλ3 (IL-28B) | R&D SYSTEMS | 5259-IL-025/CF |
| IGF-1 | Fisher | 590908 |
| Iscove's Modified Dulbecco's Medium (IMDM) | Gibco | 21980 |
| Isopropanol (2-Propanol) | Carl Roth | 9781.1 |
| Keratinocyte SFM (bovine pituitary extract (BPE) human recombinant epidermal growth factor (EGF) supplements are delivered with medium) | Thermo Fisher Scientific | 17005042 |
| LB Broth | Fisher Scientific | BP1426-500 |
| Li-Cor Intercept (TBS) Blocking Buffer | Licor | 927-60001 |
| Matrigel | Corning | 354230 |
| McCoy’s 5A (Modified) Medium | Gibco | 16600082 |
| 2-Mercaptoethanol (β-Mercaptoethanol) | Sigma-Aldrich | 8.05740 |
| Methanol | Sigma-Aldrich | 34860 |
| mPEG-SVA (Methoxy-Poly (Ethylene Glycol)-Succinimidyl Valerate) (5 kDa) | Laysan Bio Inc. | MPEG-SVA-5000 |
| N-acetyl-cysteine | Sigma-Aldrich | A9165 |
| 0.2 µm Nitrocellulose membrane | Bio-Rad | 1704158 |
| Noggin | Peptrotech | 250-38-100UG |
| Non-Essential Amino Acids Solution (100X) | Thermo Fisher Scientific | 11140050 |
| OptiMEM Reduced Serum Media | Gibco | 31985062 |
| Paraformaldehyde (PFA) | Roth | 0335.3 |
| PEI (Polyethylenimine) | Polysciences | 23966-100 |
| Penicillin Streptomycin Solution | Gibco/Life Technologies | 15140122 |
| PhoSTOP phosphatase inhibitor tablets | Roche | 04 906 837 001 |
| Pierce ECL Western Blotting Substrate | Fisher | 32209 |
| PLL(20)-g[3.5]- PEG(2) | SuSoS Surface Technology | Not available |
| PLPP gel | Alvéole Lab | NoT available |
| Polybrene Transfection Reagent | Sigma | TR-1003 |
| Poly-L-lysine solution (PLL) | Sigma-Aldrich | P8920 |
| Precision Plus Protein Standard | Bio-Rad | 161-0374 |
| ProLong Gold Antifade Mountant with DAPI | Invitrogen | P36941 |
| Puromycin | InvivoGen | ant-pr-1 |
| Putrescine | Millipore SIGMA | 51799-100MG |
| Quanti Blue Solution (Alkaline phosphatase detection medium - Liquid form) | InvivoGen | rep-qbs |
| Sodium chloride (NaCl) | Carl Roth | 9265.1 |
| Sodium dodecylsulfate (SDS) | Carl Roth | 0183 |
| Spermidine | Millipore SIGMA | S0266-1G |
| Spermine | Millipore SIGMA | S4264-1G |
| SsoAdvanced Universl SYBR Green Supermix | Bio-Rad | 172-5274 |
| Steady-Glo buffer (Luciferase Assay System) | Promerga | E2510 |
| Sulfo NHS-SS-Biotin | Thermo Fisher Scientific | 21331 |
| TEMED | Carl Roth | 2367.1 |
| Transferrin-647 | Invitrogen | T23366 |
| Tris Base | Fisher Scientific | BP152-500 |

| | | |
|---|---|---|
| Tris Hydrochloride (Tris HCl) | Sigma-Aldrich | 10812846001 |
| 0.05% Trypsin-EDTA | Gibco | 25300054 |
| 0.25% Trypsin-EDTA | Gibco | 25200056 |
| Tryptose phosphate broth | Thermo Fisher Scientific | 18050039 |
| Triton X-100 | Sigma-Aldrich | X100-500ML |
| Trypsin from bovine pancreas | Sigma-Aldrich | T1426-100MG |
| Tween-20 | MP Biomedicals | 500-018-3 |

**Table 2:** List of inhibitors

| **Inhibitors** | **Manufacturer** | **Catalog number** |
|---|---|---|
| BX795 (TBK1 inhibitor) | MedChemExpress | HY-10514 |
| Difluoromethylornithine hydrochloride hydrate (DFMO) (inhibitor of polyamine biosynthesis) | TargetMol | T2593 |
| G150 (cGAS inhibitor) | MedChemExpress | HY-128583 |
| H151 (STING inhibitor) | MedChemExpress | HY-112693 |
| Pyridine 6 (JAK inhibitor) | Calbiochem/Merck Chemicals | 420099 |
| RU.521 (cGAS inhibitor) | MedChemExpress | HY-114180 |
| STING-IN-2 (STING inhibitor) | MedChemExpress | HY-138682 |

### 4.1.2. Media and buffers

**Table 3:** Compounds and concentrations for human organoid basal and differentiation media

| **Basal media** | | **Differentiation media** | |
|---|---|---|---|
| **Compound** | **Final concentration** | **Compound** | **Final concentration** |
| Advanced DMEM/F12 + 2 mM GlutaMAX + 10 mM HEPES + 100 U/mL penicillin and 100 µg/mL streptomycin | | Advanced DMEM/F12 + 1x GlutaMAX + 10 mM HEPES +100 U/mL penicillin and 100 µg/mL streptomycin | |
| L-WRN cell conditioned supernatant (WNT, R-Spondin, Noggin) | 62.5% (v/v) | R-Spondin cell conditioned supernatant (WNT, R-Spondin, Noggin) | 10.5% (v/v) |
| B-27 Supplement | 1x | B-27 Supplement | 1x |
| EGF (recombinant mouse) | 50 ng/mL | EGF (recombinant mouse) | 50 ng/mL |
| A83-01 | 500 nM | A83-01 | 500 nM |
| IGF-1 (recombinant human) | 100 ng/mL | IGF-1 (recombinant human) | 100 ng/mL |
| FGF-basic (recombinant human) | 50 ng/mL | FGF-basic (recombinant human) | 75 ng/mL |
| Noggin (recombinant mouse) | 25 ng/ml | Noggin (recombinant mouse) | 50 ng/ml |
| Gastrin | 10 nM | Gastrin | 10 nM |
| N-acetyl-cysteine | 1 mM | | |

**Table 4:** List of buffer solutions and concentrations

| **Buffer** | **Composition** |
|---|---|
| Acid wash | 0.2 M acetic acid<br>0.5 M NaCl<br>In PBS |
| Cytosolic protein extraction buffer | 0.1 % (v/v) NP40 |

| | |
|---|---|
| | 1x cOmplete protease inhibitor<br>1x PhoSTOP phosphatase inhibitor<br>In PBS |
| Immunofluorescence blocking buffer | 3% BSA (w/v)<br>In PBS |
| Immunofluorescence fixing buffer | 2% PFA<br>In PBS |
| Immunofluorescence permeabilization buffer | 0.5% Triton X-100 (v/v)<br>In PBS |
| Immunofluorescence reagent diluent | 1% BSA (w/v)<br>In PBS |
| Leammli buffer (4x) | 200 mM Tris base (pH 6.8)<br>8% (w/v) SDS<br>40% (v/v) glycerol<br>4% (v/v) ß-mercaptoethanol<br>0.08% (v/v) bromphenol blue<br>In $H_2O$ |
| PBS (Phosphate buffered saline) | 137 mM NaCl<br>2.7 mM KCl<br>10 mM $Na_2HPO_4$<br>2 mM $KH_2PO_4$<br>In $H_2O$ |
| RIPA ++ buffer | 150 mM sodium chloride<br>1 % (v/v) Triton X-100<br>0.5 % (w/v) sodium deoxycholate<br>0.1 % (w/v) SDS<br>50 mM Tris base (pH 8.0)<br>1x cOmplete protease inhibitor<br>1x PhoSTOP phosphatase inhibitor tablets<br>In $H_2O$ |
| RNA Lysis Buffer | 4 M Guanidine Thiocyanate<br>25 mM Tris HCl (pH 7)<br>In $H_2O$<br>pH = 7 |
| RNA Wash Buffer 1 | 1 M Guanidine Thiocyanate<br>25 mM Tris HCl (pH 7)<br>10 % (v/v) Ethanol<br>In $H_2O$<br>pH = 7 |
| RNA Wash Buffer 2 | 25 mM Tris HCl (pH 7)<br>70 % (v/v) Ethanol<br>In $H_2O$<br>pH = 7 |
| SDS-PAGE running buffer | 25 mM Tris base<br>190 mM Glycine<br>0.1 % (w/v) SDS<br>In $H_2O$<br>pH = 7 |
| SDS-PAGE running gel buffer (4x) | 1.5 M Tris base (pH 8.8)<br>0.4% (w/v) SDS<br>In $H_2O$ |
| SDS-PAGE running gel (12 %) | 3.6ml Acrylamide/Bis-acrylamide solution (30%) |

| | |
|---|---|
| | 3.15 mL millipore H2O<br>2.25 mL running gel buffer<br>75 µL APS (10% w/v)<br>15 µL TEMED |
| SDS-PAGE stacking gel buffer (4x) | 0.5 M Tris base (pH 8.8)<br>0.4% (w/v) SDS<br>In $H_2O$ |
| SDS-PAGE stacking gel (5%) | 500 µL Acrylamide/Bis-acrylamide solution (30%)<br>1.75 mL millipore H2O<br>0.75 mL stacking gel buffer<br>25 µL APS (10 % w/v)<br>5 µL TEMED |
| TBS (Tris buffered saline) | 20 mM Tris base<br>137 mM Sodium chloride<br>In $H_2O$ |
| Western blot Washing buffer: 0.5% Tween20/TBS | 0.5% (v/v) Tween 20<br>In TBS |
| Western blot Blocking solution | 5% (w/v) BSA<br>0.1% (v/v) Tween 20<br>In 1x TBS |

### 4.1.3. Plasmids

**Table 5:** List of plasmids (obtained as bacteria agar stab)

| Plasmid name | Description | Antibiotic | Origin |
|---|---|---|---|
| pLKO.1 shRNA scrambled (Puromycin) | Lentiviral vector containing scrambled shRNA, serving as a knock-down control. | Bacterial resistance: Ampicillin<br>Mammalian selection: Puromycin | Boulant Lab (University of Florida) |
| psPAX | 2nd generation lentiviral packaging plasmid | Bacterial resistance: Ampicillin | Addgene #12259 |
| pmDG.2 | Envelope plasmid for production of lentiviral vector | Bacterial resistance: Ampicillin | Addgene #12259 |
| STING knock-down (KD) | Plasmid containing an shRNA sequence targeting human STING (target sequence: CAGAGCTATTTCCTTCCACA) | Bacterial resistance: Ampicillin<br>Mammalian selection: Puromycin | Millipore Sigma Mission® shRNA, #SHCLNG (Bacterial Stock), TRC Clone ID: TRCN0000163029 |
| YAP/TAZ knock-down (KD) #1 | Plasmid containing an shRNA sequence targeting human YAP/TAZ (target sequence: GCCACCAAGCTAGATAAAGAA) | Bacterial resistance: Ampicillin<br>Mammalian selection: Puromycin | Millipore Sigma Mission® shRNA, #SHCLNG (Bacterial Stock), TRC Clone ID: TRCN0000300325 |
| YAP/TAZ knock-down (KD) #2 | Plasmid containing shRNA sequence targeting human YAP/TAZ (target sequence: GCGTTCTTGTGACAGATTATA) | Bacterial resistance: Ampicillin<br>Mammalian selection: Puromycin | Millipore Sigma Mission® shRNA, #SHCLNG (Bacterial Stock), |

| | | | |
|---|---|---|---|
| | | | TRC Clone ID: TRCN0000370007 |
| YAP over-expression (OE) #1 (pGAMA-YAP) | Lentiviral over-expression vector for human YAP. Fluorescent report: mCherry | Bacterial resistance: Ampicillin | Addgene #74942 |
| YAP over-expression (OE) #2 (EFSp-GFP-YAP) | Lentiviral vector to constitutively express human YAP under control of the EFS promoter. Fluorescent report: eGFP. | Bacterial resistance: Ampicillin<br>Mammalian selection: Puromycin | Addgene #174168 |
| YAP over-expression (OE) #3 (PGKp-GFP-YAP) | Lentiviral vector to constitutively express human YAP under control of the human PGK promoter. Fluorescent reporter: eGFP. | Bacterial resistance: Ampicillin<br>Mammalian selection: Puromycin | Addgene #174172 |
| TAZ over-expression (OE) (pLL3.7 EGFPC2 TAZ) | Lentiviral vector expressing GFP-fused to human TAZ. Fluorescent reporter: GFP | Bacterial resistance: Ampicillin | Addgene #66850 |

### 4.1.4. Cell lines and Viruses

**Table 6**: List of cell lines

| **Cell line** | **Description** | **Origin** |
|---|---|---|
| A549 | Human lung carcinoma cell line | ATCC #CCL-185 |
| BHK-21 (ISA) | Golden hamster kidney fibroblasts | Obtained from Pierre-Yves Lozach Group (University Claude Bernard Lyon 1) |
| CaCo2 | Human epithelial colorectal adenocarcinoma cell line | ATCC #HTB-37 |
| CaCo2 σ2-GFP | CaCo2 cell line stably transduced with σ2 (subunit of the AP2 complex) coupled to GFP | Generated by me during my Master's thesis |
| Calu3 | Human lung carcinoma cell line | ATCC #HTB-55 |
| HEK 293T | Human embryonic kidney cell line (epithelial) | ATCC #CRL-3216 |
| HEK-Blue™ IFN-α/β cells | Type I IFN reporter HEK 293 cells | Invivogen #hkb-ifnab |
| HEK-Blue™ IFN-λ cells | Type III IFN reporter HEK 293 cells | Invivogen #hkb-ifnl |
| HK-2 | Proximal tubular cell line derived from human kidney (epithelial) | Obtained from Yogesh Scindia Group (University of Florida) |
| HT-29 | Human epithelial colorectal adenocarcinoma cell line | Stephanie Karst Lab (University of Florida) |
| Huh-7 | Human hepatocellular carcinoma (epithelial-like) | Obtained from Ralf Bartenschlager Group (University Hospital Heideberg) |
| T84 | Human colon adenocarcinoma cell line | ATCC #CCL-248 |

| | | |
|---|---|---|
| T84 IRF3 KO (clone 4b) | T84 cell line with IRF3 knockout (antibiotic resistance Puromycin) | Generated by me during my Master's thesis |
| T84 IFNλ1 KO (clone L1A4-T) | T84 cell line with a IFNλ1 knock-out (antibiotic resistance Puromycin) | Generated in the lab by Yagmur Keser |
| T84 IFNλ2/3 KO (clone L2B4-T) | T84 cell line with a IFNλ2/3 knock-out (antibiotic resistance Blasticidin) | Generated in the lab by Dorothee Reuss |
| T84 IFNAR KO | T84 cell line with a IFNAR1 knock-out | Generated in the lab by Kalliopi Pervolaraki |
| T84 IFNLR KO | T84 cell line with a IFNLR1 knock-out | Generated in the lab by Kalliopi Pervolaraki |
| T84 IFNR dKO | T84 cell line with a double knockout of IFNLR1 and IFNAR1 | Generated in the lab by Kalliopi Pervolaraki |
| T84 ZO1 KO | T84 cell line with a ZO1 KO (antibiotic resistance Blasticidin) | Generated in the lab by Patricio Doldan |
| T84 prom-Mx1-eGFP (clone 1) | T84 IFN-reporter cell line stably transduced with eGFP coupled to an Mx1 promoter (antibiotic resistance Puromycin). This cell line was used for experiments testing response to IFNs. | Generated in the lab by Patricio Doldan, single cell cloned by me |
| T84 prom-Mx1-mcherry (clone 2) | T84 IFN-reporter cell line stably transduced with mcherry coupled to an Mx1 promoter (antibiotic resistance Puromycin). This cell line was used for experiments testing basal IFN expression and signaling. | Generated in the lab by Patricio Doldan |
| T84 σ2-GFP | T84 cell line stably transduced with σ2 (subunit of the AP2 complex) coupled to GFP (antibiotic resistance Puromycin) | Generated in the lab by Markus Mukenhirn |
| T84 pLKO.1 shRNA scrambled (Puromycin) | T84 cell line stably transduced with a scrambled shRNA as a knock-down control (antibiotic resistance Puromycin) | Generated by me within this thesis |
| T84 STING KD | T84 cell line with STING knock-down by shRNA (antibiotic resistance Puromycin) | Generated by me within this thesis |
| T84 YAP/TAZ KD #1 | T84 cell line with YAP/TAZ knock-down by shRNA #1 (antibiotic resistance Puromycin) | Generated by me within this thesis |
| T84 YAP/TAZ KD #2 | T84 cell line with YAP/TAZ knock-down by shRNA #2 (antibiotic resistance Puromycin) | Generated by me within this thesis |
| T84 YAP OE #1 | T84 cell line over-expressing YAP1 using plasmid #1 | Generated by me within this thesis |
| T84 YAP OE #2 | T84 cell line over-expressing YAP1 using plasmid #2 (Puromycin) | Generated by me within this thesis |
| T84 YAP OE #3 | T84 cell line over-expressing YAP1 (using plasmid #3 (Puromycin) | Generated by me within this thesis |
| T84 YAP OE | T84 cell line over-expressing TAZ | Generated by me within this thesis |
| Vero E6 | African green monkey kidney cell line (epithelial) | ATCC #CRL-1586 |

**Table 7:** List of viruses and dilutions

| Virus | Plaque forming units (pfu) per mL | Virus dilution or Multiplicity of infection (MOI) |
|---|---|---|
| HAstV1 P2 [1] | $5.6x10^5$ pfu/mL (as determined in T84)<br>$5.6x10^7$ pfu/mL (as determined in CaCo2) | 1:50 dilution |
| GERV [2] | $7.5x10^8$ pfu/mL | MOI 10 for T84 and CaCo2 |
| GERV-Atto488 [2] | Non determined | 1:50 dilution |
| GERV-Atto647 [2] | Non determined | 1:10 dilution |
| MRV strain Type 3 Dearing (T3D), clone 9, P4 [3] | $9.1x10^1$ pfu/mL (as determined in T84) | 1:500 dilution or MOI1 for experiment of results 2.1.6. |
| Rotavirus dUnaG [4] | $7.2x10^7$ pfu/mL (as determined in MA104) | 1:500 dilution |
| SARS-CoV-2 (strain BAvPat1) P3 [5] | $3.8x10^4$ pfu/mL (as determined in T84) | 1:100 dilution |
| SFV [2] | $1.1.x10^{11}$ pfu/mL | MOI 10 for T84 and CaCo2 |
| TOSV [2] | $2.9x10^8$ pfu/mL | MOI 2.5 for T84, MOI 5 for CaCo2 |
| UUKV [2] | $8.25x10^8$ pfu/mL | MOI 10 for T84 and CaCo2 |
| Vaccinia virus (VV) E/L-GFP (*71*) [6] | $4.45 x10^8$ pfu/mL | 1:100 dilution<br>or MOI1 for experiment of results 2.1.6. |
| VSV-Luc | Non determined | 7 µL in 97 µL media (1:14.28 dilution) |

[1] Kind gift from Stacy Schultz-Cherry, St. Jude Children's Research Hospital, TN, USA

[2] Kindly provided by Pierre-Yves Lozach Research Group (University Hospital Heidelberg, Germany, and University Claude Bernard Lyon, France)

[3] Originally obtained from Bernard N. Fields

[4] Kind gift from John Patton (Indiana University)

[5] Obtained from Prof. Christian Drosten at the Charité in Berlin, Germany, and provided via the European Virology Archive

[6] Kindly provided by Jason Mercer (University of Birmingham)

### 4.1.5. Antibodies and related compounds

**Table 8:** List of primary antibodies

| Antibody | Raised in | Dilution | Manufacturer | Catalog number |
|---|---|---|---|---|
| Anti-astrovirus type 2 | mouse | IF: 1:400 | Invitrogen | MA5-16293 |
| Anti-β-actin | mouse | WB: 1:5000 | Sigma Aldrich | A5441 |
| Anti-Clathrin heavy chain (CHC) TD.1 | mouse | IF: 1:100 | abcam | ab24578 |
| Anti-Cytochrome C | mouse | IF: 1:200 | BD Biosciences | 556432 |
| Anti-GERV | guinea pig | IF: 1:200 | Generated and supplied by the PYL Group | |
| Anti-IRF3 | rabbit | WB: 1:1000 | Cell Signaling | 11904T |
| Anti-ISG15 | mouse | IF: 1:1000 | Santa Cruz Biotechnology | 166755 |
| Anti-phospho-IRF3 (Ser396) | rabbit | WB: 1:1000 | NEB/Cell Signaling | 4947 |
| Anti-Ki67/MKI67 | rabbit | IF: 1:200 | Novus Biologicals | NB500-170 |
| Anti-Lamin B1 | mouse | WB: 1:200 | Santa Cruz Biotechnology | sc-374015 |

| | | | | |
|---|---|---|---|---|
| Anti-µNS (MRV) | guinea pig | IF: 1:1000 | Antibody derived from synthetic MRV T1L-mµNS peptide and affinity purified. Peptide sequence: CKNVELDTMNQRQAK | |
| Anti-Nucleocapsid protein (NP) SARS-CoV-2 | mouse | IF: 1:1000<br>TCID$_{50}$: 1:1000 | Sino Biological | MM05 |
| Anti-RNA Pol II | rabbit | IF: 1:200 | Abcam | ab5095 |
| Anti-SFV E2 | mouse | IF: 1:200 | Generated and supplied by the PYL Group | |
| Anti-STAT1 | mouse | WB: 1:1000 | BD Biosciences | 610115 |
| Anti-phospho-STAT1 (Y701) | mouse | WB: 1:1000 | BD Biosciences | 612233 |
| Anti-STING | rabbit | WB: 1:1000 | Cell Signaling | 13647 |
| Anti-TBK1/NAK | rabbit | WB: 1:1000 | Cell Signaling | 3013S |
| Anti-phospho-TBK1/NAK (Ser172) | rabbit | WB 1:1000 | Cell Singaling | 5483S |
| Anti-TGN46 | rabbit | IF: 1:200 | Sigma | T7576 |
| Anti-TOSV | mouse | IF: 1:4000 | Generated and supplied by the PYL Group | |
| Anti-α-Tubulin | mouse | WB: 1:1000 | Sigma-Aldrich | T9026 |
| Anti-UUKV | mouse | IF: 1:1000 | Generated and supplied by the PYL Group | |
| Anti-YAP/TAZ | rabbit | WB: 1:1000 | Cell Signaling Technology | 8418 |
| Anti-YAP (also binds to TAZ) | mouse | WB: 1:500 | Santa Cruz Biotechnology | sc-101199 |
| Anti-phospho-YAP (Ser127) | rabbit | WB: 1:1000 | Cell Signaling Technology | 4911S |
| Anti-ZIKV | mouse | IF: 1:200 | RD Biotech | Non available |
| Anti-ZO1 | mouse | IF: 1:100<br>WB: 1:1000 | Molecular Probes Thermo Fisher Scientific | 339100 |
| Anti-ZO1 | rabbit | IF: 1:200<br>WB: 1:1000 | ThermoFisher - Invitrogen | 40-2200 |

*IF: immunofluorescence, WB: Western blot, TCID$_{50}$: In cell Western Analysis, PYL: Pierre-Yves Lozach

**Table 9:** List of secondary antibodies and related compounds

| **Antibody or reagent** | **Raised in** | **Dilution** | **Manufacturer** | **Catalog number** |
|---|---|---|---|---|
| Anti-guine pig Alexa Fluor 488 | goat | IF: 1:1000 | Thermo Fisher Scientific | A11073 |
| anti-guinea pig Alexa Fluor 647 | goat | IF: 1:1000 | Invitrogen | A32733 |
| anti-mouse Alexa Fluor 488 | goat | IF: 1:1000 | Invitrogen | A11001 |
| anti-mouse Alexa Fluor 647 | goat | IF: 1:1000 | Invitrogen | A21235 |
| Anti-mouse CW800 | mouse | TCID$_{50}$: 1:10000 | Licor | 926-32210 |
| anti-mouse HRP | sheep | WB: 1:5000 | GE Healthcare | NA931 |
| anti-rabbit Alexa Fluor 488 | goat | IF: 1:1000 | Invitrogen | A11008 |
| anti-rabbit Alexa Fluor 647 | goat | IF: 1:1000 | Invitrogen | A21244 |
| Anti-rabbit HRP | goat | WB: 1:5000 | Abcam | ab97051 |
| DRAQ5 | - | IF: 1:1000 | Invitrogen | 65-0880-92 |
| Phalloidin Alexa Fluor 647 | - | TCID$_{50}$: 1:10000 | Molecular Probes | A-22287 |

*IF: immunofluorescence, WB: Western blot, TCID$_{50}$: In cell Western Analysis

**Table 10:** List of primer sequence for q-PCR

| **Target Gene** | **Forward sequence (5'→3')** | **Reverse sequence (5'→3')** |
|---|---|---|
| Hamster ISG15 | AAAGCCTACAGCCATGACCT | TTAGTCAGGGGCACCAGGAA |
| Hamster Mx1 | GCGCTTCCAGACTCTTCTGA | CCTAAGATACATGCGATGGCG |
| Hamster Mx2 | CCAGTAATGTGGACATTGCC | CATCAACGACCTTGTCTTCAGTA |
| Hamster OAS3 | AGGTGCTTAAGGTGGTTAAGGG | TGCTCAGAGAAGTGCTGGAAG |
| Hamster Rpl-22 | ACGCTGCCAATTTCGAGCA | CTGGAAGTAGCGCAGCTCAT |
| Human 18S (nuclear gene) | AGAGGGACAAGTGGCGTTC | CGCTGAGCCAGTCAGTGT |
| Human IFIT1 | AAAAGCCCACATTTGAGGTG | GAAATTCCTGAAACCGACCA |
| Human IFNβ1 | GCCGCATTGACCATCTAT | GTCTCATTCCAGCCAGTG |
| Human IFNλ1 | GCAGGTTCAAATCTCTGTCACC | AAGACAGGAGAGCTGCAACTC |
| Human IFNλ2/3 | GCCACATAGCCCAGTTCAAG | TGGGAGAGGATATGGTGCAG |
| Human IFNλ2 | AATTGTGTTGCCAGTGGGGA | GCGACTGGGTGGCAATAAAT |
| Human IFNλ3 | CCCAAAAAAGGAGTCCCCTG | GGTTGCATGACTGGCGGA |
| Human IFNAR1 | ATCGGTGCTCCAAAACAGTC | GTGCTCTGGCTTTCACACAA |
| Human IFNLR1 | ATCCTCAGTTAACCTACACC | CAGATACTCCACCACAAAAC |
| Human IL-1β | CCACAGACCTTCCAGGAGAATG | GTGCAGTTCAGTGATCGTACAGG |
| Human IL-6 | GCACTGGCAGAAAACAACCT | TCAAACTCCAAAAGACCAGTGA |
| Human IL-8 | GAGAGTGATTGAGAGTGGACCAC | CACAACCCTCTGCACCCAGTTT |
| Human IL-18 | GATAGCCAGCCTAGAGGTATGG | CCTTGATGTTATCAGGAGGATTCA |
| Human ISG15 | CCTCTGAGCATCCTGGT | AGGCCGTACTCCCCCAG |
| Human nd2 (mitochondrial gene) | CACCCAAGAACAGGGTTTGT | TGGCCATGGGTATGTTGTTAA |
| Human Mx1 | GAGCTGTTCTCCTGCACCTC | CTCCCACTCCCTGAAATCTG |
| Human OAS1 | TGCGCTCAGCTTCGTACTGA | GGTGGAGAACTCGCCCTCTT |
| Human RIG-I | GGCATGTTACACAGCTGACG | TTGCAATATCCTCCACCACA |
| Human TBP (housekeeping gene) | CCACTCACAGACTCTCACAAC | CTGCGGTACAATCCCAGAACT |
| Human Viperin | GAGAGCCATTTCTTCAAGACC | CTATAATCCCTACACCACCTCC |
| HAstV1 | CCAGRCTCACAGAAGAGCAAC | CTTGCTAGCCATCRCACTTCTT |
| MRV µ2 | GTGTACACCACGACGGACAG | TCAACCCCACTCATGACAAA |
| SARS-CoV-2 N protein | GCCTCTTCTCGTTCCTCATCAC | AGCAGCATCACCGCCATT |

## 4.2. Methods

### 4.2.1. Culture of cells and organoids

All cell lines used in this thesis, their description and origin are specified in Table 6. T84 cells were maintained in a 50:50 mixture of Dulbecco's Modified Eagle's Medium (DMEM) and F12. A549, Calu3, CaCo2, IFN-α/β reporter HEK293, IFN-λ Reporter HEK293 and Vero E6 cells were grown in DMEM. Huh-7 cells were cultured in DMEM supplemented with Non-Essential Amino Acids. HEK293T cells were maintained in Iscove's modified Dulbecco's medium (IMDM). BHK-21 cells were cultured in Glasgow Modified Eagle's Medium (GMEM) supplemented with 10% tryptose phosphate broth. HK-2 cells were grown in Keratinocyte SFM supplemented with 0.05 mg/mL bovine pituitary extract (BPE) and 5 ng/mL human recombinant epidermal growth factor (EGF). HT-29 cells were grown in McCoys media. All media, except the HK-2 cell media and BHK-21, were additionally supplemented with 10% FBS, 100 U/mL penicillin and 100 µg/mL streptomycin. For BHK-21 cells, medium was supplemented with 5% FBS, 100 U/mL penicillin and 100 µg/mL streptomycin. HK-2 cells were maintained in serum-free media without penicillin and streptomycin (only supplemented with BPE and EGF as specified above). All cells were kept in a constant humid atmosphere at 37°C, 5% $CO_2$ and 21% oxygen. All cells were split every three to four days, depending on their confluence. For splitting, 0.25% Trypsin-EDTA was used for T84, CaCo2, HT-29 and Calu3 cells, and 0.05% Trypsin-EDTA for A549, HEK293T, BHK-21, HK-2, IFN-α/β reporter HEK293, IFN-λ Reporter HEK293 and Huh-7 cells.

Importantly, T84, Caco2, HT-29 and Calu3 cells must be cultured on collagen coated surfaces. Plastic surfaces (including culturing flasks and multi-well plates) were coated with 0.01 mg/mL rat tail collagen. First, rat tail collagen powder was diluted in 0.1 M acetic acid to obtain a stock concentration of 1 mg/mL, which can be stored at -20 °C. This stock was further diluted in 60% Ethanol (EtOH) to obtain a concentration of 0.01 mg/mL, and plastic surfaces were then coated for 2 h at 37°C or overnight at 4°C. Before use, the plastic surface was washed twice with PBS to fully remove the EtOH. Glass surfaces (including glass coverslips and 8 well chamber slide (Ibidi #80827)) were coated with 0.04 mg/mL human collagen diluted in water for 1 h at room-temperature (RT). Water solution was removed before seeding cells.

Human-derived organoids handling was carried out in accordance with the recommendations of the University Hospital Heidelberg with written informed consent from all subjects in accordance with the Declaration of Helsinki. All samples were received and maintained in an anonymized manner. The protocol was approved by the "Ethics commission of the University Hospital Heidelberg" under the protocol S-443/2017. Human intestinal epithelial organoids derived from ileum and colon were used in this thesis, and were cultured by Carmon Kee or Zina Maria Uckeley. Organoids were grown as 3D structures in Matrigel and maintained at 37°C, 5% $CO_2$ in basal or differentiation media (compounds specified in Table 3). Organoids were split every 7-10 days by washing once with ice-cold PBS, incubating with 0.05% Trypsin for 5 minutes at 37°C and reseeding them in fresh Matrigel.

### 4.2.2. Cell seeding

#### *4.2.2.1. Standard/medium density cell seeding*

If not specified otherwise, I seeded cells in 48-well plates (with plastic bottom). Cells were seeded in 0.5 mL medium per well of a 48-well plate. If the format was changed (upscaling or downscaling), the cell number was multiplied by the factor difference in the surface area. For example, the surface area of one well from a 48-well plate is 1.1 $cm^2$ and the surface area of one well from a 24-well plate is 1.9 $cm^2$, meaning that the factor difference is 1.1/1.9 = 1.35 (the well of a 24-well plate is 1.35 times larger than the well in a 48-well plate). An example calculation for the upscaling is as follows: If I seeded 20,000 cells per well in a 48-well plate, to have the same confluence in a 24-well plate I need to multiply it by 1.35, resulting in 27,000 cells per well.

If not specified otherwise in the text or the figure legend, I seeded the cells at standard/medium density. For standard/medium density cell seeding, 100,000 cells were seeded per well in a 48-well plate or an 8-well chamber slide (Ibidi #80827). One-day post-seeding, cells were treated.

#### *4.2.2.2. Cell seeding at high and low density*

For high cell density seeding, 225,000 cells in 0.5 mL medium were seeded per well in 48-well plates. One-day post-seeding, medium was exchanged with 0.5 mL fresh culturing medium, and two days post-seeding cells were treated. For low cell density seeding, 30,000 cells in 0.5 mL medium were seeded per well in 48-well plates. One-day post-seeding cell were treated.

#### *4.2.2.3. Cell seeding on micropatterned surface*

Micropatterning of surfaces was performed as described in the section 4.2.4 below. For cell seeding, the patterned surface was coated with 0.04 mg/mL human collagen diluted in water for 1 h at room temperature. When seeding on micropatterned 25 mm diameter coverslips using the UV-Ozone cleaner, 1,000,000 cells were seeded in 3 mL media (the coverslip was positioned in a well from a 6-well plate). When seeding cells on surfaces micropatterned by the maskless photolithography system, an excess of cells was seeded: 150,000 cells in 200 µL medium at the apical side of the transwell membrane fitting in a 24-well plate (the basal side was filled with 600 µL medium), and 300,000 cells in 200µl medium per well in the 8-well chamber slide (Ibidi #80827). Cells were incubated for 2 h at 37°C, non-adherent cells were washed away two times with PBS, and fresh medium was added. One-day post-seeding, medium change was performed for cells seeded on surfaces micropatterned by either method (UV-Ozone cleaner and maskless photolithography system), and two days post-seeding cells were treated.

#### *4.2.2.4. Cell seeding on transwell inserts and determining formation of a semipermeable polarized monolayer (TEER measurement and FITC-Dextran permeability assay)*

Cell line seeding on transwell inserts: Transwell membranes were coated with rat collagen (see coating procedure at section 4.2.1.) prior to cell seeding. 150,000 cells in 200 µL medium were then seeded on the apical side of the transwell insert, and 600 µL media was added to the basal side of the transwell. Media was exchanged every second day until a polarized cell monolayer was formed.

Formation of a polarized monolayer was assessed by measurement of the Transepithelial electrical resistance (TEER) using the EVOM3 Epithelial Volt/Ohm Meter with STX2-PLUS (Word Precision Instruments). TEER measurement was done every second day, starting at day 1 post-seeding. Media change was done immediately after TEER measurement. When a TEER of ≥ 1000 $\Omega/cm^2$ was reached, cells were considered polarized forming a tight monolayer, and could be used for further treatment.

To assess monolayer permeability and integrity, the FITC-Dextran permeability assay was done: Cells were grown on transwell inserts until monolayer formation as determined by TEER measurement. Media was removed from the apical compartment of the transwell and replaced by 200µL of fresh medium containing 2 mg/mL fluorescein isothiocyanate (FITC)-labelled dextran (4 kDa). As a negative control and to calculate the background, culture media alone was used on a well without cells. For the positive control (maximum diffusion of FITC-Dextran from apical to basolateral compartment) 200 µL of 2 mg/mL of FITC-Dextran was added to the apical side of a well without cells and 600µL culturing media were added to the basolateral compartment. Cells and controls were incubated for 3 h at 37°C and then media was collected from the basal compartment. Fluorescent signal was measured using an 800TS Microplate Reader (BioTek) at an excitation wavelength of 495nm. A standard curve by serial dilution of the FITC-Dextran in culturing media was done to assess the basolateral FITC-Dextran concentration.

#### *4.2.2.5. Organoid seeding in 2D at different densities*

Organoid seeding in 2-dimensions (2D) was done by Carmon Kee or Zina Maria Uckeley. First, 8-well chamber slides were coated either with 0.04 mg/mL human collagen (diluted in water) or 10% Matrigel (diluted in basal organoid media) for 1 h at RT. As a note, the coating itself did not show a difference in how the organoids were growing in 2D, and samples from either coating (matrigel or collagen) were used for the experiments. Organoids growing as 3-dimensional (3D) structures in Matrigel were disassembled as described in section 4.2.1., washed once with ice cold PBS and then spun down at 300 g for 5 min at 4 °C. Organoids were resuspended in 200 µL basal organoid medium and seeded in the 8-well chamber slide. To obtain different densities, different amounts of wells (one to four wells) growing 3D-organoids in Matrigel were pooled to seed one well in the 8-well chamber slide. 2 days after seeding, the organoids were used for further treatment.

#### *4.2.2.6. Organoid seeding on transwell inserts and TEER measurement*

Human gut-derived organoid seeding on transwells: Organoid seeding was performed by Zina Maria Uckeley. First, transwell membranes were coated with 10% Matrigel (diluted in basal organoid media) for 1 h at RT. It is important that Matrigel is maintained on ice when not being used, as it solidifies at RT. Organoids growing as 3-dimensional (3D) structures in Matrigel were disassembled as described in section 4.2.1., washed once with ice cold PBS and then spun down at 300 g for 5 min at 4 °C. Organoids were resuspended in 250 µL basal organoid medium and seeded on the apical side of the transwell insert. 600 µL basal organoid medium was added to the basal side of the transwell insert. At day 2 and 4 after seeding, a partial media change was done by removing 400 µL from the basal side and 100µl from the apical side of the transwell insert, and adding 500 µL and 200 µL fresh basal organoid medium to basal and apical side, respectively. At day 7 after seeding, an air liquid interface (ALI) culture system was started to induce organoid cell differentiation (*458*). To start the ALI system, a partial media change (as described above) using basal organoid media was only done at the basal side of the transwell insert, while at the apical side the medium was removed. At day 9 post seeding, a full media change was done at the basal side of the transwell insert by removing all the media and adding fresh 600 µL of organoid differentiation media (to initiate cell differentiation). The apical side of the transwell insert was kept in the ALI state without medium. At day 11 post seeding, I added 200 µL differentiation media to the apical side of the transwell insert. After 6 h, I measured the TEER measured using the EVOM3 Epithelial Volt/Ohm Meter with STX2-PLUS (Word Precision Instruments). If a TEER of ≥ 350 $\Omega/cm^2$ was reached, organoids seeded on the transwells were considered polarized forming a tight monolayer, and could be used for further treatment. If the TEER was not reached, organoids were further grown. I measured the TEER and made a full media change at the apical and basal side of the transwell insert using organoid differentiation media every second day until a TEER of ≥ 350 $\Omega/cm^2$ was reached. However, if that TEER was not reached within another 4 days, the organoids had to be discarded as they would never polarize.

### 4.2.3. Generation of knock-down and over-expression T84 cell lines

Bacteria glycerol stocks containing the knock-down and over-expression plasmids were obtained commercially, and details are specified in Table 5. Glycerol stocks were streaked on LB-agar plates supplemented with Ampicillin (0.1 mg/mL) and incubated at 37°C for 16 h. Colonies were picked and grown in 5 mL LB supplemented with Ampicillin (0.1 mg/mL) for 14h at 37°C while shaking (200rpm). 500 µL of this culture was then used to inoculate 100 mL of

LB media supplemented with Ampicillin (0.1 mg/mL), allowing for amplification of a large amount of plasmid. The plasmid was isolated using the NucleoBond® PC100 kit (Macherey-Nagel #740573.100) according to the manufacturers protocol.

A lentivirus vector system was used to efficiently deliver the knock-down or over-expression plasmids to the T84 cells. To first package the plasmid in lentivirus, HEK293T cells at 80% confluence in a 10 cm$^2$ dish were transfected with 8 µg of the plasmid, 4 µg pMDG.2 plasmid and 4 µg psPAX plasmid by using the transfection reagent Polyethylenimine (PEI) at a PEI:DNA ratio of 4:1. Precisely, 48 µL of PEI were incubated with 202 µL of Opti-MEM for 5 minutes. In parallel, 4 µg of each helper plasmid pMD2.G and psPAX2 were combined with 8 µg of the plasmids of interest in 250 µL of Opti-MEM. The contents of the tubes were then combined carefully and incubated for 20 min. The transfection mixture was added dropwise and 6 h after transfection the media was replaced. 3 d post transfection, the supernatant containing lentivirus was collected, spun down to separate it from cell debris at 4000 rcf for 10 mins, and filtered through a 0.45 µm syringe filter (Lab Unlimited #W10462100). To pellet the lentivirus, the supernatant was spun down at 27,000 rpm for 1:40 hours using a SW40 Ti rotor (Beckman Coulter). Supernatants were discarded by inverting the tubes, 100 µL of Opti-MEM was added and centrifuge tubes were left in ice at 4°C overnight. I prepared 20 µL aliquots and stored them at -80°C until further used.

Lentiviral transduction was carried out in cells seeded at low confluence. 300,000 WT T84 cells were seeded per well in a 6-well plate, and cells were transduced with 20 µL lentivirus using 3 µL Polybrene transfection reagent diluted in 3 mL media. After 3 days of incubation, transduced cells were selected with 10 µg/mL puromycin diluted in media if the plasmid had a eukaryotic selection marker. In parallel, mock-transduced T84 cells were treated with the same antibiotic to control cell death and resistance. Knock-down or over-expressing cell lines were ready to be used for experiments when mock-transduced T84 control cells were dead due to the antibiotic treatment, but the transduced cells were viable showing no cell death for at least 3 days.

The over-expression plasmids also contained a fluorescent reporter, allowing an easier assessment of transduction efficiency of cells. To obtain a homogenous over-expressing population, fluorescent cells were sorted with a CD FACS Symphony S6 at the University of Florida ICBR Cytometry Core Facility (RRID:SCR_019119). I provided ~5 million non-sorted cells in a volume of 1 mL media, and after sorting obtained 600,000-1,000,000 cells in collection media (30% FBS instead of 10% FBS). Sorted fluorescent cells were grown under normal cell culturing conditions and used for experiments.

### 4.2.4. Surface micropatterning and Picosecond Laser Detachment Assay

#### *4.2.4.1. Surface micropatterning by UV-Ozone cleaner*

For glass micropatterning by Quartz mask-based approach (ultraviolet light-Ozone (UVO)-based micropatterning of glass surfaces using a Quartz-mask) (Fig. 67 A), a quartz chromium photomask containing 200 µm diameter clear circles was custom made by Toppan Photomasks Inc. (Mask type = 1X Master, mask size = 4” x 4” x 0.06”). The UVO-based micropatterning protocol was adapted from Pitaval et al. (*459*). Briefly, glass coverslips of 25 mm diameter (Marienfeld # 0117650) were pre-cleaned with 100% ethanol for 15 min while sonicating, rinsed twice with deionized water, and dried with compressed air. The glass coverslips were activated in the UVO-Cleaner® Model 30 (Jelight Company Inc.) for 10 min and then passivated for 45 min at room temperature with 100 µl 0.1 mg/ml poly-L lysin/poly-ethylene glycol PLL(20)-g[3.5]-PEG(2) in water. After passivation, the coverslips were washed twice with deionized water for 10 min. Before the micropatterning step, the photomask was washed with acetone and isopropanol, dried with a stream of compressed air and cleaned in the UVO cleaner for 5 min (chromium/silver side up facing the UVO light). Directly after cleaning, the passivated glass coverslips were sandwiched with the photomask using 8 µl of deionized water to create an intimate contact between the chromium side (silver colored) of the photomask and the passivated surface of the coverslip. The photomask with the coverslips was placed in the UVO cleaner (quartz/black side facing up towards UVO light while coverslips are in between mask and metal tray facing down) for 5 min for the micropatterning step. After UVO exposure, the coverslips were carefully detached from the photomask and stored in PBS at 4°C until further use, but maximum for 2 days.

#### *4.2.4.2. Surface micropatterning by the maskless photolithography system*

Surface micropatterning by the maskless photolithography system (Fig. 67 A) was performed at the Max-Planck Institute for Biomedical Research (Heidelberg) in Ada Cavalcanti-Adams Research Group.

6.5 mm Transwell® with 3.0 µm Pore Polycarbonate Membrane Inserts (Costar #CLS3415) and µ-Slide 8 well glass bottom chambers (8 well chamber slide) (Ibidi #80827) were micropatterned using the maskless photolithography system. The transwell membrane or the glass surface was activated in the plasma cleaner (Tepla 100-E Plasma System) at 0.4 mbar $O_2$-pressure and 200 W for 1 min. The surface was then incubated with 0.1% (w/v) Poly-L-Lysin (PLL) solution (in $H_2O$) (100 µL for the transwell membrane or 200 µL per well for the 8 well chamber slide) for 30 min at RT, washed four times with deionized water and dried with compressed air. The surface was passivated with 90 µL for the transwell membrane or 180µL per well for the 8 well chamber slide of 90 mg/mL Methoxy-Poly (Ethylene Glycol)-Succinimidyl

Valerate (mPEG-SVA) (5000Da) in 0.1 M HEPES buffer (pH 8.4) for 1 h at RT. During this reaction the SVA ester covalently binds to the amines of the PLL, resulting in a homogenous passivation of the glass surface with a PLL-PEG polymer. The surface was washed four times with deionized water and dried with compressed air. The photoactivator PLPP-gel was put in the center of the surface. Immediately after 100% EtOH were added on the top of the PLPP-gel and the mixture was homogenized by manual rotation. 0.5 µl PLPP-gel with 16 µl EtOH were used for the transwell membrane and 0.96 µl PLPP-gel with 16 µl EtOH for the 8 well chamber slide. The surface was dried at RT and was ready for the micropatterning.

This system is able to micropattern any previously designed pattern on any surface. To design a pattern, the open-source software Inkscape (inkscape.org) was used with the following scale: 1 px corresponded to 0.28 µm. I designed circles with 200 µm diameter, which was then loaded into the Leonardo software (Alvéole Lab) for micropatterning. The micropatterning was performed on a Nikon Eclipse Ti2 Microscope with a 20x S Plan Fluor ELWD Objective (NA = 0.45). The passivated surface coated with the photoactivator PLPP was placed on the microscope stage. The photo-micropatterning was controlled with the Leonardo software and executed by the PRIMO optical module (Alvéole Lab) using the stitching mode and a 375 nm laser at a dose of 30 mJ/mm$^2$. The patterned surface was then washed six times with deionized water and stored in PBS at 4°C until further use, but maximum for 2 weeks.

#### *4.2.4.3. Creation of a new edge in the center of a population using the Picosecond Laser Detachment Assay*

The Picosecond Laser Detachment Assay was adapted from Yoshikawa et al. (*460*) and done in collaboration with Motomu Tanakas Research Group (Institute for Physical Chemistry, Heidelberg University). A picosecond Nd:YAG laser system ($\lambda$=1064 nm, Pulse Energy (max)=25 mJ, FWHM=28±3ps, EKSLPLA, Vilnius, Lithuania) was used to induce a cavitation shock waves for cell detachment.

First, I used the maskless photolithography system to create 500 µm and 1000 µm diameter micropatterns on a 35 mm cell imaging dish with glass bottom (ibidi #81218-200). I then seeded 1,500,000 T84 WT cells on the micropatterns in 2 mL media, removed the non-attached cells after 2 h and added 3 mL fresh media in the dish. One day post seeding, I did a media exchange and added 3 mL fresh media. Two days post seeded, the media exchange was repeated and then I proceeded with the Picosecond Laser Detachment assay together with Motomu Tanagas research group. Seeded cells in the dish were placed on the stage of an inverted microscope (Eclipse TE2000-U, Nikon, Amstelveen, Netherlands Europe). The picosecond laser pulse was focused through a 20x objective lens (N.A. = 0.75, Nikon Instruments Inc.). The focus was set into the culture medium at a distance of 750µm above the cells. A laser power of approx. 17 mV for 500 µm big colonies or 27-37 mV for 1000 µm big colonies was used to detach the cells in the center of a population and automatically create a new edge. Immediately after the Picosecond Laser Detachment Assay, cells were infected with HAstV for 16h.

### 4.2.5. Cell treatment and infections

#### *4.2.5.1. IFN treatment*

Cells were treated with 2000 IU/mL IFNβ1 or as described in the figure legend. Cells were treated by a cocktail of all three type III IFNs (IFNλ1, IFNλ2 and IFNλ3) in a ratio of 1:1:1, resulting in a final concentration of 300 ng/mL or as described in the figure legend. Cells were treated with IFNs diluted in culturing media (250 µL for 48-well plate, 200 µL for 8-well chamber slide, 200 µL for apical transwell treatment, 600 µL for basolateral transwell treatment, 1 mL for patterned coverslips) and the duration of the treatment is stated in the figure legends.

#### *4.2.5.2. Treatment with inhibitors and agonist of immune signaling pathways*

Several drugs were used to inhibit cGAS-STING signaling: cGAS was inhibited with 10 µM RU521 or 10 µM G150, STING was inhibited with 20 µM H151 or 2 µM STING-IN2, and TBK1 was inhibited with 1 µM BX795. Given that the drugs were dissolved in DMSO, I consistently included a DMSO control to assess any cytotoxic effects or alterations arising from the solvent itself (diluent/solvent control). For treatment, the drugs were added during the seeding process directly into the cells in suspension. The inhibitor was re-added during media changes or treatment to ensure a constant exposure of the cells to the drug. Vaccinia virus (diluted 1:1000) served as an agonist for cGAS and infection was done for 16 hrs. diABZ served as an agonist for STING, and cells were treated with 10µM diABZ for 6 hrs. Cells seeded on 48-well plates were treated with a volume of 0.5 mL of medium containing the diluted inhibitors and agonists.

I used Pyridine to inhibit JAK/STAT signaling during virus infection of cell populations seeded on micropatterned glass (25 mm diameter coverslips). Cells populations were incubated with 2 µM Pyridine diluted in 2 mL culture medium for 50min at 37°C. Immediately after, cells were infected with 500µL astrovirus in a total volume of 2 mL medium supplemented with 2 µM Pyridine. Incubation occurred for 16h at 37°C. Cells were then fixed for immunofluorescence staining.

#### *4.2.5.3. Virus infection*

Cells were infected with different viruses at a dilution or MOI specified in Table 7. For infection, I removed culture medium and added the virus diluted in media to the cells. The infection volume was: 2 mL per well for cells seeded in a 6 well plate format (also applies to cells seeded on micropatterned 25 mm diameter coverslips), 250 µL per well for cells seeded in a 48 well plate, 200 µL per well for cells seeded in an 8-well chamber slide, and 800 µL per well for cells seeded on transwell insert (200 µL at the apical side and 600 µL at the basal side). Cells and viruses were incubated for 16 h or as long as specified in the results section. After infection, samples were further processed as specified in the results section.

Infection for the following viruses was carried out differently to what is specified above: For SARS-CoV-2 infection, the culture medium was removed, the virus was diluted in medium and was added to the cells, followed by incubation for 1 h at 37°C. After incubation, the virus was removed, and fresh medium or medium supplemented with the indicated IFN concentrations (see results section) was added back to the cells. I incubated the virus for 24 h or as long as specified in the results section, and then processed the samples as specified in the results section. Infection with VSV-Luc is described in section 4.2.6.7. For rotavirus infection, first, I activated the rotavirus stock by adding the virus to serum-free media containing 2 µg/mL trypsin and incubated it at 37°C for 30 minutes in the absence of cells. Then, I washed the cells twice with serum free media and added the activated virus. 1 h post-infection, I aspirated the media containing rotavirus and re-added serum free media containing 2 µg/mL trypsin. Infection was allowed to continue for 16 h and samples/cells were then processed as described in the results.

#### *4.2.5.4. VSV luciferase assay*

One day before the assay, I seeded 25,000 T84 cells per well in a black F-bottom 96-well plate. Cells were then treated as indicated in the results part and infected with 7 µL VSV-Luc diluted in 97 µL media (total infection media was 100 µL). VSV-Luc infection was carried out for 6 h at 37°C. At the end of the infection, the medium was removed, and the cells were washed once with PBS and lysed with 30µL Glo lysis buffer per well at RT for 20 min. Subsequently, 30 µL Steady Glo buffer was added per well and incubated for 15 min at RT in the dark. The luminescence was read using an Omega Luminometer.

### 4.2.6. Analytical assays addressing RNA transcription, protein expression, virus infection and immune response

#### *4.2.6.1. RNA purification, cDNA synthesis and quantitative PCR*

For assessment of RNA expression levels in the cell: Total RNA was purified using a home-made RNA extraction kit and the Epoch Life Science Inc EconoSpin® RNA Mini Spin Columns with lid (Fisher Scientific #NC0772081). First, adherent cells were washed once with PBS and lysed with 350 µL RNA lysis buffer for 5 min at 37°C. Lysed cells were transferred to a 1.5 mL Eppi and thoroughly mixed with 250 µL 95% EtOH by vortexing. The 600 µL mixture was transferred to a Mini Spin Column and spun down for 15 s at 11,000 g. To obtain a higher RNA yield, the flow-through was re-loaded onto the column and spun down again. The RNA should now be bound to the column and the flow-through was discarded. 500 µL RNA Wash Buffer 1 was added to the Mini Spin Column, the columns were spun down for 15 s at 11,000 g and the flow-through was discarded. Then, 500 µL RNA Wash Buffer 2 was added to the Mini Spin Column, the columns were spun down for 15 s at 11,000 g and the flow-through was discarded. A final washing step was done by adding 500 µL RNA Wash Buffer 2 to the Mini Spin Column, the columns were spun down for 2 min at 11,000 g and the flow-through was discarded. To dry the column and remove all the RNA Wash Buffer, columns were spun down for 1 min at 11,000 g and then placed on a fresh 1.5 mL Eppi. The RNA bound to the column was then eluted with 30 µL DNase/RNase-Free Distilled Water by adding it to the column, incubating 1 min at RT and then spinning down for 1 min at 11,000 g. The RNA concentration in the eluate was measured using the NanoDrop Lite spectrophotometer and 200ng total RNA was reverse transcribed into cDNA using the iScript™ cDNA Synthesis kit (BioRad Laboratories#1708891): 1µl Reverse Transcriptase, 4µl Reaction Mix and 15µl RNA template were mixed. After the reverse transcription, cDNA was diluted 1:2 in $H_2O$. Following protocol for reverse transcription was used:

| Step | Temperature | Time | Cycles |
|---|---|---|---|
| Priming | 25°C | 5min | 1 |
| Reverse transcription | 42°C | 30min | 1 |
| RT inactivation | 85°C | 5min | 1 |

Quantitative RT-PCR assay was performed using iTaq SYBR green (BioRad), the respective primer (Table 10) and the Bio-Rad CFX96 Real-Time PCR Detection System as per manufacturer's instructions. For each reaction, the following pipetting scheme was used:

| | |
|---|---|
| iTaq SYBR green | 7.5µl |
| Forward primer (2µM) | 1.9µl |
| Reverse primer (2µM) | 1.9µl |
| Millipore H2O | 1.7µl |
| cDNA | 2µl cDNA |

The q-PCR was performed as follows:

| Step | Temperature | Time | Cycles |
|---|---|---|---|
| Activation | 95°C | 30s | 1 |
| Melting | 95°C | 5s | 40 |
| Primer annealing and elongation | 60°C | 30s | |
| Plate read | | | |
| Melting curve generation | 65°C | 5s | 1 |
| | +05°C/cycle to 95°C | | |

At the end of each run a melting curve was created to determine the melting point of the amplicons and exclude non-specific amplified DNA. The data was processed using the Bio-Rad CFX Manager 3.0 to determine the Cq value for each reaction. For the analysis of gene of interest (GOI) transcript expression levels, the Cq values were first normalized to the housekeeping gene (TBP for human cells and Rpl-22 for hamster cells) by subtracting the housekeeping gene Cq from the GOI Cq. Then the relative expression levels were calculated resulting in following formula: relative expression (rel. exp. GOI) = $2^{-(Cq(GOI) - Cq(TBP))}$. The fold change was obtained by dividing relative gene expression of a treatment by the relative expression of the control: fold change = treatment (rel. exp. GOI) / control (rel. exp. GOI).

### *4.2.6.2. Total Cell lysis, cellular fractionation, Sodium dodecyl sulfate polyacrylamide gel electrophoresis (SDS-PAGE) and Western blot*

For total cell lysis, adherent cells were washed one time with PBS and then lysed with 60-75 µL RIPA++ per 48-well plate for 5 min at 37°C. To remove cell debris, the sample was centrifuged at 13,000 rpm for 10 min at 4°C, and the supernatant was taken and stored at -80°C until further processing.

For cellular fractionation, a large amount of cells was required. For high density I pooled 6 wells from 12-well plates, and for low density I pooled 24 wells from 12-well plates. A schematic of the method is depicted in Fig. 66. Adherent cells were washed with PBS and then detached with trypsin at 37°C. Trypsinization was stopped using cold media (containing FBS to inhibit the trypsin) and cells were collected. All steps listed below are performed on ice or at 4°C. Cells were then spun down at 2000 rpm for 5 min at 4°C, the supernatant was discarded and the cells were resuspended in 1 mL cold PBS. For washing, cells were spun down again at 2000 rpm for 5 min at 4°C, the supernatant was discarded and the cells were resuspended in 1 mL cold PBS. I then removed 200 µL, which corresponds to the total lysate fraction (TL-fraction). The TL-fraction was spun down at 2000 rpm for 5 min at 4°C. The supernatant was discarded, the cell pellet was resuspended in 60 µL RIPA++, and cells were lysed by incubating on ice for 20 min. To remove cell debris, the sample was centrifuged at 13,000 rpm for 10 min at 4°C and the supernatant was then taken corresponding to the TL-fraction lysate. Going back to the cells resuspended in cold PBS, I used the remaining 800 µL to separate the cells into nuclear and cytosolic fraction. Cells were spun down at 2000 rpm for 5min at 4°C and supernatant was discarded. The pellet was resuspended in 100 µL cytosolic extraction buffer (0.1% NP40 in PBS containing protease and phosphatase inhibitors) and incubated for 2 min on ice. The cytosolic extraction buffer disrupts the cell membrane without affecting the nuclear membrane, therefore releasing the cytoplasmic but not the nuclear content. Samples were centrifuged at 6,500 rpm for 1 min at 4°C, which separates the cytoplasm (supernatant) from the nucleus (pellet). The supernatant was removed and stored as the cytosolic fraction (C-fraction). The pellet was then washed twice with 500 µL cytosolic extraction buffer by centrifuging cells at 2000 rpm for 5 min at 4°C and resuspending the pellet in the buffer. After the second wash, the supernatant was removed and the pellet was resuspended in 40 µL RIPA++. The samples were then incubated for 20 min on ice and centrifuged at 13,000 rpm for 10 min at 4°C. The supernatant was then taken, corresponding to the Nuclear fraction (N-fraction). Lysates of the different fractions were stored at -80°C until further processing.

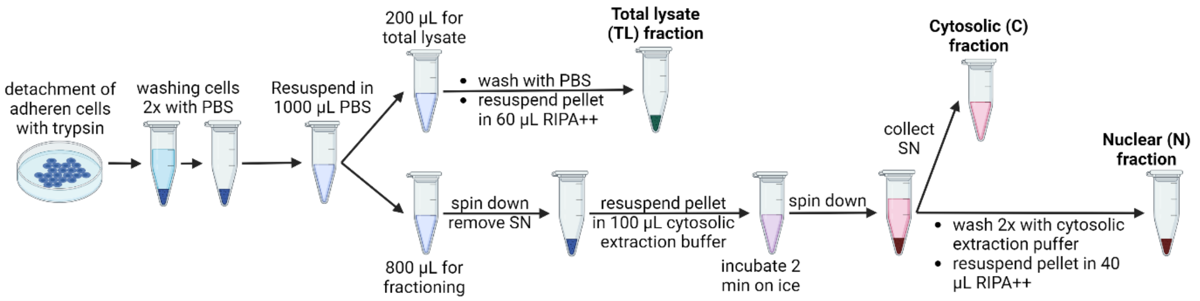

**Fig. 66. Schematic showing the experimental procedure for cellular fractioning.**

Lysate protein concentration was measured using the Pierce BCA Protein Assay Kit assay (Thermo Scientific #23225) according to the manufacturer's protocol. 5-8 µg of protein per condition were separated by SDS-PAGE and blotted onto a 0.2 µm nitrocellulose membrane using a Trans-Blot® Turbo™ Transfer System (Bio-Rad). Membranes were blocked with 0.5% Tween in TBS (TBS-T) containing 5% Bovine Serum Albumin (BSA) (blocking buffer) for 2 h at room temperature. Primary antibodies (Table 8) were diluted in the same blocking buffer and nitrocellulose membranes were incubated with the antibodies diluted in the blocking buffer overnight at 4°C. Membranes were then washed three times with TBS-T for 5 min at RT while rocking. Secondary antibodies coupled with horseradish peroxidase (HRP) (Table 9) were used at 1:5000 dilution in blocking buffer and incubated at RT for 1 h while rocking. Membranes were washed three times with TBS-T for 5 min at RT while rocking. The Pierce ECL Western

Blotting Substrate was used for detection according to manufacturer instructions. The nitrocellulose membrane was imaged with the ImageQuant™ LAS 4000 (GE Healthcare). Quantification was done using the open image analysis software ImageJ. Relative abundance of a protein of interest was normalized to the housekeeping protein control. I used α-tubulin (55 kDa) and β-actin (42 kDa) as housekeeping protein controls for total cell lysates, α-tubulin (55 kDa) as housekeeping control for the cytosolic fraction, and Lamin B1 (66-70 kDa) as housekeeping control for the nuclear fraction.

#### *4.2.6.3. Indirect immunofluorescence assay*

Adherent cells were washed one time with PBS and fixed in 2% PFA (diluted in PBS) for 20 min at RT. Cells were washed in PBS three times and permeabilized in 0.5% Triton-X100 diluted in PBS for 15 mins at RT. Cells were blocked using 3% BSA in PBS for 30 min at RT. Primary antibodies (Table 8) were diluted in 1% BSA (in PBS) and incubated for 1 h at RT. Cells were washed with PBS three times, incubated with Alexa Fluor® conjugated secondary antibody (Table 9) with/without DAPI, both diluted 1:1000 in 1% BSA (in PBS) for 30 min at RT. For cells infected with Vaccinia Virus E/L-GFP or Rotavirus dUnaG, immunostaining was omitted since those virus strains express fluorescent proteins, and only the DAPI staining was done to visualize cell nuclei. Cells were washed in PBS three times. Cells seeded on coverslips were mounted in ProLong Gold Antifade with DAPI, cells seeded in multiwells were maintained in PBS until imaging, and for cells seeded on transwell inserts the membrane was cut out and mounted in ProLong Gold Antifade with DAPI.

#### *4.2.6.4. In-cell Western analyses (TCID$_{50}$) for SARS-CoV-2 de novo production*

Vero E6 cells were seeded at 30,000 cells per well into a 96-well plate 24 h prior to infection. First, 100 µL of supernatant was added to the wells, and seven 1:5 serial dilutions were made. The cells were incubated for 24 h and then fixed with 2% PFA (in PBS) for 20 min at room temperature. Cells were washed twice with PBS and then permeabilized for 15 min with 0.5% Triton-X in PBS. Blocking was carried out with 1:2 dilution of Li-Cor blocking buffer in TBS for 30 min at RT. The cells were then incubated with a primary mouse monoclonal antibody against SARS-CoV-2 nucleocapsid protein (Table 8) for 1 h at room temperature. The cells were washed three times with PBS and then incubated with secondary antibody (anti-mouse CW800) and DNA dye DRAQ5 (Table 9) diluted 1:10,000 in blocking buffer for 1 h at RT. The cells were then washed again three times with PBS, and the plate was imaged on a LICOR (Li-Cor) imager.

#### *4.2.6.5. Detection of IFNs in the supernatant after SARS-CoV-2 infection by HEK-Blue assay*

To carry out HEK-Blue assays, the medium must contain heat inactivated serum. I prepared DMEM/F12 medium containing 100 U/mL penicillin, 100 µg/mL streptomycin and 10% FBS previously inactivated in a water bath at 56°C for 30 minutes, and used it to culture both T84 and HEK-Blue cells. One day before the assay, 25,000 HEK-Blue cells were seeded per well of a 96-well plate. 16-24 post seeding, cells were treated with 50 µL undiluted supernatant of infected cells or with 50 µL recombinant purified IFN (to generate a standard curve) for 24 hours. For the type I IFNs standard curve, I treated HEK-Blue cells with five 1:2 serial dilutions of IFNβ1 in medium (containing heat inactivated serum) starting at 10,000 IU/mL and leaving the last dilution without IFNs. For the type-III IFNs standard curve, I used five 1:3 dilutions in medium (containing heat inactivated serum) of 1:1:1 mixture of IFNλ1, IFNλ2 and IFNλ3, starting at 300 ng/mL total, leaving the last wells empty as negative controls. For the colorimetric assay, Quanti Blue Solution was used to determine the amount of Secreted embryonic alkaline phosphatase (SEAP). First, 24hrs post-incubation, the supernatant from each well was pipetted up and down several times and 30 µL were transferred to a new 96-well plate. I added 120 µL of Quanti Blue solution to each well with a multichannel pipette, covered the plates with aluminum foil and kept them at 37°C to accelerate the reaction. Plates were checked every 5 minutes until the standard curve started changing from pink to blue, and plates were scanned at 620 nm an 800TS Microplate Reader (BioTek). As a note, I scanned the plate every 15 min, and then chose the best setting (time) in which the colorimetric signal of my samples are within the linear range of the standard curve and not saturated. The amount of IFNs was determined by comparing the colorimetric values of the cell samples to the linear standard curve.

### 4.2.7. Specialized assays

#### *4.2.7.1. Mitochondrial DNA depletion*

Mitochondrial DNA (mtDNA) was depleted either by Ethidium bromide (EtBr) (protocol adjusted from King et al. (*461*)) or 2'-3'-dideoxycytidine (ddC) (protocol adjusted from Rongvaux et al. (*113*)). For an efficient depletion of mtDNA, I exposed cells for at least 6 days to 300 ng/mL EtBr or 100 µg/mL ddC. Cells were seeded in 48-well plates at low density in 0.5 mL medium supplemented with EtBr or ddC. At day one, three and five after seeding, medium change was done with fresh 0.5 mL media supplemented with EtBr or ddC. During the course of the experiment, cells continued to grow and become more confluent. Therefore, to obtain cells at high and low density depleted of mtDNA, I followed different procedures:

(a) For cells at high density depleted of mtDNA: Due to continuous cell growth throughout the experiment, by day 6 after seeding, the cells had reached full confluence, similar to the high-density cell seeding conditions detailed in section 4.2.2.2. Therefore, at day 6 post-seeding, cells were harvested as 'high density' samples for further processing.

(b) For cells at low density depleted of mtDNA: Cells were grown in media supplemented with EtBr or ddC as described above. At day 5 post-seeding, cells were detached by trypsin, counted and re-seeded at low density in medium supplemented with EtBr or ddC (cell seeding concentration at low density condition see section 4.2.2.2). One day after this re-seeding procedure (equivalent to 6 days of treatment), mtDNA depleted cells at low density were harvested for further processing.

For assessment of mitochondrial to nuclear DNA ratio in the cells: Adherent cells were washed and total DNA was purified from using the PureLink™ Genomic DNA Mini Kit (Thermo Fisher Scientific #K182002) following the manufacturer's instructions. DNA was eluted from the column using 30 µL $H_2O$ and DNA concentration was measured using the NanoDrop Lite spectrophotometer.

Quantitative RT-PCR assay was performed using iTaq SYBR green (BioRad), primers targeting mitochondrial gene nd2 and nuclear gene S18 (Table 10), and the Bio-Rad CFX96 Real-Time PCR Detection System as per manufacturer's instructions. For each reaction, the following pipetting scheme was used:

| | |
|---|---|
| iTaq SYBR green | 7.5µl |
| Forward primer (2µM) | 1.9µl |
| Reverse primer (2µM) | 1.9µl |
| Millipore H2O | 1.7µl |
| DNA (from total cell DNA) | 50 ng total DNA in 2µL volume (diluted in $H_2O$) |

The q-PCR was performed as follows:

| Step | Temperature | Time | Cycles |
|---|---|---|---|
| Activation | 95°C | 30s | 1 |
| Melting | 95°C | 5s | 40 |
| Primer annealing and elongation | 60°C | 30s | |
| Plate read | | | |
| Melting curve generation | 65°C | 5s | 1 |
| | +05°C/cycle to 95°C | | |

At the end of each run a melting curve was created to determine the melting point of the amplicons and exclude non-specific amplified DNA. The data was processed using the Bio-Rad CFX Manager 3.0 to determine the Cq value for each reaction. For the analysis of mitochondrial DNA depletion, first the gene abundance was calculated independently for mitochondrial gene nd2 or nuclear gene S18 using this formula: relative gene abundance = $2^{-Cq}$. Then the relative mitochondrial DNA was determined relative to the nuclear DNA, by dividing the mitochondrial nd2 DNA gene abundance by the nuclear 18S DNA gene abundance.

#### *4.2.7.2. Binding and endocytosis assay*

The binding and endocytosis assays were adjusted from Meier et al. (*462*). The GERV-Atto488 and GERV-Atto647 virus particles were kindly supplied by Zina Maria Uckeley and the Pierre-Yves Lozach Group (University Hospital Heidelberg). These assays were performed on cell populations seeded on micropatterned 8-well chamber slides or micropatterned transwell membranes. The treatment volume per well for the 8-well chamber slide was 200µL and for the transwell membrane was 800 µl (200 µL at the apical side and 600 µL at the basal side of the transwell insert).

Binding assay: Cells were washed one time with ice cold medium, ice cold medium was then added to the samples, and cells were kept on ice for 10 min to halt endocytic processes. I then treated the cells with virus diluted in cold medium. To allow virus particle binding without internalization, the cells were incubated on ice for 1.5 h. Cells were then washed once with cold medium and then once with cold PBS and immediately fixed with cold 4% PFA (diluted in PBS) for 20 min at RT. Samples were then washed twice with PBS and incubated with DAPI (1:1000 diluted in 0.5% BSA in PBS) for 20 min at RT to stain cell nuclei. Cells were then washed twice with PBS. For samples in 8-well chamber slide PBS was added and samples were maintained at 4°C until imaging. For samples on transwell inserts, the membrane was cut out, mounted with ProLong Gold antifade reagent and kept at 4°C until imaging.

Endocytosis assay: Cells were washed one time with ice cold medium, cold medium was added to the sample, and cells were kept on ice for 10 min to halt endocytic processes. I then treated the cells with virus diluted in cold medium. Cells were incubated on ice for 1 h to allow virus binding, and non-bound virus particles were then removed by washing twice with cold PBS. To allow internalization of bound particles, PBS was removed and prewarmed (37 °C) medium was added on cells, and cells were incubated for 1 h at 37 °C. Cells were then washed once with cold medium and once with cold PBS, and immediately fixed with cold 4% PFA (diluted in PBS) for 20 min at RT. Samples were then washed twice with PBS and incubated with DAPI (1:1000 diluted in 0.5% BSA in PBS) for 20 min at RT to stain cell nuclei. Cells were then washed twice with PBS. For samples in 8-well chamber slides, PBS was added and samples were maintained at 4°C until imaging. For samples on transwell inserts, the membrane was cut out, mounted with ProLong Gold antifade reagent and kept at 4°C until imaging. When working with GERV-Atto488, bound but not internalized particle fluorescent signal was quenched using Trypan blue (*4*). For samples in 8-well chamber slides, 0.01% Trypan blue (diluted in PBS) was added to the sample prior to imaging. For samples on transwell inserts, a drop of 0.01% Trypan blue (diluted in PBS) was carefully put on the membrane before mounting with ProLong Gold antifade reagent.

### *4.2.7.3. Transferrin and dextran uptake assay*

The transferrin and dextran uptake assays were done on cell populations seeded on micropatterned 25 mm diameter glass coverslips (fitting in a 6-well plate) or micropatterned 6.5 mm diameter transwell membrane (fitting in a 24-well plate).

Transferrin-647 uptake assay: Medium was removed and FBS-free medium supplemented with 50 µg/mL Transferrin-Alexa647 was added to the cells: 1 mL on cells seeded on 25 mm diameter glass coverslips, or 800 µL total volume on cell seeded on transwell inserts (200 µL on apical side and 600 µL on basal side). Transferrin-Alexa647 uptake was allowed to proceed for 7 min at 37°C. Cells were washed once with an acid wash, three times with PBS and then fixed with 2% PFA/PBS. After washing three times with PBS, cells were mounted in ProLong Gold Antifade with DAPI and imaged by fluorescence microscopy.

FITC-Dextran uptake assay: Medium was removed and FBS-free medium supplemented with 1 mg/mL FITC-Dextran was added to the cells: 1 mL on cells seeded on 25 mm diameter glass coverslips, or 800 µL total volume on cell seeded on transwell inserts (200 µL on apical side and 600 µL on basal side). FITC-Dextran uptake was allowed to proceed for 30 min at 37°C. Cells were washed once with an acid wash, three times with PBS and fixed with 2% PFA in PBS. After washing three times with PBS, cells were mounted in ProLong Gold Antifade with DAPI and imaged by fluorescence microscopy.

### *4.2.7.4. Polyamines and virus infection in T84 cell populations*

T84 cells were grown as 200 µm diameter populations on micropatterned glass (25 mm diameter coverslips fitting in 6-well plates).

Polyamine treatment: Cells were treated with a mix of 1:1:1 of spermidine, spermine and putrescine, with a final polyamine concentration of 300 µM in a volume of 2 mL media. Treatment was performed either 16 h prior to infection or during infection. Cells were then infected with Mammalian reovirus (MRV) (1:500 diluted) in a total volume of 2 mL media. For both conditions (polyamine 16 h pre-treated cells and cells treated during infection) 300 µM polyamines were supplemented to the media containing MRV. Infection occurred for 16 h, cells were then washed once with PBS and fixed with 2 % PFA. I proceeded with immunostaining against the MRV protein µNS.

Difluoromethylornithine hydrochloride hydrate (DFMO) treatment: For DFMO treatment, the media can only contain 2% FBS. Therefore, during the seeding process and throughout the whole experiment, I maintained and treated the cells in a 50:50 mixture of DMEM and F12 supplemented with 2% FBS, 100 U/mL penicillin and 100 µg/mL streptomycin. During the seeding procedure (volume 2 mL), the media was supplemented with 1, 5 or 10 mM DFMO. Media was exchanged every 48 h and fresh 2 mL media supplemented with the respective DFMO concentration was added. After 96 h of the DFMO pre-treatment, cells were infected with MRV (1:500) supplemented with the respective DFMO concentration in a volume of 2 mL. Infection occurred for 16 h, cells were then washed once with PBS and fixed with 2 % PFA. I proceeded with immunostaining against the MRV protein µNS.

### 4.2.8. Surface biotinylation and surface proteome analysis by mass spectrometry

Surface biotinylation and surface proteome analysis was done by Francesco Muraca from my lab and Benno Kuropka (Christian Freund Group at the Freie Universität Berlin, Institute of Chemistry and Biochemistry). T84 WT cells were in transwell inserts (as described in section 4.2.2.4) until formation of a polarized monolayer as determined by TEER measurement. Cells were then washed thrice in PBS and treated with 1 mg/ml Sulfo NHS-SS-Biotin in biotinylation buffer (10 mM HEPES, 130 mM NaCl, 2 mM $MgSO_4$, 1 mM $CaCl_2$, pH 7.9) on the apical or basolateral side for 15 minutes on ice (biotinylation buffer alone was added to the opposite side to prevent drying). After incubation, cells were washed with 100 mM glycine for three times (last wash was left on cells for 10 minutes) to remove and quench excess biotin. Membranes were then cut and added to cell lysis buffer (50 mM HEPES, 150 mM NaCl, 5 mM EDTA, 1% Triton x-100, 0.1% SDS, pH 7.4) for 30 minutes in ice. After brief sonication and sedimentation of insoluble fragments, the protein amount was quantified using the the Pierce BCA Protein Assay Kit assay (Thermo Scientific #23225). The same amount of total lysate for each sample (apical, basolateral and no biotinylation sample (background)) was loaded with High Capacity Neutravidin Agarose beads (Thermo Fisher #29202) and incubated overnight at 4°C on an orbital shaker. The day after, supernatant was removed and beads were washed twice with high salt buffer (1M NaCl, 50 mM HEPES, 0.1% Triton x-100, pH 7.4) and twice in 50 mM HEPES (pH 7.4). Beads were then incubated in Laemmli buffer for 20 minutes at RT on an orbital shaker. The supernatant containing the biotinylated surface proteins was then harvested, and loaded and ran on an SDS-PAGE for purification. Bands were excised and digested wit trypsin using a standard protocol (*463*). After digestion, peptides were extracted and dried for LC-MS analysis. Peptides were reconstituted in 15 µl of 0.05% trifluoroacetic acid, 4% acetonitrile, and 6.6 µl were analyzed by an Ultimate 3000 reversed-phase capillary nano liquid chromatography system connected to a Q Exactive HF mass spectrometer (Thermo Fisher Scientific). Samples were injected and concentrated on a trap column (PepMap100 C18, 3 µm, 100 Å, 75 µm i.d. x 2 cm, Thermo Fisher Scientific) equilibrated with 0.05% trifluoroacetic acid in water. LC separations were performed on a capillary column (Acclaim PepMap100 C18, 2 µm, 100 Å, 75 µm i.d. x 25 cm, Thermo Fisher Scientific) at an eluent flow rate of 300 nl/min. Mobile phase A contained 0.1 % formic acid in water, and mobile phase B contained 0.1% formic acid in 80 % acetonitrile / 20% water. The column was pre-equilibrated with 5% mobile phase B followed by an increase of 5-44% mobile phase B in 100 min. Mass spectra were acquired in a data-dependent mode utilising a single MS survey scan (m/z 350–1650) with a resolution of 60,000 and MS/MS scans of the 15 most intense precursor ions with a resolution of 15,000. The dynamic exclusion time was set to 20 seconds and automatic gain control was set to $3x10^6$ and $1x10^5$ for MS and MS/MS scans, respectively.

MS and MS/MS raw data were analyzed using the MaxQuant software package (version 1.6.14.0) with implemented Andromeda peptide search engine (*464*). Data were searched against the human reference proteome downloaded from Uniprot (75,074 sequences, taxonomy 9606, last modified March 10, 2020) using the default parameters except for the following changes: label-free quantification (LFQ) enabled, match between runs enabled, iBAQ enabled, max missed cleavages: 3.

Perseus downstream analysis was performed as follows: Proteins were cross referenced with the UniProt human database for gene ontology terms (Plasma membrane, plasma membrane part, cell surface, cell outer membrane), then filtered out if they had less than 3 replicates or if they had no GO term matching the above mentioned search. Background samples were used to filter out any protein non-specifically bound to the Neutravidin beads. Significantly enriched proteins on the apical or basolateral side were assigned based on their log(2) LFQ signal between apical- and basolateral-biotinylated samples, using pairwise t-tests coupled with sample randomization with false discovery rate (FDR) = 0.05.

### 4.2.9. RNA-Sequencing

I seeded T84 WT cells at high and low density (see section 4.2.4.3.) in a 12-well plate configuration to ensure enough RNA yield. Additionally, for low density seeding, cells from 2 wells were pooled. For each condition, I seeded 4 biological replicates. RNA extraction was done using the RNeasy Plus Mini Kit (Qiagen # 74034) following the manufacturer's instruction and the RNA concentration was measured using the NanoDrop Lite spectrophotometer. 500

ng of RNA in 20 µL $H_2O$ were sent to GENEWIZ (Azenta Life Sciences) to perform Standard RNA sequencing. Genewiz prepared the library targeting mRNA by using the Poly(A) RNA selection method. Illumina® NovaSeq™ was used to do paired end sequencing at a 2x150 bp configuration. I obtained the sample quality control report (FAST QC Report) and the raw data as FASTQ files (R1.fastq.gz and R2.fastq.gz since paired end sequencing was done).

The scripts for the RNA sequencing data analysis were kindly provided by the Hermann Group (BioQuant Heidelberg). I was trained by Daria Doncevic to use these scripts. I performed the analysis in the Curry-Cluster (high-performance computer cluster) from the BioQuant (Heidelberg) using the RStudio server. First, I ensured the quality of the sequencing data with the FAST QC Report. Then I trimmed the adapters and the poor quality reads from the raw data R1.fastq.gz and R2.fastq.gz files and aligned the reads of both FASTQ files to the Homo sapiens reference genome (GRCh38.p14, www.ncbi.nlm.nih.gov), resulting in BAM (Binary Alignment Map) files. This was performed in conda, as the command had to be run in an environment that has *snakemake* installed. The pipeline was previously established by the Hermann Group (BioQuant Heidelberg), and access to their database is required to run it. To command to run the pipeline on qsub (user-accessible batch client that submits a script) is as follows:

```
snakemake -k -w 50 --jobs 50 \
        --use-singularity \
        --singularity-args "--bind /media/ag-cherrmann/projects/19_Hipoxia_organoids/ --bind
/media/ag-cherrmann/hdsu/data/assemblies/RNAseq_pipeline" \
        --cluster-config cluster/qsub.yaml \
        --cluster "qsub -l walltime={cluster.walltime} -l nodes={cluster.cores} -l
mem={cluster.memory} -N {cluster.name} -o {cluster.output} -e {cluster.error}" \
        --configfile configs/rnaseq_configfile_hypoxia.yaml --rerun-incomplete
```

*Directory containing the raw FASTQ files

Using the resulting BAM files, I created a table aggregating counts (raw read counts) and tpm (transcript per million, a normalized representation of the transcripts per gene) from all samples. This table was used to perform a Principal Component Analysis (PCA) using the built-in R function *prcomp()*, and Differential Gene Expression Analysis using the built-in R function *DESeqDataSetFromMatrix()* and *DESeq()*. Gene Set Enrichment Analysis was performed with the differential gene expression analysis table by using the function *gage()* (*327*). Finally, the counts and tpm table was used to assess pathway activities using the function *progeny()* (PROGENy: Pathway RespOnsive GENes for activity inference) (*328*).

### 4.2.10. Spatial metabolomics

I seeded T84 and CaCo2 cells as populations (200 µm diameter) on micropatterned 25 mm diameter coverslips as described in section 4.2.4.4. I prepared the samples in two different ways for the spatial metabolomics procedure, allowing me to detect different metabolites. In the first procedure, I used 10 mM ammonium acetate for the washing steps. Ammonium acetate removes any residual salts such as sodium phosphate, which can crystalize and suppress matrix-assisted laser desorption/ionization (MALDI). The cell populations were washed three times with 10 mM ammonium acetate and then cells were fixed with 4% PFA (in PBS) for 15 min at RT. Three times washing was repeated with 10 mM ammonium acetate and then the cell nuclei were stained with DAPI (1:1000 diluted in $H_2O$). Finally, the samples were washed three times with 10 mM ammonium acetate followed by washing three times with $H_2O$. In the second procedure, PBS was used for the washing steps instead. Shortly, cells seeded as populations were washed three times with PBS and fixed with 4% PFA (in PBS) for 15 min at RT. After washing three times with PBS, cell nuclei were stained with DAPI (1:1000 diluted in PBS) for 15 min at RT, and followed by three times washing with $H_2O$. After staining and washing samples with either procedure, cells were desiccated under vacuum for 1 h at RT using the Synthware™ Vacuum Glass Desiccator (Thermo Scientific). The coverslips were then mounted on a glass slide with the cells facing up (not sandwiched between the coverslip and the glass slide) by adding a droplet of water between coverslip and slide. The samples had to be further processed as quick as possible to avoid lipid oxidation.

The spatial metabolomics was performed by Mans Ekelov and the Alexandrov Team (European Molecular Biology Laboratory (EMBL) Heidelberg) using the SpaceM method (*465*). SpaceM is a MALDI-based single-cell metabolomics method which assigns metabolite intensities to individual cells located in a 2-dimensional space. In short, SpaceM integrates MALDI-imaging with light microscopy followed by image segmentation and registration. The readout is a spatio-molecular matrix for each cell containing a normalized metabolic profile. The detailed procedure used for SpaceM analysis of my cell populations is described in Rappez et al. (*465*). SpaceM was done at a resolution of 5 µm and 10 µm per pixel. 5 µm/pixel was chosen to have a higher spatial resolution. However, depending on the lipid abundance and how easy it is to ionize the lipid, the lower 10 µm/pixel had to be used to collect the target ions. The imaging mass spectrometry data was uploaded to the METASPACE platform (metaspace2020.eu) for metabolite annotations of imaging mass spectrometry data. The METASPACE platform also contains a database to identify and assign specific metabolites to the MALDI annotations. I analyzed the data from the T84 and CaCo2 cell populations in the METASPACE data and selected the annotations with a 10% FDR (False Discovery Rate) which showed a heterogeneous spatial distribution. Using the METASPACE database, I then chose the annotations that were linked to identifiable candidate molecules. The results were visualized as heatmap images showing the intensity of a metabolite in a certain area of the cell population.

## 4.3. Fluorescence imaging and image analysis

### 4.3.1. Imaging

Images of fixed samples were acquired using the epifluorescent Nikon Eclipse Ti-S inverted microscope (S Plan Fluor ELWD 20x Objective with a Numerical Aperture (N.A.)=0.45), the confocal spinning disc Nikon Ti Andor microscope (CFI Pl Apo 40x objective with a N.A.=0.95), and the ZEISS Celldiscoverer 7 Widefield microscope (Plan-Apochromat 5x 1x with a N.A.=0.25, Plan-Apochromat 20x/0.7autocorr 1x with a N.A.=0.7, Plan-Apochromat 20x/0.95autocorr 0.5x with a N.A.=0.5, and Plan-Apochromat 20x/0.95autocorr 1x with a N.A.=0.8).

Live cell fluorescence microscopy was performed using the ZEISS Celldiscoverer 7 Widefield microscope (Plan-Apochromat 20x/0.95autocorr 0.5x with a N.A.=0.5, and Plan-Apochromat 20x/0.95autocorr 1x with a N.A.=0.8). For live cell fluorescence microscopy, cells were kept at 37°C and 5% $CO_2$ during the whole procedure.

### 4.3.2. Image analysis: Quantification of the number of infected cells

Cells seeded at different densities were infected with virus as described in the results part. Virus infection was immunostained and infection levels were imaged by fluorescence microscopy. To quantify the number of infected cells, I first used the Pixel Classification + Object Classification workflow from ilastik 1.2.0 to segment the nuclei from raw DAPI images. Ilastik is based on machine learning algorithms where the user teaches the program what nuclei and what background is. Therefore, to obtain a precise segmentation, it is important to use at least 10 raw DAPI images that cover the different seeding conditions (e.g. very densely seeded cells to less dense). The resulting Object Prediction masks represented all nuclei as individual objects in a 2-dimensional plane and were saved as 16 bit Tagged Image File Format. To measure the single-cell fluorescence intensity for immunostained virus infection, I developed a pipeline using CellProfiler 3.1.9. Briefly, first the raw grayscale images corresponding to the viral fluorescent signals was uploaded on the pipeline. These images were specified as images to be measured. The corresponding Object Prediction masks previously generated by Ilastik were then uploaded, converted into binary nuclei masks and used to define the objects to be measured. Finally, with a MeasureObjectIntesity module the mean fluorescence intensity was measured within the identified objects from the binary nuclei mask. The outcome was exported to a spreadsheet and contained the mean fluorescence intensity units rescaled from 0 to 1 of the virus fluorescent signals for each single cell. To determine the infection status for every cell, a threshold was calculated using the virus mean fluorescent intensity signal of mock-treated versus representative infected cells. Finally, the percentage of infected cells was calculated by using this formula: (number of infected cells above the threshold/total number of cells) x 100. Importantly, when setting the threshold, it is essential to control that the percentage of virus infected cells obtained from the analysis fits the raw imaging data. To this end, random images were picked, positive cells were counted and compared with the analysis results.

### 4.3.3. Image analysis: Spatial heterogeneity of IFN-dependent immune response using the DBSCAN-CellX-App

T84 prom-Mx1-GFP cells seeded at medium density on glass bottom 8-well chamber slides were mock treated or treated with IFNs for 24 h and fixed in 2% PFA (in PBS) for 20 min at RT. Cells were washed once with PBS and permeabilized in 0.5% Triton-X-100 (in PBS) for 15 min at RT. Cell nuclei were stained with DAPI diluted 1:1000 in PBS for 20 min. Cells were washed with PBS three times and maintained in PBS. Cells were imaged on a ZEISS Celldiscoverer 7 Widefield microscope using a 20 x 0.5 magnification (N.A.=0.5).

To analyze the spatial heterogeneity of IFN-dependent immune response, I first generated masks from DAPI images representing each nucleus as an individual object with the segmentation software Ilastik 1.2.0 as described in section 4.3.2. These masks were then used in a CellProfiler pipeline (similar as described in section 4.3.2) to determine (a) the XY-localization of each object (nucleus) within its 2-dimensional plane and (b) to measure the prom-Mx1-GFP fluorescence intensity within each object (nucleus). Using the information on the XY-localization, I applied the DBSCAN-CellX-App (https://github.com/GrawLab/DBSCAN-CellX/) to the data to assess whether a cell is localized at the edge or the center of a cluster, and to determine the edge degree of a cell. The cell localization and cell edge degree were plotted against the percentage of prom-Mx1-eGFP positive cells (as compared to the mock-treated samples) within each sub-population group, resulting in the visualization of the immune response of single cells within their population context.

### 4.3.4. Image analysis: Assessing the distribution of events within epithelial cell populations

WT, knock-out or reporter cell lines were grown as populations (200 µm diameter) on micropatterned surfaces, treated as described in the results part and images were acquired by fluorescence microscopy. To analyze the segregation of events, CellProfiler 3.1.9 was first used to generate masks from the acquired images that divide each population into an edge region and a center region. As a note, separate/unique masks were generated for each population using the DAPI signal.

Spatial distribution in IFN response: The spatial heterogeneity during IFN response was assessed by with the T84 prom-Mx1-eGFP reporter cell line. After creating the edge and center mask, I used CellProfiler 3.1.9 to measure the mean fluorescence intensity (MFI) at the edge and the center of a population at 0, 12 and 24 h post IFN treatment. Reporter expression levels at the edge and the center of a population were expressed as normalized fluorescence, which was calculated by dividing the MFI from 12 and 24 h post-treatment by the MFI of the 0 h timepoint.

Spatial distribution in virus infection (Fig. 45 B): To assess the spatial segregation of virus infection, images of virus infected cell populations were used. After creating the edge and center mask, I used CellProfiler 3.1.9 to measure (a) the area of the whole population, the edge region and the center region, and (b) the integrated intensity (sum of the grey values within an area of interest) of the whole population, the edge region and the center region. Since the area of the edge and center region were not identical between different populations, I first had to normalize it to the total population area (dividing the edge and center region by the total population area). The sum of the normalized edge and center area is 1. Similarly, the integrated intensity at the edge and the center were also normalized to the integrated intensity of the total population. Finally, the relative infection was calculated by dividing the normalized integrated intensity at the edge and center region by the corresponding normalized area. This allowed to represent the infection values at the edge and center as relative to each other: When fluorescence/infection levels are similar at the edge and the center (i.e. no spatial segregation of events), the relative infection values will be close to 1. Conversely, if there are differences between edge and center, the values will deviate from 1. If a point is above 1, it means that the fluorescence/infection is higher as compared the corresponding counterpart region of the population, and if a point is below 1 it indicates that the fluorescence/infection is lower as compared to the corresponding counterpart region. For example, the relative infection value of the edge of a population is 1.5 and the relative infection value of the center of the same population is 0.8. This means that the edge and the center are differentially infected (because the values are not close to 1), and that the edge is more infected than the center.

### 4.3.5. Image analysis: Assessing the induction of basal ISG expression over time as cells become confluent (Fig. 35)

T84 prom-Mx1-mCherry cells were seeded at low density on glass bottom 8-well chamber slides. Cells were imaged for a period of 10 days with 3 h time interval, as described in the main text. To analyze the induction of basal IFN-dependent immune signaling as cells grow confluent, ilastik 1.2.0 was first used to generate masks from the Brightfield images. The masks covered the area on which cells are growing for each time-point. After creating the masks, I used CellProfiler 3.1.9 to measure the mean fluorescence intensity (MFI) within the mask and the area of the mask, which is the area occupied by the cells for each timepoint. The mean fluorescence was then plotted against the time and the area occupied by the cells.

### 4.4. Statistics and Softwares

If not specified otherwise, all statistical analyses were performed with the GraphPad Prism 5.0 software. The number of biological replicates and statistical tests used are specified in the Figure Legends.

If not specified otherwise, all schematics and illustrations were created with BioRender.com. All Figures were assembled with the Affinity Designer 1.10.0 software. If not specified otherwise, the data was plotted with the GraphPad Prism 5.0 software.

All additional softwares used in this thesis and their purpose are specified in the Results (section 2) and the Material and methods (section 4).

# 5. Annex

## 5.1. Micropatterning system to study the population behavior of epithelial cells

I exploited a micropatterning technique to study how the position of epithelial cells relative to each other influences immune signaling and virus infection. The micropatterning method enables me to create cell populations of defined and uniform sizes, embedding cells in a standardized population context. This setup facilitated the development of automated analysis processes to evaluate the spatial heterogeneity of events. This methodology has been exploited in my results sections 2.1. and 2.3.

### 5.1.1. Micropatterning of different surfaces, cell seeding and treatment

A detailed schematic of the methodological approach can be found in Fig. 67 A. First, a surface is passivated with PLL-PEG, an antifouling agent that prevents protein binding and cell adhesion. Subsequently, the micropatterning step is performed, based on a controlled depletion of the antifouling agent in specific regions through exposure to ultraviolet (UV) light. I employed two different techniques for this purpose. In the Quartz-mask based approach, a Quartz-Mask imprinted with transparent patterns is overlaid on the passivated surface and illuminated with UV-light in the presence of ozone. As Quartz reflects light, the UV-light can only pass through the transparent areas, thereby depleting the PLL-PEG at discrete locations creating size- and shape-specific patterns on which cells can grow. This technique is limited to glass coverslips and predetermined patterns outlined by the Quartz-mask. In the maskless photolithography approach (Alvéole company), specific patterns are designed as binary images. An optical system connected to an inverted microscope employs a Digital Micromirror Device (DMD) to shape UV light, reproducing the previously designed patterns onto the surface. Compared to the Quartz-mask based approach, this method offers more flexibility by enabling the patterning of any desired design on a variety of surfaces. The resulting micropatterned surface consists of distinct regions where PLL-PEG has been removed, rendering them suitable for protein coating and cell seeding. I typically generated micropatterns in the form of circles with a diameter of 200µm. This resulted in cell populations of consistent size once they were seeded on the patterns. Following cell seeding, the cell populations underwent specific treatments and were subsequently imaged through fluorescence microscopy. Due to the uniform character of the cell populations, I could develop standardized pipelines employing FIJI, Ilastik and CellProfiler to analyze high content imaging data.

Depending on the purpose of the experiment, I micropatterned glass surfaces using one the two previously described micropatterning techniques (Fig. 67 B) or transwell membranes using specifically the maskless photolithography system (Fig. 67 C). When cell populations were seeded on glass surfaces, only the apical cell membrane is in contact with the medium while the basal membrane adheres to the glass surface (Fig. 67 B). This setup restricted treatment to the apical membrane only (Fig. 67 B). On the other hand, when cell populations were seeded onto transwell membranes, both the apical and basal membrane of the cells were exposed to the medium, enabling simultaneous treatment from both sides (Fig. 67 C).

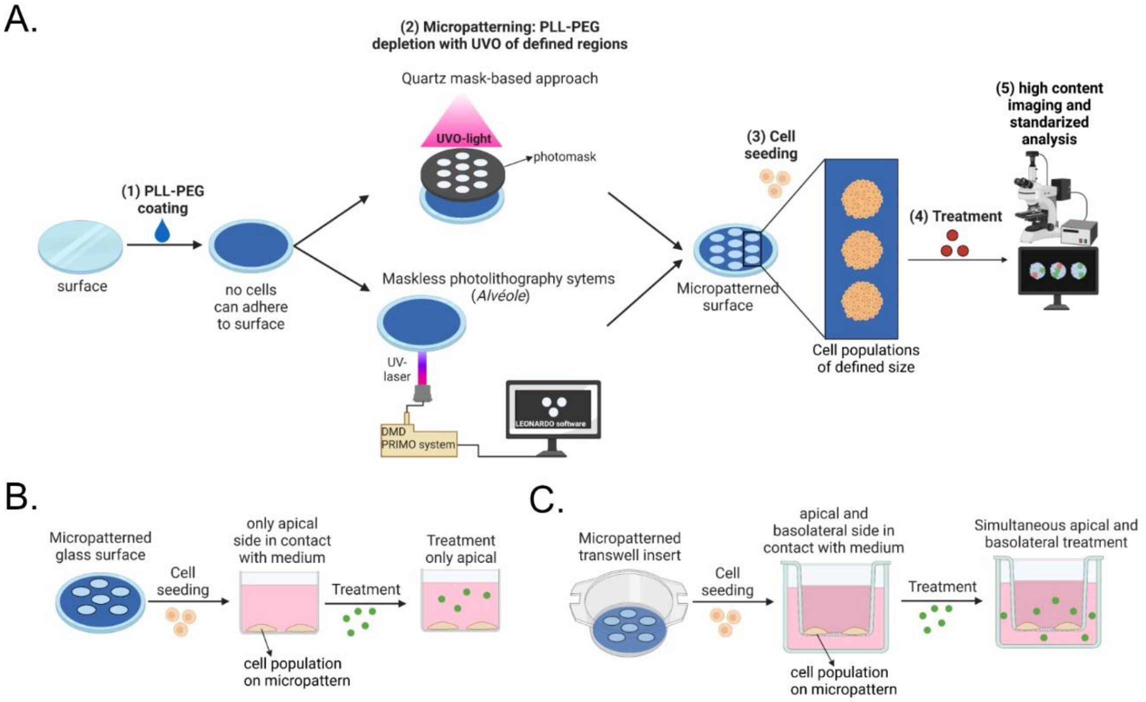

**Fig. 67. Micropatterning system to study the population behavior of epithelial cells.** (A) Schematic showing micropatterning of surfaces using the Quartz mask-based approach or the maskless photolithography system. Cells are seeded on micropatterns and grown as homogenous populations, which can be treated and analyzed by fluorescence imaging. (B) Schematic showing micropatterning and cell seeding of glass surfaces, which only allows for apical cell treatment. (C) Schematic showing micropatterning and cell seeding of transwell inserts, which allows simultaneous apical and basal cell treatment.

### 5.1.2. Characterization of epithelial cell populations seeded on micropatterns

I employed a range of molecular techniques to thoroughly analyze and describe the epithelial cell populations seeded on micropatterns. T84 WT cells were seeded on micropatterned glass and immunostained for various proteins that provide insights into particular molecular states (Fig. 68). To address the polarization status of cells across the population and the intercellular connections that these cells form, I analyzed ZO1 and F-actin proteins. Z-projection of the apical view revealed that ZO1 localized to the junctional complexes in center cells of a population, forming a network of intercellular connections (Fig. 68 A, upper panels). On the contrary, cells situated at the population's outer edges exhibited minimal presence of this protein (Fig. 68 A, upper panels, red arrows). ZO1 localization to junctional complexes, which form at the upper lateral area between polarized cells, is clearer depicted in the transversal view in Fig. 68 A (lower panels, yellow arrows). Since formation of junctional complexes is a marker for cell polarization, this suggests that only center and not edge cells within a population are polarized. This is underlined by F-actin staining using Phalloidin-647. When IECs polarize, F-actin accumulates to the apical region of the cell to support the formation of microvilli structures and tight junction (*466*). F-actin is notably concentrated at the apical area of center cells within the population, while less expressed in edge cells (Fig. 68 A, lower panels, yellow arrows). The transversal view depicting the DAPI channel also shows that center cells adopt a columnar shape as observed for polarized cells, while edge cells are flatter and larger in area (Fig. 68 A, lower panels, white arrows). In summary, cells situated at the center of a population undergo polarization, resulting in the formation of distinct apical and basolateral membranes, along with the establishment of intercellular connections. Conversely, cells located at the periphery lack polarization and exhibit minimal connections with neighboring cells. Furthermore, these edge cells have at least one side that lacks adjacent neighbors.

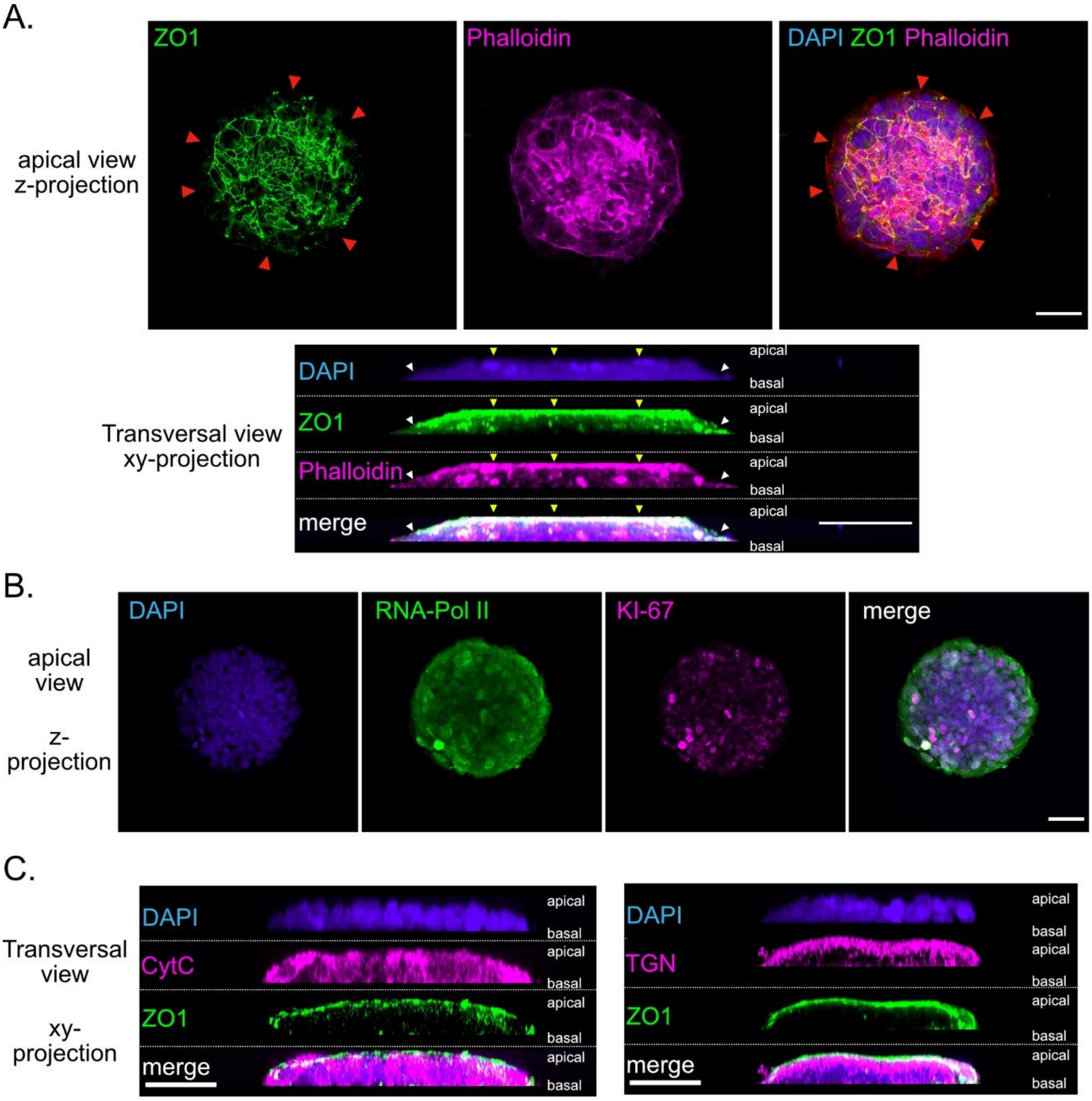

**Fig. 68. Protein expression and protein localization in epithelial cell populations seeded on micropatterns.** T84 WT cells were seeded on micropatterns as populations and fixed. Immunostaining

was performed against a variety of proteins. Cells were imaged with spinning disc microscopy at different focal-planes (Z-stack), and visualized as apical view (with z-projection) or transversal view (xy-projection). (A) Representative images showing ZO1 protein (green) and Phalloidin-647 (magenta) which stains for F-actin. Red arrows point out edge cells lacking ZO1 protein, white arrows point towards edge cells that are flat and large in area, and yellow arrows show localization of ZO1 and F-actin to the apical side of the populations. (B) Representative images showing RNA Polymerase II (RNA-Pol II, green) and marker of proliferation Ki-67 (magenta) in T84 cell populations along the XY-axis. (C) Representative images showing the mitochondria marker Cytochrom C (CytC), Trans-Golgi Network (TGN) and ZO1 in epithelial cell populations along the Z-axis. (A-C) Cell nuclei were stained with DAPI (blue). Scale bar=50 µm.

To address whether epithelial cell populations exhibit a heterogeneous pattern of RNA transcription and proliferation, I immunostained the RNA-Pol II and KI67 in T84 cells seeded on micropatterned glass, respectively. Both RNA-Pol II and KI67 proteins appeared to be stronger expressed at the edge of the population than in the center (Fig. 68 B), suggesting increased RNA biogenesis and proliferation at the edges. However, further experiments are required to support this observation. Finally, mitochondria (as seen by Cytochrome C (CytC) staining) appeared to be localized homogenously across cells seeded on micropatterns, while the Trans-Golgi Network (TGN) localized to the apical side of polarized cells (Fig. 68 C).

In collaboration with the Alexandrov Team (EMBL Heidelberg), I employed a spatial metabolomics method on T84 and CaCo2 cells seeded on micropatterned glass to assess potential differences in metabolite abundance across epithelial cell populations. Interestingly, DNA bases including adenine, guanine and cytosine were enriched in edge cells of the population (Fig. 69 A). This observation is consistent with the results obtained from KI67 staining (Fig. 68 B), and reinforces the idea that cells situated at the population's periphery exhibit higher levels of proliferation. Also the polyamine spermine and analogues (Fig. 69 B) as well as phosphorycholine (Fig. 69 C) displayed a heterogeneous pattern, and were more abundant in edge cells as compared to center cells in a population.

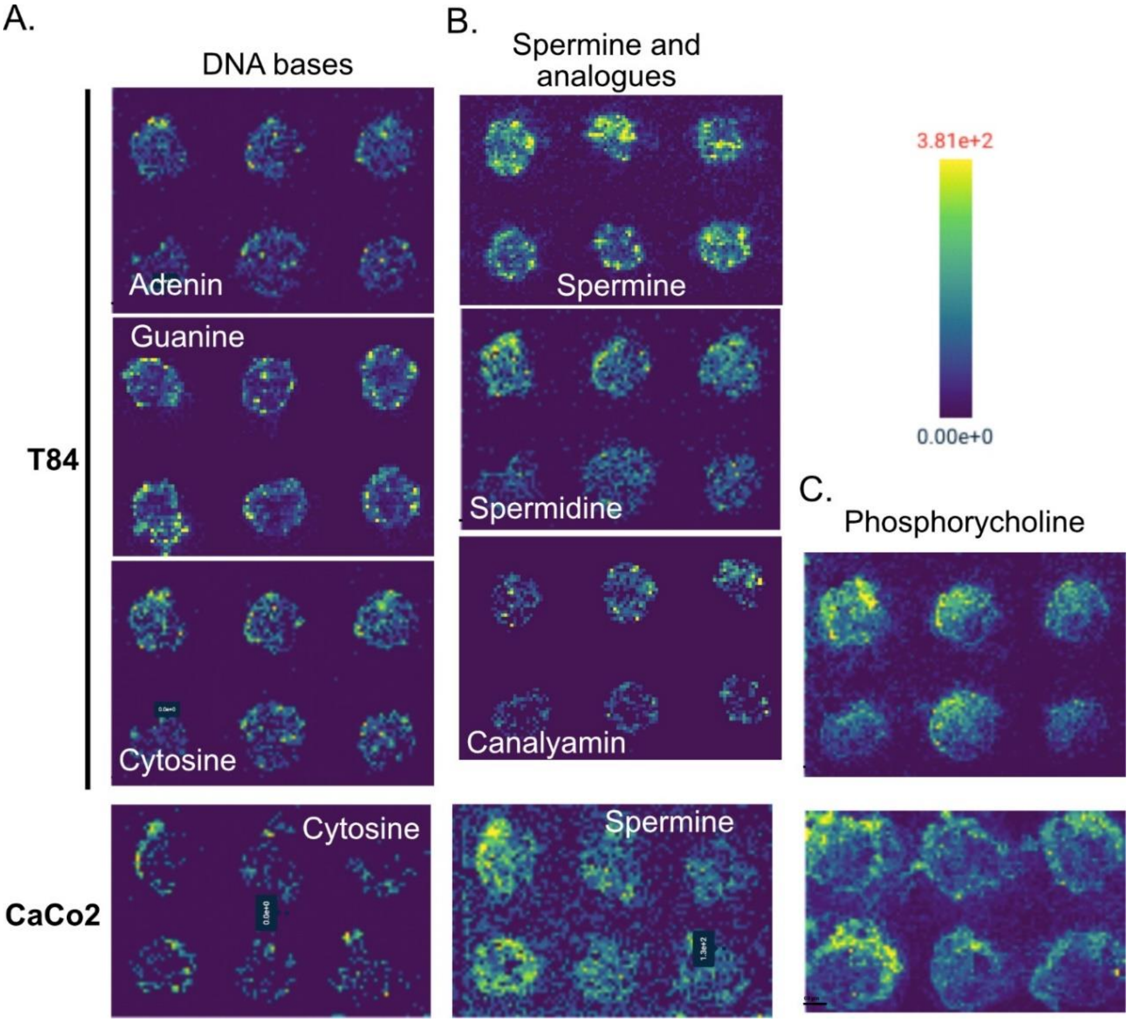

**Fig. 69. Spatial metabolomics of epithelial cell population.** T84 and CaCo2 cells were seeded on micropatterned glass and grown as 200 µm diameter populations. Spatial metabolomics was used on these populations using the SpaceM method (*465*), a MALDI-based single-cell metabolomics which assigns metabolite intensities to individual cells located in a 2-dimensional space. Figure shows metabolites that were spatially segregated within the epithelial cell populations. These included (A) DNA bases, (B) Spermine and analogues and (C) Phosphorycholine. Scale: blue to red, blue signalizes no detection of the metabolite.

To assess the distribution of endocytic events across a population, I performed the transferrin assay to visualize clathrin-mediated endocytosis (CME) and the Dextran assay to study macropinocytosis. When T84 and CaCo2 cell populations were seeded on glass, only cells positioned at the population's periphery displayed endocytosis of Transferrin-647 (Fig. 70 A). In contrast, all cells within the population exhibited uptake of FITC-Dextran (Fig. 70 A). Importantly, quantification of the relative Transferrin-647 and FITC-Dextran uptake, highlighted a notably heterogeneous distribution of endocytic events (Fig. 70 B). CME predominantly occurred at the population edges, while macropinocytosis was more prevalent in center cells (Fig. 70 B). The observation that apical treatment of epithelial cell populations on micropatterned glass primarily led to Transferrin uptake at the population edges is not surprising, given that the transferrin receptor is localized to the basolateral membrane of polarized cells (*467*). Indeed, when T84 cell populations seeded on micropatterned transwells were simultaneously exposed to Transferrin-647 from both the apical and basolateral sides, the spatial heterogeneity in endocytosis was abrogated and center also endocytosed Transferrin-647 (Fig. 70 C). FITC-Dextran uptake in cell populations seeded on transwells (Fig. 70 C) resembled that of cell populations on glass (Fig. 70 A).

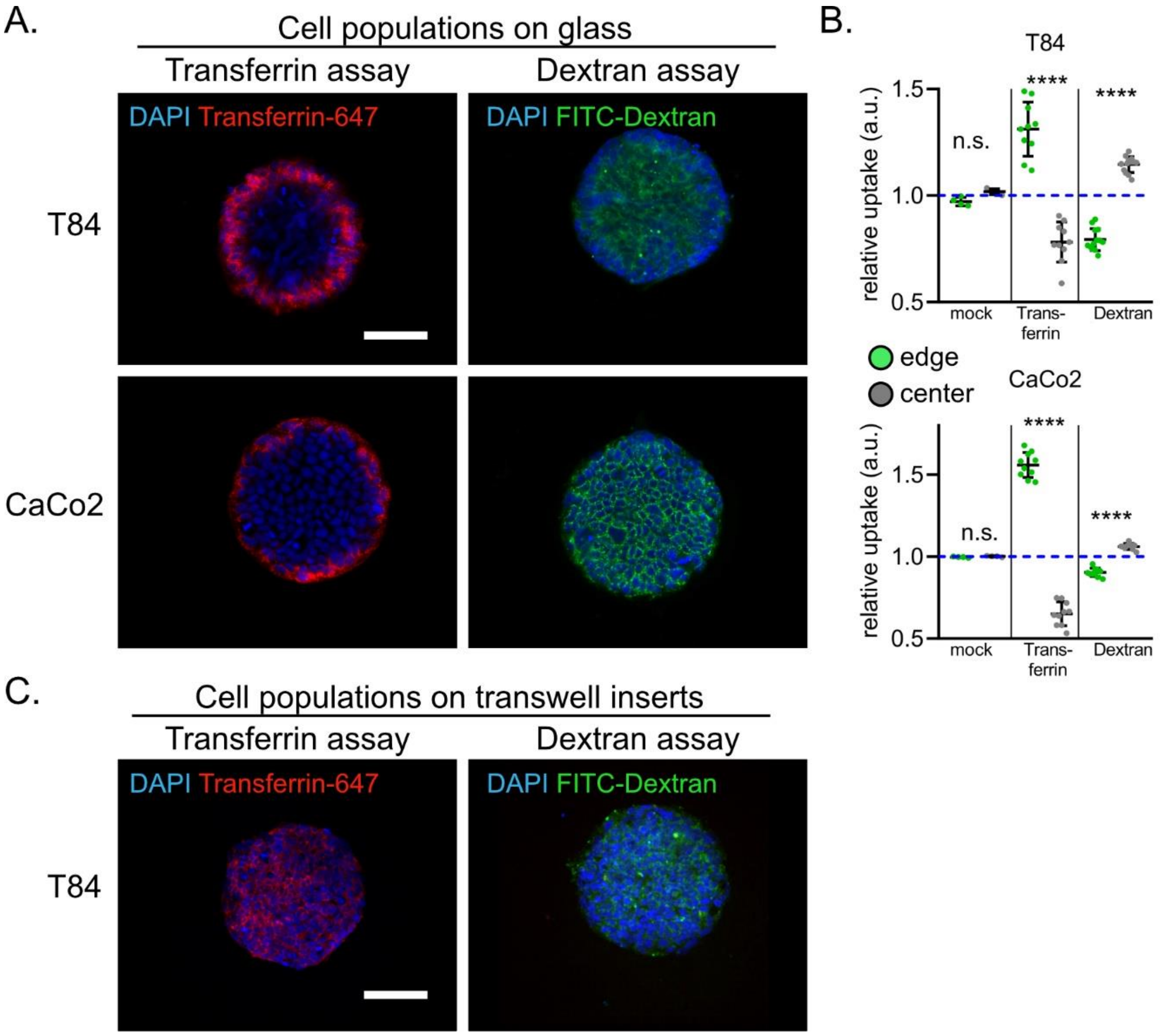

**Fig. 70. Endocytic events across epithelial cell populations.** T84 and CaCo2 cells were grown as populations on (A, B) micropatterned glass and (C) micropatterned transwell inserts. The transferrin (to test clathrin-mediated endocytosis) and dextran (to determine macropinocytosis) uptake assays were performed by treating cells either (A, B) from the apical side only or (C) simultaneously from the apical and basal side. Cells were fixed, mounted in ProLong Gold Antifade with DAPI and imaged by fluorescence microscopy. (A, C) Representative images showing endocytosis of Transferrin-647 (red) or FITC-Dextran (green) in epithelial cell population. Cell nuclei were stained with DAPI (blue). Scale bar=100 µm. (B) Quantification from (A) of the relative Transferrin-647 or FITC-Dextran uptake at the edge and the center of a population. n ≥ 3 biological replicates, error bars indicate the standard deviation. n.s.=not significant. P <0.0001 **** as determined by Paired t test.

The different assays employed offer a comprehensive insight into behavior of cells within epithelial populations seeded on micropatterns. It is evident that cells located at the population edge and center exhibit markedly different phenotypes. Concluding, the micropatterning system enables to study cells that are embedded within distinct population contexts while being subjected to identical treatment conditions.

## 5.2. Differential Gene Expression Analysis of T84 cells seeded at high vs. low density

RNA-Sequencing was done on T84 WT cells seeded at high and low density as described in Section 4.2.9. I performed a Differential Gene Expression Analysis using the built-in R function *DESeqDataSetFromMatrix()* and *DESeq()*. I selected the most up- and down-regulated genes at high vs. low density using following criteria: absolute(log2FoldChange)>2 and padj>0.05. A list with the 100 most upregulated and all down regulated genes in cells seeded at high vs. low density using those filtering criteria are in Tables 11 and 12 below (lfcSE is the standard error for the log2 fold change, pvalue is the P-value, and padj is the adjusted P-value for multiple testing).

**Table 11:** List of 100 most upregulated genes in cells seeded at high vs. low density

| Gene Symbol | log2 Fold Change | lfcSE | pvalue | padj |
|---|---|---|---|---|
| LGI4 | 7.7 | 0.3 | 9.4E-143 | 3.5E-141 |
| SLC36A2 | 6.8 | 1.0 | 2.6E-14 | 9.2E-14 |
| GABRA2 | 6.8 | 0.3 | 3.3E-99 | 7.2E-98 |
| TRIM22 | 6.3 | 0.1 | 0.0E+00 | 0.0E+00 |
| STC1 | 6.2 | 0.8 | 1.1E-15 | 4.0E-15 |
| SLC39A2 | 6.2 | 0.2 | 4.3E-247 | 4.0E-245 |
| IFI44L | 6.1 | 0.1 | 0.0E+00 | 0.0E+00 |
| MX2 | 5.7 | 0.1 | 0.0E+00 | 0.0E+00 |
| C1QL1 | 5.6 | 0.2 | 6.5E-158 | 2.9E-156 |
| AQP8 | 5.6 | 0.3 | 1.7E-93 | 3.4E-92 |
| LGALS17A | 5.5 | 1.1 | 1.0E-09 | 2.9E-09 |
| CA9 | 5.5 | 0.2 | 1.7E-171 | 8.2E-170 |
| NDUFA4L2 | 5.5 | 0.3 | 5.6E-95 | 1.1E-93 |
| LCN8 | 5.4 | 1.1 | 3.9E-09 | 1.1E-08 |
| S1PR4 | 5.2 | 1.1 | 5.7E-09 | 1.6E-08 |
| CEACAM7 | 5.2 | 0.3 | 2.7E-74 | 3.9E-73 |
| FPR3 | 5.1 | 0.2 | 3.2E-170 | 1.5E-168 |
| OAS2 | 5.0 | 0.1 | 0.0E+00 | 0.0E+00 |
| CHP2 | 4.9 | 0.4 | 9.7E-32 | 5.8E-31 |
| TCAF2 | 4.9 | 0.6 | 1.6E-16 | 6.1E-16 |
| IFI6 | 4.8 | 0.1 | 0.0E+00 | 0.0E+00 |
| RNF186 | 4.8 | 0.1 | 0.0E+00 | 0.0E+00 |
| DMBT1 | 4.8 | 0.1 | 0.0E+00 | 0.0E+00 |
| NXPE4 | 4.8 | 0.2 | 2.8E-94 | 5.7E-93 |
| FABP1 | 4.7 | 0.1 | 0.0E+00 | 0.0E+00 |
| ZBP1 | 4.6 | 0.2 | 5.7E-191 | 3.2E-189 |
| CCR1 | 4.6 | 0.3 | 3.1E-43 | 2.4E-42 |
| PPFIA4 | 4.6 | 0.4 | 2.4E-40 | 1.8E-39 |
| SLC22A16 | 4.5 | 0.3 | 8.6E-59 | 9.4E-58 |
| PNCK | 4.5 | 0.2 | 3.9E-80 | 6.2E-79 |
| PDE6A | 4.5 | 0.3 | 3.8E-45 | 3.1E-44 |
| ADAM2 | 4.4 | 1.2 | 3.6E-07 | 9.1E-07 |

| | | | | |
|---|---|---|---|---|
| ALDOC | 4.4 | 0.1 | 4.6E-216 | 3.2E-214 |
| CMPK2 | 4.4 | 0.1 | 0.0E+00 | 0.0E+00 |
| MX1 | 4.4 | 0.1 | 0.0E+00 | 0.0E+00 |
| PTPRN | 4.4 | 1.2 | 4.7E-07 | 1.2E-06 |
| TIMD4 | 4.3 | 0.3 | 2.6E-43 | 2.0E-42 |
| SLC26A3 | 4.3 | 0.3 | 2.9E-63 | 3.5E-62 |
| LCN15 | 4.3 | 0.1 | 0.0E+00 | 0.0E+00 |
| MIR210HG | 4.3 | 0.1 | 5.5E-298 | 6.4E-296 |
| RTBDN | 4.3 | 1.2 | 6.5E-07 | 1.6E-06 |
| CYP4F2 | 4.3 | 0.5 | 2.7E-22 | 1.2E-21 |
| TNS1 | 4.3 | 0.4 | 4.7E-28 | 2.6E-27 |
| IFIT1 | 4.3 | 0.1 | 0.0E+00 | 0.0E+00 |
| SAMD9L | 4.2 | 0.1 | 3.2E-261 | 3.2E-259 |
| SLC26A2 | 4.2 | 0.1 | 5.4E-293 | 6.2E-291 |
| HAVCR1 | 4.1 | 0.1 | 0.0E+00 | 0.0E+00 |
| NXPE1 | 4.1 | 0.3 | 1.5E-54 | 1.5E-53 |
| LGALS9 | 4.1 | 0.1 | 0.0E+00 | 0.0E+00 |
| LAMP3 | 4.0 | 0.1 | 0.0E+00 | 0.0E+00 |
| XAF1 | 4.0 | 0.1 | 0.0E+00 | 0.0E+00 |
| UBE2L6 | 4.0 | 0.0 | 0.0E+00 | 0.0E+00 |
| CDIPTOSP | 4.0 | 0.9 | 5.6E-09 | 1.6E-08 |
| LOC102724908 | 4.0 | 0.7 | 1.6E-11 | 5.2E-11 |
| UBXN10 | 3.9 | 1.4 | 3.7E-06 | 8.8E-06 |
| UPK3A | 3.9 | 1.0 | 1.2E-07 | 3.0E-07 |
| NDRG1 | 3.9 | 0.1 | 1.2E-213 | 8.4E-212 |
| SLC15A3 | 3.9 | 0.1 | 1.3E-251 | 1.2E-249 |
| LOC100506271 | 3.9 | 0.6 | 3.8E-12 | 1.2E-11 |
| DUOXA2 | 3.9 | 1.0 | 1.6E-07 | 4.1E-07 |
| CKB | 3.8 | 0.1 | 0.0E+00 | 0.0E+00 |
| HTR3C | 3.8 | 1.2 | 2.3E-06 | 5.4E-06 |
| LOC101929718 | 3.8 | 1.2 | 2.4E-06 | 5.7E-06 |
| NUPR1 | 3.8 | 0.1 | 4.0E-241 | 3.5E-239 |
| EPSTI1 | 3.8 | 0.1 | 0.0E+00 | 0.0E+00 |
| IFITM1 | 3.8 | 0.0 | 0.0E+00 | 0.0E+00 |
| CABP7 | 3.8 | 0.4 | 1.4E-21 | 6.2E-21 |
| NRN1 | 3.8 | 1.3 | 4.8E-06 | 1.1E-05 |
| SLC5A9 | 3.8 | 0.9 | 4.4E-08 | 1.2E-07 |
| ADAM23 | 3.7 | 0.9 | 3.6E-08 | 9.5E-08 |
| LOC154761 | 3.7 | 1.2 | 4.1E-06 | 9.6E-06 |
| VTCN1 | 3.7 | 0.3 | 5.8E-35 | 3.8E-34 |
| IFITM3 | 3.6 | 0.0 | 0.0E+00 | 0.0E+00 |
| PFKFB4 | 3.6 | 0.1 | 4.2E-158 | 1.8E-156 |
| CLCA1 | 3.6 | 0.1 | 1.6E-246 | 1.5E-244 |
| IFI27 | 3.6 | 0.0 | 0.0E+00 | 0.0E+00 |
| IRF7 | 3.6 | 0.1 | 0.0E+00 | 0.0E+00 |
| LGALS9C | 3.6 | 0.8 | 1.3E-08 | 3.5E-08 |
| CYS1 | 3.6 | 0.3 | 5.5E-40 | 4.0E-39 |

| | | | | |
|---|---|---|---|---|
| ZG16 | 3.6 | 0.1 | 0.0E+00 | 0.0E+00 |
| SMPD3 | 3.6 | 0.2 | 1.3E-96 | 2.8E-95 |
| CES3 | 3.6 | 0.1 | 8.9E-130 | 2.9E-128 |
| TNFSF10 | 3.6 | 0.1 | 0.0E+00 | 0.0E+00 |
| CFB | 3.6 | 0.2 | 3.9E-105 | 9.2E-104 |
| MYH7 | 3.6 | 0.4 | 2.7E-24 | 1.3E-23 |
| PIGR | 3.5 | 0.1 | 2.2E-148 | 8.9E-147 |
| IFIT3 | 3.5 | 0.0 | 0.0E+00 | 0.0E+00 |
| GBP4 | 3.5 | 0.2 | 7.7E-72 | 1.1E-70 |
| TFF3 | 3.5 | 0.1 | 7.6E-161 | 3.5E-159 |
| JAML | 3.5 | 0.2 | 3.4E-119 | 9.6E-118 |
| LINC01659 | 3.4 | 0.4 | 8.0E-17 | 3.0E-16 |
| LINC01645 | 3.4 | 0.5 | 1.9E-16 | 7.3E-16 |
| EXOC3L1 | 3.3 | 0.1 | 4.3E-187 | 2.4E-185 |
| DDIT4 | 3.3 | 0.1 | 3.9E-296 | 4.5E-294 |
| HIF1A-AS3 | 3.3 | 0.3 | 7.4E-27 | 3.9E-26 |
| RSAD2 | 3.3 | 0.1 | 0.0E+00 | 0.0E+00 |
| F7 | 3.3 | 0.7 | 1.3E-08 | 3.6E-08 |
| IL37 | 3.3 | 0.4 | 7.3E-24 | 3.5E-23 |
| GATM | 3.3 | 0.1 | 0.0E+00 | 0.0E+00 |
| CDH16 | 3.3 | 0.4 | 8.6E-20 | 3.7E-19 |

**Table 11:** List of downregulates genes in cells seeded at high vs. low density

| Gene symbol | log2 Fold Change | lfcSE | pvalue | padj |
|---|---|---|---|---|
| DKK1 | -2.0 | 0.0 | 0.0E+00 | 0.0E+00 |
| KRTAP3-1 | -2.0 | 0.1 | 2.6E-59 | 2.9E-58 |
| AADAC | -2.0 | 0.8 | 1.3E-04 | 2.6E-04 |
| ANXA1 | -2.0 | 0.0 | 0.0E+00 | 0.0E+00 |
| SERPINE1 | -2.1 | 0.1 | 6.6E-90 | 1.2E-88 |
| NAV3 | -2.1 | 0.1 | 3.8E-81 | 6.2E-80 |
| GALNT5 | -2.1 | 0.0 | 0.0E+00 | 0.0E+00 |
| IGSF9B | -2.1 | 0.1 | 8.3E-192 | 4.8E-190 |
| FERMT2 | -2.1 | 0.5 | 1.1E-06 | 2.7E-06 |
| CORO1A | -2.1 | 0.1 | 3.8E-53 | 3.7E-52 |
| LINC01204 | -2.1 | 0.2 | 3.8E-24 | 1.9E-23 |
| ZBED2 | -2.1 | 0.2 | 4.5E-37 | 3.1E-36 |
| KRT17 | -2.2 | 0.0 | 0.0E+00 | 0.0E+00 |
| RAET1L | -2.2 | 0.1 | 3.2E-144 | 1.2E-142 |
| CLMP | -2.2 | 0.1 | 3.8E-84 | 6.6E-83 |
| CREB5 | -2.2 | 0.2 | 7.9E-35 | 5.2E-34 |
| MPV17L | -2.2 | 0.2 | 2.9E-42 | 2.2E-41 |
| ABCG2 | -2.2 | 0.3 | 1.6E-17 | 6.3E-17 |
| SLC16A2 | -2.3 | 0.2 | 5.4E-32 | 3.2E-31 |
| KRT81 | -2.3 | 0.2 | 2.6E-38 | 1.9E-37 |
| LINC01215 | -2.3 | 0.7 | 6.8E-06 | 1.6E-05 |
| TESC | -2.3 | 0.1 | 0.0E+00 | 0.0E+00 |

| | | | | |
|---|---|---|---|---|
| MANCR | -2.3 | 0.3 | 3.9E-20 | 1.7E-19 |
| RPS6KL1 | -2.3 | 0.1 | 3.1E-103 | 7.0E-102 |
| LINC02273 | -2.4 | 0.6 | 1.8E-06 | 4.3E-06 |
| LINC02831 | -2.4 | 0.5 | 5.2E-09 | 1.4E-08 |
| MMP10 | -2.4 | 0.3 | 7.3E-21 | 3.2E-20 |
| KRTAP2-3 | -2.4 | 0.2 | 1.8E-42 | 1.4E-41 |
| VGLL3 | -2.4 | 0.1 | 5.6E-75 | 8.3E-74 |
| DUSP4 | -2.5 | 0.1 | 0.0E+00 | 0.0E+00 |
| FJX1 | -2.5 | 0.1 | 1.5E-156 | 6.6E-155 |
| SEMA7A | -2.5 | 0.1 | 0.0E+00 | 0.0E+00 |
| SHC4 | -2.5 | 0.2 | 5.4E-40 | 4.0E-39 |
| ALDH1A3 | -2.6 | 0.1 | 8.4E-171 | 4.1E-169 |
| SPOCD1 | -2.6 | 0.1 | 4.5E-128 | 1.5E-126 |
| RPE65 | -2.6 | 0.4 | 1.6E-12 | 5.1E-12 |
| CORO2B | -2.6 | 0.3 | 3.3E-22 | 1.5E-21 |
| MPO | -2.7 | 0.3 | 2.9E-23 | 1.4E-22 |
| ETS1 | -2.7 | 0.0 | 0.0E+00 | 0.0E+00 |
| PTHLH | -2.7 | 0.4 | 7.5E-13 | 2.5E-12 |
| RAB7B | -2.7 | 0.7 | 6.6E-07 | 1.6E-06 |
| MAOB | -2.7 | 0.1 | 4.4E-129 | 1.4E-127 |
| ADAM19 | -2.8 | 0.1 | 0.0E+00 | 0.0E+00 |
| GLIPR1 | -2.8 | 0.1 | 3.2E-273 | 3.4E-271 |
| TDRD9 | -2.8 | 0.6 | 1.6E-08 | 4.4E-08 |
| DCLK1 | -2.9 | 0.6 | 2.2E-09 | 6.1E-09 |
| LOC105369187 | -2.9 | 0.8 | 6.4E-07 | 1.6E-06 |
| MYH15 | -3.0 | 0.1 | 2.2E-233 | 1.8E-231 |
| LINC00460 | -3.0 | 0.1 | 3.2E-93 | 6.2E-92 |
| PCDH7 | -3.0 | 0.6 | 1.7E-09 | 4.9E-09 |
| MMP1 | -3.0 | 0.1 | 1.6E-117 | 4.3E-116 |
| TAGLN | -3.1 | 0.0 | 0.0E+00 | 0.0E+00 |
| CSF2 | -3.2 | 0.8 | 3.8E-07 | 9.5E-07 |
| AKAP12 | -3.2 | 0.0 | 0.0E+00 | 0.0E+00 |
| GLI2 | -3.2 | 0.3 | 1.3E-24 | 6.5E-24 |
| IL13RA2 | -3.5 | 0.1 | 2.8E-132 | 9.7E-131 |
| TNC | -3.5 | 0.1 | 0.0E+00 | 0.0E+00 |
| ACTG2 | -3.5 | 0.3 | 1.9E-38 | 1.3E-37 |
| MARCHF4 | -3.6 | 0.1 | 1.4E-134 | 4.9E-133 |
| TAGLN3 | -3.7 | 0.3 | 1.2E-36 | 7.9E-36 |
| FGF1 | -3.8 | 0.6 | 5.7E-12 | 1.8E-11 |
| SERPINB2 | -4.1 | 0.1 | 6.3E-181 | 3.3E-179 |
| MMP3 | -4.3 | 0.4 | 8.9E-27 | 4.7E-26 |

## 6. References

1. I. V. Kuzmin, C. E. Rupprecht, Encyclopedia of Virology. *Encycl. Virol.*, 367–373 (2008).
2. S. Boulant, M. Stanifer, P. Y. Lozach, Dynamics of virus-receptor interactions in virus binding, signaling, and endocytosis. *Viruses*. **7**, 2794–2815 (2015).
3. T. J. English, D. A. Hammer, The Effect of Cellular Receptor Diffusion on Receptor-Mediated Viral Binding Using Brownian Adhesive Dynamics (BRAD) Simulations. *Biophys. J.* **88**, 1666–1675 (2005).
4. P. Y. Lozach, A. Kühbacher, R. Meier, R. Mancini, D. Bitto, M. Bouloy, A. Helenius, DC-SIGN as a Receptor for Phleboviruses. *Cell Host Microbe*. **10**, 75–88 (2011).
5. P. Cossart, A. Helenius, Endocytosis of Viruses and Bacteria. *Cold Spring Harb. Perspect. Biol.* **6**, a016972 (2014).
6. P. Cossart, A. Helenius, Endocytosis of viruses and bacteria. *Cold Spring Harb. Perspect. Biol.* **6** (2014), doi:10.1101/CSHPERSPECT.A016972.
7. B. D, Expression of animal virus genomes. *Bacteriol. Rev.* **35**, 235–241 (1971).
8. S. W. Bird, K. Kirkegaard, Escape of non-enveloped virus from intact cells. *Virology*. **479–480**, 444–449 (2015).
9. I. A. Owusu, O. Quaye, K. D. Passalacqua, C. E. Wobus, Egress of non-enveloped enteric RNA viruses. *J. Gen. Virol.* **102**, 1557 (2021).
10. W. Mothes, N. M. Sherer, J. Jin, P. Zhong, Virus cell-to-cell transmission. *J. Virol.* **84**, 8360–8368 (2010).
11. B. D. Hallowell, T. Chavers, U. Parashar, J. E. Tate, Global Estimates of Rotavirus Hospitalizations Among Children Below 5 Years in 2019 and Current and Projected Impacts of Rotavirus Vaccination. *J. Pediatric Infect. Dis. Soc.* **11**, 149–158 (2022).
12. U. Desselberger, Rotaviruses. *Virus Res.* **190**, 75–96 (2014).
13. C. F. Arias, D. Silva-Ayala, S. López, Rotavirus entry: a deep journey into the cell with several exits. *J. Virol.* **89**, 890–893 (2015).
14. S. Lopez, C. F. Arias, Early steps in rotavirus cell entry. *Curr. Top. Microbiol. Immunol.* **309**, 39–66 (2006).
15. J. M. Torres-Flores, D. Silva-Ayala, M. A. Espinoza, S. López, C. F. Arias, The tight junction protein JAM-A functions as coreceptor for rotavirus entry into MA104 cells. *Virology*. **475**, 172–178 (2015).
16. M. A. Martínez, S. López, C. F. Arias, P. Isa, Gangliosides have a functional role during rotavirus cell entry. *J. Virol.* **87**, 1115–1122 (2013).
17. M. Gutiérrez, P. Isa, C. Sánchez-San Martin, J. Pérez-Vargas, R. Espinosa, C. F. Arias, S. López, Different rotavirus strains enter MA104 cells through different endocytic pathways: the role of clathrin-mediated endocytosis. *J. Virol.* **84**, 9161–9169 (2010).
18. M. A. Díaz-Salinas, P. Romero, R. Espinosa, Y. Hoshino, S. López, C. F. Arias, The spike protein VP4 defines the endocytic pathway used by rotavirus to enter MA104 cells. *J. Virol.* **87**, 1658–1663 (2013).
19. E. C. Settembre, J. Z. Chen, P. R. Dormitzer, N. Grigorieff, S. C. Harrison, Atomic model of an infectious rotavirus particle. *EMBO J.* **30**, 408–416 (2011).
20. L. S. Silvestri, Z. F. Taraporewala, J. T. Patton, Rotavirus replication: plus-sense templates for double-stranded RNA synthesis are made in viroplasms. *J. Virol.* **78**, 7763–7774 (2004).
21. M. S. McNulty, W. L. Curran, J. B. McFerran, The morphogenesis of a cytopathic bovine rotavirus in Madin-Darby bovine kidney cells. *J. Gen. Virol.* **33**, 503–508 (1976).
22. A. Gardet, M. Breton, P. Fontanges, G. Trugnan, S. Chwetzoff, Rotavirus spike protein VP4 binds to and remodels actin bundles of the epithelial brush border into actin bodies. *J. Virol.* **80**, 3947–3956 (2006).
23. A. B. Sabin, Reoviruses. A new group of respiratory and enteric viruses formerly classified as ECHO type 10 is described. *Science*. **130**, 1387–1389 (1959).
24. A. Steyer, I. Gutiérrez-Aguire, M. Kolenc, S. Koren, D. Kutnjak, M. Pokorn, M. Poljsak-Prijatelj, N. Racki, M. Ravnikar, M. Sagadin, A. F. Steyer, N. Toplak, High similarity of novel orthoreovirus detected in a child hospitalized with acute gastroenteritis to

mammalian orthoreoviruses found in bats in Europe. *J. Clin. Microbiol.* **51**, 3818–3825 (2013).

25. L. A. Ouattara, F. Barin, M. A. Barthez, B. Bonnaud, P. Roingeard, A. Goudeau, P. Castelnau, G. Vernet, G. Paranhos-Baccalà, F. Komurian-Pradel, Novel human reovirus isolated from children with acute necrotizing encephalopathy. *Emerg. Infect. Dis.* **17** (2011), doi:10.3201/EID1708.101528.
26. K. M. Coombs, Reovirus structure and morphogenesis. *Curr. Top. Microbiol. Immunol.* **309**, 117–167 (2006).
27. K. M. Guglielmi, E. M. Johnson, T. Stehle, T. S. Dermody, Attachment and cell entry of mammalian orthoreovirus. *Curr. Top. Microbiol. Immunol.* **309**, 1–38 (2006).
28. P. Danthi, G. H. Holm, T. Stehle, T. S. Dermody, Reovirus receptors, cell entry, and proapoptotic signaling. *Adv. Exp. Med. Biol.* **790**, 42–71 (2013).
29. A. N. Roth, P. Aravamudhan, I. Fernández de Castro, R. Tenorio, C. Risco, T. S. Dermody, Ins and Outs of Reovirus: Vesicular Trafficking in Viral Entry and Egress. *Trends Microbiol.* **29**, 363–375 (2021).
30. C. L. Miller, M. M. Arnold, T. J. Broering, C. E. Hastings, M. L. Nibert, Localization of mammalian orthoreovirus proteins to cytoplasmic factory-like structures via nonoverlapping regions of microNS. *J. Virol.* **84**, 867–882 (2010).
31. S. Schultz-Cherry, Astroviruses. *Ref. Modul. Biomed. Sci.* (2014), doi:10.1016/B978-0-12-801238-3.02539-3.
32. G. Donelli, F. Superti, A. Tinari, M. L. Marziano, Mechanism of astrovirus entry into Graham 293 cells. *J. Med. Virol.* **38**, 271–277 (1992).
33. E. Méndez, C. Muñoz-Yañez, C. Sánchez-San Martín, G. Aguirre-Crespo, M. del R. Baños-Lara, M. Gutierrez, R. Espinosa, Y. Acevedo, C. F. Arias, S. López, Characterization of human astrovirus cell entry. *J. Virol.* **88**, 2452–2460 (2014).
34. M. R. Eledge, M. D. Zita, K. W. Boehme, Reovirus: Friend and Foe. *Curr. Clin. Microbiol. Reports*. **6**, 132–138 (2019).
35. Family Astroviridae. *Viruses*, 125–128 (2017).
36. R. Tenorio, I. F. de Castro, J. J. Knowlton, P. F. Zamora, D. M. Sutherland, C. Risco, T. S. Dermody, Function, Architecture, and Biogenesis of Reovirus Replication Neoorganelles. *Viruses*. **11** (2019), doi:10.3390/V11030288.
37. J. D. Beckham, D. M. Pastula, A. Massey, K. L. Tyler, Zika Virus as an Emerging Global Pathogen: Neurological Complications of Zika Virus. *JAMA Neurol.* **73**, 875–879 (2016).
38. M. A. Robert, A. M. Stewart-Ibarra, E. L. Estallo, Climate change and viral emergence: evidence from Aedes-borne arboviruses. *Curr. Opin. Virol.* **40**, 41–47 (2020).
39. A. Braito, M. G. Ciufolini, L. Pippi, R. Corbisiero, C. Fiorentini, A. Gistri, L. Toscano, Phlebotomus-transmitted toscana virus infections of the central nervous system: a seven-year experience in Tuscany. *Scand. J. Infect. Dis.* **30**, 505–508 (1998).
40. C. RN, B. L, de L. X, Emergence of Toscana virus in the mediterranean area. *World J. Virol.* **1**, 135 (2012).
41. M. ML, A. JC, La Crosse encephalitis in children. *N. Engl. J. Med.* **345**, 148–149 (2001).
42. A. K. Överby, R. F. Pettersson, K. Grünewald, J. T. Huiskonen, Insights into bunyavirus architecture from electron cryotomography of Uukuniemi virus. *Proc. Natl. Acad. Sci. U. S. A.* **105**, 2375–2379 (2008).
43. A. N. Freiberg, M. B. Sherman, M. C. Morais, M. R. Holbrook, S. J. Watowich, Three-dimensional organization of Rift Valley fever virus revealed by cryoelectron tomography. *J. Virol.* **82**, 10341–10348 (2008).
44. T. A. Bowden, D. Bitto, A. McLees, C. Yeromonahos, R. M. Elliott, J. T. Huiskonen, Orthobunyavirus ultrastructure and the curious tripodal glycoprotein spike. *PLoS Pathog.* **9** (2013), doi:10.1371/JOURNAL.PPAT.1003374.
45. R. M. Elliott, Orthobunyaviruses: recent genetic and structural insights. *Nat. Rev. Microbiol.* **12**, 673–685 (2014).
46. T. Thamamongood, A. Aebischer, V. Wagner, M. W. Chang, R. Elling, C. Benner, A. García-Sastre, G. Kochs, M. Beer, M. Schwemmle, A Genome-Wide CRISPR-Cas9 Screen Reveals the Requirement of Host Cell Sulfation for Schmallenberg Virus

Infection. *J. Virol.* **94** (2020), doi:10.1128/JVI.00752-20.

47. S. Murakami, A. Takenaka-Uema, T. Kobayashi, K. Kato, M. Shimojima, M. Palmarini, T. Horimoto, Heparan Sulfate Proteoglycan Is an Important Attachment Factor for Cell Entry of Akabane and Schmallenberg Viruses. *J. Virol.* **91** (2017), doi:10.1128/JVI.00503-17.
48. J. T. Monteiro, K. Schön, T. Ebbecke, R. Goethe, J. Ruland, W. Baumgärtner, S. C. Becker, B. Lepenies, The CARD9-Associated C-Type Lectin, Mincle, Recognizes La Crosse Virus (LACV) but Plays a Limited Role in Early Antiviral Responses against LACV. *Viruses*. **11** (2019), doi:10.3390/V11030303.
49. H. Hofmann, X. Li, X. Zhang, W. Liu, A. Kühl, F. Kaup, S. S. Soldan, F. González-Scarano, F. Weber, Y. He, S. Pöhlmann, Severe fever with thrombocytopenia virus glycoproteins are targeted by neutralizing antibodies and can use DC-SIGN as a receptor for pH-dependent entry into human and animal cell lines. *J. Virol.* **87**, 4384–4394 (2013).
50. N. Bangphoomi, A. Takenaka-Uema, T. Sugi, K. Kat O, H. Akashi, T. Horimoto, Akabane virus utilizes alternative endocytic pathways to entry into mammalian cell lines. *J. Vet. Med. Sci.* **76**, 1471–1478 (2014).
51. R. I. M. Santos, A. H. Rodrigues, M. L. Silva, R. A. Mortara, M. A. Rossi, M. C. Jamur, C. Oliver, E. Arruda, Oropouche virus entry into HeLa cells involves clathrin and requires endosomal acidification. *Virus Res.* **138**, 139–143 (2008).
52. B. S. Hollidge, N. B. Nedelsky, M.-V. Salzano, J. W. Fraser, F. González-Scarano, S. S. Soldan, Orthobunyavirus entry into neurons and other mammalian cells occurs via clathrin-mediated endocytosis and requires trafficking into early endosomes. *J. Virol.* **86**, 7988–8001 (2012).
53. A. Papa, H. Zelená, E. Papadopoulou, J. Mrázek, Uukuniemi virus, Czech Republic. *Ticks Tick. Borne. Dis.* **9**, 1129–1132 (2018).
54. P. Y. Lozach, R. Mancini, D. Bitto, R. Meier, L. Oestereich, A. K. Överby, R. F. Pettersson, A. Helenius, Entry of bunyaviruses into mammalian cells. *Cell Host Microbe*. **7**, 488–499 (2010).
55. Y. Sun, J. Li, G. F. Gao, P. Tien, W. Liu, Bunyavirales ribonucleoproteins: the viral replication and transcription machinery. *Crit. Rev. Microbiol.* **44**, 522–540 (2018).
56. M. Spiegel, T. Plegge, S. Pöhlmann, The Role of Phlebovirus Glycoproteins in Viral Entry, Assembly and Release. *Viruses*. **8** (2016), doi:10.3390/V8070202.
57. G. J. Atkins, B. J. Sheahan, P. Liljeström, The molecular pathogenesis of Semliki Forest virus: a model virus made useful? *J. Gen. Virol.* **80 ( Pt 9)**, 2287–2297 (1999).
58. O. Zimmerman, A. C. Holmes, N. M. Kafai, L. J. Adams, M. S. Diamond, Entry receptors - the gateway to alphavirus infection. *J. Clin. Invest.* **133** (2023), doi:10.1172/JCI165307.
59. M. K. S. van Duijl-Richter, T. E. Hoornweg, I. A. Rodenhuis-Zybert, J. M. Smit, Early Events in Chikungunya Virus Infection-From Virus Cell Binding to Membrane Fusion. *Viruses*. **7**, 3647–3674 (2015).
60. J. Y. S. Leung, M. M. L. Ng, J. J. H. Chu, Replication of alphaviruses: a review on the entry process of alphaviruses into cells. *Adv. Virol.* **2011** (2011), doi:10.1155/2011/249640.
61. C. S. S. Martín, C. Y. Liu, M. Kielian, Dealing with low pH: entry and exit of alphaviruses and flaviviruses. *Trends Microbiol.* **17**, 514–521 (2009).
62. H. Andersson, B. U. Barth, M. Ekström, H. Garoff, Oligomerization-dependent folding of the membrane fusion protein of Semliki Forest virus. *J. Virol.* **71**, 9654–9663 (1997).
63. K. E. Owen, R. J. Kuhn, Alphavirus budding is dependent on the interaction between the nucleocapsid and hydrophobic amino acids on the cytoplasmic domain of the E2 envelope glycoprotein. *Virology*. **230**, 187–196 (1997).
64. Alphavirus ~ ViralZone, (available at https://viralzone.expasy.org/625?outline=all_by_species).
65. T. Pechenick Jowers, R. J. Featherstone, D. K. Reynolds, H. K. Brown, J. James, A. Prescott, I. R. Haga, P. M. Beard, RAB1A promotes Vaccinia virus replication by facilitating the production of intracellular enveloped virions. *Virology*. **475**, 66–73 (2015).

66. B. Moss, Smallpox vaccines: targets of protective immunity. *Immunol. Rev.* **239**, 8–26 (2011).
67. H. Meyer, R. Ehmann, G. L. Smith, Smallpox in the Post-Eradication Era. *Viruses*. **12** (2020), doi:10.3390/V12020138.
68. F. I. Schmidt, C. K. E. Bleck, J. Mercer, Poxvirus host cell entry. *Curr. Opin. Virol.* **2**, 20–27 (2012).
69. A. Vanderplasschen, G. L. Smith, A novel virus binding assay using confocal microscopy: demonstration that the intracellular and extracellular vaccinia virions bind to different cellular receptors. *J. Virol.* **71**, 4032–4041 (1997).
70. M. Law, G. G. Carter, K. L. Roberts, M. Hollinshead, G. L. Smith, Ligand-induced and nonfusogenic dissolution of a viral membrane. *Proc. Natl. Acad. Sci. U. S. A.* **103**, 5989–5994 (2006).
71. J. Mercer, A. Helenius, Vaccinia virus uses macropinocytosis and apoptotic mimicry to enter host cells. *Science (80-. ).* **320**, 531–535 (2008).
72. C.-Y. Huang, T.-Y. Lu, C.-H. Bair, Y.-S. Chang, J.-K. Jwo, W. Chang, A novel cellular protein, VPEF, facilitates vaccinia virus penetration into HeLa cells through fluid phase endocytosis. *J. Virol.* **82**, 7988–7999 (2008).
73. J. Mercer, S. Knébel, F. I. Schmidt, J. Crouse, C. Burkard, A. Helenius, Vaccinia virus strains use distinct forms of macropinocytosis for host-cell entry. *Proc. Natl. Acad. Sci. U. S. A.* **107**, 9346–9351 (2010).
74. K. J. Sandgren, J. Wilkinson, M. Miranda-Saksena, G. M. McInerney, K. Byth-Wilson, P. J. Robinson, A. L. Cunningham, A differential role for macropinocytosis in mediating entry of the two forms of vaccinia virus into dendritic cells. *PLoS Pathog.* **6**, 1–16 (2010).
75. A. C. Townsley, A. S. Weisberg, T. R. Wagenaar, B. Moss, Vaccinia virus entry into cells via a low-pH-dependent endosomal pathway. *J. Virol.* **80**, 8899–8908 (2006).
76. F. I. Schmidt, C. K. E. Bleck, A. Helenius, J. Mercer, Vaccinia extracellular virions enter cells by macropinocytosis and acid-activated membrane rupture. *EMBO J.* **30**, 3647–3661 (2011).
77. J. Mercer, A. Helenius, Virus entry by macropinocytosis. *Nat. Cell Biol.* **11**, 510–520 (2009).
78. B. Moss, Poxvirus DNA replication. *Cold Spring Harb. Perspect. Biol.* **5** (2013), doi:10.1101/CSHPERSPECT.A010199.
79. G. C. Katsafanas, B. Moss, Colocalization of transcription and translation within cytoplasmic poxvirus factories coordinates viral expression and subjugates host functions. *Cell Host Microbe*. **2**, 221–228 (2007).
80. B. Moss, Poxvirus cell entry: how many proteins does it take? *Viruses*. **4**, 688–707 (2012).
81. G. McFadden, Poxvirus tropism. *Nat. Rev. Microbiol.* **3**, 201–213 (2005).
82. S. N. Shchelkunov, G. A. Shchelkunova, Genes that Control Vaccinia Virus Immunogenicity. *Acta Naturae*. **12**, 33 (2020).
83. D. Shi, P. He, Y. Song, S. Cheng, R. J. Linhardt, J. S. Dordick, L. Chi, F. Zhang, Kinetic and Structural Aspects of Glycosaminoglycan–Monkeypox Virus Protein A29 Interactions Using Surface Plasmon Resonance. *Molecules*. **27** (2022), doi:10.3390/MOLECULES27185898.
84. T. Kawai, S. Akira, Innate immune recognition of viral infection. *Nat. Immunol.* **7** (2006), pp. 131–137.
85. J. Rehwinkel, M. U. Gack, RIG-I-like receptors: their regulation and roles in RNA sensing. *Nat. Rev. Immunol.* **20**, 537–551 (2020).
86. A. Decout, J. D. Katz, S. Venkatraman, A. Ablasser, The cGAS-STING pathway as a therapeutic target in inflammatory diseases. *Nat. Rev. Immunol.* **21**, 548–569 (2021).
87. L. G. Webb, A. Fernandez-Sesma, RNA viruses and the cGAS-STING pathway: reframing our understanding of innate immune sensing. *Curr. Opin. Virol.* **53** (2022), doi:10.1016/J.COVIRO.2022.101206.
88. G. Ni, Z. Ma, B. Damania, cGAS and STING: At the intersection of DNA and RNA virus-sensing networks. *PLoS Pathog.* **14** (2018), doi:10.1371/JOURNAL.PPAT.1007148.

89. S. Aguirre, P. Luthra, M. T. Sanchez-Aparicio, A. M. Maestre, J. Patel, F. Lamothe, A. C. Fredericks, S. Tripathi, T. Zhu, J. Pintado-Silva, L. G. Webb, D. Bernal-Rubio, A. Solovyov, B. Greenbaum, V. Simon, C. F. Basler, L. C. F. Mulder, A. García-Sastre, A. Fernandez-Sesma, Dengue virus NS2B protein targets cGAS for degradation and prevents mitochondrial DNA sensing during infection. *Nat. Microbiol.* **2** (2017), doi:10.1038/NMICROBIOL.2017.37.
90. A. S. Jahun, F. Sorgeloos, Y. Chaudhry, S. E. Arthur, M. Hosmillo, I. Georgana, R. Izuagbe, I. G. Goodfellow, Leaked genomic and mitochondrial DNA contribute to the host response to noroviruses in a STING-dependent manner. *Cell Rep.* **42** (2023), doi:10.1016/J.CELREP.2023.112179.
91. M. Motwani, S. Pesiridis, K. A. Fitzgerald, DNA sensing by the cGAS–STING pathway in health and disease. *Nat. Rev. Genet. 2019 2011*. **20**, 657–674 (2019).
92. Ö. Strannegård, Interferons and their Therapeutic Applications. *EJIFCC*. **11**, 52 (1999).
93. N. A. De Weerd, T. Nguyen, The interferons and their receptors—distribution and regulation. *Immunol. Cell Biol.* **90**, 483 (2012).
94. E. A. Hemann, M. Gale, R. Savan, Interferon Lambda Genetics and Biology in Regulation of Viral Control. *Front. Immunol.* **8** (2017), doi:10.3389/FIMMU.2017.01707.
95. H. H. Gad, C. Dellgren, O. J. Hamming, S. Vends, S. R. Paludan, R. Hartmann, Interferon-λ Is Functionally an Interferon but Structurally Related to the Interleukin-10 Family. *J. Biol. Chem.* **284**, 20869–20875 (2009).
96. C. Sommereyns, S. Paul, P. Staeheli, T. Michiels, IFN-lambda (IFN-lambda) is expressed in a tissue-dependent fashion and primarily acts on epithelial cells in vivo. *PLoS Pathog.* **4** (2008), doi:10.1371/JOURNAL.PPAT.1000017.
97. J. Fenimore, H. A. Young, Regulation of IFN-γ Expression. *Adv. Exp. Med. Biol.* **941**, 1–19 (2016).
98. K. Schroder, P. J. Hertzog, T. Ravasi, D. A. Hume, Interferon-gamma: an overview of signals, mechanisms and functions. *J. Leukoc. Biol.* **75**, 163–189 (2004).
99. H. M. Lazear, J. W. Schoggins, M. S. Diamond, Shared and Distinct Functions of Type I and Type III Interferons. *Immunity*. **50**, 907 (2019).
100. C. Odendall, J. C. Kagan, The unique regulation and functions of type III interferons in antiviral immunity. *Curr. Opin. Virol.* **12**, 47–52 (2015).
101. D. E. Levy, I. J. Marié, J. E. Durbin, Induction and function of type i and III interferon in response to viral infection. *Curr. Opin. Virol.* **1** (2011), pp. 476–486.
102. G. Y. Chen, G. Nuñez, Sterile inflammation: sensing and reacting to damage. *Nat. Rev. Immunol.* **10**, 826–837 (2010).
103. E. Vénéreau, C. Ceriotti, M. E. Bianchi, DAMPs from Cell Death to New Life. *Front. Immunol.* **6** (2015), doi:10.3389/FIMMU.2015.00422.
104. P. Scaffidi, T. Misteli, M. E. Bianchi, Release of chromatin protein HMGB1 by necrotic cells triggers inflammation. *Nature*. **418**, 191–195 (2002).
105. F. J. Quintana, I. R. Cohen, Heat shock proteins as endogenous adjuvants in sterile and septic inflammation. *J. Immunol.* **175**, 2777–2782 (2005).
106. M. J. L. Bours, E. L. R. Swennen, F. Di Virgilio, B. N. Cronstein, P. C. Dagnelie, Adenosine 5'-triphosphate and adenosine as endogenous signaling molecules in immunity and inflammation. *Pharmacol. Ther.* **112**, 358–404 (2006).
107. H. Kono, C. J. Chen, F. Ontiveros, K. L. Rock, Uric acid promotes an acute inflammatory response to sterile cell death in mice. *J. Clin. Invest.* **120**, 1939–1949 (2010).
108. S. Grazioli, J. Pugin, Mitochondrial Damage-Associated Molecular Patterns: From Inflammatory Signaling to Human Diseases. *Front. Immunol.* **9** (2018), doi:10.3389/FIMMU.2018.00832.
109. M. Moriyama, T. Koshiba, T. Ichinohe, Influenza A virus M2 protein triggers mitochondrial DNA-mediated antiviral immune responses. *Nat. Commun.* **10** (2019), doi:10.1038/S41467-019-12632-5.
110. K. Maringer, A. Fernandez-Sesma, Message in a bottle: lessons learned from antagonism of STING signalling during RNA virus infection. *Cytokine Growth Factor Rev.* **25**, 669–679 (2014).

111. T. Kawai, S. Akira, The role of pattern-recognition receptors in innate immunity: update on Toll-like receptors. *Nat. Immunol.* **11**, 373–384 (2010).
112. W. G. Land, The Role of Damage-Associated Molecular Patterns in Human Diseases: Part I - Promoting inflammation and immunity. *Sultan Qaboos Univ. Med. J.* **15**, e9 (2015).
113. M. J. White, K. McArthur, D. Metcalf, R. M. Lane, J. C. Cambier, M. J. Herold, M. F. Van Delft, S. Bedoui, G. Lessene, M. E. Ritchie, D. C. S. Huang, B. T. Kile, Apoptotic caspases suppress mtDNA-induced STING-mediated type i IFN production. *Cell*. **159**, 1549–1562 (2014).
114. A. Rongvaux, R. Jackson, C. C. D. Harman, T. Li, A. P. West, M. R. De Zoete, Y. Wu, B. Yordy, S. A. Lakhani, C. Y. Kuan, T. Taniguchi, G. S. Shadel, Z. J. Chen, A. Iwasaki, R. A. Flavell, Apoptotic caspases prevent the induction of type i interferons by mitochondrial DNA. *Cell*. **159**, 1563–1577 (2014).
115. S. Crotta, S. Davidson, T. Mahlakoiv, C. J. Desmet, M. R. Buckwalter, M. L. Albert, P. Staeheli, A. Wack, Type I and Type III Interferons Drive Redundant Amplification Loops to Induce a Transcriptional Signature in Influenza-Infected Airway Epithelia. *PLoS Pathog.* **9** (2013), doi:10.1371/journal.ppat.1003773.
116. P. I. Österlund, T. E. Pietilä, V. Veckman, S. V. Kotenko, I. Julkunen, IFN regulatory factor family members differentially regulate the expression of type III IFN (IFN-lambda) genes. *J. Immunol.* **179**, 3434–3442 (2007).
117. J. E. Darnell, I. M. Kerr, G. R. Stark, Jak-STAT pathways and transcriptional activation in response to IFNs and other extracellular signaling proteins. *Science*. **264**, 1415–1421 (1994).
118. T. A. Selvakumar, S. Bhushal, U. Kalinke, D. Wirth, H. Hauser, M. Köster, M. W. Hornef, Identification of a predominantly interferon-λ-induced transcriptional profile in murine intestinal epithelial cells. *Front. Immunol.* **8** (2017), doi:10.3389/fimmu.2017.01302.
119. A. Forero, S. Ozarkar, H. Li, C. H. Lee, E. A. Hemann, M. S. Nadjsombati, M. R. Hendricks, L. So, R. Green, C. N. Roy, S. N. Sarkar, J. von Moltke, S. K. Anderson, M. Gale, R. Savan, Differential Activation of the Transcription Factor IRF1 Underlies the Distinct Immune Responses Elicited by Type I and Type III Interferons. *Immunity*. **51**, 451-464.e6 (2019).
120. H. Novatt, L. Renn, T. Theisen, T. Massie, T. Massie, R. L. Rabin, *J. Immunol.*, in press, doi:10.4049/JIMMUNOL.196.SUPP.68.12.
121. Z. Zhou, O. J. Hamming, N. Ank, S. R. Paludan, A. L. Nielsen, R. Hartmann, Type III Interferon (IFN) Induces a Type I IFN-Like Response in a Restricted Subset of Cells through Signaling Pathways Involving both the Jak-STAT Pathway and the Mitogen-Activated Protein Kinases. *J. Virol.* **81**, 7749–7758 (2007).
122. C. R. Bolen, S. Ding, M. D. Robek, S. H. Kleinstein, Dynamic expression profiling of type I and type III interferon-stimulated hepatocytes reveals a stable hierarchy of gene expression. *Hepatology*. **59**, 1262–1272 (2014).
123. K. Pervolaraki, S. Rastgou Talemi, D. Albrecht, F. Bormann, C. Bamford, J. L. Mendoza, K. C. Garcia, J. McLauchlan, T. Höfer, M. L. Stanifer, S. Boulant, Differential induction of interferon stimulated genes between type I and type III interferons is independent of interferon receptor abundance. *PLoS Pathog.* **14** (2018), doi:10.1371/journal.ppat.1007420.
124. A. Kohli, X. Zhang, J. Yang, R. S. Russell, R. P. Donnelly, F. Sheikh, A. Sherman, H. Young, T. Imamichi, R. A. Lempicki, H. Masur, S. Kottilil, Distinct and overlapping genomic profiles and antiviral effects of Interferon-λ and -α On HCV-infected and noninfected hepatoma cells. *J. Viral Hepat.* **19**, 843–853 (2012).
125. E. A. Voigt, J. Yin, Kinetic Differences and Synergistic Antiviral Effects Between Type I and Type III Interferon Signaling Indicate Pathway Independence. *J. Interf. Cytokine Res.* **35**, 734–747 (2015).
126. S. J. Lee, W. J. Kim, S. K. Moon, Role of the p38 MAPK signaling pathway in mediating interleukin-28A-induced migration of UMUC-3 cells. *Int. J. Mol. Med.* **30**, 945–952 (2012).

127. C. Odendall, E. Dixit, F. Stavru, H. Bierne, K. M. Franz, A. F. Durbin, S. Boulant, L. Gehrke, P. Cossart, J. C. Kagan, Diverse intracellular pathogens activate type III interferon expression from peroxisomes. *Nat. Immunol.* **15**, 717–726 (2014).
128. K. Pervolaraki, M. L. Stanifer, S. Münchau, L. A. Renn, D. Albrecht, S. Kurzhals, E. Senís, D. Grimm, J. Schröder-Braunstein, R. L. Rabin, S. Boulant, Type I and type III interferons display different dependency on mitogen-activated protein kinases to mount an antiviral state in the human gut. *Front. Immunol.* **8** (2017), doi:10.3389/fimmu.2017.00459.
129. H. Yan, K. Krishnan, J. T. E. Lim, L. G. Contillo, J. J. Krolewski, Molecular characterization of an alpha interferon receptor 1 subunit (IFNaR1) domain required for TYK2 binding and signal transduction. *Mol. Cell. Biol.* **16**, 2074–2082 (1996).
130. H. J. A. Wallweber, C. Tam, Y. Franke, M. A. Starovasnik, P. J. Lupardus, Structural basis of recognition of interferon-α receptor by tyrosine kinase 2. *Nat. Struct. Mol. Biol.* **21**, 443–448 (2014).
131. D. S. Finbloom, K. D. Winestock, IL-10 induces the tyrosine phosphorylation of tyk2 and Jak1 and the differential assembly of STAT1 alpha and STAT3 complexes in human T cells and monocytes. *J. Immunol.* **155**, 1079–1090 (1995).
132. A. Y. Kreins, M. J. Ciancanelli, S. Okada, X. F. Kong, N. Ramírez-Alejo, S. S. Kilic, J. El Baghdadi, S. Nonoyama, S. A. Mahdaviani, F. Ailal, A. Bousfiha, D. Mansouri, E. Nievas, C. S. Ma, G. Rao, A. Bernasconi, H. S. Kuehn, J. Niemela, J. Stoddard, P. Deveau, A. Cobat, S. El Azbaoui, A. Sabri, C. K. Lim, M. Sundin, D. T. Avery, R. Halwani, A. V. Grant, B. Boisson, D. Bogunovic, Y. Itan, M. Moncada-Velez, R. Martinez-Barricarte, M. Migaud, C. Deswarte, L. Alsina, D. Kotlarz, C. Klein, I. Muller-Fleckenstein, B. Fleckenstein, V. Cormier-Daire, S. Rose-John, C. Picard, L. Hammarstrom, A. Puel, S. Al-Muhsen, L. Abel, D. Chaussabel, S. D. Rosenzweig, Y. Minegishi, S. G. Tangye, J. Bustamante, J. L. Casanova, S. Boisson-Dupuis, Human TYK2 deficiency: Mycobacterial and viral infections without hyper-IgE syndrome. *J. Exp. Med.* **212**, 1641–1662 (2015).
133. S. Fuchs, P. Kaiser-Labusch, J. Bank, S. Ammann, A. Kolb-Kokocinski, C. Edelbusch, H. Omran, S. Ehl, Tyrosine kinase 2 is not limiting human antiviral type III interferon responses. *Eur. J. Immunol.* **46**, 2639–2649 (2016).
134. G. BARBIERI, L. VELAZQUEZ, M. SCROBOGNA, M. FELLOUS, S. PELLEGRINI, Activation of the protein tyrosine kinase tyk2 by interferon alpha/beta. *Eur. J. Biochem.* **223**, 427–435 (1994).
135. H. H. Ho, L. B. Ivashkiv, Role of STAT3 in type I interferon responses. Negative regulation of STAT1-dependent inflammatory gene activation. *J. Biol. Chem.* **281**, 14111–14118 (2006).
136. W.-B. Wang, D. E. Levy, C.-K. Lee, STAT3 negatively regulates type I IFN-mediated antiviral response. *J. Immunol.* **187**, 2578–2585 (2011).
137. R. Mahony, S. Gargan, K. L. Roberts, N. Bourke, S. E. Keating, A. G. Bowie, C. O’Farrelly, N. J. Stevenson, A novel anti-viral role for STAT3 in IFN-α signalling responses. *Cell. Mol. Life Sci.* **74**, 1755–1764 (2017).
138. K. Pervolaraki, C. Guo, D. Albrecht, S. Boulant, M. L. Stanifer, Type-Specific Crosstalk Modulates Interferon Signaling in Intestinal Epithelial Cells. *J. Interferon Cytokine Res.* **39**, 650–660 (2019).
139. J. W. Schoggins, C. M. Rice, Interferon-stimulated genes and their antiviral effector functions. *Curr. Opin. Virol.* **1**, 519–525 (2011).
140. W. M. Schneider, M. D. Chevillotte, C. M. Rice, Interferon-stimulated genes: a complex web of host defenses. *Annu. Rev. Immunol.* **32**, 513–545 (2014).
141. R. Jagus, B. Joshi, G. N. Barber, PKR, apoptosis and cancer. *Int. J. Biochem. Cell Biol.* **31**, 123–138 (1999).
142. A. Zhou, J. Paranjape, T. L. Brown, H. Nie, S. Naik, B. Dong, A. Chang, B. Trapp, R. Fairchild, C. Colmenares, R. H. Silverman, Interferon action and apoptosis are defective in mice devoid of 2’,5’-oligoadenylate-dependent RNase L. *EMBO J.* **16**, 6355–6363 (1997).

143. M. Stawowczyk, S. Van Scoy, K. P. Kumar, N. C. Reich, The interferon stimulated gene 54 promotes apoptosis. *J. Biol. Chem.* **286**, 7257–7266 (2011).
144. O. Haller, G. Kochs, Human MxA protein: an interferon-induced dynamin-like GTPase with broad antiviral activity. *J. Interferon Cytokine Res.* **31**, 79–87 (2011).
145. A. J. Sadler, B. R. G. Williams, Interferon-inducible antiviral effectors. *Nat. Rev. Immunol.* **8** (2008), pp. 559–568.
146. S. Ghosh, E. N. G. Marsh, Viperin: An ancient radical SAM enzyme finds its place in modern cellular metabolism and innate immunity. *J. Biol. Chem.* **295**, 11513–11528 (2020).
147. C. Zhao, M. N. Collins, T. Y. Hsiang, R. M. Krug, Interferon-induced ISG15 pathway: an ongoing virus-host battle. *Trends Microbiol.* **21**, 181–186 (2013).
148. X. Wang, E. R. Hinson, P. Cresswell, The interferon-inducible protein viperin inhibits influenza virus release by perturbing lipid rafts. *Cell Host Microbe*. **2**, 96–105 (2007).
149. L. Ye, D. Schnepf, P. Staeheli, Interferon-λ orchestrates innate and adaptive mucosal immune responses. *Nat. Rev. Immunol.* **19**, 614–625 (2019).
150. M. Mordstein, E. Neugebauer, V. Ditt, B. Jessen, T. Rieger, V. Falcone, F. Sorgeloos, S. Ehl, D. Mayer, G. Kochs, M. Schwemmle, S. Günther, C. Drosten, T. Michiels, P. Staeheli, Lambda Interferon Renders Epithelial Cells of the Respiratory and Gastrointestinal Tracts Resistant to Viral Infections. *J. Virol.* **84**, 5670–5677 (2010).
151. R. R. Goel, S. V. Kotenko, M. J. Kaplan, Interferon lambda in inflammation and autoimmune rheumatic diseases. *Nat. Rev. Rheumatol.* **17**, 349–362 (2021).
152. T. Mahlakõiv, P. Hernandez, K. Gronke, A. Diefenbach, P. Staeheli, Leukocyte-Derived IFN-α/β and Epithelial IFN-λ Constitute a Compartmentalized Mucosal Defense System that Restricts Enteric Virus Infections. *PLoS Pathog.* **11** (2015), doi:10.1371/journal.ppat.1004782.
153. P. P. Hernández, T. Mahlakõiv, I. Yang, V. Schwierzeck, N. Nguyen, F. Guendel, K. Gronke, B. Ryffel, C. Hölscher, L. Dumoutier, J. C. Renauld, S. Suerbaum, P. Staeheli, A. Diefenbach, Interferon-λ and interleukin 22 act synergistically for the induction of interferon-stimulated genes and control of rotavirus infection. *Nat. Immunol.* **16**, 698–707 (2015).
154. M. L. Stanifer, M. Mukenhirn, S. Muenchau, K. Pervolaraki, T. Kanaya, D. Albrecht, C. Odendall, T. Hielscher, V. Haucke, J. C. Kagan, S. Bartfeld, H. Ohno, S. Boulant, Asymmetric distribution of TLR3 leads to a polarized immune response in human intestinal epithelial cells. *Nat. Microbiol.* **5**, 181–191 (2020).
155. K. Saxena, L. M. Simon, X. L. Zeng, S. E. Blutt, S. E. Crawford, N. P. Sastri, U. C. Karandikar, N. J. Ajami, N. C. Zachos, O. Kovbasnjuk, M. Donowitz, M. E. Conner, C. A. Shaw, M. K. Estes, A paradox of transcriptional and functional innate interferon responses of human intestinal enteroids to enteric virus infection. *Proc. Natl. Acad. Sci. U. S. A.* **114**, E570–E579 (2017).
156. M. Hosmillo, Y. Chaudhry, K. Nayak, F. Sorgeloos, B. K. Koo, A. Merenda, R. Lillestol, L. Drumright, M. Zilbauer, I. Goodfellow, Norovirus Replication in Human Intestinal Epithelial Cells Is Restricted by the Interferon-Induced JAK/STAT Signaling Pathway and RNA Polymerase II-Mediated Transcriptional Responses. *MBio*. **11** (2020), doi:10.1128/MBIO.00215-20.
157. J. Pott, T. Mahlakõiv, M. Mordstein, C. U. Duerr, T. Michiels, S. Stockinger, P. Staeheli, M. W. Hornef, IFN-λ determines the intestinal epithelial antiviral host defense. *Proc. Natl. Acad. Sci. U. S. A.* **108**, 7944–7949 (2011).
158. M. T. Baldridge, S. Lee, J. J. Brown, N. McAllister, K. Urbanek, T. S. Dermody, T. J. Nice, H. W. Virgin, Expression of Ifnlr1 on Intestinal Epithelial Cells Is Critical to the Antiviral Effects of Interferon Lambda against Norovirus and Reovirus. *J. Virol.* **91** (2017), doi:10.1128/JVI.02079-16.
159. C. Metz-Zumaran, C. Kee, P. Doldan, C. Guo, M. L. Stanifer, S. Boulant, Increased Sensitivity of SARS-CoV-2 to Type III Interferon in Human Intestinal Epithelial Cells. *J. Virol.* (2022), doi:10.1128/jvi.01705-21.
160. P. Doldan, J. Dai, C. Metz-Zumaran, J. T. Patton, M. L. Stanifer, S. Boulant, Type III

and Not Type I Interferons Efficiently Prevent the Spread of Rotavirus in Human Intestinal Epithelial Cells. *J. Virol.* **96** (2022), doi:10.1128/jvi.00706-22.

161. M. L. Stanifer, C. Kee, M. Cortese, T. Alexandrov, R. Bartenschlager, S. Boulant, C. M. Zumaran, S. Triana, M. Mukenhirn, H.-G. Kraeusslich, Critical Role of Type III Interferon in Controlling SARS-CoV-2 Infection in Human Intestinal Epithelial Cells ll Critical Role of Type III Interferon in Controlling SARS-CoV-2 Infection in Human Intestinal Epithelial Cells. *CellReports*. **32**, 107863 (2020).
162. T. J. Nice, M. T. Baldridge, B. T. McCune, J. M. Norman, H. M. Lazear, M. Artyomov, M. S. Diamond, H. W. Virgin, Interferon-λ cures persistent murine norovirus infection in the absence of adaptive immunity. *Science (80-. ).* **347**, 269–273 (2015).
163. V. Espinosa, O. Dutta, C. McElrath, P. Du, Y. J. Chang, B. Cicciarelli, A. Pitler, I. Whitehead, J. J. Obar, J. E. Durbin, S. V. Kotenko, A. Rivera, Type III interferon is a critical regulator of innate antifungal immunity. *Sci. Immunol.* **2** (2017), doi:10.1126/SCIIMMUNOL.AAN5357.
164. J. M. Fox, J. M. Crabtree, L. K. Sage, S. M. Tompkins, R. A. Tripp, Interferon Lambda Upregulates IDO1 Expression in Respiratory Epithelial Cells After Influenza Virus Infection. *J. Interferon Cytokine Res.* **35**, 554–562 (2015).
165. I. E. Galani, V. Triantafyllia, E. E. Eleminiadou, O. Koltsida, A. Stavropoulos, M. Manioudaki, D. Thanos, S. E. Doyle, S. V. Kotenko, K. Thanopoulou, E. Andreakos, Interferon-λ Mediates Non-redundant Front-Line Antiviral Protection against Influenza Virus Infection without Compromising Host Fitness. *Immunity*. **46**, 875-890.e6 (2017).
166. N. A. Jewell, T. Cline, S. E. Mertz, S. V. Smirnov, E. Flaño, C. Schindler, J. L. Grieves, R. K. Durbin, S. V. Kotenko, J. E. Durbin, Lambda interferon is the predominant interferon induced by influenza A virus infection in vivo. *J. Virol.* **84**, 11515–11522 (2010).
167. T. Okabayashi, T. Kojima, T. Masaki, S. ichi Yokota, T. Imaizumi, H. Tsutsumi, T. Himi, N. Fujii, N. Sawada, Type-III interferon, not type-I, is the predominant interferon induced by respiratory viruses in nasal epithelial cells. *Virus Res.* **160**, 360–366 (2011).
168. J. Klinkhammer, D. Schnepf, L. Ye, M. Schwaderlapp, H. H. Gad, R. Hartmann, D. Garcin, T. Mahlakõiv, P. Staeheli, IFN-λ prevents influenza virus spread from the upper airways to the lungs and limits virus transmission. *Elife*. **7** (2018), doi:10.7554/eLife.33354.
169. M. Goritzka, L. R. Durant, C. Pereira, S. Salek-Ardakani, P. J. M. Openshaw, C. Johansson, Alpha/beta interferon receptor signaling amplifies early proinflammatory cytokine production in the lung during respiratory syncytial virus infection. *J. Virol.* **88**, 6128–6136 (2014).
170. M. Goritzka, S. Makris, F. Kausar, L. R. Durant, C. Pereira, Y. Kumagai, F. J. Culley, M. Mack, S. Akira, C. Johansson, Alveolar macrophage-derived type I interferons orchestrate innate immunity to RSV through recruitment of antiviral monocytes. *J. Exp. Med.* **212**, 699–714 (2015).
171. A. Broggi, S. Ghosh, B. Sposito, R. Spreafico, F. Balzarini, A. Lo Cascio, N. Clementi, M. de Santis, N. Mancini, F. Granucci, I. Zanoni, Type III interferons disrupt the lung epithelial barrier upon viral recognition. *Science*. **369**, 706–712 (2020).
172. B. P. Daniels, D. W. Holman, L. Cruz-Orengo, H. Jujjavarapu, D. M. Durrant, R. S. Klein, Viral pathogen-associated molecular patterns regulate blood-brain barrier integrity via competing innate cytokine signals. *MBio*. **5** (2014), doi:10.1128/MBIO.01476-14.
173. H. M. Lazear, B. P. Daniels, A. K. Pinto, A. C. Huang, S. C. Vick, S. E. Doyle, M. Gale, R. S. Klein, M. S. Diamond, Interferon-λ restricts West Nile virus neuroinvasion by tightening the blood-brain barrier. *Sci. Transl. Med.* **7**, 284ra57 (2015).
174. F. Douam, Y. E. Soto Albrecht, G. Hrebikova, E. Sadimin, C. Davidson, S. V. Kotenko, A. Ploss, Type III Interferon-Mediated Signaling Is Critical for Controlling Live Attenuated Yellow Fever Virus Infection In Vivo. *MBio*. **8** (2017), doi:10.1128/MBIO.00819-17.
175. K. S. LeMessurier, H. Häcker, L. Chi, E. Tuomanen, V. Redecke, Type I interferon protects against pneumococcal invasive disease by inhibiting bacterial transmigration across the lung. *PLoS Pathog.* **9** (2013), doi:10.1371/JOURNAL.PPAT.1003727.

176. H. Boland, A. Endres, A. Burger-Kentischer, D. Jonigk, P. Braubach, G. Rohde, C. Bellinghausen, Protective effect of interferon type I on barrier function of the human airway epithelium during rhinovirus infections in vitro. *ERJ Open Res.* **9**, 41 (2023).
177. C. Odendall, A. A. Voak, J. C. Kagan, Type III IFNs Are Commonly Induced by Bacteria-Sensing TLRs and Reinforce Epithelial Barriers during Infection. *J. Immunol.* **199**, 3270–3279 (2017).
178. S. H. Ferguson, D. M. Foster, B. Sherry, S. T. Magness, D. M. Nielsen, J. L. Gookin, Interferon-λ3 Promotes Epithelial Defense and Barrier Function Against Cryptosporidium parvum Infection. *Cell. Mol. Gastroenterol. Hepatol.* **8**, 1–20 (2019).
179. D. Ahn, M. Wickersham, S. Riquelme, A. Prince, The Effects of IFN-λ on Epithelial Barrier Function Contribute to Klebsiella pneumoniae ST258 Pneumonia. *Am. J. Respir. Cell Mol. Biol.* **60**, 158–166 (2019).
180. J. Major, S. Crotta, M. Llorian, T. M. McCabe, H. H. Gad, S. L. Priestnall, R. Hartmann, A. Wack, Type I and III interferons disrupt lung epithelial repair during recovery from viral infection. *Science*. **369**, 712–717 (2020).
181. M. L. Stanifer, C. Guo, P. Doldan, S. Boulant, Importance of Type I and III Interferons at Respiratory and Intestinal Barrier Surfaces. *Front. Immunol.* **11** (2020), doi:10.3389/FIMMU.2020.608645.
182. M. Richard, A. Kok, D. de Meulder, T. M. Bestebroer, M. M. Lamers, N. M. A. Okba, M. Fentener van Vlissingen, B. Rockx, B. L. Haagmans, M. P. G. Koopmans, R. A. M. Fouchier, S. Herfst, SARS-CoV-2 is transmitted via contact and via the air between ferrets. *Nat. Commun.* **11** (2020), doi:10.1038/S41467-020-17367-2.
183. C. Huang, Y. Wang, X. Li, L. Ren, J. Zhao, Y. Hu, L. Zhang, G. Fan, J. Xu, X. Gu, Z. Cheng, T. Yu, J. Xia, Y. Wei, W. Wu, X. Xie, W. Yin, H. Li, M. Liu, Y. Xiao, H. Gao, L. Guo, J. Xie, G. Wang, R. Jiang, Z. Gao, Q. Jin, J. Wang, B. Cao, Clinical features of patients infected with 2019 novel coronavirus in Wuhan, China. *Lancet*. **395**, 497–506 (2020).
184. W. Guan, Z. Ni, Y. Hu, W. Liang, C. Ou, J. He, L. Liu, H. Shan, C. Lei, D. S. C. Hui, B. Du, L. Li, G. Zeng, K.-Y. Yuen, R. Chen, C. Tang, T. Wang, P. Chen, J. Xiang, S. Li, J. Wang, Z. Liang, Y. Peng, L. Wei, Y. Liu, Y. Hu, P. Peng, J. Wang, J. Liu, Z. Chen, G. Li, Z. Zheng, S. Qiu, J. Luo, C. Ye, S. Zhu, N. Zhong, Clinical Characteristics of Coronavirus Disease 2019 in China. *N. Engl. J. Med.* **382**, 1708–1720 (2020).
185. L. Lin, X. Jiang, Z. Zhang, S. Huang, Z. Zhang, Z. Fang, Z. Gu, L. Gao, H. Shi, L. Mai, Y. Liu, X. Lin, R. Lai, Z. Yan, X. Li, H. Shan, Gastrointestinal symptoms of 95 cases with SARS-CoV-2 infection. *Gut*. **69**, 997–1001 (2020).
186. A. E. Livanos, D. Jha, F. Cossarini, A. S. Gonzalez-Reiche, M. Tokuyama, T. Aydillo, T. L. Parigi, M. S. Ladinsky, I. Ramos, K. Dunleavy, B. Lee, R. E. Dixon, S. T. Chen, G. Martinez-Delgado, S. Nagula, E. A. Bruce, H. M. Ko, B. S. Glicksberg, G. Nadkarni, E. Pujadas, J. Reidy, S. Naymagon, A. Grinspan, J. Ahmad, M. Tankelevich, Y. Bram, R. Gordon, K. Sharma, J. Houldsworth, G. J. Britton, A. Chen-Liaw, M. P. Spindler, T. Plitt, P. Wang, A. Cerutti, J. J. Faith, J. F. Colombel, E. Kenigsberg, C. Argmann, M. Merad, S. Gnjatic, N. Harpaz, S. Danese, C. Cordon-Cardo, A. Rahman, R. E. Schwartz, N. A. Kumta, A. Aghemo, P. J. Bjorkman, F. Petralia, H. van Bakel, A. Garcia-Sastre, S. Mehandru, Intestinal Host Response to SARS-CoV-2 Infection and COVID-19 Outcomes in Patients With Gastrointestinal Symptoms. *Gastroenterology*. **160**, 2435-2450.e34 (2021).
187. R. Wölfel, V. M. Corman, W. Guggemos, M. Seilmaier, S. Zange, M. A. Müller, D. Niemeyer, T. C. Jones, P. Vollmar, C. Rothe, M. Hoelscher, T. Bleicker, S. Brünink, J. Schneider, R. Ehmann, K. Zwirglmaier, C. Drosten, C. Wendtner, Virological assessment of hospitalized patients with COVID-2019. *Nature*. **581**, 465–469 (2020).
188. Y. Wu, C. Guo, L. Tang, Z. Hong, J. Zhou, X. Dong, H. Yin, Q. Xiao, Y. Tang, X. Qu, L. Kuang, X. Fang, N. Mishra, J. Lu, H. Shan, G. Jiang, X. Huang, Prolonged presence of SARS-CoV-2 viral RNA in faecal samples. *Lancet Gastroenterol. Hepatol.* **5** (2020), pp. 434–435.
189. Y. H. Xing, W. Ni, Q. Wu, W. J. Li, G. J. Li, W. Di Wang, J. N. Tong, X. F. Song, G.

Wing-Kin Wong, Q. S. Xing, Prolonged viral shedding in feces of pediatric patients with coronavirus disease 2019. *J. Microbiol. Immunol. Infect.* **53** (2020), pp. 473–480.

190. Y. Xu, X. Li, B. Zhu, H. Liang, C. Fang, Y. Gong, Q. Guo, X. Sun, D. Zhao, J. Shen, H. Zhang, H. Liu, H. Xia, J. Tang, K. Zhang, S. Gong, Characteristics of pediatric SARS-CoV-2 infection and potential evidence for persistent fecal viral shedding. *Nat. Med.* **26**, 502–505 (2020).
191. M. Guo, W. Tao, R. A. Flavell, S. Zhu, Reply to: Rectally shed SARS-CoV-2 lacks infectivity: time to rethink faecal–oral transmission? *Nat. Rev. Gastroenterol. Hepatol.* **18** (2021), pp. 669–670.
192. F. Xiao, M. Tang, X. Zheng, Y. Liu, X. Li, H. Shan, Evidence for Gastrointestinal Infection of SARS-CoV-2. *Gastroenterology*. **158**, 1831-1833.e3 (2020).
193. M. Lehmann, K. Allers, C. Heldt, J. Meinhardt, F. Schmidt, Y. Rodriguez-Sillke, D. Kunkel, M. Schumann, C. Böttcher, C. Stahl-Hennig, S. Elezkurtaj, C. Bojarski, H. Radbruch, V. M. Corman, T. Schneider, C. Loddenkemper, V. Moos, C. Weidinger, A. A. Kühl, B. Siegmund, Human small intestinal infection by SARS-CoV-2 is characterized by a mucosal infiltration with activated CD8+ T cells. *Mucosal Immunol.* (2021), doi:10.1038/s41385-021-00437-z.
194. M. M. Lamers, J. Beumer, J. Van Der Vaart, K. Knoops, J. Puschhof, T. I. Breugem, R. B. G. Ravelli, J. P. Van Schayck, A. Z. Mykytyn, H. Q. Duimel, E. Van Donselaar, S. Riesebosch, H. J. H. Kuijpers, D. Schipper, W. J. V. De Wetering, M. De Graaf, M. Koopmans, E. Cuppen, P. J. Peters, B. L. Haagmans, H. Clevers, SARS-CoV-2 productively infects human gut enterocytes. *Science (80-. ).* **369**, 50–54 (2020).
195. S. Triana, C. Metz-Zumaran, C. Ramirez, C. Kee, P. Doldan, M. Shahraz, D. Schraivogel, A. R. Gschwind, A. K. Sharma, L. M. Steinmetz, C. Herrmann, T. Alexandrov, S. Boulant, M. L. Stanifer, Single-cell analyses reveal SARS-CoV-2 interference with intrinsic immune response in the human gut. *Mol. Syst. Biol.* **17** (2021), doi:10.15252/msb.202110232.
196. R. Zang, M. F. G. Castro, B. T. McCune, Q. Zeng, P. W. Rothlauf, N. M. Sonnek, Z. Liu, K. F. Brulois, X. Wang, H. B. Greenberg, M. S. Diamond, M. A. Ciorba, S. P. J. Whelan, S. Ding, TMPRSS2 and TMPRSS4 promote SARS-CoV-2 infection of human small intestinal enterocytes. *Sci. Immunol.* **5** (2020), doi:10.1126/sciimmunol.abc3582.
197. P. V'kovski, A. Kratzel, S. Steiner, H. Stalder, V. Thiel, Coronavirus biology and replication: implications for SARS-CoV-2. *Nat. Rev. Microbiol.* **19** (2021), pp. 155–170.
198. C. B. Jackson, M. Farzan, B. Chen, H. Choe, Mechanisms of SARS-CoV-2 entry into cells. *Nat. Rev. Mol. Cell Biol.* **23**, 3–20 (2022).
199. E. A. Madden, M. S. Diamond, Host cell-intrinsic innate immune recognition of SARS-CoV-2. *Curr. Opin. Virol.* **52**, 30–38 (2022).
200. Y. M. Kim, E. C. Shin, Type I and III interferon responses in SARS-CoV-2 infection. *Exp. Mol. Med.* **53**, 750–760 (2021).
201. N. Desai, A. Neyaz, A. Szabolcs, A. R. Shih, J. H. Chen, V. Thapar, L. T. Nieman, A. Solovyov, A. Mehta, D. J. Lieb, A. S. Kulkarni, C. Jaicks, K. H. Xu, M. J. Raabe, C. J. Pinto, D. Juric, I. Chebib, R. B. Colvin, A. Y. Kim, R. Monroe, S. E. Warren, P. Danaher, J. W. Reeves, J. Gong, E. H. Rueckert, B. D. Greenbaum, N. Hacohen, S. M. Lagana, M. N. Rivera, L. M. Sholl, J. R. Stone, D. T. Ting, V. Deshpande, Temporal and spatial heterogeneity of host response to SARS-CoV-2 pulmonary infection. *Nat. Commun.* **11** (2020), doi:10.1038/s41467-020-20139-7.
202. H. Katsura, V. Sontake, A. Tata, Y. Kobayashi, C. E. Edwards, B. E. Heaton, A. Konkimalla, T. Asakura, Y. Mikami, E. J. Fritch, P. J. Lee, N. S. Heaton, R. C. Boucher, S. H. Randell, R. S. Baric, P. R. Tata, Human Lung Stem Cell-Based Alveolospheres Provide Insights into SARS-CoV-2-Mediated Interferon Responses and Pneumocyte Dysfunction. *Cell Stem Cell*. **27**, 890-904.e8 (2020).
203. D. Blanco-Melo, B. E. Nilsson-Payant, W. C. Liu, S. Uhl, D. Hoagland, R. Møller, T. X. Jordan, K. Oishi, M. Panis, D. Sachs, T. T. Wang, R. E. Schwartz, J. K. Lim, R. A. Albrecht, B. R. tenOever, Imbalanced Host Response to SARS-CoV-2 Drives Development of COVID-19. *Cell*. **181**, 1036-1045.e9 (2020).

204. H. Chu, J. F. W. Chan, Y. Wang, T. T. T. Yuen, Y. Chai, H. Shuai, D. Yang, B. Hu, X. Huang, X. Zhang, Y. Hou, J. P. Cai, A. J. Zhang, J. Zhou, S. Yuan, K. K. W. To, I. F. N. Hung, T. T. Cheung, A. T. L. Ng, I. Hau-Yee Chan, I. Y. H. Wong, S. Y. K. Law, D. C. C. Foo, W. K. Leung, K. Y. Yuen, SARS-CoV-2 Induces a More Robust Innate Immune Response and Replicates Less Efficiently Than SARS-CoV in the Human Intestines: An Ex Vivo Study With Implications on Pathogenesis of COVID-19. *CMGH*. **11**, 771–781 (2021).
205. H. Shuai, H. Chu, Y. Hou, D. Yang, Y. Wang, B. Hu, X. Huang, X. Zhang, Y. Chai, J. P. Cai, J. F. W. Chan, K. Y. Yuen, Differential immune activation profile of SARS-CoV-2 and SARS-CoV infection in human lung and intestinal cells: Implications for treatment with IFN-β and IFN inducer. *J. Infect.* **81**, e1–e10 (2020).
206. A. Vanderheiden, P. Ralfs, T. Chirkova, A. A. Upadhyay, M. G. Zimmerman, S. Bedoya, H. Aoued, G. M. Tharp, K. L. Pellegrini, C. Manfredi, E. Sorscher, B. Mainou, J. L. Lobby, J. E. Kohlmeier, A. C. Lowen, P.-Y. Shi, V. D. Menachery, L. J. Anderson, A. Grakoui, S. E. Bosinger, M. S. Suthar, Type I and Type III Interferons Restrict SARS-CoV-2 Infection of Human Airway Epithelial Cultures. *J. Virol.* **94** (2020), doi:10.1128/jvi.00985-20.
207. E. Meffre, A. Iwasaki, Interferon deficiency can lead to severe COVID. *Nature*. **587** (2020), pp. 374–376.
208. U. Felgenhauer, A. Schoen, H. H. Gad, R. Hartmann, A. R. Schaubmar, K. Failing, C. Drosten, F. Weber, Inhibition of SARS–CoV-2 by type I and type III interferons. *J. Biol. Chem.* **295**, 13958–13964 (2020).
209. A. Park, A. Iwasaki, Type I and Type III Interferons – Induction, Signaling, Evasion, and Application to Combat COVID-19. *Cell Host Microbe*. **27** (2020), pp. 870–878.
210. A. Rebendenne, A. L. Chaves Valadão, M. Tauziet, G. Maarifi, B. Bonaventure, J. McKellar, R. Planès, S. Nisole, M. Arnaud-Arnould, O. Moncorgé, C. Goujon, SARS-CoV-2 Triggers an MDA-5-Dependent Interferon Response Which Is Unable To Control Replication in Lung Epithelial Cells. *J. Virol.* **95** (2021), doi:10.1128/jvi.02415-20.
211. I. Busnadiego, S. Fernbach, M. O. Pohl, U. Karakus, M. Huber, A. Trkola, S. Stertz, B. G. Hale, Antiviral activity of type i, ii, and iii interferons counterbalances ace2 inducibility and restricts sars-cov-2. *MBio*. **11**, 1–10 (2020).
212. J. S. Lee, E. C. Shin, The type I interferon response in COVID-19: implications for treatment. *Nat. Rev. Immunol.* **20**, 585–586 (2020).
213. A. J. Wilk, A. Rustagi, N. Q. Zhao, J. Roque, G. J. Martínez-Colón, J. L. McKechnie, G. T. Ivison, T. Ranganath, R. Vergara, T. Hollis, L. J. Simpson, P. Grant, A. Subramanian, A. J. Rogers, C. A. Blish, A single-cell atlas of the peripheral immune response in patients with severe COVID-19. *Nat. Med.* **26**, 1070–1076 (2020).
214. L. Zhu, P. Yang, Y. Zhao, Z. Zhuang, Z. Wang, R. Song, J. Zhang, C. Liu, Q. Gao, Q. Xu, X. Wei, H. X. Sun, B. Ye, Y. Wu, N. Zhang, G. Lei, L. Yu, J. Yan, G. Diao, F. Meng, C. Bai, P. Mao, Y. Yu, M. Wang, Y. Yuan, Q. Deng, Z. Li, Y. Huang, G. Hu, Y. Liu, X. Wang, Z. Xu, P. Liu, Y. Bi, Y. Shi, S. Zhang, Z. Chen, J. Wang, X. Xu, G. Wu, F. S. Wang, G. F. Gao, L. Liu, W. J. Liu, Single-Cell Sequencing of Peripheral Mononuclear Cells Reveals Distinct Immune Response Landscapes of COVID-19 and Influenza Patients. *Immunity*. **53**, 685-696.e3 (2020).
215. Z. Zhou, L. Ren, L. Zhang, J. Zhong, Y. Xiao, Z. Jia, L. Guo, J. Yang, C. Wang, S. Jiang, D. Yang, G. Zhang, H. Li, F. Chen, Y. Xu, M. Chen, Z. Gao, J. Yang, J. Dong, B. Liu, X. Zhang, W. Wang, K. He, Q. Jin, M. Li, J. Wang, Heightened Innate Immune Responses in the Respiratory Tract of COVID-19 Patients. *Cell Host Microbe*. **27**, 883-890.e2 (2020).
216. C. Lucas, P. Wong, J. Klein, T. B. R. Castro, J. Silva, M. Sundaram, M. K. Ellingson, T. Mao, J. E. Oh, B. Israelow, T. Takahashi, M. Tokuyama, P. Lu, A. Venkataraman, A. Park, S. Mohanty, H. Wang, A. L. Wyllie, C. B. F. Vogels, R. Earnest, S. Lapidus, I. M. Ott, A. J. Moore, M. C. Muenker, J. B. Fournier, M. Campbell, C. D. Odio, A. Casanovas-Massana, A. Obaid, A. Lu-Culligan, A. Nelson, A. Brito, A. Nunez, A. Martin, A. Watkins, B. Geng, C. Kalinich, C. Harden, C. Todeasa, C. Jensen, D. Kim, D. McDonald, D.

Shepard, E. Courchaine, E. B. White, E. Song, E. Silva, E. Kudo, G. DeIuliis, H. Rahming, H. J. Park, I. Matos, J. Nouws, J. Valdez, J. Fauver, J. Lim, K. A. Rose, K. Anastasio, K. Brower, L. Glick, L. Sharma, L. Sewanan, L. Knaggs, M. Minasyan, M. Batsu, M. Petrone, M. Kuang, M. Nakahata, M. Campbell, M. Linehan, M. H. Askenase, M. Simonov, M. Smolgovsky, N. Sonnert, N. Naushad, P. Vijayakumar, R. Martinello, R. Datta, R. Handoko, S. Bermejo, S. Prophet, S. Bickerton, S. Velazquez, T. Alpert, T. Rice, W. Khoury-Hanold, X. Peng, Y. Yang, Y. Cao, Y. Strong, R. Herbst, A. C. Shaw, R. Medzhitov, W. L. Schulz, N. D. Grubaugh, C. Dela Cruz, S. Farhadian, A. I. Ko, S. B. Omer, A. Iwasaki, Longitudinal analyses reveal immunological misfiring in severe COVID-19. *Nature*. **584**, 463–469 (2020).

217. S. Perlman, COVID-19 poses a riddle for the immune system. *Nature*. **584**, 345–346 (2020).
218. J. S. Lee, S. Park, H. W. Jeong, J. Y. Ahn, S. J. Choi, H. Lee, B. Choi, S. K. Nam, M. Sa, J. S. Kwon, S. J. Jeong, H. K. Lee, S. H. Park, S. H. Park, J. Y. Choi, S. H. Kim, I. Jung, E. C. Shin, Immunophenotyping of COVID-19 and influenza highlights the role of type I interferons in development of severe COVID-19. *Sci. Immunol.* **5** (2020), doi:10.1126/SCIIMMUNOL.ABD1554.
219. B. Israelow, E. Song, T. Mao, P. Lu, A. Meir, F. Liu, M. M. Alfajaro, J. Wei, H. Dong, R. J. Homer, A. Ring, C. B. Wilen, A. Iwasaki, Mouse model of SARS-CoV-2 reveals inflammatory role of type i interferon signaling. *J. Exp. Med.* **217** (2020), doi:10.1084/JEM.20201241.
220. I. E. Galani, N. Rovina, V. Lampropoulou, V. Triantafyllia, M. Manioudaki, E. Pavlos, E. Koukaki, P. C. Fragkou, V. Panou, V. Rapti, O. Koltsida, A. Mentis, N. Koulouris, S. Tsiodras, A. Koutsoukou, E. Andreakos, Untuned antiviral immunity in COVID-19 revealed by temporal type I/III interferon patterns and flu comparison. *Nat. Immunol.* **22**, 32–40 (2021).
221. M. G. Tovey, M. Streuli, I. Gresser, J. Gugenheim, B. Blanchard, J. Guymarho, F. Vignaux, M. Gigou, Interferon messenger RNA is produced constitutively in the organs of normal individuals. *Proc. Natl. Acad. Sci. U. S. A.* **84**, 5038–5042 (1987).
222. D. J. Gough, N. L. Messina, C. J. P. Clarke, R. W. Johnstone, D. E. Levy, Constitutive type I interferon modulates homeostatic balance through tonic signaling. *Immunity*. **36**, 166–174 (2012).
223. A. J. Fleetwood, H. Dinh, A. D. Cook, P. J. Hertzog, J. A. Hamilton, GM-CSF- and M-CSF-dependent macrophage phenotypes display differential dependence on type I interferon signaling. *J. Leukoc. Biol.* **86**, 411–421 (2009).
224. D. J. Gough, N. L. Messina, L. Hii, J. A. Gould, K. Sabapathy, A. P. S. Robertson, J. A. Trapani, D. E. Levy, P. J. Hertzog, C. J. P. Clarke, R. W. Johnstone, Functional crosstalk between type I and II interferon through the regulated expression of STAT1. *PLoS Biol.* **8** (2010), doi:10.1371/JOURNAL.PBIO.1000361.
225. K. Y. Fung, N. E. Mangan, H. Cumming, J. C. Horvat, J. R. Mayall, S. A. Stifter, N. De Weerd, L. C. Roisman, J. Rossjohn, S. A. Robertson, J. E. Schjenken, B. Parker, C. E. Gargett, H. P. T. Nguyen, D. J. Carr, P. M. Hansbro, P. J. Hertzog, Interferon-ε protects the female reproductive tract from viral and bacterial infection. *Science*. **339** (2013), doi:10.1126/SCIENCE.1233321.
226. R. C. Coldbeck-Shackley, O. Romeo, S. Rosli, L. J. Gearing, J. A. Gould, S. S. Lim, K. H. Van der Hoek, N. S. Eyre, B. Shue, S. A. Robertson, S. M. Best, M. D. Tate, P. J. Hertzog, M. R. Beard, Constitutive expression and distinct properties of IFN-epsilon protect the female reproductive tract from Zika virus infection. *PLoS Pathog.* **19** (2023), doi:10.1371/JOURNAL.PPAT.1010843.
227. W. Wang, Y. Yin, L. Xu, J. Su, F. Huang, Y. Wang, P. P. C. Boor, K. Chen, W. Wang, W. Cao, X. Zhou, P. Liu, L. J. W. Van Der Laan, J. Kwekkeboom, M. P. Peppelenbosch, Q. Pan, Unphosphorylated ISGF3 drives constitutive expression of interferon-stimulated genes to protect against viral infections. *Sci. Signal.* **10** (2017), doi:10.1126/SCISIGNAL.AAH4248.
228. M. S. Hakim, S. Chen, S. Ding, Y. Yin, A. Ikram, X. X. Ma, W. Wang, M. P.

Peppelenbosch, Q. Pan, Basal interferon signaling and therapeutic use of interferons in controlling rotavirus infection in human intestinal cells and organoids. *Sci. Rep.* **8** (2018), doi:10.1038/S41598-018-26784-9.

229. M. A. G. Essers, S. Offner, W. E. Blanco-Bose, Z. Waibler, U. Kalinke, M. A. Duchosal, A. Trumpp, IFNalpha activates dormant haematopoietic stem cells in vivo. *Nature*. **458**, 904–908 (2009).
230. J. W. Schoggins, D. A. MacDuff, N. Imanaka, M. D. Gainey, B. Shrestha, J. L. Eitson, K. B. Mar, R. B. Richardson, A. V. Ratushny, V. Litvak, R. Dabelic, B. Manicassamy, J. D. Aitchison, A. Aderem, R. M. Elliott, A. García-Sastre, V. Racaniello, E. J. Snijder, W. M. Yokoyama, M. S. Diamond, H. W. Virgin, C. M. Rice, Pan-viral specificity of IFN-induced genes reveals new roles for cGAS in innate immunity. *Nature*. **505**, 691–695 (2014).
231. K. M. Franz, W. J. Neidermyer, Y. J. Tan, S. P. J. Whelan, J. C. Kagan, STING-dependent translation inhibition restricts RNA virus replication. *Proc. Natl. Acad. Sci. U. S. A.* **115**, E2058–E2067 (2018).
232. Y. Liu, A. A. Jesus, B. Marrero, D. Yang, S. E. Ramsey, G. A. Montealegre Sanchez, K. Tenbrock, H. Wittkowski, O. Y. Jones, H. S. Kuehn, C.-C. R. Lee, M. A. DiMattia, E. W. Cowen, B. Gonzalez, I. Palmer, J. J. DiGiovanna, A. Biancotto, H. Kim, W. L. Tsai, A. M. Trier, Y. Huang, D. L. Stone, S. Hill, H. J. Kim, C. St. Hilaire, S. Gurprasad, N. Plass, D. Chapelle, I. Horkayne-Szakaly, D. Foell, A. Barysenka, F. Candotti, S. M. Holland, J. D. Hughes, H. Mehmet, A. C. Issekutz, M. Raffeld, J. McElwee, J. R. Fontana, C. P. Minniti, S. Moir, D. L. Kastner, M. Gadina, A. C. Steven, P. T. Wingfield, S. R. Brooks, S. D. Rosenzweig, T. A. Fleisher, Z. Deng, M. Boehm, A. S. Paller, R. Goldbach-Mansky, Activated STING in a vascular and pulmonary syndrome. *N. Engl. J. Med.* **371**, 507–518 (2014).
233. Y. Wang, R. Karki, R. Mall, B. R. Sharma, R. C. Kalathur, S. J. Lee, B. Kancharana, M. So, K. L. Combs, T. D. Kanneganti, Molecular mechanism of RIPK1 and caspase-8 in homeostatic type I interferon production and regulation. *Cell Rep.* **41** (2022), doi:10.1016/J.CELREP.2022.111434.
234. X. Tu, T. T. Chu, D. Jeltema, K. Abbott, K. Yang, C. Xing, J. Han, N. Dobbs, N. Yan, Interruption of post-Golgi STING trafficking activates tonic interferon signaling. *Nat. Commun.* **13** (2022), doi:10.1038/S41467-022-33765-0.
235. N. Hata, M. Sato, A. Takaoka, M. Asagiri, N. Tanaka, T. Taniguchi, Constitutive IFN-alpha/beta signal for efficient IFN-alpha/beta gene induction by virus. *Biochem. Biophys. Res. Commun.* **285**, 518–525 (2001).
236. S. Balachandran, A. A. Beg, Defining emerging roles for NF-κB in antivirus responses: revisiting the interferon-β enhanceosome paradigm. *PLoS Pathog.* **7** (2011), doi:10.1371/JOURNAL.PPAT.1002165.
237. S. H. Basagoudanavar, R. J. Thapa, S. Nogusa, J. Wang, A. A. Beg, S. Balachandran, Distinct roles for the NF-kappa B RelA subunit during antiviral innate immune responses. *J. Virol.* **85**, 2599–2610 (2011).
238. Y. Wang, R. Karki, R. Mall, B. R. Sharma, R. C. Kalathur, S. J. Lee, B. Kancharana, M. So, K. L. Combs, T. D. Kanneganti, Molecular mechanism of RIPK1 and caspase-8 in homeostatic type I interferon production and regulation. *Cell Rep.* **41** (2022), doi:10.1016/j.celrep.2022.111434.
239. F. Arakura, S. Hida, E. Ichikawa, C. Yajima, S. Nakajima, T. Saida, S. Taki, Genetic control directed toward spontaneous IFN-alpha/IFN-beta responses and downstream IFN-gamma expression influences the pathogenesis of a murine psoriasis-like skin disease. *J. Immunol.* **179**, 3249–3257 (2007).
240. K. Honda, S. Sakaguchi, C. Nakajima, A. Watanabe, H. Yanai, M. Matsumoto, T. Ohteki, T. Kaisho, A. Takaoka, S. Akira, T. Seya, T. Taniguchi, Selective contribution of IFN-alpha/beta signaling to the maturation of dendritic cells induced by double-stranded RNA or viral infection. *Proc. Natl. Acad. Sci. U. S. A.* **100**, 10872–10877 (2003).
241. C. S. Cheng, K. E. Feldman, J. Lee, S. Verma, D. Bin Huang, K. Huynh, M. Chang, J. V. Ponomarenko, S. C. Sun, C. A. Benedict, G. Ghosh, A. Hoffmann, The specificity of

innate immune responses is enforced by repression of interferon response elements by NF-κB p50. *Sci. Signal.* **4** (2011), doi:10.1126/SCISIGNAL.2001501.

242. D. Thanos, T. Maniatis, Virus induction of human IFN beta gene expression requires the assembly of an enhanceosome. *Cell*. **83**, 1091–1100 (1995).
243. H. Harada, T. Fujita, M. Miyamoto, Y. Kimura, M. Maruyama, A. Furia, T. Miyata, T. Taniguchi, Structurally similar but functionally distinct factors, IRF-1 and IRF-2, bind to the same regulatory elements of IFN and IFN-inducible genes. *Cell*. **58**, 729–739 (1989).
244. O. R. Colamonici, P. Domanski, L. C. Platanias, M. O. Diaz, Correlation between interferon (IFN) alpha resistance and deletion of the IFN alpha/beta genes in acute leukemia cell lines suggests selection against the IFN system. *Blood*. **80**, 744–749 (1992).
245. M. Heyman, D. Grandér, K. Bröndum-Nielsen, B. Cederblad, Y. Liu, B. Xu, S. Einhorn, Interferon system defects in malignant T-cells. *Leukemia* (1994).
246. C. Billard, F. Sigaux, S. Castaigne, F. Valensi, G. Flandrin, L. Degos, E. Falcoff, M. Aguet, Treatment of hairy cell leukemia with recombinant alpha interferon: II. In vivo down-regulation of alpha interferon receptors on tumor cells. *Blood*. **67**, 821–826 (1986).
247. H. M. Chen, N. Tanaka, Y. Mitani, E. Oda, H. Nozawa, J. Z. Chen, H. Yanai, H. Negishi, M. K. Choi, T. Iwasaki, H. Yamamoto, T. Taniguchi, A. Takaoka, Critical role for constitutive type I interferon signaling in the prevention of cellular transformation. *Cancer Sci.* **100**, 449–456 (2009).
248. The Down-Regulation of α-Interferon Receptors in Human Lymphoblastoid Cells: Relation to Cellular Responsiveness to the Antiproliferative Action of α-Interferon1 | Cancer Research | American Association for Cancer Research, (available at https://aacrjournals.org/cancerres/article/50/9/2654/496452/The-Down-Regulation-of-Interferon-Receptors-in).
249. D. H. Kaplan, V. Shankaran, A. S. Dighe, E. Stockert, M. Aguet, L. J. Old, R. D. Schreiber, Demonstration of an interferon gamma-dependent tumor surveillance system in immunocompetent mice. *Proc. Natl. Acad. Sci. U. S. A.* **95**, 7556–7561 (1998).
250. L. H. Wong, K. G. Krauer, I. Hatzinisiriou, M. J. Estcourt, P. Hersey, N. D. Tam, S. Edmondson, R. J. Devenish, S. J. Ralph, Interferon-resistant human melanoma cells are deficient in ISGF3 components, STAT1, STAT2, and p48-ISGF3gamma. *J. Biol. Chem.* **272**, 28779–28785 (1997).
251. S. Landolfo, A. Guarini, L. Riera, M. Gariglio, G. Gribaudo, A. Cignetti, I. Cordone, E. Montefusco, F. Mandelli, R. Foa, Chronic myeloid leukemia cells resistant to interferon-alpha lack STAT1 expression. *Hematol. J. Off. J. Eur. Haematol. Assoc.* **1**, 7–14 (2000).
252. M. K. Crow, Type I interferon in organ-targeted autoimmune and inflammatory diseases. *Arthritis Res. Ther.* **12 Suppl 1** (2010), doi:10.1186/AR2886.
253. K. A. Kirou, C. Lee, S. George, K. Louca, M. G. E. Peterson, M. K. Crow, Activation of the interferon-alpha pathway identifies a subgroup of systemic lupus erythematosus patients with distinct serologic features and active disease. *Arthritis Rheum.* **52**, 1491–1503 (2005).
254. Q. Lu, N. Shen, X. M. Li, S. L. Chen, Genomic view of IFN-alpha response in pre-autoimmune NZB/W and MRL/lpr mice. *Genes Immun.* **8**, 590–603 (2007).
255. Y. J. Crow, D. B. Stetson, The type I interferonopathies: 10 years on. *Nat. Rev. Immunol.* **22**, 471–483 (2022).
256. D. St Johnston, J. Ahringer, Cell polarity in eggs and epithelia: parallels and diversity. *Cell*. **141**, 757–774 (2010).
257. J. D. Cording, Interaction, Function and Regulation of the Tight Junction Protein Tricellulin (2015), doi:10.17169/REFUBIUM-9584.
258. R. Fu, X. Jiang, G. Li, Y. Zhu, H. Zhang, Junctional complexes in epithelial cells: sentinels for extracellular insults and intracellular homeostasis. *FEBS J.* **289**, 7314–7333 (2022).
259. H. K. Campbell, J. L. Maiers, K. A. DeMali, Interplay between tight junctions & adherens junctions. *Exp. Cell Res.* **358**, 39–44 (2017).
260. A. Alizadeh, P. Akbari, J. Garssen, J. Fink-Gremmels, S. Braber, Epithelial integrity,

junctional complexes, and biomarkers associated with intestinal functions. *Tissue barriers*. **10** (2022), doi:10.1080/21688370.2021.1996830.
261. J. Xu, P. J. Kausalya, D. C. Y. Phua, S. M. Ali, Z. Hossain, W. Hunziker, Early embryonic lethality of mice lacking ZO-2, but Not ZO-3, reveals critical and nonredundant roles for individual zonula occludens proteins in mammalian development. *Mol. Cell. Biol.* **28**, 1669–1678 (2008).
262. M. Adachi, A. Inoko, M. Hata, K. Furuse, K. Umeda, M. Itoh, S. Tsukita, Normal establishment of epithelial tight junctions in mice and cultured cells lacking expression of ZO-3, a tight-junction MAGUK protein. *Mol. Cell. Biol.* **26**, 9003–9015 (2006).
263. M. Perez-Moreno, M. A. Davis, E. Wong, H. A. Pasolli, A. B. Reynolds, E. Fuchs, p120-catenin mediates inflammatory responses in the skin. *Cell*. **124**, 631–644 (2006).
264. M. Perez-Moreno, W. Song, H. A. Pasolli, S. E. Williams, E. Fuchs, Loss of p120 catenin and links to mitotic alterations, inflammation, and skin cancer. *Proc. Natl. Acad. Sci. U. S. A.* **105**, 15399–15404 (2008).
265. L. Qin, S. Qin, Y. Zhang, C. Zhang, H. Ma, N. Li, L. Liu, X. Wang, R. Wu, p120 modulates LPS-induced NF-κB activation partially through RhoA in bronchial epithelial cells. *Biomed Res. Int.* **2014** (2014), doi:10.1155/2014/932340.
266. A. Kobielak, E. Fuchs, Links between alpha-catenin, NF-kappaB, and squamous cell carcinoma in skin. *Proc. Natl. Acad. Sci. U. S. A.* **103**, 2322–2327 (2006).
267. M. Lee, V. Vasioukhin, Cell polarity and cancer--cell and tissue polarity as a non-canonical tumor suppressor. *J. Cell Sci.* **121**, 1141–1150 (2008).
268. G. F. Weber, M. A. Bjerke, D. W. DeSimone, Integrins and cadherins join forces to form adhesive networks. *J. Cell Sci.* **124**, 1183–1193 (2011).
269. B. Chang, K. K. H. Svoboda, X. Liu, Cell polarization: From epithelial cells to odontoblasts. *Eur. J. Cell Biol.* **98**, 1–11 (2019).
270. F. Martin-Belmonte, M. Perez-Moreno, Epithelial cell polarity, stem cells and cancer. *Nat. Rev. Cancer 2011 121*. **12**, 23–38 (2011).
271. M. B. Elowitz, A. J. Levine, E. D. Siggia, P. S. Swain, Stochastic gene expression in a single cell. *Science*. **297**, 1183–1186 (2002).
272. E. M. Ozbudak, M. Thattai, I. Kurtser, A. D. Grossman, A. Van Oudenaarden, Regulation of noise in the expression of a single gene. *Nat. Genet.* **31**, 69–73 (2002).
273. S. J. Altschuler, L. F. Wu, Cellular Heterogeneity: Do Differences Make a Difference? *Cell*. **141** (2010), pp. 559–563.
274. B. Snijder, L. Pelkmans, Origins of regulated cell-to-cell variability. *Nat. Rev. Mol. Cell Biol.* **12**, 119–125 (2011).
275. O. Symmons, A. Raj, What's Luck Got to Do with It: Single Cells, Multiple Fates, and Biological Nondeterminism. *Mol. Cell*. **62**, 788–802 (2016).
276. J. M. Raser, E. K. O'Shea, Control of stochasticity in eukaryotic gene expression. *Science*. **304**, 1811–1814 (2004).
277. J. M. Levsky, S. M. Shenoy, R. C. Pezo, R. H. Singer, Single-cell gene expression profiling. *Science*. **297**, 836–840 (2002).
278. A. Raj, C. S. Peskin, D. Tranchina, D. Y. Vargas, S. Tyagi, Stochastic mRNA synthesis in mammalian cells. *PLoS Biol.* **4**, 1707–1719 (2006).
279. A. Raj, P. van den Bogaard, S. A. Rifkin, A. van Oudenaarden, S. Tyagi, Imaging individual mRNA molecules using multiple singly labeled probes. *Nat. Methods*. **5**, 877–879 (2008).
280. I. Golding, J. Paulsson, S. M. Zawilski, E. C. Cox, Real-time kinetics of gene activity in individual bacteria. *Cell*. **123**, 1025–1036 (2005).
281. K. H. Chen, A. N. Boettiger, J. R. Moffitt, S. Wang, X. Zhuang, RNA imaging. Spatially resolved, highly multiplexed RNA profiling in single cells. *Science*. **348** (2015), doi:10.1126/SCIENCE.AAA6090.
282. E. Lubeck, A. F. Coskun, T. Zhiyentayev, M. Ahmad, L. Cai, Single-cell in situ RNA profiling by sequential hybridization. *Nat. Methods*. **11**, 360–361 (2014).
283. D. Grün, L. Kester, A. Van Oudenaarden, Validation of noise models for single-cell transcriptomics. *Nat. Methods*. **11**, 637–640 (2014).

284. G. K. Marinov, B. A. Williams, K. McCue, G. P. Schroth, J. Gertz, R. M. Myers, B. J. Wold, From single-cell to cell-pool transcriptomes: stochasticity in gene expression and RNA splicing. *Genome Res.* **24**, 496–510 (2014).
285. A. R. Wu, N. F. Neff, T. Kalisky, P. Dalerba, B. Treutlein, M. E. Rothenberg, F. M. Mburu, G. L. Mantalas, S. Sim, M. F. Clarke, S. R. Quake, Quantitative assessment of single-cell RNA-sequencing methods. *Nat. Methods*. **11**, 41–46 (2014).
286. K. Achim, J. B. Pettit, L. R. Saraiva, D. Gavriouchkina, T. Larsson, D. Arendt, J. C. Marioni, High-throughput spatial mapping of single-cell RNA-seq data to tissue of origin. *Nat. Biotechnol.* **33**, 503–509 (2015).
287. J. P. Junker, E. S. Noël, V. Guryev, K. A. Peterson, G. Shah, J. Huisken, A. P. McMahon, E. Berezikov, J. Bakkers, A. Van Oudenaarden, Genome-wide RNA Tomography in the zebrafish embryo. *Cell*. **159**, 662–675 (2014).
288. R. Satija, J. A. Farrell, D. Gennert, A. F. Schier, A. Regev, Spatial reconstruction of single-cell gene expression data. *Nat. Biotechnol.* **33**, 495–502 (2015).
289. J. Elf, G. W. Li, X. S. Xie, Probing transcription factor dynamics at the single-molecule level in a living cell. *Science*. **316**, 1191–1194 (2007).
290. P. Hammar, P. Leroy, A. Mahmutovic, E. G. Marklund, O. G. Berg, J. Elf, The lac repressor displays facilitated diffusion in living cells. *Science*. **336**, 1595–1598 (2012).
291. K. Shah, S. Tyagi, Barriers to transmission of transcriptional noise in a c-fos c-jun pathway. *Mol. Syst. Biol.* **9** (2013), doi:10.1038/MSB.2013.45.
292. Z. B. Bjornson, G. P. Nolan, W. J. Fantl, Single-cell mass cytometry for analysis of immune system functional states. *Curr. Opin. Immunol.* **25**, 484–494 (2013).
293. R. Zenobi, Single-cell metabolomics: analytical and biological perspectives. *Science*. **342** (2013), doi:10.1126/SCIENCE.1243259.
294. S. S. Andrews, T. Dinh, A. P. Arkin, "Stochastic Models of Biological Processes" in *Encyclopedia of Complexity and Systems Science* (Springer New York, 2009; https://link.springer.com/referenceworkentry/10.1007/978-0-387-30440-3_524), pp. 8730–8749.
295. J. Paulsson, Summing up the noise in gene networks. *Nature*. **427**, 415–418 (2004).
296. J. A. Shapiro, Thinking about bacterial populations as multicellular organisms. *Annu. Rev. Microbiol.* **52**, 81–104 (1998).
297. C. M. Waters, B. L. Bassler, Quorum sensing: cell-to-cell communication in bacteria. *Annu. Rev. Cell Dev. Biol.* **21**, 319–346 (2005).
298. S. Kavaliauskiene, C. M. Nymark, J. Bergan, R. Simm, T. Sylvänne, H. Simolin, K. Ekroos, T. Skotland, K. Sandvig, Cell density-induced changes in lipid composition and intracellular trafficking. *Cell. Mol. Life Sci.* **71**, 1097–1116 (2014).
299. K. Trajkovic, C. Valdez, D. Ysselstein, D. Krainc, Fluctuations in cell density alter protein markers of multiple cellular compartments, confounding experimental outcomes. *PLoS One*. **14** (2019), doi:10.1371/journal.pone.0211727.
300. J. R. Misra, K. D. Irvine, The Hippo Signaling Network and Its Biological Functions. *Annu. Rev. Genet.* **52**, 65–87 (2018).
301. Z. Meng, T. Moroishi, K. L. Guan, Mechanisms of Hippo pathway regulation. *Genes Dev.* **30**, 1–17 (2016).
302. M. Aragona, T. Panciera, A. Manfrin, S. Giulitti, F. Michielin, N. Elvassore, S. Dupont, S. Piccolo, A mechanical checkpoint controls multicellular growth through YAP/TAZ regulation by actin-processing factors. *Cell*. **154**, 1047–1059 (2013).
303. B. Zhao, X. Wei, W. Li, R. S. Udan, Q. Yang, J. Kim, J. Xie, T. Ikenoue, J. Yu, L. Li, P. Zheng, K. Ye, A. Chinnaiyan, G. Halder, Z. C. Lai, K. L. Guan, Inactivation of YAP oncoprotein by the Hippo pathway is involved in cell contact inhibition and tissue growth control. *Genes Dev.* **21**, 2747–2761 (2007).
304. N. G. Kim, E. Koh, X. Chen, B. M. Gumbiner, E-cadherin mediates contact inhibition of proliferation through Hippo signaling-pathway components. *Proc. Natl. Acad. Sci. U. S. A.* **108**, 11930–11935 (2011).
305. T. Yue, A. Tian, J. Jiang, The cell adhesion molecule echinoid functions as a tumor suppressor and upstream regulator of the Hippo signaling pathway. *Dev. Cell*. **22**, 255–

267 (2012).

306. B. Zhou, P. Flodby, J. Luo, D. R. Castillo, Y. Liu, F. X. Yu, A. McConnell, B. Varghese, G. Li, N. O. Chimge, M. Sunohara, M. N. Koss, W. Elatre, P. Conti, J. M. Liebler, C. Yang, C. N. Marconett, I. A. Laird-Offringa, P. Minoo, K. Guan, B. R. Stripp, E. D. Crandall, Z. Borok, Claudin-18-mediated YAP activity regulates lung stem and progenitor cell homeostasis and tumorigenesis. *J. Clin. Invest.* **128**, 970–984 (2018).
307. K. Schlegelmilch, M. Mohseni, O. Kirak, J. Pruszak, J. R. Rodriguez, D. Zhou, B. T. Kreger, V. Vasioukhin, J. Avruch, T. R. Brummelkamp, F. D. Camargo, Yap1 acts downstream of α-catenin to control epidermal proliferation. *Cell*. **144**, 782–795 (2011).
308. C. Ibar, E. Kirichenko, B. Keepers, E. Enners, K. Fleisch, K. D. Irvine, Tension-dependent regulation of mammalian Hippo signaling through LIMD1. *J. Cell Sci.* **131** (2018), doi:10.1242/JCS.214700.
309. X. Varelas, The Hippo pathway effectors TAZ and YAP in development, homeostasis and disease. *Development*. **141**, 1614–1626 (2014).
310. K. Schauer, T. Duong, K. Bleakley, S. Bardin, M. Bornens, B. Goud, Probabilistic density maps to study global endomembrane organization. *Nat. Methods*. **7**, 560–566 (2010).
311. B. Snijder, R. Sacher, P. Rämö, E. M. Damm, P. Liberali, L. Pelkmans, Population context determines cell-to-cell variability in endocytosis and virus infection. *Nature*. **461**, 520–523 (2009).
312. U. Rand, M. Rinas, J. S. Werk, G. Nöhren, M. Linnes, A. Kröger, M. Flossdort, K. Kály-Kullai, H. Hauser, T. Höfer, M. Köster, Multi-layered stochasticity and paracrine signal propagation shape the type-I interferon response. *Mol. Syst. Biol.* **8** (2012), doi:10.1038/msb.2012.17.
313. B. Schmid, M. Rinas, A. Ruggieri, E. G. Acosta, M. Bartenschlager, A. Reuter, W. Fischl, N. Harder, J. P. Bergeest, M. Flossdorf, K. Rohr, T. Höfer, R. Bartenschlager, Live Cell Analysis and Mathematical Modeling Identify Determinants of Attenuation of Dengue Virus 2'-O-Methylation Mutant. *PLoS Pathog.* **11** (2015), doi:10.1371/journal.ppat.1005345.
314. S. Bhushal, M. Wolfsmüller, T. A. Selvakumar, L. Kemper, D. Wirth, M. W. Hornef, H. Hauser, M. Köster, Cell polarization and epigenetic status shape the heterogeneous response to type III interferons in intestinal epithelial cells. *Front. Immunol.* **8** (2017), doi:10.3389/fimmu.2017.00671.
315. B. D. Maier, L. U. Aguilera, S. Sahle, P. Mutz, P. Kalra, C. Dächert, R. Bartenschlager, M. Binder, U. Kummer, Stochastic dynamics of Type-I interferon responses. *PLoS Comput. Biol.* **18** (2022), doi:10.1371/journal.pcbi.1010623.
316. O. Bauhofer, A. Ruggieri, B. Schmid, P. Schirmacher, R. Bartenschlager, Persistence of HCV in quiescent hepatic cells under conditions of an interferon-induced antiviral response. *Gastroenterology*. **143**, 429-438.e8 (2012).
317. A. K. Shalek, R. Satija, X. Adiconis, R. S. Gertner, J. T. Gaublomme, R. Raychowdhury, S. Schwartz, N. Yosef, C. Malboeuf, D. Lu, J. J. Trombetta, D. Gennert, A. Gnirke, A. Goren, N. Hacohen, J. Z. Levin, H. Park, A. Regev, Single-cell transcriptomics reveals bimodality in expression and splicing in immune cells. *Nature*. **498**, 236–240 (2013).
318. Y. M. El-Sherbiny, A. Psarras, M. Y. M. Yusof, E. M. A. Hensor, R. Tooze, G. Doody, A. A. A. Mohamed, D. McGonagle, M. Wittmann, P. Emery, E. M. Vital, A novel two-score system for interferon status segregates autoimmune diseases and correlates with clinical features. *Sci. Rep.* **8** (2018), doi:10.1038/S41598-018-24198-1.
319. M. Czerkies, Z. Korwek, W. Prus, M. Kochańczyk, J. Jaruszewicz-Błońska, K. Tudelska, S. Błoński, M. Kimmel, A. R. Brasier, T. Lipniacki, Cell fate in antiviral response arises in the crosstalk of IRF, NF-κB and JAK/STAT pathways. *Nat. Commun.* **9** (2018), doi:10.1038/S41467-017-02640-8.
320. S. Mostafavi, H. Yoshida, D. Moodley, H. Leboité, K. Rothamel, T. Raj, C. J. Ye, N. Chevrier, S. Y. Zhang, T. Feng, M. Lee, J. L. Casanova, J. D. Clark, M. Hegen, J. B. Telliez, N. Hacohen, P. L. De Jager, A. Regev, D. Mathis, C. Benoist, Parsing the Interferon Transcriptional Network and Its Disease Associations. *Cell*. **164**, 564–578 (2016).

321. J. T. O'Neal, A. A. Upadhyay, A. Wolabaugh, N. B. Patel, S. E. Bosinger, M. S. Suthar, West Nile Virus-Inclusive Single-Cell RNA Sequencing Reveals Heterogeneity in the Type I Interferon Response within Single Cells. *J. Virol.* **93** (2019), doi:10.1128/JVI.01778-18.
322. D. Levin, D. Harari, G. Schreiber, Stochastic receptor expression determines cell fate upon interferon treatment. *Mol. Cell. Biol.* **31**, 3252–3266 (2011).
323. L. J. Klunder, K. N. Faber, G. Dijkstra, S. C. D. Van Ijzendoorn, Mechanisms of Cell Polarity–Controlled Epithelial Homeostasis and Immunity in the Intestine. *Cold Spring Harb. Perspect. Biol.* **9** (2017), doi:10.1101/CSHPERSPECT.A027888.
324. B. Snijder, R. Sacher, P. Rämö, E.-M. Damm, P. Liberali, L. Pelkmans, Population context determines cell-to-cell variability in endocytosis and virus infection. *Zurich PhD Progr. Mol. Life Sci.* **461** (2009), doi:10.1038/nature08282.
325. S. Bhushal, M. Wolfsmüller, T. A. Selvakumar, L. Kemper, D. Wirth, M. W. Hornef, H. Hauser, M. Köster, Cell Polarization and Epigenetic Status Shape the Heterogeneous Response to Type III Interferons in Intestinal Epithelial Cells. *Front. Immunol.* **8**, 671 (2017).
326. V. K. Mootha, C. M. Lindgren, K. F. Eriksson, A. Subramanian, S. Sihag, J. Lehar, P. Puigserver, E. Carlsson, M. Ridderstråle, E. Laurila, N. Houstis, M. J. Daly, N. Patterson, J. P. Mesirov, T. R. Golub, P. Tamayo, B. Spiegelman, E. S. Lander, J. N. Hirschhorn, D. Altshuler, L. C. Groop, PGC-1α-responsive genes involved in oxidative phosphorylation are coordinately downregulated in human diabetes. *Nat. Genet. 2003 343*. **34**, 267–273 (2003).
327. W. Luo, M. S. Friedman, K. Shedden, K. D. Hankenson, P. J. Woolf, GAGE: generally applicable gene set enrichment for pathway analysis. *BMC Bioinformatics*. **10** (2009), doi:10.1186/1471-2105-10-161.
328. M. Schubert, B. Klinger, M. Klünemann, A. Sieber, F. Uhlitz, S. Sauer, M. J. Garnett, N. Blüthgen, J. Saez-Rodriguez, Perturbation-response genes reveal signaling footprints in cancer gene expression. *Nat. Commun.* **9** (2018), doi:10.1038/S41467-017-02391-6.
329. G. L. Smith, C. T. O. Benfield, C. Maluquer de Motes, M. Mazzon, S. W. J. Ember, B. J. Ferguson, R. P. Sumner, Vaccinia virus immune evasion: mechanisms, virulence and immunogenicity. *J. Gen. Virol.* **94**, 2367–2392 (2013).
330. R. D. Leibowitz, The effect of ethidium bromide on mitochondrial DNA synthesis and mitochondrial DNA structure in HeLa cells. *J. Cell Biol.* **51**, 116–122 (1971).
331. L. S. Kaguni, DNA polymerase gamma, the mitochondrial replicase. *Annu. Rev. Biochem.* **73**, 293–320 (2004).
332. Q. Zhang, F. Meng, S. Chen, S. W. Plouffe, S. Wu, S. Liu, X. Li, R. Zhou, J. Wang, B. Zhao, J. Liu, J. Qin, J. Zou, X. H. Feng, K. L. Guan, P. Xu, Hippo signalling governs cytosolic nucleic acid sensing through YAP/TAZ-mediated TBK1 blockade. *Nat. Cell Biol.* **19**, 362–374 (2017).
333. S. Wang, F. Xie, F. Chu, Z. Zhang, B. Yang, T. Dai, L. Gao, L. Wang, L. Ling, J. Jia, H. Van Dam, J. Jin, L. Zhang, F. Zhou, YAP antagonizes innate antiviral immunity and is targeted for lysosomal degradation through IKKε-mediated phosphorylation. *Nat. Immunol.* **18**, 733–743 (2017).
334. J. Koch, Q. Xin, M. Obr, A. Schäfer, N. Rolfs, H. A. Anagho, A. Kudulyte, L. Woltereck, S. Kummer, J. Campos, Z. M. Uckeley, L. Bell-Sakyi, H.-G. Kräusslich, F. K. Schur, C. Acuna, P.-Y. Lozach, The phenuivirus Toscana virus makes an atypical use of vacuolar acidity to enter host cells. *PLoS Pathog.* **19**, e1011562 (2023).
335. S. Windhaber, Q. Xin, Z. M. Uckeley, J. Koch, M. Obr, C. Garnier, C. Luengo-Guyonnot, M. Duboeuf, F. K. M. Schur, P.-Y. Lozach, The Orthobunyavirus Germiston Enters Host Cells from Late Endosomes. *J. Virol.* **96** (2022), doi:10.1128/JVI.02146-21.
336. M. Kaksonen, A. Roux, Mechanisms of clathrin-mediated endocytosis. *Nat. Rev. Mol. Cell Biol.* **19**, 313–326 (2018).
337. T. M. Kicmal, P. M. Tate, C. N. Dial, J. J. Esin, B. C. Mounce, Polyamine Depletion Abrogates Enterovirus Cellular Attachment. *J. Virol.* **93** (2019), doi:10.1128/jvi.01054-19.

338. L. Nie, W. Feng, R. Diaz, M. A. Gratton, K. J. Doyle, E. N. Yamoah, Functional consequences of polyamine synthesis inhibition by L-alpha-difluoromethylornithine (DFMO): cellular mechanisms for DFMO-mediated ototoxicity. *J. Biol. Chem.* **280**, 15097–15102 (2005).
339. C. F. Arias, P. Romero, V. Alvarez, S. López, Trypsin activation pathway of rotavirus infectivity. *J. Virol.* **70**, 5832–5839 (1996).
340. U. Rand, M. Rinas, J. S. Werk, G. Nöhren, M. Linnes, A. Kröger, M. Flossdort, K. Kály-Kullai, H. Hauser, T. Höfer, M. Köster, Multi-layered stochasticity and paracrine signal propagation shape the type-I interferon response. *Mol. Syst. Biol.* **8** (2012), doi:10.1038/msb.2012.17.
341. B. Snijder, L. Pelkmans, Origins of regulated cell-to-cell variability. *Nat. Rev. Mol. Cell Biol.* **12**, 119–125 (2011).
342. N. Q. Balaban, J. Merrin, R. Chait, L. Kowalik, S. Leibler, Bacterial persistence as a phenotypic switch. *Science*. **305**, 1622–1625 (2004).
343. L. L. Campbell, K. Polyak, Breast tumor heterogeneity: cancer stem cells or clonal evolution? *Cell Cycle*. **6**, 2332–2338 (2007).
344. S. V. Sharma, D. Y. Lee, B. Li, M. P. Quinlan, F. Takahashi, S. Maheswaran, U. McDermott, N. Azizian, L. Zou, M. A. Fischbach, K. K. Wong, K. Brandstetter, B. Wittner, S. Ramaswamy, M. Classon, J. Settleman, A Chromatin-Mediated Reversible Drug-Tolerant State in Cancer Cell Subpopulations. *Cell*. **141**, 69–80 (2010).
345. K. E. Gascoigne, S. S. Taylor, Cancer cells display profound intra- and interline variation following prolonged exposure to antimitotic drugs. *Cancer Cell*. **14**, 111–122 (2008).
346. A. A. Cohen, N. Geva-Zatorsky, E. Eden, M. Frenkel-Morgenstern, I. Issaeva, A. Sigal, R. Milo, C. Cohen-Saidon, Y. Liron, Z. Kam, L. Cohen, T. Danon, N. Perzov, U. Alon, Dynamic proteomics of individual cancer cells in response to a drug. *Science*. **322**, 1511–1516 (2008).
347. L. Wu, L. Ke, Z. Zhang, J. Yu, X. Meng, Development of EGFR TKIs and Options to Manage Resistance of Third-Generation EGFR TKI Osimertinib: Conventional Ways and Immune Checkpoint Inhibitors. *Front. Oncol.* **10** (2020), doi:10.3389/FONC.2020.602762.
348. Y. Fang, R. Sullivan, C. H. Graham, Confluence-dependent resistance to doxorubicin in human MDA-MB-231 breast carcinoma cells requires hypoxia-inducible factor-1 activity. *Exp. Cell Res.* **313**, 867–877 (2007).
349. L. Meli, E. T. Jordan, D. S. Clark, R. J. Linhardt, J. S. Dordick, Influence of a three-dimensional, microarray environment on human Cell culture in drug screening systems. *Biomaterials*. **33**, 9087–9096 (2012).
350. I. Jaspers, J. M. Ciencewicki, L. E. Brighton, Localization of type i interferon receptor limits interferon-induced TLR3 in epithelial cells. *J. Interf. Cytokine Res.* **29**, 289–297 (2009).
351. A. L. Humlicek, L. J. Manzel, C. L. Chin, L. Shi, K. J. D. A. Excoffon, M. C. Winter, D. M. Shasby, D. C. Look, Paracellular Permeability Restricts Airway Epithelial Responses to Selectively Allow Activation by Mediators at the Basolateral Surface. *J. Immunol.* **178**, 6395–6403 (2007).
352. M. L. Stanifer, A. Rippert, A. Kazakov, J. Willemsen, D. Bucher, S. Bender, R. Bartenschlager, M. Binder, S. Boulant, Reovirus intermediate subviral particles constitute a strategy to infect intestinal epithelial cells by exploiting TGF-β dependent pro-survival signaling. *Cell. Microbiol.* **18**, 1831–1845 (2016).
353. F. Civril, T. Deimling, C. C. De Oliveira Mann, A. Ablasser, M. Moldt, G. Witte, V. Hornung, K. P. Hopfner, Structural mechanism of cytosolic DNA sensing by cGAS. *Nature*. **498**, 332–337 (2013).
354. J. Kim, H. S. Kim, J. H. Chung, Molecular mechanisms of mitochondrial DNA release and activation of the cGAS-STING pathway. *Exp. Mol. Med.* **55**, 510–519 (2023).
355. P. Pérez-Treviño, M. Velásquez, N. García, Mechanisms of mitochondrial DNA escape and its relationship with different metabolic diseases. *Biochim. Biophys. acta. Mol. basis Dis.* **1866** (2020), doi:10.1016/J.BBADIS.2020.165761.

356. Z. T. Schafer, S. Kornbluth, The apoptosome: physiological, developmental, and pathological modes of regulation. *Dev. Cell*. **10**, 549–561 (2006).
357. K. McArthur, L. W. Whitehead, J. M. Heddleston, L. Li, B. S. Padman, V. Oorschot, N. D. Geoghegan, S. Chappaz, S. Davidson, H. S. Chin, R. M. Lane, M. Dramicanin, T. L. Saunders, C. Sugiana, R. Lessene, L. D. Osellame, T. L. Chew, G. Dewson, M. Lazarou, G. Ramm, G. Lessene, M. T. Ryan, K. L. Rogers, M. F. Van Delft, B. T. Kile, BAK/BAX macropores facilitate mitochondrial herniation and mtDNA efflux during apoptosis. *Science*. **359** (2018), doi:10.1126/SCIENCE.AAO6047.
358. J. S. Riley, G. Quarato, C. Cloix, J. Lopez, J. O'Prey, M. Pearson, J. Chapman, H. Sesaki, L. M. Carlin, J. F. Passos, A. P. Wheeler, A. Oberst, K. M. Ryan, S. W. Tait, Mitochondrial inner membrane permeabilisation enables mtDNA release during apoptosis. *EMBO J.* **37** (2018), doi:10.15252/EMBJ.201899238.
359. J. Kim, R. Gupta, L. P. Blanco, S. Yang, A. Shteinfer-Kuzmine, K. Wang, J. Zhu, H. E. Yoon, X. Wang, M. Kerkhofs, H. Kang, A. L. Brown, S. J. Park, X. Xu, E. Z. van Rilland, M. K. Kim, J. I. Cohen, M. J. Kaplan, V. Shoshan-Barmatz, J. H. Chung, VDAC oligomers form mitochondrial pores to release mtDNA fragments and promote lupus-like disease. *Science*. **366**, 1531–1536 (2019).
360. N. Jeremiah, B. Neven, M. Gentili, I. Callebaut, S. Maschalidi, M. C. Stolzenberg, N. Goudin, M. L. Frémond, P. Nitschke, T. J. Molina, S. Blanche, C. Picard, G. I. Rice, Y. J. Crow, N. Manel, A. Fischer, B. Bader-Meunier, F. Rieux-Laucat, Inherited STING-activating mutation underlies a familial inflammatory syndrome with lupus-like manifestations. *J. Clin. Invest.* **124**, 5516–5520 (2014).
361. B. Lin, R. Berard, A. Al Rasheed, B. Aladba, P. J. Kranzusch, M. Henderlight, A. Grom, D. Kahle, S. Torreggiani, A. G. Aue, J. Mitchell, A. A. de Jesus, G. S. Schulert, R. Goldbach-Mansky, A novel STING1 variant causes a recessive form of STING-associated vasculopathy with onset in infancy (SAVI). *J. Allergy Clin. Immunol.* **146**, 1204-1208.e6 (2020).
362. J. An, L. Durcan, R. M. Karr, T. A. Briggs, G. I. Rice, T. H. Teal, J. J. Woodward, K. B. Elkon, Expression of Cyclic GMP-AMP Synthase in Patients With Systemic Lupus Erythematosus. *Arthritis Rheumatol. (Hoboken, N.J.)*. **69**, 800–807 (2017).
363. D. B. Stetson, J. S. Ko, T. Heidmann, R. Medzhitov, Trex1 prevents cell-intrinsic initiation of autoimmunity. *Cell*. **134**, 587–598 (2008).
364. K. Peschke, M. Achleitner, K. Frenzel, A. Gerbaulet, S. R. Ada, N. Zeller, S. Lienenklaus, M. Lesche, C. Poulet, R. Naumann, A. Dahl, U. Ravens, C. Günther, W. Müller, K.-P. Knobeloch, M. Prinz, A. Roers, R. Behrendt, Loss of Trex1 in Dendritic Cells Is Sufficient To Trigger Systemic Autoimmunity. *J. Immunol.* **197**, 2157–2166 (2016).
365. G. J. Seo, A. Yang, B. Tan, S. Kim, Q. Liang, Y. Choi, W. Yuan, P. Feng, H. S. Park, J. U. Jung, Akt Kinase-Mediated Checkpoint of cGAS DNA Sensing Pathway. *Cell Rep.* **13**, 440–449 (2015).
366. B. Yang, Y. Liu, Y. Cui, D. Song, G. Zhang, S. Ma, Y. Liu, M. Chen, F. Chen, H. Wang, J. Wang, RNF90 negatively regulates cellular antiviral responses by targeting MITA for degradation. *PLoS Pathog.* **16** (2020), doi:10.1371/JOURNAL.PPAT.1008387.
367. B. Zhong, L. Zhang, C. Lei, Y. Li, A. P. Mao, Y. Yang, Y. Y. Wang, X. L. Zhang, H. B. Shu, The ubiquitin ligase RNF5 regulates antiviral responses by mediating degradation of the adaptor protein MITA. *Immunity*. **30**, 397–407 (2009).
368. V. Pokatayev, K. Yang, X. Tu, N. Dobbs, J. Wu, R. G. Kalb, N. Yan, Homeostatic regulation of STING protein at the resting state by stabilizer TOLLIP. *Nat. Immunol.* **21**, 158–167 (2020).
369. N. Dobbs, N. Burnaevskiy, D. Chen, V. K. Gonugunta, N. M. Alto, N. Yan, STING Activation by Translocation from the ER Is Associated with Infection and Autoinflammatory Disease. *Cell Host Microbe*. **18**, 157–168 (2015).
370. E. Ogawa, K. Mukai, K. Saito, H. Arai, T. Taguchi, The binding of TBK1 to STING requires exocytic membrane traffic from the ER. *Biochem. Biophys. Res. Commun.* **503**, 138–145 (2018).
371. Z. Deng, Z. Chong, C. S. Law, K. Mukai, F. O. Ho, T. Martinu, B. J. Backes, W. L.

Eckalbar, T. Taguchi, A. K. Shum, A defect in COPI-mediated transport of STING causes immune dysregulation in COPA syndrome. *J. Exp. Med.* **217** (2020), doi:10.1084/JEM.20201045.

372. K. Mukai, E. Ogawa, R. Uematsu, Y. Kuchitsu, F. Kiku, T. Uemura, S. Waguri, T. Suzuki, N. Dohmae, H. Arai, A. K. Shum, T. Taguchi, Homeostatic regulation of STING by retrograde membrane traffic to the ER. *Nat. Commun. 2021 121*. **12**, 1–9 (2021).
373. V. K. Gonugunta, T. Sakai, V. Pokatayev, K. Yang, J. Wu, N. Dobbs, N. Yan, Trafficking-Mediated STING Degradation Requires Sorting to Acidified Endolysosomes and Can Be Targeted to Enhance Anti-tumor Response. *Cell Rep.* **21**, 3234–3242 (2017).
374. W. Zhao, Negative regulation of TBK1-mediated antiviral immunity. *FEBS Lett.* **587**, 542–548 (2013).
375. C. A. Jefferies, Regulating IRFs in IFN Driven Disease. *Front. Immunol.* **10** (2019), doi:10.3389/FIMMU.2019.00325.
376. T. Taniguchi, K. Ogasawara, A. Takaoka, N. Tanaka, IRF family of transcription factors as regulators of host defense. *Annu. Rev. Immunol.* **19**, 623–655 (2001).
377. S. W. Plouffe, K. C. Lin, J. L. Moore, F. E. Tan, S. Ma, Z. Ye, Y. Qiu, B. Ren, K. L. Guan, The Hippo pathway effector proteins YAP and TAZ have both distinct and overlapping functions in the cell. *J. Biol. Chem.* **293**, 11230–11240 (2018).
378. M. Fu, Y. Hu, T. Lan, K. L. Guan, T. Luo, M. Luo, The Hippo signalling pathway and its implications in human health and diseases. *Signal Transduct. Target. Ther.* **7** (2022), doi:10.1038/S41392-022-01191-9.
379. J. Wu, A. M. Minikes, M. Gao, H. Bian, Y. Li, B. R. Stockwell, Z. N. Chen, X. Jiang, Intercellular interaction dictates cancer cell ferroptosis via NF2-YAP signalling. *Nature*. **572**, 402–406 (2019).
380. S. Z. Shalhout, P. Y. Yang, E. M. Grzelak, K. Nutsch, S. Shao, C. Zambaldo, J. Iaconelli, L. Ibrahim, C. Stanton, S. R. Chadwick, E. Chen, M. DeRan, S. Li, M. Hull, X. Wu, A. K. Chatterjee, W. Shen, F. D. Camargo, P. G. Schultz, M. J. Bollong, YAP-dependent proliferation by a small molecule targeting annexin A2. *Nat. Chem. Biol.* **17**, 767–775 (2021).
381. B. Zhao, L. Li, L. Wang, C. Y. Wang, J. Yu, K. L. Guan, Cell detachment activates the Hippo pathway via cytoskeleton reorganization to induce anoikis. *Genes Dev.* **26**, 54–68 (2012).
382. S. Y. Kim, S. Y. Park, H. S. Jang, Y. D. Park, S. H. Kee, Yes-Associated Protein Is Required for ZO-1-Mediated Tight-Junction Integrity and Cell Migration in E-Cadherin-Restored AGS Gastric Cancer Cells. *Biomedicines*. **9** (2021), doi:10.3390/BIOMEDICINES9091264.
383. A. W. Hong, Z. Meng, K. L. Guan, The Hippo pathway in intestinal regeneration and disease. *Nat. Rev. Gastroenterol. Hepatol.* **13**, 324–337 (2016).
384. L. Zheng, C. J. Kelly, S. P. Colgan, Physiologic hypoxia and oxygen homeostasis in the healthy intestine. A Review in the Theme: Cellular Responses to Hypoxia. *Am. J. Physiol. Cell Physiol.* **309**, C350–C360 (2015).
385. B. Ma, Y. Chen, L. Chen, H. Cheng, C. Mu, J. Li, R. Gao, C. Zhou, L. Cao, J. Liu, Y. Zhu, Q. Chen, S. Wu, Hypoxia regulates Hippo signalling through the SIAH2 ubiquitin E3 ligase. *Nat. Cell Biol.* **17**, 95–103 (2015).
386. L. Yan, Q. Cai, Y. Xu, Hypoxic conditions differentially regulate TAZ and YAP in cancer cells. *Arch. Biochem. Biophys.* **562**, 31–36 (2014).
387. B. Ma, H. Cheng, R. Gao, C. Mu, L. Chen, S. Wu, Q. Chen, Y. Zhu, Zyxin-Siah2-Lats2 axis mediates cooperation between Hippo and TGF-β signalling pathways. *Nat. Commun.* **7** (2016), doi:10.1038/NCOMMS11123.
388. E. W. Tao, H. L. Wang, W. Y. Cheng, Q. Q. Liu, Y. X. Chen, Q. Y. Gao, A specific tRNA half, 5'tiRNA-His-GTG, responds to hypoxia via the HIF1α/ANG axis and promotes colorectal cancer progression by regulating LATS2. *J. Exp. Clin. Cancer Res.* **40** (2021), doi:10.1186/S13046-021-01836-7.
389. S. E. Cavanaugh, A. M. Holmgren, G. F. Rall, Homeostatic interferon expression in neurons is sufficient for early control of viral infection. *J. Neuroimmunol.* **279**, 11–19

(2015).

390. S. V. Kotenko, J. E. Durbin, Contribution of type III interferons to antiviral immunity: location, location, location. *J. Biol. Chem.* **292**, 7295–7303 (2017).
391. H. M. Lazear, T. J. Nice, M. S. Diamond, Interferon-λ: Immune Functions at Barrier Surfaces and Beyond. *Immunity*. **43**, 15–28 (2015).
392. A. Wack, E. Terczyńska-Dyla, R. Hartmann, Guarding the frontiers: the biology of type III interferons. *Nat. Immunol.* **16**, 802–809 (2015).
393. A. I. Wells, C. B. Coyne, Type III Interferons in Antiviral Defenses at Barrier Surfaces. *Trends Immunol.* **39**, 848–858 (2018).
394. K. Jundi, C. M. Greene, Transcription of Interleukin-8: How Altered Regulation Can Affect Cystic Fibrosis Lung Disease. *Biomolecules*. **5**, 1386–1398 (2015).
395. E. Hoffmann, O. Dittrich-Breiholz, H. Holtmann, M. Kracht, Multiple control of interleukin-8 gene expression. *J. Leukoc. Biol.* **72**, 847–855 (2002).
396. N. Vij, M. O. Amoako, S. Mazur, P. L. Zeitlin, CHOP transcription factor mediates IL-8 signaling in cystic fibrosis bronchial epithelial cells. *Am. J. Respir. Cell Mol. Biol.* **38**, 176–184 (2008).
397. J. Hisatsune, M. Nakayama, H. Isomoto, H. Kurazono, N. Mukaida, A. K. Mukhopadhyay, T. Azuma, Y. Yamaoka, J. Sap, E. Yamasaki, K. Yahiro, J. Moss, T. Hirayama, Molecular characterization of Helicobacter pylori VacA induction of IL-8 in U937 cells reveals a prominent role for p38MAPK in activating transcription factor-2, cAMP response element binding protein, and NF-kappaB activation. *J. Immunol.* **180**, 5017–5027 (2008).
398. M. Baggiolini, Chemokines and leukocyte traffic. *Nature*. **392**, 565–568 (1998).
399. J. B. Y. Richman-Eisenstat, P. G. Jorens, C. A. Hebert, I. Ueki, J. A. Nadel, Interleukin-8: an important chemoattractant in sputum of patients with chronic inflammatory airway diseases. *Am. J. Physiol.* **264** (1993), doi:10.1152/AJPLUNG.1993.264.4.L413.
400. T. L. Bonfield, J. R. Panuska, M. W. Konstan, K. A. Hilliard, J. B. Hilliard, H. Ghnaim, M. Berger, Inflammatory cytokines in cystic fibrosis lungs. *Am. J. Respir. Crit. Care Med.* **152**, 2111–2118 (1995).
401. S. D. Sagel, R. Kapsner, I. Osberg, M. K. Sontag, F. J. Accurso, Airway inflammation in children with cystic fibrosis and healthy children assessed by sputum induction. *Am. J. Respir. Crit. Care Med.* **164**, 1425–1431 (2001).
402. N. Mayer-Hamblett, M. L. Aitken, F. J. Accurso, R. A. Kronmal, M. W. Konstan, J. L. Burns, S. D. Sagel, B. W. Ramsey, Association between pulmonary function and sputum biomarkers in cystic fibrosis. *Am. J. Respir. Crit. Care Med.* **175**, 822–828 (2007).
403. I. Y. Lee, J. M. Lim, H. Cho, E. Kim, Y. Kim, H. K. Oh, W. S. Yang, K. H. Roh, H. W. Park, J. S. Mo, J. H. Yoon, H. K. Song, E. J. Choi, MST1 Negatively Regulates TNFα-Induced NF-κB Signaling through Modulating LUBAC Activity. *Mol. Cell*. **73**, 1138-1149.e6 (2019).
404. M. Kapoor, J. Martel-Pelletier, D. Lajeunesse, J. P. Pelletier, H. Fahmi, Role of proinflammatory cytokines in the pathophysiology of osteoarthritis. *Nat. Rev. Rheumatol.* **7**, 33–42 (2011).
405. Y. Lv, K. Kim, Y. Sheng, J. Cho, Z. Qian, Y. Y. Zhao, G. Hu, D. Pan, A. B. Malik, G. Hu, YAP Controls Endothelial Activation and Vascular Inflammation Through TRAF6. *Circ. Res.* **123**, 43–56 (2018).
406. Y. Deng, J. Lu, W. Li, A. Wu, X. Zhang, W. Tong, K. K. Ho, L. Qin, H. Song, K. K. Mak, Reciprocal inhibition of YAP/TAZ and NF-κB regulates osteoarthritic cartilage degradation. *Nat. Commun.* **9** (2018), doi:10.1038/S41467-018-07022-2.
407. T. J. Hagenbeek, J. D. Webster, N. M. Kljavin, M. T. Chang, T. Pham, H. J. Lee, C. Klijn, A. G. Cai, K. Totpal, B. Ravishankar, N. Yang, D. H. Lee, K. B. Walsh, G. Hatzivassiliou, C. C. De La Cruz, S. E. Gould, X. Wu, W. P. Lee, S. Yang, Z. Zhang, Q. Gu, Q. Ji, E. L. Jackson, D. S. Lim, A. Dey, The Hippo pathway effector TAZ induces TEAD-dependent liver inflammation and tumors. *Sci. Signal.* **11** (2018), doi:10.1126/SCISIGNAL.AAJ1757.
408. M. Mooring, B. H. Fowl, S. Z. C. Lum, Y. Liu, K. Yao, S. Softic, R. Kirchner, A. Bernstein,

A. D. Singhi, D. G. Jay, C. R. Kahn, F. D. Camargo, D. Yimlamai, Hepatocyte Stress Increases Expression of Yes-Associated Protein and Transcriptional Coactivator With PDZ-Binding Motif in Hepatocytes to Promote Parenchymal Inflammation and Fibrosis. *Hepatology*. **71**, 1813–1830 (2020).

409. H. L. Piao, Y. Yuan, M. Wang, Y. Sun, H. Liang, L. Ma, α-catenin acts as a tumour suppressor in E-cadherin-negative basal-like breast cancer by inhibiting NF-κB signalling. *Nat. Cell Biol.* **16**, 245–254 (2014).
410. I. Turcan, M. F. Jonkman, Blistering disease: insight from the hemidesmosome and other components of the dermal-epidermal junction. *Cell Tissue Res.* **360**, 545–569 (2015).
411. J. C. Lessard, S. Piña-Paz, J. D. Rotty, R. P. Hickerson, R. L. Kaspar, A. Balmain, P. A. Coulombe, Keratin 16 regulates innate immunity in response to epidermal barrier breach. *Proc. Natl. Acad. Sci. U. S. A.* **110**, 19537–19542 (2013).
412. Y. Zhang, B. J. Hwang, Z. Liu, N. Li, K. Lough, S. E. Williams, J. Chen, S. W. Burette, L. A. Diaz, M. A. Su, S. Xiao, Z. Liu, BP180 dysfunction triggers spontaneous skin inflammation in mice. *Proc. Natl. Acad. Sci. U. S. A.* **115**, 6434–6439 (2018).
413. C. Niculescu, G. Ganguli-Indra, V. Pfister, V. Dupé, N. Messaddeq, A. De Arcangelis, E. Georges-Labouesse, Conditional ablation of integrin alpha-6 in mouse epidermis leads to skin fragility and inflammation. *Eur. J. Cell Biol.* **90**, 270–277 (2011).
414. A. De Arcangelis, H. Hamade, F. Alpy, S. Normand, E. Bruyère, O. Lefebvre, A. Méchine-Neuville, S. Siebert, V. Pfister, P. Lepage, P. Laquerriere, D. Dembele, A. Delanoye-Crespin, S. Rodius, S. Robine, M. Kedinger, I. Van Seuningen, P. Simon-Assmann, M. Chamaillard, M. Labouesse, E. Georges-Labouesse, Hemidesmosome integrity protects the colon against colitis and colorectal cancer. *Gut*. **66**, 1748–1760 (2017).
415. L. Samuelov, O. Sarig, R. M. Harmon, D. Rapaport, A. Ishida-Yamamoto, O. Isakov, J. L. Koetsier, A. Gat, I. Goldberg, R. Bergman, R. Spiegel, O. Eytan, S. Geller, S. Peleg, N. Shomron, C. S. M. Goh, N. J. Wilson, F. J. D. Smith, E. Pohler, M. A. Simpson, W. H. I. McLean, A. D. Irvine, M. Horowitz, J. A. McGrath, K. J. Green, E. Sprecher, Desmoglein 1 deficiency results in severe dermatitis, multiple allergies and metabolic wasting. *Nat. Genet.* **45**, 1244–1248 (2013).
416. G. Z. Tao, P. Strnad, Q. Zhou, A. Kamal, L. Zhang, N. D. Madani, S. Kugathasan, S. R. Brant, J. H. Cho, M. B. Omary, R. H. Duerr, Analysis of keratin polypeptides 8 and 19 variants in inflammatory bowel disease. *Clin. Gastroenterol. Hepatol.* **5**, 857–864 (2007).
417. D. W. Owens, N. J. Wilson, A. J. M. Hill, E. L. Rugg, R. M. Porter, A. M. Hutcheson, R. A. Quinlan, D. van Heel, M. Parkes, D. P. Jewell, S. S. Campbell, S. Ghosh, J. Satsangi, E. B. Lane, Human keratin 8 mutations that disturb filament assembly observed in inflammatory bowel disease patients. *J. Cell Sci.* **117**, 1989–1999 (2004).
418. R. W. Walters, T. Grunst, J. M. Bergelson, R. W. Finberg, M. J. Welsh, J. Zabner, Basolateral localization of fiber receptors limits adenovirus infection from the apical surface of airway epithelia. *J. Biol. Chem.* **274**, 10219–10226 (1999).
419. S. Fuller, C. H. von Bonsdorff, K. Simons, Vesicular stomatitis virus infects and matures only through the basolateral surface of the polarized epithelial cell line, MDCK. *Cell*. **38**, 65–77 (1984).
420. S. D. Fuller, C. H. von Bonsdorff, K. Simons, Cell surface influenza haemagglutinin can mediate infection by other animal viruses. *EMBO J.* **4**, 2475–2485 (1985).
421. P. D. Vermeer, J. McHugh, T. Rokhlina, D. W. Vermeer, J. Zabner, M. J. Welsh, Vaccinia virus entry, exit, and interaction with differentiated human airway epithelia. *J. Virol.* **81**, 9891–9899 (2007).
422. D. Rodriguez, J. R. Rodriguez, G. K. Ojakian, M. Esteban, Vaccinia virus preferentially enters polarized epithelial cells through the basolateral surface. *J. Virol.* **65**, 494–498 (1991).
423. D. H. Rubin, Reovirus serotype 1 binds to the basolateral membrane of intestinal epithelial cells. *Microb. Pathog.* **3**, 215–219 (1987).

424. K. J. D. A. Excoffon, K. M. Guglielmi, J. D. Wetzel, N. D. Gansemer, J. A. Campbell, T. S. Dermody, J. Zabner, Reovirus preferentially infects the basolateral surface and is released from the apical surface of polarized human respiratory epithelial cells. *J. Infect. Dis.* **197**, 1189–1197 (2008).
425. D. Cevallos Porta, S. López, C. F. Arias, P. Isa, Polarized rotavirus entry and release from differentiated small intestinal cells. *Virology.* **499**, 65–71 (2016).
426. T. Cui, S. Theuns, J. Xie, H. J. Nauwynck, Porcine rotavirus mainly infects primary porcine enterocytes at the basolateral surface. *Vet. Res.* **50** (2019), doi:10.1186/S13567-019-0728-X.
427. M. A. Jarvis, C. E. Wang, H. L. Meyers, P. P. Smith, C. L. Corless, G. J. Henderson, J. Vieira, W. J. Britt, J. A. Nelson, Human cytomegalovirus infection of caco-2 cells occurs at the basolateral membrane and is differentiation state dependent. *J. Virol.* **73**, 4552–4560 (1999).
428. E. S. Barton, J. C. Forrest, J. L. Connolly, J. D. Chappell, Y. Liu, F. J. Schnell, A. Nusrat, C. A. Parkos, T. S. Dermody, Junction adhesion molecule is a receptor for reovirus. *Cell.* **104**, 441–451 (2001).
429. F. Salamanna, M. Maglio, M. P. Landini, M. Fini, Body Localization of ACE-2: On the Trail of the Keyhole of SARS-CoV-2. *Front. Med.* **7** (2020), doi:10.3389/FMED.2020.594495.
430. F. J. Warner, R. A. Lew, A. I. Smith, D. W. Lambert, N. M. Hooper, A. J. Turner, Angiotensin-converting enzyme 2 (ACE2), but not ACE, is preferentially localized to the apical surface of polarized kidney cells. *J. Biol. Chem.* **280**, 39353–39362 (2005).
431. S. Hao, K. Ning, C. A. Kuz, K. Vorhies, Z. Yan, J. Qiu, Long-Term Modeling of SARS-CoV-2 Infection of In Vitro Cultured Polarized Human Airway Epithelium. *MBio.* **11**, 1–17 (2020).
432. T. Pelaseyed, J. H. Bergström, J. K. Gustafsson, A. Ermund, G. M. H. Birchenough, A. Schütte, S. van der Post, F. Svensson, A. M. Rodríguez-Piñeiro, E. E. L. Nyström, C. Wising, M. E. V. Johansson, G. C. Hansson, The mucus and mucins of the goblet cells and enterocytes provide the first defense line of the gastrointestinal tract and interact with the immune system. *Immunol. Rev.* **260**, 8–20 (2014).
433. K. B. Adler, M. J. Tuvim, B. F. Dickey, Regulated mucin secretion from airway epithelial cells. *Front. Endocrinol. (Lausanne).* **4** (2013), doi:10.3389/FENDO.2013.00129.
434. J. H. Klinkspoor, K. S. Mok, B. J. W. Van Klinken, G. N. J. Tytgat, S. P. Lee, A. K. Groen, Mucin secretion by the human colon cell line LS174T is regulated by bile salts. *Glycobiology.* **9**, 13–19 (1999).
435. D. H. Hong, G. Petrovics, W. B. Anderson, J. Forstner, G. Forstner, Induction of mucin gene expression in human colonic cell lines by PMA is dependent on PKC-epsilon. *Am. J. Physiol.* **277** (1999), doi:10.1152/AJPGI.1999.277.5.G1041.
436. F. Martín-Belmonte, J. A. Martínez-Menárguez, J. F. Aranda, J. Ballesta, M. C. De Marco, M. A. Alonso, MAL regulates clathrin-mediated endocytosis at the apical surface of Madin-Darby canine kidney cells. *J. Cell Biol.* **163**, 155–164 (2003).
437. H. Y. Naim, D. T. Dodds, C. B. Brewer, M. G. Roth, Apical and basolateral coated pits of MDCK cells differ in their rates of maturation into coated vesicles, but not in the ability to distinguish between mutant hemagglutinin proteins with different internalization signals. *J. Cell Biol.* **129**, 1241–1250 (1995).
438. S. Boulant, C. Kural, J. C. Zeeh, F. Ubelmann, T. Kirchhausen, Actin dynamics counteract membrane tension during clathrin-mediated endocytosis. *Nat. Cell Biol.* **13**, 1124–1132 (2011).
439. X. P. Lin, J. D. Mintern, P. A. Gleeson, Macropinocytosis in Different Cell Types: Similarities and Differences. *Membranes (Basel).* **10**, 1–21 (2020).
440. T. A. Selvakumar, S. Bhushal, U. Kalinke, D. Wirth, H. Hauser, M. Köster, M. W. Hornef, Identification of a Predominantly Interferon-λ-Induced Transcriptional Profile in Murine Intestinal Epithelial Cells. *Front. Immunol.* **8** (2017), doi:10.3389/FIMMU.2017.01302.
441. T. Marcello, A. Grakoui, G. Barba-Spaeth, E. S. Machlin, S. V. Kotenko, M. R. Macdonald, C. M. Rice, Interferons α and λ Inhibit Hepatitis C Virus Replication With

Distinct Signal Transduction and Gene Regulation Kinetics. *Gastroenterology*. **131**, 1887–1898 (2006).

442. N. Jilg, W. Lin, J. Hong, E. A. Schaefer, D. Wolski, J. Meixong, K. Goto, C. Brisac, P. Chusri, D. N. Fusco, S. Chevaliez, J. Luther, K. Kumthip, T. J. Urban, L. F. Peng, G. M. Lauer, R. T. Chung, Kinetic differences in the induction of interferon stimulated genes by interferon-α and interleukin 28B are altered by infection with hepatitis C virus. *Hepatology*. **59**, 1250–1261 (2014).
443. Z. Zhou, O. J. Hamming, N. Ank, S. R. Paludan, A. L. Nielsen, R. Hartmann, Type III Interferon (IFN) Induces a Type I IFN-Like Response in a Restricted Subset of Cells through Signaling Pathways Involving both the Jak-STAT Pathway and the Mitogen-Activated Protein Kinases. *J. Virol.* **81**, 7749–7758 (2007).
444. J. Da Lin, N. Feng, A. Sen, M. Balan, H. C. Tseng, C. McElrath, S. V. Smirnov, J. Peng, L. L. Yasukawa, R. K. Durbin, J. E. Durbin, H. B. Greenberg, S. V. Kotenko, Distinct Roles of Type I and Type III Interferons in Intestinal Immunity to Homologous and Heterologous Rotavirus Infections. *PLoS Pathog.* **12** (2016), doi:10.1371/journal.ppat.1005600.
445. M. L. Stanifer, C. Kee, M. Cortese, C. M. Zumaran, S. Triana, M. Mukenhirn, H. G. Kraeusslich, T. Alexandrov, R. Bartenschlager, S. Boulant, Critical Role of Type III Interferon in Controlling SARS-CoV-2 Infection in Human Intestinal Epithelial Cells. *Cell Rep.* **32** (2020), doi:10.1016/J.CELREP.2020.107863.
446. E. M. Coccia, B. Krust, A. G. Hovanessian, Specific inhibition of viral protein synthesis in HIV-infected cells in response to interferon treatment. *J. Biol. Chem.* **269**, 23087–23094 (1994).
447. M. S. Diamond, E. Harris, Interferon inhibits dengue virus infection by preventing translation of viral RNA through a PKR-independent mechanism. *Virology*. **289**, 297–311 (2001).
448. A. J. Sadler, B. R. G. Williams, Interferon-inducible antiviral effectors. *Nat. Rev. Immunol.* **8**, 559–568 (2008).
449. M. S. Diamond, M. Farzan, The broad-spectrum antiviral functions of IFIT and IFITM proteins. *Nat. Rev. Immunol.* **13** (2013), pp. 46–57.
450. G. I. Vladimer, M. W. Górna, G. Superti-Furga, IFITs: Emerging roles as key anti-viral proteins. *Front. Immunol.* **5** (2014), , doi:10.3389/fimmu.2014.00094.
451. M. Biggioggero, L. Gabbriellini, P. L. Meroni, "Type I interferon therapy and its role in autoimmunity" in *Autoimmunity* (Taylor & Francis, 2010; https://www.tandfonline.com/doi/abs/10.3109/08916930903510971), vol. 43, pp. 248–254.
452. D. Jhuti, A. Rawat, C. M. Guo, L. A. Wilson, E. J. Mills, J. I. Forrest, Interferon Treatments for SARS-CoV-2: Challenges and Opportunities. *Infect. Dis. Ther.* **11**, 953–972 (2022).
453. D. Ma, X. Wang, M. Li, C. Hu, L. Tang, Reconsideration of interferon treatment for viral diseases: Lessons from SARS, MERS, and COVID-19. *Int. Immunopharmacol.* **121** (2023), doi:10.1016/J.INTIMP.2023.110485.
454. G. Reis, E. A. S. Moreira Silva, D. C. Medeiros Silva, L. Thabane, V. H. S. Campos, T. S. Ferreira, C. V. Q. Santos, A. M. R. Nogueira, A. P. F. G. Almeida, L. C. M. Savassi, A. D. Figueiredo-Neto, A. C. F. Dias, A. M. Freire Júnior, C. Bitarães, A. C. Milagres, E. D. Callegari, M. I. C. Simplicio, L. B. Ribeiro, R. Oliveira, O. Harari, L. A. Wilson, J. I. Forrest, H. Ruton, S. Sprague, P. McKay, C. M. Guo, E. H. Limbrick-Oldfield, S. Kanters, G. H. Guyatt, C. R. Rayner, C. Kandel, M. J. Biondi, R. Kozak, B. Hansen, M. A. Zahoor, P. Arora, C. Hislop, I. Choong, J. J. Feld, E. J. Mills, J. S. Glenn, Early Treatment with Pegylated Interferon Lambda for Covid-19. *N. Engl. J. Med.* **388**, 518–528 (2023).
455. A. G. Laing, A. Lorenc, I. del Molino del Barrio, A. Das, M. Fish, L. Monin, M. Muñoz-Ruiz, D. R. McKenzie, T. S. Hayday, I. Francos-Quijorna, S. Kamdar, M. Joseph, D. Davies, R. Davis, A. Jennings, I. Zlatareva, P. Vantourout, Y. Wu, V. Sofra, F. Cano, M. Greco, E. Theodoridis, J. Freedman, S. Gee, J. N. E. Chan, S. Ryan, E. Bugallo-Blanco, P. Peterson, K. Kisand, L. Haljasmägi, L. Chadli, P. Moingeon, L. Martinez, B. Merrick,

K. Bisnauthsing, K. Brooks, M. A. A. Ibrahim, J. Mason, F. Lopez Gomez, K. Babalola, S. Abdul-Jawad, J. Cason, C. Mant, J. Seow, C. Graham, K. J. Doores, F. Di Rosa, J. Edgeworth, M. Shankar-Hari, A. C. Hayday, A dynamic COVID-19 immune signature includes associations with poor prognosis. *Nat. Med.* **26**, 1623–1635 (2020).

456. E. Y. Wang, T. Mao, J. Klein, Y. Dai, J. D. Huck, F. Liu, N. S. Zheng, T. Zhou, B. Israelow, P. Wong, C. Lucas, J. Silva, J. E. Oh, E. Song, E. S. Perotti, S. Fischer, M. Campbell, J. B. Fournier, A. L. Wyllie, C. B. F. Vogels, I. M. Ott, C. C. Kalinich, M. E. Petrone, A. E. Watkins, Yale IMPACT Team, C. Dela Cruz, S. F. Farhadian, W. L. Schulz, N. D. Grubaugh, A. I. Ko, A. Iwasaki, A. M. Ring, Diverse Functional Autoantibodies in Patients with COVID-19. *medRxiv Prepr. Serv. Heal. Sci.* (2021), doi:10.1101/2020.12.10.20247205.
457. S. B, B. A, P. L, C. S, C. N, F. R, S. S, C. E, S. R, L. JM, A. A, L. E, F. V, S. L, B. S, M. L, F. FA, B. A, F. T, C. R, C. M, T. E, C. J, P. AE, M. F, W. A, M. N, Z. I, The interferon landscape along the respiratory tract impacts the severity of COVID-19. *Cell*. **184** (2021), doi:10.1016/J.CELL.2021.08.016.
458. Y. Wang, I. L. Chiang, T. E. Ohara, S. Fujii, J. Cheng, B. D. Muegge, A. Ver Heul, N. D. Han, Q. Lu, S. Xiong, F. Chen, C. W. Lai, H. Janova, R. Wu, C. E. Whitehurst, K. L. VanDussen, T. C. Liu, J. I. Gordon, L. D. Sibley, T. S. Stappenbeck, Long-Term Culture Captures Injury-Repair Cycles of Colonic Stem Cells. *Cell*. **179**, 1144-1159.e15 (2019).
459. A. Pitaval, Q. Tseng, M. Bornens, M. Théry, Cell shape and contractility regulate ciliogenesis in cell cycle-arrested cells. *J. Cell Biol.* **191**, 303–312 (2010).
460. H. Y. Yoshikawa, F. F. Rossetti, S. Kaufmann, T. Kaindl, J. Madsen, U. Engel, A. L. Lewis, S. P. Armes, M. Tanaka, Quantitative evaluation of mechanosensing of cells on dynamically tunable hydrogels. *J. Am. Chem. Soc.* **133**, 1367–1374 (2011).
461. M. P. King, G. Attardi, Human cells lacking mtDNA: repopulation with exogenous mitochondria by complementation. *Science*. **246**, 500–503 (1989).
462. R. Meier, A. Franceschini, P. Horvath, M. Tetard, R. Mancini, C. von Mering, A. Helenius, P.-Y. Lozach, Genome-wide small interfering RNA screens reveal VAMP3 as a novel host factor required for Uukuniemi virus late penetration. *J. Virol.* **88**, 8565–8578 (2014).
463. A. Shevchenko, M. Wilm, O. Vorm, M. Mann, Mass spectrometric sequencing of proteins silver-stained polyacrylamide gels. *Anal. Chem.* **68**, 850–858 (1996).
464. S. Tyanova, T. Temu, J. Cox, The MaxQuant computational platform for mass spectrometry-based shotgun proteomics. *Nat. Protoc.* **11**, 2301–2319 (2016).
465. L. Rappez, M. Stadler, S. Triana, R. M. Gathungu, K. Ovchinnikova, P. Phapale, M. Heikenwalder, T. Alexandrov, SpaceM reveals metabolic states of single cells. *Nat. Methods*. **18**, 799–805 (2021).
466. T. Pelaseyed, A. Bretscher, Regulation of actin-based apical structures on epithelial cells. *J. Cell Sci.* **131** (2018), doi:10.1242/JCS.221853.
467. G. J. Anderson, M. D. Walsh, L. W. Powell, J. W. Halliday, Intestinal transferrin receptors and iron absorption in the neonatal rat. *Br. J. Haematol.* **77**, 229–236 (1991).